AFWAL-TR-80-3070

LEVEL II

(2)

AD A101121-0

HIGH ANGLE OF ATTACK MISSILE AERODYNAMICS AT MACH NUMBERS 0.30 TO 1.5

Valentine Dahlem
Jack I. Flaherty
Donald E. Shereda
High-Speed Aero-Performance Branch
Aeromechanics Division

Christian E. G. Przirembel
Rutgers, The State University of New Jersey

DTIC
ELECTE
JUL 0 9 1981
S D
E

November 1980

TECHNICAL REPORT AFWAL-TR-80-3070

Final Report for Period March 1975 to April 1979

Approved for Public Release; Distribution Unlimited

DTIC FILE COPY

FLIGHT DYNAMICS LABORATORY
AIR FORCE WRIGHT AERONAUTICAL LABORATORIES
AIR FORCE SYSTEMS COMMAND
WRIGHT-PATTERSON AIR FORCE BASE OHIO 45433

81 7 10 095

NOTICE

When Government drawings, specifications, or other data are used for any purpose other than in connection with a definitely related Government procurement operation, the United States Government thereby incurs no responsibility nor any obligation whatsoever; and the fact that the government may have formulated, furnished, or in any way supplied the said drawings, specifications, or other data, is not to be regarded by implication or otherwise as in any manner licensing the holder or any other person or corporation, or conveying any rights or permission to manufacture use, or sell any patented invention that may in any way be related thereto.

This report has been reviewed by the Office of Public Affairs (ASD/PA) and is releasable to the National Technical Information Service (NTIS). At NTIS, it will be available to the general public, including foreign nations.

This technical report has been reviewed and is approved for publication.

DONALD E. SHEREDA
Project Engineer
High Speed Aerodynamics Group

VALENTINE DAHLEM
Acting Chief, High Speed Aero Perf. Br.
Aeromechanics Division

FOR THE COMMANDER

PETER J. BUTKEWICZ
COLONEL, USAF
Chief, Aeromechanics Division

"If your address has changed, if you wish to be removed from our mailing list, or if the addressee is no longer employed by your organization please notify AFWAL/FIMG, *W-PAFB, OH 45433 to help us maintain a current mailing list".*

Copies of this report should not be returned unless return is required by security considerations, contractual obligations, or notice on a specific document.

AIR FORCE/56780/23 June 1981 — 75

SECURITY CLASSIFICATION OF THIS PAGE (When Data Entered)

REPORT DOCUMENTATION PAGE

READ INSTRUCTIONS BEFORE COMPLETING FORM

1. REPORT NUMBER: AFWAL-TR-80-3070

2. GOVT ACCESSION NO.: AD-101 210

3. RECIPIENT'S CATALOG NUMBER:

4. TITLE (and Subtitle): HIGH ANGLE OF ATTACK MISSILE AERODYNAMICS AT MACH NUMBERS 0.30 TO 1.5

5. TYPE OF REPORT & PERIOD COVERED: Final Report - Mar 1975 - Apr 1979,

6. PERFORMING ORG. REPORT NUMBER:

7. AUTHOR(S): Valentine Dahlem, Christian E.G. Przirembel, Jack I. Flaherty, Donald E. Shereda

8. CONTRACT OR GRANT NUMBER(s): *

9. PERFORMING ORGANIZATION NAME AND ADDRESS: Flight Dynamics Laboratory (AFWAL/FIMG), AF Wright Aeronautical Laboratories, Wright-Patterson AFB, OH 45433

10. PROGRAM ELEMENT, PROJECT, TASK AREA & WORK UNIT NUMBERS: PE 62201F, Project 2404, Task 240407, Work Unit 24040701

11. CONTROLLING OFFICE NAME AND ADDRESS: Flight Dynamics Laboratory (AFWAL/FIM), AF Wright Aeronautical Laboratories, Wright-Patterson AFB, OH 45433

12. REPORT DATE: November 1980

13. NUMBER OF PAGES: 330

14. MONITORING AGENCY NAME & ADDRESS (if different from Controlling Office):

15. SECURITY CLASS (of this report): Unclassified

15a. DECLASSIFICATION/DOWNGRADING SCHEDULE:

16. DISTRIBUTION STATEMENT (of this Report): Approved for public release; distribution unlimited.

17. DISTRIBUTION STATEMENT (of the abstract entered in Block 20, if different from Report):

18. SUPPLEMENTARY NOTES: * Rutgers, The State University of New Jersey

19. KEY WORDS (Continue on reverse side if necessary and identify by block number):
Asymmetric lee-side vortices
High angles of attack
Slender missile configurations
Induced side forces and yawing moments

20. ABSTRACT (Continue on reverse side if necessary and identify by block number):
A large body of wind tunnel data was generated by tests of a smooth missile model with several interchangable nose parts. The tests were conducted at subsonic through supersonic speeds at angles of attack from 0 to 180 degrees. They were part of the FDL and SAMSO technology studies which preceded design of the MX missile. Measurements of both surface pressures and total forces and moments were made at a variety of Mach numbers and Reynolds number combinations. This data was supplemented with wake flow-field measurements of the impact pressure and flow direction at angles of attack where maximum induced side force was

DD FORM 1 JAN 73 1473 EDITION OF 1 NOV 65 IS OBSOLETE

SECURITY CLASSIFICATION OF THIS PAGE (When Data Entered)

392 662

expected to occur. A review of the literature for subsonic and transonic aerodynamic characteristics of bodies of revolution was conducted. A comprehensive discussion is provided of the important variables of the high angle of attack flow phenomena. The test data provided insight into the effect of several variables that had not been adequately treated in the past. The high angle of attack data was analyzed to deduce the vortex shedding location, the vortex strength, and the vortex paths in the wake. Discrete vortex theory was examined as a method which could be modified, based on experimental data, and used to predict the aerodynamic characteristics of missiles to greater accuracy. An alternate approach to developing a prediction method was explored by means of a correlation of the surface pressure data. The out-of-plane forces were observed to exhibit a statistical pattern. There is a most probable level and an upper bound. A correlation of the maximum aerodynamic loads was made using the concept of a crossflow lift coefficient and the Strouhal number. The influence of nose geometry and free-stream variables is shown.

FOREWORD

This technical report summarizes research performed in-house at the High Speed Aero Performance Branch, Aeromechanics Division, Flight Dynamics Laboratory, Air Force Wright Aeronautical Laboratories, Wright-Patterson Air Force Base. The analytical work was performed under Project 2404, "Aeromechanics," Task 240407, "Aeroperformance and Aeroheating Technology." The experimental work was performed as technical support to the Space and Missile System Organization (SAMSO). The study period was March 1974 to April 1979.

The report was written by Valentine Dahlem, Donald E. Shereda, and Jack I. Flaherty of the High Speed Aero-Performance Branch. One section, the Literature Review, was written by Dr. Christian E.G. Przirembel, Professor of Mechanical Engineering, Rutgers, The State University of New Jersey. Professor Przirembel conducted a review of the high angle-of-attack problem as part of a USAF-ASEE Summer Faculty Research Program at the Flight Dynamics Laboratory.

The experimental program described in this report produced a very large amount of data. The results are summarized here, but in many cases the results of a particular test condition are omitted. Data lists are available to qualified research engineers upon request from the High Speed Aero Performance Branch.

Accession For
NTIS GRA&I ☒
DTIC TAB ☐
Unannounced ☐
Justification
By
Distribution/
Availability Codes
Avail and/or
Dist Special
A

TABLE OF CONTENTS

SECTION		PAGE
I	INTRODUCTION	20
II	LITERATURE REVIEW: STATUS OF THE PROBLEM	22
	1. Basic Physical Features of Various Aerodynamic Regimes	22
	2. Current Status of Experimental Investigation: Regime II	23
	3. Current Status of Experimental Investigations: Regime III	27
	a. Mach Number Effects	28
	b. Reynolds Number Effects	29
	c. Nose Fineness Ratio and Bluntness Effects	31
	d. Geometric Changes to Reduce Side Forces and Yawing Moments	32
	e. Roll Angle and Nose Misalignments	33
	f. Flow Field Unsteadiness	34
	g. Vortex Shedding and Spacing	36
III	EXPERIMENTAL PROGRAM	39
	1. Test Facility	43
	2. Test Hardware and Instrumentation	43
	a. Pressure and Force Tests	43
	b. Flow Field Test	56
	3. Data Reduction	60
	a. Pressure and Force Tests	60
	b. Flow Field Test	64
	4. Precision of Measurements	65
	a. Pressure and Force Tests	65
	b. Flow Field Test	66

TABLE OF CONTENTS (Continued)

SECTION		PAGE
IV	EXPERIMENTAL RESULTS OF THE PRESSURE AND FORCE TESTS	67
	1. Pressure Integration	67
	2. Asymmetric Forces	68
	3. Reynolds Number Effects	81
	4. Mach Number Effects	103
	5. Nose Shape Effects	103
	6. Body Length Effects	169
	7. Roll Angle Effects	191
	8. Grit Effects	200
	9. Strut/Sting Effects	224
	10. Rocket Exhaust Effects	241
V	EXPERIMENTAL FLOW FIELD RESULTS	257
	1. Crossflow Velocity	257
	2 Separation Locations	263
	3. Side Force Coefficient Distributions	265
	4. Unsteady Wake-Pressure Data	265
VI	ANALYSIS OF THE WAKE FLOW FIELD AND MISSILE AERODYNAMICS USING DISCRETE VORTEX THEORY	269
	1. Theoretical Model	269
	a. Velocity Relationships	272
	b. Vortex Strengths and Calculated Vortex Paths	276
	2. Theory Data Comparisons	281
	a. Crossflow Velocity	281
	b. Pressure Coefficient Distributions	285
	c. Normal Force and Side Force Coefficient Distributions	[illegible]

TABLE OF CONTENTS (Continued)

SECTION		PAGE
VII	DEVELOPMENT OF AN EMPIRICAL CORRELATION TECHNIQUE USING PRESSURE DATA	293
	1. Experimental Observations	293
	2. Correlation Development	299
	3. Prediction Method	303
	4. Freestream and Configuration Effects	308
VIII	CONCLUSIONS AND RECOMMENDATIONS	312
	1. Pressure and Force Tests	312
	2. Flow Field Test	313
	3. Flow Field Analysis	314
	4. Correlation Technique	315
	5. Recommendations	315
	REFERENCES	317
	BIBLIOGRAPHY	322

LIST OF ILLUSTRATIONS

FIGURE		PAGE
1	Steady Symmetric Vortices, Regime II ($5° \leq \alpha \leq 20°$)	24
2	Steady Asymmetric Vortices, Regime III ($20° \leq \alpha \leq 70°$)	25
3	Location of Model in Test Section	44
	a. Sting-Mounted Model	44
	b. Sting-Strut-Mounted Model	45
4	Installation of Model	46
	a. Sting-Mounted Model	46
	b. Sting-Strut Mounted Model	47
5	Model Dimensions	48
6	Nose Configurations	52
7	Pressure Orifice and Microphone Location, N2B1 Configuration	54
8	Exhaust Nozzle Details	55
9	Model Support Arrangements	57
10	Model Support Dimensions	58
11	Nose Ring Grit Patterns	61
12	Model Installation for Flow Field Test	62
13	Cone Probe Rake	63
14	Comparisons Between Integrated Pressure and Force Balance Data for Normal Force Coefficient	69
	a. N2B1 Configuration	69
	b. N6B2 Configuration	70
15	Comparison Between Integrated Pressure and Force Balance Data for Axial Force Coefficient	71
	a. N2B1 Configuration	71
	b. N6B2 Configuration	72
16	Comparisons Between Integrated Pressure and Force Balance Data at Various Mach Numbers	73
	a. N2B1 Configuration	73
	b. N6B2 Configuration	74

LIST OF ILLUSTRATIONS (Continued)

FIGURE		PAGE
17	Effect of Angle-of-Attack and Configuration Geometry on the Ratio of Side Force/Normal Force Coefficient	75
	a. Mach 0.4, B1 Body	75
	b. Mach 0.4, B2 Body	76
	c. Mach 0.6, B1 Body	77
	d. Mach 0.6, B2 Body	78
	e. Mach 0.8, B1 Body	79
	f. Mach 0.8, B2 Body	80
18	Variation of Crossflow Reynolds Number with Crossflow Mach Number	83
19	Variation of Crossflow Drag Coefficient with Crossflow Reynolds Number	84
20	Effect of Reynolds Number on Local Pressure Coefficient Distribution	85
	a. x = 10.5	85
	b. x = 17.5	86
	c. x = 26.5	87
	d. x = 46.5	88
	e. x = 66.5	89
	f. x = 77.5	90
21	Effect of Reynolds Number on Force and Moment Coefficients. N2B1 Configuration	92
	a. Effect on Normal Force Coefficient	92
	b. Effect on Side Force Coefficient	93
	c. Effect on Yawing Moment Coefficient	94
22	Effect of Reynolds Number on Force and Moment Coefficient. N3B2 Configuration	95
	a. Effect on Normal Force Coefficient	95
	b. Effect on Side Force Coefficient	96
	c. Effect on Yawing Moment Coefficient	97
23	Force and Moment Coefficients vs Unit Reynolds Number - Sting-Mounted Data	98
	a. N2B1 Configuration	98
	b. N3B2 Configuration	99
	c. N6B2 Configuration	100
24	Force and Moment Coefficients vs Unit Reynolds Number for the N3B2 Configuration - Strut-Mounted Data	101

LIST OF ILLUSTRATIONS (Continued)

FIGURE		PAGE
25	Integrated Pressure Force and Moment Coefficient vs Unit Reynolds Number - N2B1 Configuration	102
26	Normal Force Coefficient vs Mach Number at α = 35°	104
	a. Configurations N2B1, N3B1 and N4B1	104
	b. Configurations N3B2 and N4B2	105
	c. Configurations N5B2 and N6B2	106
27	Side Force and Yawing Moment Coefficient vs Mach Number	107
	a. Configurations N2B1, N3B1 and N4B1 at α = 35°	107
	b. Configurations N2B1, N3B1 and N4B1 at α = 45°	108
	c. Configurations N3B2 and N4B2 at α = 35°	109
	d. Configurations N3B2 and N4B2 at α = 45°	110
	e. Configurations N5B2 and N6B2 at α = 35°	111
	f. Configurations N5B2 and N6B2 at α = 45°	112
28	Model Configurations and Nomenclature	113
29	Effect of Nose Shape on Normal Force Coefficient/B1 Body	114
	a. M = 0.4	114
	b. M = 0.6	115
	c. M = 0.8	116
30	Effect of Nose Shape on Side Force Coefficient/B1 Body	117
	a. M = 0.4	117
	b. M = 0.6	118
	c. M = 0.8	119
31	Effect of Nose Shape on Yawing Moment Coefficient/B1 Body	120
	a. M = 0.4	120
	b. M = 0.6	121
	c. M = 0.8	122
32	Effect of Nose Shape on Normal Coefficient/B2 Body	124
	a. M = 0.4	124
	b. M = 0.6	125
	c. M = 0.8	126
33	Effect of Nose Shape on Side Force Coefficient/B2 Body	127
	a. M = 0.4	127
	b. M = 0.6	128
	c. M = 0.8	129

LIST OF ILLUSTRATIONS (Continued)

FIGURE		PAGE
34	Effect of Nose Shape on Yawing Moment Coefficient/B2 Body	130
	a. M = 0.4	130
	b. M = 0.6	131
	c. M = 0.8	132
35	Comparisons of the 5-Caliber Triconic Nose Shapes--Normal Force Coefficient	133
	a. M = 0.4	133
	b. M = 0.6	134
	c. M = 0.8	135
36	Comparisons of the 5-Caliber Triconic Nose Shapes--Side Force Coefficient	136
	a. M = 0.4	136
	b. M = 0.6	137
	c. M = 0.8	138
37	Comparisons of the 5-Caliber Triconic Nose Shapes--Yawing Moment Coefficient	139
	a. M = 0.4	139
	b. M = 0.6	140
	c. M = 0.8	141
38	Comparisons of the 4-Caliber Triconic Nose Shape - Normal Force Coefficient	142
	a. M = 0.4	142
	b. M = 0.6	143
	c. M = 0.8	144
39	Comparisons of the 4-Caliber Triconic Nose Shapes-Side Force Coefficient	145
	a. M = 0.4	145
	b. M = 0.6	146
	c. M = 0.8	147
40	Comparisons of the 4-Caliber Triconic Nose Shape-Yawing Moment Coefficient	148
	a. M = 0.4	148
	b. M = 0.6	149
	c. M = 0.8	150

LIST OF ILLUSTRATIONS (Continued)

FIGURE		PAGE
41	Comparisons of the Normal Force Coefficient for 3-Caliber Nose Shapes	151
	a. M = 0.4	151
	b. M = 0.6	152
	c. M = 0.7	153
42	Comparisons of the Side Force Coefficient for 3-Caliber Nose Shapes	154
	a. M = 0.4	154
	b. M = 0.6	155
	c. M = 0.7	156
43	Comparisons of the Yawing Moment Coefficient for 3-Caliber Nose Shapes	157
	a. M = 0.4	157
	b. M = 0.6	158
	c. M = 0.7	159
44	Effect of Fineness Ratio of the Triconic Nose Shapes on Normal Force Coefficient - Bluntness Ratio = 0.04D	160
	a. M = 0.4	160
	b. M = 0.6	161
	c. M = 0.8	162
45	Effect of Fineness Ratio of the Triconic Nose Shapes on Side Force Coefficient - Bluntness Ratio = 0.04D	163
	a. M = 0.4	163
	b. M = 0.6	164
	c. M = 0.8	165
46	Effect of Fineness Ratio of the Triconic Nose Shapes on Yawing Moment Coefficient - Bluntness Ratio = 0.04D	166
	a. M = 0.4	166
	b. M = 0.6	167
	c. M = 0.8	168
47	Effect of Fineness Ratio of the Triconic Nose Shapes on Normal Force Coefficients - Bluntness Ratio = 0.08D	170
	a. M = 0.4	170
	b. M = 0.6	171
	c. M = 0.7	172

LIST OF ILLUSTRATIONS (Continued)

FIGURE		PAGE
48	Effect of Fineness Ratio of the Triconic Nose Shapes on Side Force Coefficients - Bluntness Ratio = 0.08D	173
	a. M = 0.4	173
	b. M = 0.6	174
	c. M = 0.7	175
49	Effect of Fineness Ratio of the Triconic Nose Shapes on Yawing Moment Coefficients - Bluntness Ratio = 0.08D	176
	a. M = 0.4	176
	b. M = 0.6	177
	c. M = 0.7	178
50	Comparison of the N3 Ogive Nose and the N5 Triconic Nose - Normal Force Coefficient	179
	a. M = 0.4	179
	b. M = 0.6	180
	c. M = 0.8	181
51	Comparison of the N3 Ogive Nose and N5 Triconic Nose - Side Force Coefficient	182
	a. M = 0.4	182
	b. M = 0.6	183
	c. M = 0.8	184
52	Comparison of the N3 Ogive Nose and N5 Triconic Nose-Yawing Moment Coefficient	185
	a. M = 0.4	185
	b. M = 0.6	186
	c. M = 0.8	187
53	Effect of Body Length on Force Coefficients	188
	a. M = 0.4	188
	b. M = 0.6	189
	c. M = 0.8	190
54	Effect of Body Length on the Distributed Force Coefficients at Mach 0.4	192
55	Effect of Body Length on the Distributed Force Coefficients at Mach 0.6	193

LIST OF ILLUSTRATIONS (Continued)

FIGURE		PAGE
56	Effect of Roll Angle on Normal Force Coefficient/N2B2 Configuration	194
	a. M = 0.4	194
	b. M = 0.6	195
	c. M = 0.7	196
57	Effect of Roll Angle on Side Force Coefficient/N2B2 Configuration	197
	a. M = 0.4	197
	b. M = 0.6	198
	c. M = 0.7	199
58	Effect of Roll Angle on Normal Force Coefficient for the N14 B2 Configuration	201
	a. M = 0.4	201
	b. M = 0.6	202
	c. M = 0.7	203
59	Effect of Roll Angle on Side Force Coefficient for the N14B2 Configurations	204
	a. M = 0.4	204
	b. M = 0.6	205
	c. M = 0.7	206
60	Effect of Nose Geometry and Roll on the Normal Force Coefficient	207
61	Effect of Nose Geometry and Roll on the Side Force Coefficient	208
62	Nose Ring Grit Patterns	209
63	Grit Effects on Normal Force and Axial Force Coefficients	210
	a. Normal Force Coefficient	210
	b. Axial Force Coefficient	211
64	Incremental Differences Between Force and Moment Coefficients with and without Grit	213
	a. Incremental Normal Force Coefficient	213
	b. Incremental Axial Force Coefficient	214
	c. Incremental Side Force Coefficient	215
	d. Incremental Yawing Moment Coefficient	216

LIST OF ILLUSTRATIONS (Continued)

FIGURE		PAGE
65	Grit Effect on Pressure Distribution at X = 3.5	217
66	Comparison Between Grit Strips and Grit Rings Effects on Normal and Axial Force Coefficient	218
	a. M = 0.4	218
	b. M = 0.6	219
67	Comparison Between Grit Strips and Grit Rings Effects on Side Force and Yawing Moment Coefficient	220
	a. M = 0.4	220
	b. M = 0.6	221
68	Effect of Grit wtih Reynolds Number Variation on Force and Moment Coefficients	222
	a. Normal and Axial Force Coefficients	222
	b. Side Force and Yawing Moment Coefficients	223
69	Comparisons Between Strut and Sting Force and Moment Coefficients at Mach 0.4	225
	a. Normal Force Coefficient	225
	b. Axial Force Coefficient	226
	c. Side Force Coefficient	227
	d. Pitching Moment Coefficient	228
	e. Yawing Moment Coefficient	229
70	Comparisons Between Strut and Sting Force and Moment Coefficients at Mach 0.6	230
	a. Normal Force Coefficient	230
	b. Axial Force Coefficient	231
	c. Side Force Coefficient	232
	d. Pitching Moment Coefficient	233
	e. Yawing Moment Coefficient	234
71	Comparison Between Integrated Pressure Data and Balance Data at Mach 0.6/N3B2 Configuration	235
	a. Normal Force Coefficient	235
	b. Side Force Coefficient	236
72	Comparison Between Integrated Pressure and Balance Normal Force Coefficient/N2B1 Configuration	237
	a. M = 0.4	237
	b. M = 0.6	238

LIST OF ILLUSTRATIONS (Continued)

FIGURE		PAGE
73	Comparison Between Integrated Pressure and Balance Side Force Coefficient/N2B1 Configuration	239
	a. M = 0.4	239
	b. M = 0.6	240
74	Percentage Difference Between Sting and Strut Normal Force Coefficient for the N3B2 Configuration vs Mach Number	242
75	Comparison Between Simulated and Flight Nozzle Parameters	243
	a. Exit Pressure Ratio	243
	b. Exit Momentum Flux Ratio	244
76	Effect of Jet Plume on Local Pressure Coefficient Distribution	246
	a. x = 64.58	246
	b. x = 53.58	247
	c. x = 43.58	248
	d. x = 33.58	249
	e. x = 23.58	250
77	Effect of Jet Plume on the Normal Force Coefficient	251
	a. M = 0.6	251
	b. M = 0.8	252
78	Effect of Jet Plume on the Pitching Moment Coefficient	253
	a. M = 0.6	253
	b. M = 0.8	254
79	Integrated Pressure Results Showing Jet Plume Effects on Normal Force Coefficient at M = 0.6	255
80	Experimental Crossflow Perturbation Velocities at Mach 0.4 and Alpha = 45°	259
	a. X/D = 3.78	259
	b. X/D = 7.4	260
	c. X/D = 8.8	260
81	Experimental Crossflow Perturbation Velocities at Mach 0.4 and Alpha = 40°	261
	a. X/D = 7.4	261
	b. X/D = 8.8	261

LIST OF ILLUSTRATIONS (Continued)

FIGURE		PAGE
82	Experimental Crossflow Perturbation Velocities at Mach 0.6 and Alpha = 40°	262
	a. X/D = 7.4	262
83	Deduced Vortex Separation Locations	264
84	Axial Distribution of Local Side Force Coefficient	266
85	Axial Distribution of the Unsteady Wake Pressure Coefficient	268
86	Flow Field Model for the Concentrated Vortex Anzlysis	271
87	Coordinate System	273
88	Nondimensional Vortex Strength vs Crossflow Mach Number	277
89	Estimates of Vortex Paths and Strengths	278
	a. Mach 0.4	278
	b. Mach 0.6	279
	c. Mach 0.8	280
90	Vortex Path in the Crossflow Plane	282
91	Comparison Between Measured and Computed Crossflow Velocity	283
	a. x/d = 7.4	283
	b. x/d = 8.8	284
92	Theoretical and Experimental Pressure Coefficient Distributions at X/D = 4.8 and 8.8	287
	a. Mach 0.4	287
	b. Mach 0.6	288
	c. Mach 0.8	289
93	Comparison Between Experimental and Computed Normal Force and Side Force Coefficient Distributions	290
	a. Mach 0.4	290
	b. Mach 0.6	291
	c. Mach 0.8	292

LIST OF ILLUSTRATIONS (Concluded)

FIGURE		PAGE
94	Local Side Force Coefficients Normalized by C_y^* at Angle of Attack from 30 Degrees to 65 Degrees, Mach = 0.6	294
	a. Re = 0.5 x 10^6/ft	294
	b. Re = 1.0 x 10^6/ft	295
	c. Re = 3.0 x 10^6/ft	296
	d. Re = 5.6 x 10^6/ft	297
95	Pressure Coefficient Distribution, N2B1	298
96	Local Side Load Coefficient, N2B1	300
97	Maximum Crossflow Lift Coefficient for Configuration N2B1	304
	a. Mach 0.4	304
	b. Mach 0.6	305
98	Predicted Envelope of the Side Force and Yawing Moment Coefficient from the Data Correlation Analysis	307
99	Crossflow Lift Coefficient Variation with Crossflow Reynolds Number	309
100	Nose Shape Effects on Crossflow Lift Coefficient	311

LIST OF TABLES

TABLE		PAGE
1	Matrix of Representative Flight Conditions and Configuration Variables of Wind Tunnel Test	40

LIST OF SYMBOLS

a	Maximum Body Radius, $d/2$
C_A	Axial Force Coefficient, $F_A/q_\infty S$
C_{ℓ_c}	Crossflow Lift Coefficient
C_M	Pitching Moment Coefficient, $M_m/q_\infty Sd$
C_N	Normal Force Coefficient, $\dfrac{F_N}{q_\infty \pi a^2}$
C_n	Yawing Moment Coefficient, $M_n/q_\infty Sd$
C_P	Pressure Coefficient, $\dfrac{p-p_\infty}{1/2\gamma p_\infty M_\infty^2} = \dfrac{p-p_\infty}{q_\infty}$
C_Y	Side Force Coefficient, $\dfrac{F_Y}{q_\infty \pi a^2}$
d,D	Reference Body Diameter
$\dfrac{dC_N}{d(x/d)}$	Distributed Normal Force Coefficient
$\dfrac{dC_Y}{d(x/d)}$	Distributed Side Force Coefficient
F_A	Axial Force
F_B	Body Fineness Ratio, ℓ_B/d
F_N	(a) Normal Force, (b) Nose Fineness Ratio, ℓ_N/d
F_Y	Side Force
g	Distance Between Breakaway Points of Vortex Lines of Like Sign, Figure (86)

K	Number of Concentrated Vortices in the Flow
L_β, ℓ_β	Body Length
L_N, ℓ_N	Nose Length
L	Total Model Length, $\ell_N + \ell_\beta$
MFR	Momentum Flux Ratio
M_m	Pitching Moment
M_n	Yawing Moment
M_∞	Freestream Mach Number
M_C	Crossflow Mach Number, $[M_\infty \sin \alpha]$
n	Frequency of Shedding of Vortices of Like Sign
P_C	Nozzle Chamber Pressure
P_e	Nozzle Exit Static Pressure
P_o	Impact Pressure
P_∞	Freestream Static Pressure
q_∞	Freestream Dynamic Pressure
R_{e_∞}	Freestream Unit Reynolds Number per Foot
R_{e_c}	Crossflow Reynolds Number Based on Cylinder Diameter, $[R_{e_D} \sin \alpha]$
R_{e_D}	Freestream Reynolds Number Based on Cylinder Diameter
R_{e_s}	"Surface Streamline" Reynolds Number Based on Cylinder Diameter
r	Local Body Radius, $r(x)$ In General
r_j	Radius of the jth Vortex, $\sqrt{y_j^2 + z_j^2}$
S	Strouhal Number
U	Crossflow Velocity Component, $U_\infty \sin\alpha$

U_∞, V_∞	Freestream Velocity
u	x - Component of Velocity (Perturbation)
v	y - Component of Velocity (Perturbation)
w	z - Component of Velocity (Perturbation)
x	Cartesian Coordinate, Aligned Along the Body Axis Pointing Aft
y	Cartesian Coordinate, Pointing Left When Looking Aft Along the Body Axis
z	Cartesian Coordinate, Pointing Upward in the Body Axis System
y_j, z_j	y and z Coordinate of the jth Vortex

Greek Symbols

α	Angle-of-Attack
δ_j	Nozzle Deflection Angle
ξ	Angle Between the Vortex Lines and the Body Axis, Figure 83
Φ	Complex Potential, Defined by Equation 9
ϕ	Polar Angle, Figure 87
Γ	Circulation, $\oint V ds$
Γ_0	Single Equivalent Circulation About Missile Centerline
γ	Ratio of Specific Heats Cp/Cv
ν	Kinematic Coefficient of Viscosity
ρ	Density
ζ	Complex Variable, y + iz

SECTION I

INTRODUCTION

The need to determine forces and moments acting on bodies of revolution at angles-of-attack originally arose in connection with airships. During the early stages of the development of subsonic airplanes, interest in this problem diminished because of the relatively minor contribution of the fuselage to the aerodynamic characteristics of the total aircraft configuration. The advent of highly maneuverable aircraft and missile design concepts has required a major effort in understanding the problem of slender bodies of revolution at high angles-of-attack. For that case the body is a major contributor to the overall aerodynamics of the system.

The primary impetus for the current investigation is the problem associated with the prediction of the subsonic and transonic flight characteristics of slender missiles at large angles-of-attack. These large angles will occur during the launch phase of an air-mobile intercontinental missile. The same flight environment may also exist during the launch of highly maneuverable air-to-air missiles. Although in both cases the launch phase represents only a very short portion of the total missile flight time, the control of strong side forces and yawing moments is crucial to the completion of the desired mission.

The Flight Dynamics Laboratory conducted an extensive experimental investigation to determine the aerodynamic forces and moments, the pressures, and the lee-side flow field for a smooth body missile at large angle-of-attack. The tests, undertaken in support of the MX program, were sponsored by the Air Force Space and Missile System Organization (SAMSO). The MX experiments explored the aerodynamic loads, associated with air launch, encountered by a large missile at subsonic and transonic speeds. The aerodynamic data were needed to establish the structural and control system requirements.

This report presents a summary of the experimental aerodynamic characteristics, provides a review of the existing data and the analysis methods that relate to bodies at high angles-of-attack, and presents the results of analytical developments based on the MX data.

SECTION II

LITERATURE REVIEW AND STATUS OF THE PROBLEM

In viewing the overall fluid dynamics problem associated with flow about bodies of revolution at angles-of-attack, the important features may be delineated which contribute to the complexity of the analysis. The complete analysis must treat the inviscid flow field and the three-dimensional boundary layer on the vehicle surface (see Reference 1). At sufficiently high angles the interacting viscous and inviscid flow field produce an adverse pressure gradient on the lee side of the body which causes the three-dimensional boundary layer to separate. The separated shear layer rolls up into a vortex in the wake, which influences the pressure distribution on the body and may interfere with the flow about control surfaces. The conflicting conclusions from many experimental studies illustrate a major problem of interpreting, scaling, and extrapolating wind tunnel data from high angle-of-attack tests.

1. BASIC PHYSICAL FEATURES OF VARIOUS AERODYNAMIC REGIMES

As a slender body of revolution traverses the range of angles-of-attack from 0 to 90 degrees, there are at least four distinct aerodynamic regimes that must be considered in the analysis of this problem. The appearance and disappearance of each regime as a function of angle-of-attack is also dependent on many other factors. The most important are nose shape, overall fineness ratio, crossflow Mach number, and Reynolds number. Other factors may include roll angle, free stream turbulence, surface roughness, acoustic environment and model vibrations. The following regimes can be identified for the subonic analysis of a slender body of revolution.

Regime I ($0° < \alpha < 5°$): At very low angles-of-attack there is no discernable boundary layer separation and the flow can be characterized by a classical potential flow field and an attached laminar or turbulent boundary layer.

Regime II ($5° < \alpha < 20°$): Boundary layer separation occurs on the lee side of the body. The separated boundary layer becomes a free shear layer, which rolls up into two symmetrical concentrated vortices. The vortices are steady with time. A schematic of the flow field is depicted in Figure 1. No side force or yawing moment is present. Normal force is the parameter of interest.

Regime III ($20° < \alpha < 60°$): In this regime the concentrated vortices break away from the slender body from alternate sides. The vortices are shed from the right and left sides in a pattern normally associated with the classical von Karman vortex, but the vortices are arrayed in the spacial sense and not in the temporal sense. This flow field is shown in Figure 2. These asymmetrical vortices give rise to significant side forces and yawing moments. This flow regime is of primary interest in the current study. Note that several experimental investigations have shown some random flow switching and flow instabilities at the higher end of this angle-of-attack range. Some workers in the field have defined this unsteady portion as a separate flow regime.

Regime IV ($60° < \alpha < 90°$): The flow field is characterized by some form of temporal vortex shedding, as has been observed for infinite length right circular cylinders. A von Karman vortex trail is usually assumed to be present in the wake.

2. CURRENT STATUS OF EXPERIMENTAL INVESTIGATIONS: REGIME II

This section and the following one is primarily concerned with those experimental investigations which have provided physical insight into the important aerodynamic and geometric variables governing the flow field in Regime II and III. Because of the similarities between the current problem and the more classical problem of the infinite right circular cylinder normal to the freestream, some of the important concepts from the latter problem will also be included.

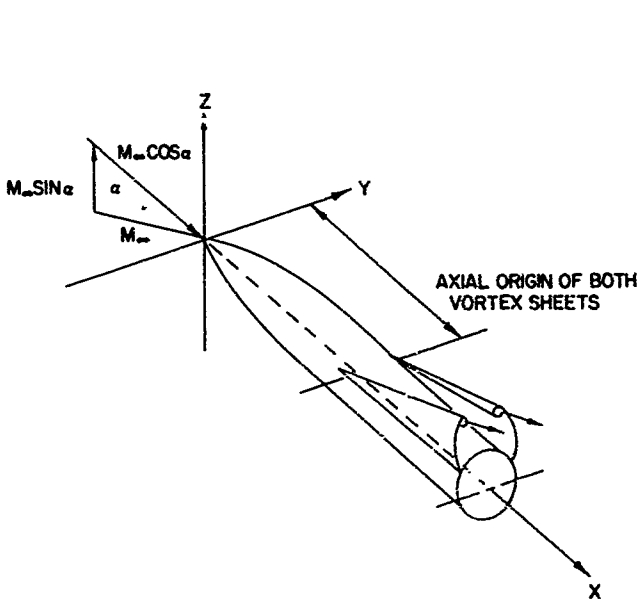

Figure 1. Steady Symmetric Vortices, Regime II ($5° \leq \alpha \leq 20°$)

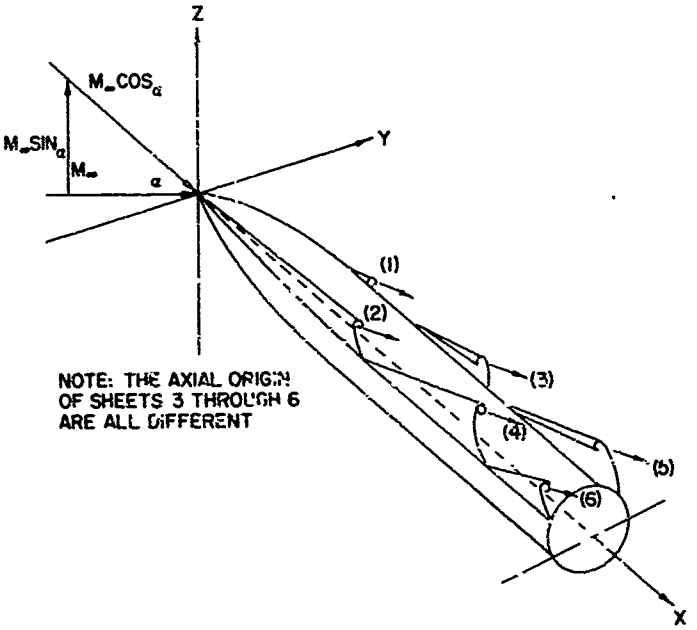

Figure 2. Steady Asymmetric Vortices, Regime III ($20° \leq \alpha \leq 70°$)

Following the publication of Allen's analysis of the flow about a body of revolution at small angles-of-attack using the crossflow drag concept (Reference 2), there was a significant flurry of experimental investigations conducted by NACA and later NASA. Extensive experimental data was obtained for a model consisting of an ogive nose 3 diameters long and a cylindrical body 7.7 diameters long. Normal forces, surface pressure distributions and vortex wake characteristics for both subsonic and supersonic approach flows were reported by Perkins and Jorgensen (Reference 3), Jorgensen and Perkins (Reference 4), and Tinling and Allen (Reference 5). The latter two references are of particular importance in that they provide quantitative data on the location of the symmetric vortex centers and the strength of the vortices at various stations along the body. Jorgensen and Perkins (Reference 4) also attempted to locate the separation line on the model by tracing potential streamlines on a plot of isobars. The authors also proposed that the strengths of the concentrated vortices could be estimated from the normal force distribution and vortex positions. Perkins and Kuehn (Reference 6) obtained pressure distributions and force characteristics for a body of similar geometric characteristics, but for a larger range of angles-of-attack. At an angle of 35 degrees, the starting point of separation was reported to be at the vertex of the model. The crossflow Reynolds number, R_{e_c}, at which the crossflow drag coefficient decreased was observed to be less that the familiar critical value for a right circular cylinder. Furthermore, the crossflow Mach number was greater than the critical Mach number for a circular cylinder.

Gowen and Perkins (Reference 7) used the vapor screen flow visualization technique to investigate the effect of body shape on the characteristics of the vortex wakes at Mach 2. Primary emphasis was placed on determining the angle-of-attack at which the vortices indicated an unsteady behavior. Gowen and Perkins found that the angle-of-attack at which the vortex wake became unsteady could be increased by reducing the nose bluntness. Additional experimental data on normal forces and pressure distributions for various geometric shapes may be found in Allen and

Perkins (References 8,9,10). More recently Grosche (Reference 11) reported some very detailed experimental measurements of velocity direction and impact pressures for symmetrical vortices in incompressible flow at high Reynolds numbers.

Experimental measurements on ellipsoidal bodies of revolution, at small angles-of-attack have been reported by Rodgers (Reference 12) and Atraghji (Reference 13). Both investigations combine surface oil flow observations with detailed surface pressure distributions. As a result, it is possible to determine the free shear layer separation point on the crossflow pressure distributions.

Rodgers (Reference 12) found that the actual surface streamlines do not differ significantly from those of the potential solution on the windward side of the body. However, there is a significant difference between potential and real surface streamlines on the leeward side. These observations are particularly important in any theoretical attempts of applying existing boundary layer separation criteria to crossflow pressure distributions.

Atraghji (Reference 13) has some particularly illuminating graphs in which the oil flow results and the isobar plots show the presence of both primary separation, i.e., separation of the attached boundary layer growing from the front stagnation point, and separation and attachment of the boundary layer growing beneath the free vortex. The influence of this secondary separated flow region has not been determined for either the symmetric primary vortices (Regime II) or the asymmetric primary vortices (Regime III).

3. CURRENT STATUS OF EXPERIMENTAL INVESTIGATIONS: REGIME III

Over 28 years ago Allen and Perkins (Reference 9), presented visual evidence of asymmetric vortices in the wake of an inclined slender body of revolution. The first measurements of substantial side forces and

yawing moments were obtained by Letko (Reference 14) in an investigation of the directional characteristics of a sharp-nosed fuselage model at large angles-of-attack. After these early investigations of these aerodynamic phenomena, there was no real effort to understand the problem until the extensive experimental and theoretical study of asymmetric vortices by Thompson and Morrison (Reference 15). Their investigation of flow around very long slender bodies of revolution at high angles-of-attack suggested that the vortex pattern was periodic in a spatial sense and could be related to some aspects of the two-dimensional flow in the wake of an impulsively started circular cylinder. The particular description for this type of flow field proposed in their paper has had a major influence on subsequent experimental investigations. In fact, since the publication of their paper, the number of reported experimental and theoretical studies has increased considerably. References 16 through 29 are the primary experimental investigations published in recent years. A Bibliography of additional publications (not reviewed) is included herein.

As indicated previously there are many aerodynamic and geometric parameters that influence the existence and magnitude of large side forces and yawing moments. Also, as expected, these various parameters interact non-linearly, precluding the application of the principle of superposition. Hence, in reviewing the current physical understanding of the flow field in Regime III, each major variable is considered separately, and the basic changes in side and normal force is discussed.

a. Mach Number Effects

Side forces and yawing moments decrease in magnitude at transonic Mach numbers. This trend has been measured by Pick (Reference 16), Fleeman and Nelson (Reference 21), Keener, Chapman and Kruse (Reference 27), and Jorgensen and Nelson (References 22,24). Although this trend is generally observed, there are exceptions. For instance, Keener and Chapman (Reference 20) and Pick (Reference 16) show very irregular trends.

For instance, Pick's models with a nose fineness ratio of four and nose bluntness of 5% show first a decrease of maximum side force for Mach numbers between 0.5 to 0.8, and then a substantial increase from 0.8 to 1.1. Fleeman and Nelson (Reference 21) show a disappearance of side force and yawing moment as the freestream Mach number approaches unity, and then they reappear at supersonic Mach numbers.

Keener and Chapman (Reference 20) found that the onset of side force was not influenced by Mach number.

b. Reynolds Number Effects

There are three different Reynolds numbers that have been used in the literature to describe the state of the flow around a slender body of revolution at angles-of-attack. For reference they are listed below:

(1) Freestream Reynolds numbers based on maximum diameter of the model

$$R_{e_D} = \frac{V_\infty D}{\nu} \tag{1}$$

(2) Crossflow Reynolds number based on crossflow velocity component

$$R_{e_c} = \frac{(V_\infty \sin \alpha) D}{\nu} \tag{2}$$

(3) Surface Streamline Reynolds number based on characteristic length in freestream direction

$$R_{e_s} = \frac{V_\infty \frac{D}{(\sin \alpha)}}{\nu} \tag{3}$$

The latter Reynolds number was first suggested by Bursnall and Loftin (Reference 30) while investigating the pressure distribution about

a yawed circular cylinder in the critical Reynolds number range. Lamont and Hunt (Reference 31) also suggested that this Reynolds number may be more appropriate in describing the condition of the attached boundary layer. Both papers claim that the critical Reynolds number for transition to turbulent flow is independent of the angle-of-attack if R_{e_s} is used. Hence, it is possible to determine the critical Reynolds number from tests at 90° angle-of-attack. This Reynolds number, however, has not found general acceptance in the literature, and the current discussion will be restricted to variations with the crossflow Reynolds number or freestream Reynolds number, an important factor is the condition of the attached boundary layer, either laminar, transitional, or turbulent.

Pick (Reference 16), found that the magnitude of the average side force was decreased by as much as 80 percent, for most Mach numbers and geometrical configurations, when the attached boundary layer was tripped on the windward side. The freestream Reynolds number range for these tests was from 0.25×10^6 to 0.39×10^6.

Fleeman and Nelson (Reference 21), show significant variation of both the side force and yawing moment with Reynolds number. For a model consisting of a tangent ogive nose (l/D - 2.5) and a cylindrical afterbody (l/D - 12), the side force and yawing moment increased up to R_{e_D} - 2.5×10^5, and then decreased with increasing Reynolds numbers. Peak values of side force and yawing moment occurred at crossflow Reynolds numbers between 1.4×10^5 and 2.5×10^5. For approximately the same freestream Reynolds number, Coe, Chambers and Letko (Reference 17) observed no significant Reynolds number effect.

Jorgensen and Nelson (Reference 22) observed that the normal forces and side forces for a model with a high fineness ratio nose were significantly affected by a change in the freestream Reynolds number. However, no trends were clearly established. Similar results were also presented by Keener, Chapman and Kruse (Reference 27). They report the largest side force at R_{e_D} - 4.3×10^5.

c. Nose Fineness Ratio and Bluntness Effects

For ogive cylinder bodies, the magnitude of the average side force increases with increased fineness ratio. This trend was reported by Pick (Reference 16), Jorgersen and Nelson (Reference 22), Keener and Chapman (Reference 20), and Keener, Chapman and Kruse (Reference 27).

Several investigations have shown that for a given nose fineness ratio, a judicious choice of nose bluntness will reduce the maximum side force associated with a particular model. Keener and Chapman (Reference 20) found a decrease in the side force coefficient for nose bluntness values of 4.2% and 8.4% (nose radius referenced to maximum body radius). In fact, for a pointed tangent ogive (l/D - 3.5), the latter value resulted in almost negligible side force at Mach 0.25. However, as the nose bluntness was increased, the measured side force began to become significant again. For the most slender tangent ogive (l/D - 5.0), the largest nose bluntness value produced significant unsteadiness in the flow field.

Pick (Reference 16) reported that in general an increase in nose bluntness reduced the maximum values of the side forces. The reduction was most pronounced at the lower Mach numbers. However, for a model with a nose fineness ratio of 2 the side force actually increased for bluntness ratios greater than 5%.

Jorgensen and Nelson (Reference 22) recorded significant decreases in measured side forces and yawing moments for a model with a blunted ogive nose (l/D - 3.0), when compared with the original sharp ogive nose (l/D - 3.5). However, they noted that the same reduction in side forces and yawing moments could be achieved with a sharp ogive nose of equivalent nose fineness (l/D - 3.0).

In summary, nose bluntness may reduce the side forces and yawing moments. However, some caution must be used in the choice of the appropriate value of the nose bluntness ratio. In view of the

uncertainty in the current understanding of the flow mechanism, experimental measurements should be used for design purposes.

d. Geometric Changes to Reduce Side Forces and Yawing Moments

One of the principle objectives of the available studies has been to eliminate or at least reduce the magnitude of induced side forces and yawing moments. Hence, a series of devices or techniques have been investigated on a somewhat trial and error basis. Letko (Reference 14) found that a small strake on the nose of a conical yaw and pitch tube eliminated unsteady pressure measurements, which were attributed to the random asymmetric vortex flow-field switching. Letko also reported that a ring or other roughness on the nose of a sharp-nosed fuselage model reduced the yawing moment. The effect of nose strakes on forebodies was investigated by Keener and Chapman (Reference 20), and Coe, Chambers and Letko (Reference 17). In general, symmetric nose strakes significantly reduced or eliminated side forces and yawing moments for sharp-nosed tangent ogives (l/D - 3.5). The flow mechanism of the nose strakes is to force the local boundary layer separation to occur symmetrically. This condition is obviously very sensitive to roll and yaw angles.

Jorgensen and Nelson (References 22,24) found that nose strakes on a model with an ogive nose (l/D - 3.0) and a cylindrical afterbody (l/D - 7.0) made little or no change in the measured side forces and yawing moments. Nose strakes did increase the normal force and moved the aerodynamic force center forward.

The use of boundary layer trips in the form of grit rings or strips has met with mixed results. For grit rings on a pointed tangent ogive, Keener and Chapman (Reference 20) obtained significant reduction in the side forces. For meridional grit strips on the windward side, Pick (Reference 16) and Keener and Chapman (Reference 20) measured decreases in the side forces. Clark, Peoples and Briggs (Reference 18) had some success in reducing side forces in a model with a blunt nose

and cylindrical afterbody by placing grit rings on the nose. However, Jorgensen and Nelson (Reference 22) observed no changes in side forces and yawing moments for a ring of grit placed on the noses of models with pointed ogive noses (l/D ~ 3.5).

Other devices that have reduced side forces include nose-mounted vortex generators (Reference 18) and nose booms (Reference 20). Changes in the cross-sectional shape of models have also been shown to decrease side forces.

e. Roll Angle and Nose Misalignments

An additional complexity in the aerodynamic problem of slender bodies of revolution at high angle-of-attack is the variation of side force and yawing moment with roll angle and/or model nose misalignment. Thomson and Morrison (Reference 15) reported that rotation of a seemingly axisymmetric model (cone-cylinder with a measured nose misalignment of less than 5×10^{-4} in.) changed the flow pattern from one vortex sequence to the other. For one test model, Pick (Reference 16) found that not only did the sign of the measured side force change but also the magnitude of the side force, as the model was rolled 180°; however, for a second model, only the sign of the side force changed as it was again rolled 180°. Other investigators reporting changes in side force with roll angle are Wardlaw (Reference 32), Lamont and Hunt (References 31,33), Keener and Chapman (Reference 20), and Clark, Peoples and Briggs (Reference 18).

The results obtained by Keener and Chapman (Reference 20), are particularly interesting. They found that by rotating the entire model, which was a pointed tangent ogive (l/D ~ 3.5), the changes in side force are consistent with previous results, presented above. They also conducted similar experiments in which the removable nose tip (length of 0.19 l_n) was rotated.

The results of these tests are very similar to the results obtained in the earlier tests. Hence, it appears that the asymmetry of the vortex flow is very sensitive to the nose geometry. Similar results were also obtained by Clark, Peoples and Briggs (Reference 18). In these tests, either the entire nose was rolled with respect to the body or the entire body was rolled. Under either condition, the magnitude of the measured yawing moment changed substantially.

These results have very serious implications for the designer who must rely on wind tunnel test data. Unless the particular model was tested at several roll angles, the selected data may not represent the maximum possible side forces or yawing moments. In fact, using existing experimental data to evaluate the accuracy of existing analytical techniques is equally as hazardous.

To complicate this problem further, an experimental investigation by Coe, Chambers and Letko (Reference 17) of roll angle effect on a tangent ogive (l/D - 3.5) and a cone (l/D - 3.5) showed no significant changes in the yawing moment coefficient.

f. Flow Field Unsteadiness

Several experimenters have reported various manifestations of flow field unsteadiness or time-dependent behavior. Letko (Reference 14) observed an aperiodic pressure variation for yaw pressure orifices on a yaw and pitch probe at high angles-of-attack. These results seemed to imply that complete flow reversal or flow switching existed. Letko eliminated this problem by placing a small nose strake on the probe. Similar investigations of a pointed fuselage model indicated only partial flow reversal. Thomson and Morrison (Reference 15) found some gross instabilities for certain incidence ranges between 30° to 40°. These wake instabilities occurred either at various angles-of-attack for a fixed roll angle, or at fixed angles-of-attack and varying roll angle. From visual observation, the authors concluded that the vortex system

appeared to oscillate between the two stable flow patterns which existed on either side of the instability. Thomson and Morrison (Reference 15) proposed that the instabilities are initiated by asymmetries in the flow very close to the nose. These asymmetries may be related to either nose geometry or approach flow direction, or both. From a typical oscillograph output in Fick's paper (Reference 16), it appears that the measured side force oscillates at about 20 hz. However, there is no discussion or comment in the paper concerning the existence, frequency and/or magnitude of the time dependent variation of the side force. Clark and Nelson (Reference 26) reported visual observation in a water tunnel, which seemed to show flow switching between two distinctly different flow patterns. Keener, Chapman and Kruse (Reference 27) observed flow unsteadiness above an angle-of-attack of 45°. In fact, the amplitudes of the unsteady side force were sometimes as large as 30% of the balance load capacities. The mean side forces were obtained by electronic filtering.

In contrast to the above qualitative observations of flow unsteadiness, Coe, Chambers, and Letko (Reference 17), using a tuft grid to investigate the free vortex system, found that the various flow patterns were relatively steady with time.

Lamont and Hunt (Reference 33) made some time-dependent surface pressure measurements on models with circular arc ogive noses and cylindrical afterbodies. They observed various degrees of unsteadiness at various angles-of-attack. At angles-of-attack between 30° and 50°, it appeared as if random, partial or sometimes, complete flow field switching occurred. The flow seems to have a preferred state but was disturbed in a random fashion. At inclinations of 65° to 70°, complete flow switching occurred more often, and at higher angles-of-attack periodic vortex shedding was observed. Note that all these tests were carefully controlled to maintain laminar boundary layer conditions.

As a result of these tests, Lamont and Hunt (Reference 33) suggest that the random flow switching behavior may be attributed to

the turbulence level in the approaching freestream. It is proposed that if eddies of sufficient size are convected past the cylinder, then these turbulent eddies will influence the local value of circulation about the model at any instant, and cause a change in the free vortex orientation. A similar approach has been used by Tunstall and Harvey (Reference 34) to explain the switching of secondary circulation in the flow in pipes with sharp bends.

These uncertainties associated with flow switching and the results reported by Smith and Nunn (Reference 35) on the effect of pitch rate should be a strong warning to experimentalists in choosing appropriate time scales for time-averaged pressure and force measurements. Particular attention must be given to total sample time per data point and frequency response characteristics of instruments and recorders. Also, the dynamic characteristics of the model support system must be taken into consideration.

g. Vortex Shedding and Spacing

The alternate spatial shedding of vortices is an integral part of the flow field in Regime III. Most investigators have assumed explicity or implicity that the local maximum side force occurs at the axial station at which the vortex breaks away from the model.

In view of the above and the concept of the impulsive flow analogy, it is necessary to predict the locations of the shedding points. Since the shedding process is continuous, some criterion has to be given to define the aerodynamic condition indicating the shedding point. Thomson and Morrison (Reference 15) used Schlieren photographs and yawmeter traverses to obtain the location of the free vortex core after shedding. Since the vortex core path away from the model was reasonably straight, they calculated a "Strouhal number" for the spatial shedding problem.

Pick (Reference 16), following Thomson's and Morrison's path of inquiry, obtained similar results. He showed that an increase in the crossflow Mach number, M_c moved the virtual vortex origin downstream along the model. Also, for the same geometry and approach flow conditions, the vortex breakaway points moved downstream as the boundary layer changed from laminar to turbulent.

Using cavitation as a means of flow visualization, Clark and Nelson (Reference 26) observed body vortex cores in the wake of a model consisting of a tangent ogive nose (l/D - 2.5) and a cylindrical afterbody (l/D - 12.5). They found that the vortex starting positions move toward the nose as the angle-of-attack or the crossflow Mach number increased.

All three available investigations used extrapolated data to determine the breakaway point, without having any surface pressure measurements or other model surface measurements. It seems instructive then to look to the analogous time-dependent shedding problem for a right circular cylinder normal to a uniform stream. There have been carefully documented experimental investigations on the formation of vortices. The most illuminating measurements of the temporal shedding of vortices and their effect on the oscillating lift and drag of a right circular cylinder have been reported by Drescher (Reference 36). By combining simultaneous time-dependent pressure measurements with synchronized flow visualization motion pictures of the formation and path of the shed vortices, Drescher was able to show the lift and drag force dependence on both the location of the shed vortices and the associated surface pressure distribution. In view of the impulsive flow analogy it seems instructive to compare the time-dependent pressure distribution variations along an inclined slender body. The only other time-dependent pressure measurements for a right circular cylinder have been reported by Naumann and Pfeiffer (Reference 37) and Naumann, Morsbach and Kramer (Reference 38). The latter investigations are of particular interest in assessing the effect of shock formation on the model as the local crossflow Mach number exceeds unity.

The work of Gerrard and his co-worker Bloor (References 39,40,41) also provides significant insight into the formation of wake vortices. Of particular importance to the problem under investigation is the detailed mechanism of the development of the free vortex. Gerrard (Reference 40) has shown that the circulation of the free vortex is less than the vorticity associated with the free shear layer leaving the body. This is because, in the formation process, vorticity of opposite sign is entrained by the vortex sheet from the other side of the model. This entrainment process occurs very close to the model surface and, therefore, has a substantial effect on the local pressure distribution. This, in turn, influences the magnitude of the local side force.

SECTION III

EXPERIMENTAL PROGRAM

The primary purpose of the experimental program was to determine the aerodynamic loads on a smooth missile at conditions of high angle-of-attack at subsonic and transonic speeds. Nose shape was the principal variable. Initially the data were intended to develop design criteria for a missile concept, but were subsequently used to expand the basic understanding of complex flow phenomena that have application to several missile and aircraft analysis problems.

The selection of the AEDC 16-Foot Transonic Test Facility was based on a need to obtain data at near full-scale conditions, since this type of data could not be corrected for large changes in Mach number or Reynolds number with confidence. An extrapolation method had not been developed for flows involving asymmetric vortex separation at angle-of-attack. The data presented in this report were obtained at a Reynolds number range from 3.17×10^5 to 3.55×10^6, based on body diameter. The latter represents some of the highest Reynolds number data obtained to date at these high angle-of-attack conditions.

Testing was accomplished during six tunnel entries, covering the complete angle-of-attack range from 0° to 180°. Measurements were made of the surface static pressures, surface pressure oscillations, total forces and moments, and the flow field velocities on the lee side of the missile. During the early pressure tests a high-pressure air supply system was connected to simulate the rocket exhaust for missile angles-of-attack above 40°.

The particular conditions of Mach number, Reynolds number, and angle-of-attack which comprise the test series are shown in Table 1. The model designation, type of test, and the use of boundary layer trips or rocket plume simulation is also noted.

TABLE 1

MATRIX OF REPRESENTATIVE FLIGHT CONDITIONS AND CONFIGURATION VARIABLES OF WIND TUNNEL TEST

		N18I					N28I										N38I	N48I	N88I	N18I	N38I
		0	5	45	G	5GS	0		5	45		90		135			0	0	5	5	5
M_∞	R_e	F	P	F	P	P	F	P	P	F	P	P_u	P	P_u	P	P_u	P	P	G P	G P	G P
.3	1.0	310 291·		105			273 248·		321	85											
	2.0	320 289·		103			274 246·		322	83	30								290·	303·	
.4	.5	312 293·	285		272	297· 259/	277 250·		327 326/	87											
	1.0	311 292·	284	106	271		276 249·	44 33·		86	28						82·	68·			
	2.0	309 290·	283	104	269 270/	292· 334/	275 247·	45 34·	323· 326/	84	29	14	3	4	10	11	103 83·	69·	292·	304·	
.6	.5	313 294·	282	107	273	290· 282/	283 251·	37 36·	329 330/	88	27						84·				
	1.0	316 297·	281	110	274		282 252·	38 39·	332	91	19	18					87·	77·			
	3.0	317 298·	280	111	275		281 253·	61 40·	333	92	20	17					89·	76·			
	5.0	318 299·	279	112	276	293· 255/	280 254·		334· 336/	93	21	16							294·	305·	
	5.6							63 41·			22		7	6			104 106·	70·			
.7	.5						252·														
	1.0						253·		331												
	5.0	319 300·		113			279 255·		339· 342	94							90·		295·	306·	
.8	.5	314 295·		108			284 261·	37·		89							85·				
	1.0	315 296·		109			285 262·	59 38·		90	26						86·	79·			
	3.0							60									88·	78·			
	5.0	320 301·		114			278 270·	64 44·	343	95	23						105 95·	71·	296·	307·	314·
.9	4.8	302·		115			266·	42·		96	24						106 96·	72·	297·	308·	315·
1.0	4.6	303·					267·	43·		97							107 97·	73·	298·	309·	313·
1.1	4.4							47·		98	25						108 98·	74·			
1.2	4.2	304·					269·														
1.3	4.0	305·					269·	48·		99							99·	75·	299·	310·	316·

·GRIT /-FORCE P-PRESSURE JUET ON RE=MILLION G-GRIT RING S-GRIT STRIPS /-ROLL RUN

TABLE 1 (Continued)

		N2B2		N3B2												N4B2			
		0		0	5	45				90		135				0	5	45	
M_∞	R_E	F	F_{ϕ_S}	F	P	F	P	P_J	P_{JD}	F	P_{JD}	F	P	P_J	P_{JD}	F	P	F	P
.3	1.0			145 140·	246	46													
	2.0			143 122·	245	31		162	154	22	143	10	124	125	138	175·		74	178
.4	.5	591	592 593	147 137·		47													
	1.0			144 138·		33				24		12				178·	233	76	179
	2.0	594 573·	596 1/596 1/596·	144 139·	243 244	32		163	155	23	144	11	126	127	139	174·	232	75	177
.6	.5	601	602 603	148 137·		34													
	1.0			153 131·		35				25	145	13	128 131	132		172·	234	77	180
	3.0	607	605 606	154 130·		36				26		17				171·	235		
	5.0	604 577·	578· 579·	155 129·	241	37	165	164	156	27	146 147	16	129	133	140	170·	236	78	174
.7	.3	611	612 613	149 133·															
	1.0			152 136·															
	5.0	608 580·	610 610	150 128·	242	45										169·	237		175
.8	.5			150 134·		40													
	1.0			151 135·		39						14				173·			
	5.0	581·		157 127·		38	167	166	157			15	130	135	141	168·	238	79	176
.9	4.8	582·		148 123·		41	168									167·			
1.0	4.6	583·		126·		42	169									164·			
1.1	4.4			124·		43													
1.2	4.2	586·					170									165·			
1.3	4.0	587·		125·		44										166·			
1.5	3.0	588·																	

P-PRESSURE J-JET ON D-JET DEFLECTED ∅-ROLL RUN ϕ_S-ROLL SWEEP SRI --FORCE

TABLE 1 (Concluded)

		N5B2		N6B2			N7B2		N77B2		N8B2		N9B2		N10B2		N11B2		N13B2		N14B2	
		O		O		45	F		F		F		F		F		F		F		F	
M_∞	R_E	F	P	F	P	F	O	ϕ_S	O	ϕ_S	O	ϕ_S	O	ϕ_S	O	ϕ_S	O	ϕ_S	O	ϕ_S	O	ϕ_S
.3	1.0	209·		229 203·		55																
	2.0	207·	223·	227 204·	187·	70	471·				519·				420·							
.4	.5	211·		231 200·		56																
	1.0	210·		230 201·	189·	68																
	2.0	208·	222·	228 202·	188· 190·ø	69	472·	481· 489·	499·	500· 502·	520·	521· 524·	549·	551· 552·	422·	445· 446·	451·	452· 453·	617·	618· 619·	630·	631· 632·
.6	.5	212·		232 195·	193·	57																
	1.0	216·		237 193·	192·	65																
	3.0	217·		238 192·	195·	64					543·	544· 545·										
	5.0	218·	220· 221·ø	239 191·	196· 200·ø	63			503· 514·	504· 505·	526·	527· 530·	554·	555· 556·	426·		455·	456· 457·	621·	622· 623·	633·	634· 635·
.7	.5	213·		233 197·																		
	1.0	214·		236 196·																		
	5.0	219·	218· 219·ø	240 190·	202· 206·ø				506·		531· 532·	533· 534·	557·	558· 559·	433·	434· 436·	458·	460· 461·			636·	637· 638·
.8	.5			234 198·		67																
	1.0	215·		235 199·	194·	66																
	5.0	220·	217·	241 185·	208·	62			507·		535·		564·		439·				624·		640·	
.9	4.8	221·		242 184·	209·	58			508·		536·		560·		440·						639·	
1.0	4.6	222·		187·	210·	61			509·		537·		565·		441·							
1.1	4.4					59																
1.2	4.2	223·		188·	211·				513·		538·		561·		442·		462·		625·			
1.3	4.0	224·		189·	212·	60			512·		539·		562·		443·							
1.5	3.0								510·		542·		563·		444·				626·			

·GRIT F-FORCE P-PRESSURE $R_E = R_E/FT \times 10^{-6}$ ø-ROLL RUN ϕ_S-ROLL SWEEP

1. TEST FACILITY

The AEDC 16-Foot Transonic Test Facility (16T) is a closed-circuit continuous-flow wind tunnel with a range of operation at Mach numbers from 0.20 to 1.60. The tunnel is capable of operating within a stagnation pressure range from approximately 120 to 4000 psfa, depending on the Mach number, and over a stagnation temperature range from about 80°F to a maximum of 160°F. The specific humidity of the air is controlled by removing tunnel air and supplying conditioned make-up air from an atmospheric dryer.

The high angle-of-attack missile tests were conducted over a range of Mach numbers from 0.30 to 1.40. In the range 0.60 to 1.40 the tunnel has a maximum dynamic pressure of nominally 750 psfa. This corresponds to a maximum unit Reynolds number of 5.5×10^6 per foot at Mach 0.60 and 3.5×10^6 per foot at Mach 1.40.

In 16T the contour of each sidewall of the nozzle is adjusted by motor-driven actuators. The test section is 16 feet square in cross section and 40 feet long. The test sections are completely enclosed in a plenum chamber which can be evacuated, allowing part of the tunnel main flow to be removed through the test section perforated walls, thereby unchoking the test section at near sonic speeds and alleviating wall interference effects. A more extensive description of the tunnel and its operating characteristics is contained in Reference 42.

2. TEST HARDWARE AND INSTRUMENTATION

a. Pressure and Force Tests

The missile configuration consisted of a 7.6-inch-diameter cylindrical body and a set of interchangeable nose parts of various shape and bluntness. A sketch showing the model located in the wind tunnel test section is shown in Figure 3, and installation photographs of the model are presented in Figure 4. The model was tested with two basic body lengths and with various combinations of three ogive and three triconic nose configurations. Major details and dimensions of the model are shown in Figure 5, and a photograph of the ogive nose configurations is shown in Figure 6.

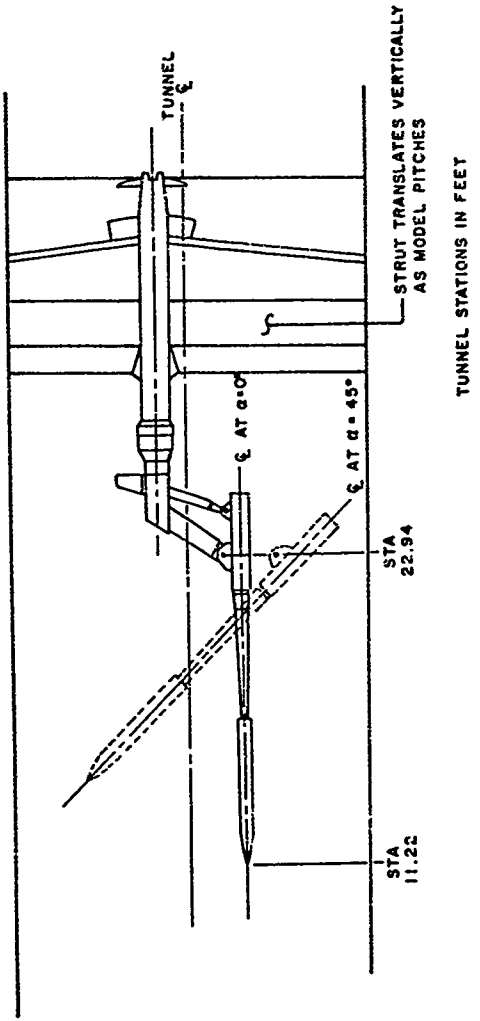

a. Sting-Mounted Model

Figure 3. Location of Model in Test Section

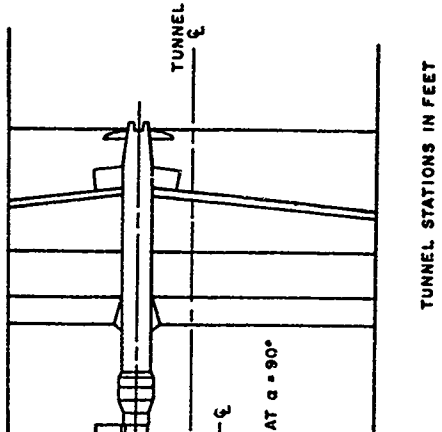

b. Sting-Strut-Mounted Model

Figure 3 (Concluded)

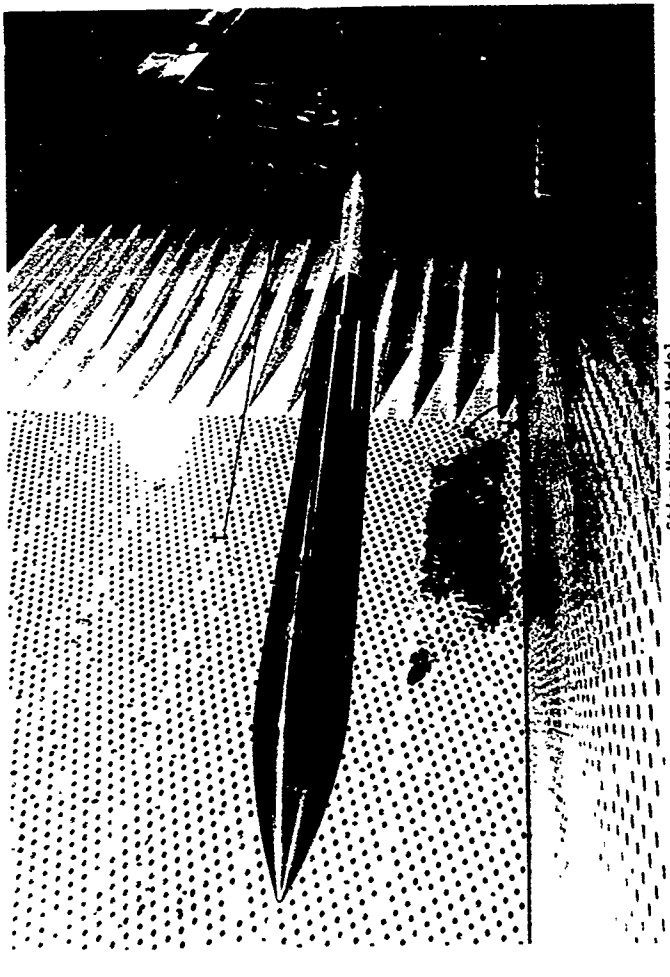

a. Sting-Mounted Model

Figure 4. Installation of Model

b. Sting-Strut-Mounted Model

Figure 4 (Concluded)

NOSE	A	B	R
N1	53.2	19.695	0
N2	53.2	19.345	0.231
N3	38.0	16.258	0.231
N4	22.8	12.411	0.231

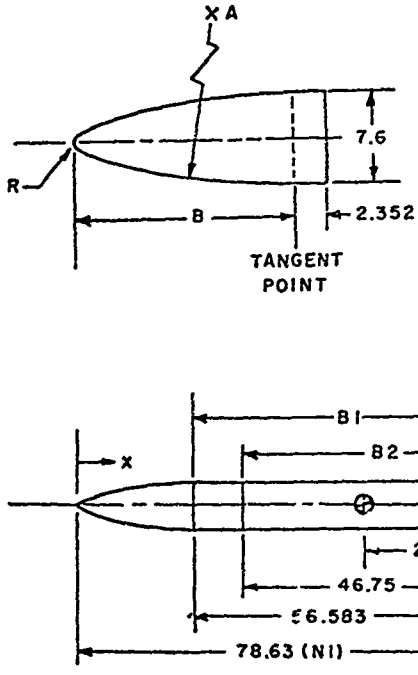

Figure 5. Model Dimensions

NOSE	A	R_1	R_2
N5	5.243	0.304	0.288
N6	4.169	0.608	0.582

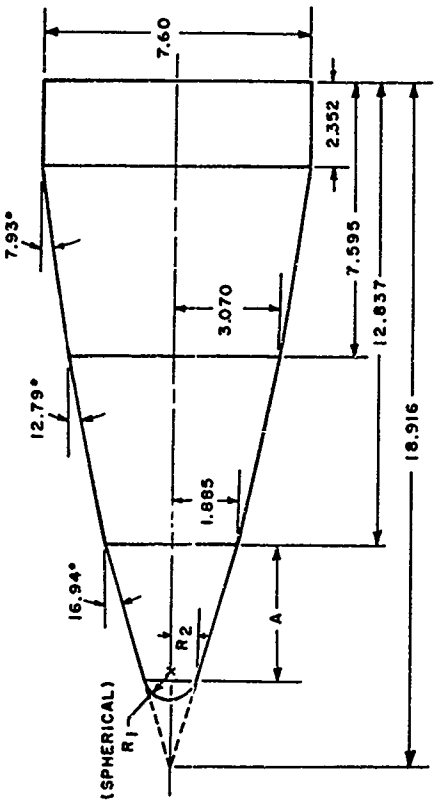

DIMENSIONS IN INCHES

Figure 5 (Continued)

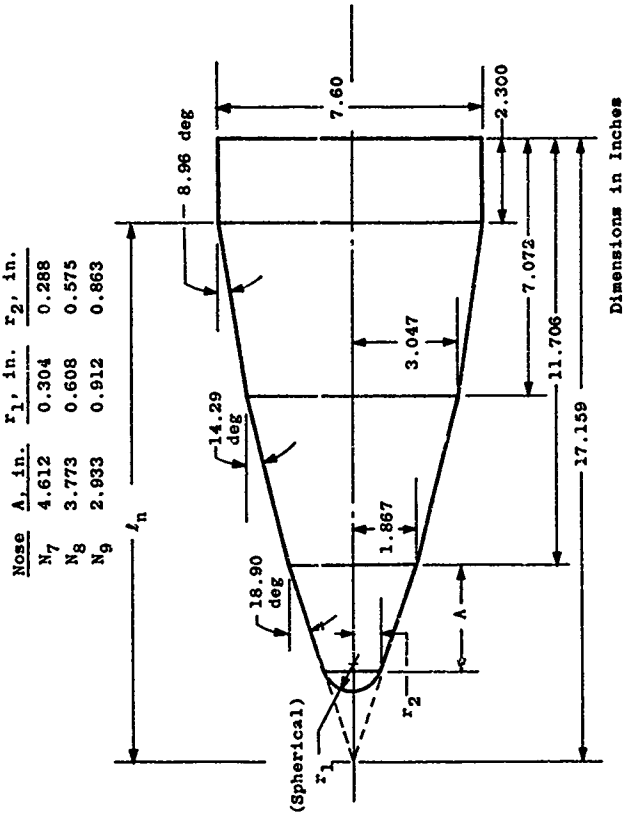

Figure 5 (Continued)

Nose	A, in.	r_1, in.	r_2, in.
N_{10}	3.988	0.704	0.282
N_{11}	3.288	0.608	0.564
N_{13}	1.888	1.216	1.128

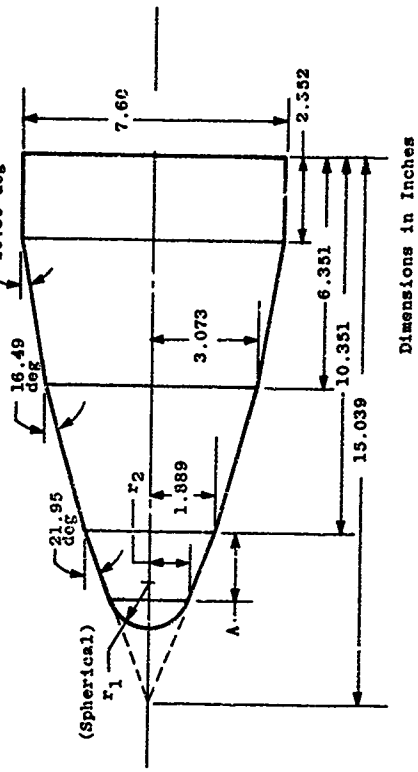

Figure 5 (Concluded)

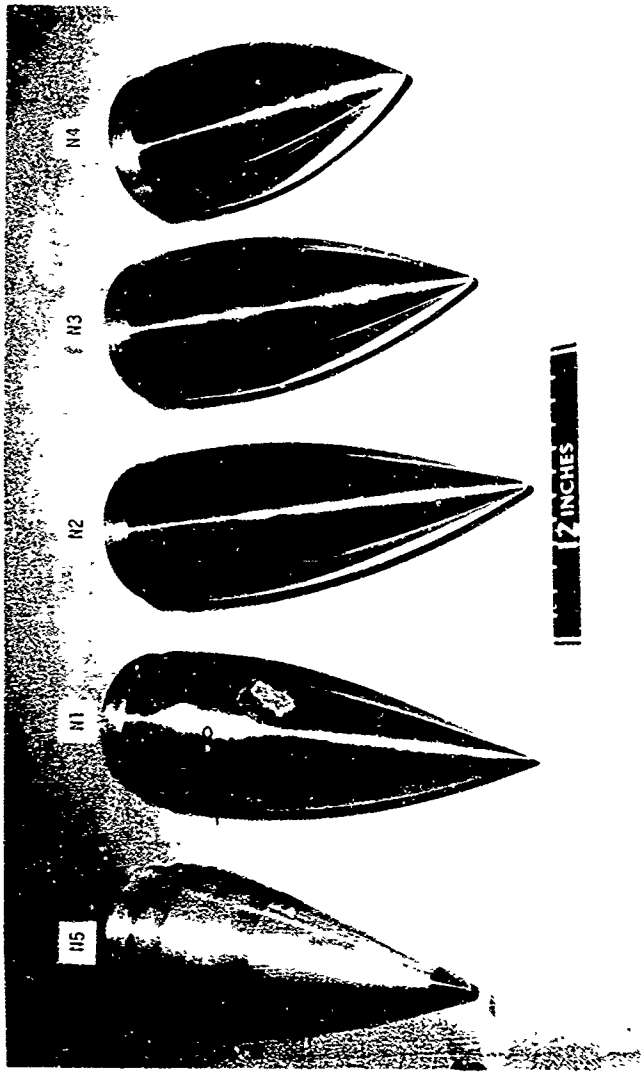

Figure 6. Nose Configurations

One of the primary test variables was the shape of the nose. Thirteen different nose configurations were tested at various conditions during the force and pressure testing. Figure 5 shows sketches of 12 of the nose shapes that were built for wind tunnel testing. The five basic noses were N2, N3, N6, N8 and N11; the 7-caliber, 5-caliber and triconic noses, respectively. Caliber as defined in this report is the radius of the arc from the body tangent point divided by the diameter as shown in Figure 28. The N1 nose was the N2 nose with material added to the tip and machined to a sharp point. N4 was a 3-caliber nose tested to give parametric data on the effect of fineness ratio. The N5, N7, N9, N10, N12 and N13 noses were made by changing the nose "button", a removable screw-in nosetip on the basic triconic shape, to change the bluntness of the triconic configuration. The N14 nose was a 3-caliber nose (like N4) with increased nosetip bluntness. The triconic nose configurations, were developed to increase usable volume in the nose while reducing nose length, allowing increased body cylindrical length within a fixed maximum-overall-length missile.

The pressure models were instrumented with up to 308 pressure orifices. Shown in Figure 7 is Configuration N2B1 with 244 pressure orifices. For the various nose configurations the station location of the nose pressure rings varied slightly and are called out as a nominal X/D location in this report. The data were obtained with up to seven internally mounted 48-port Scanivalves[R] with strain gage pressure transducers. The first two test entry models included 32 microphone taps with the static taps. These data are reported in AFFDL TR 76-109, Reference 52. The cold-air nozzles which simulated the rocket plume are shown in Figure 8. The exhaust nozzle weight flow was determined from chamber pressure and temperature measurements and the internal geometry of the exhaust nozzle. A pitch indicator mounted on the pitch support system was used to determine the model angle-of-attack.

The external contour of the force model was identical to the pressure model except the force model did not have the surface pressure orifices. The support system hardware was also the same for both models with the addition of six-component strain gage balance. The pitch attitude

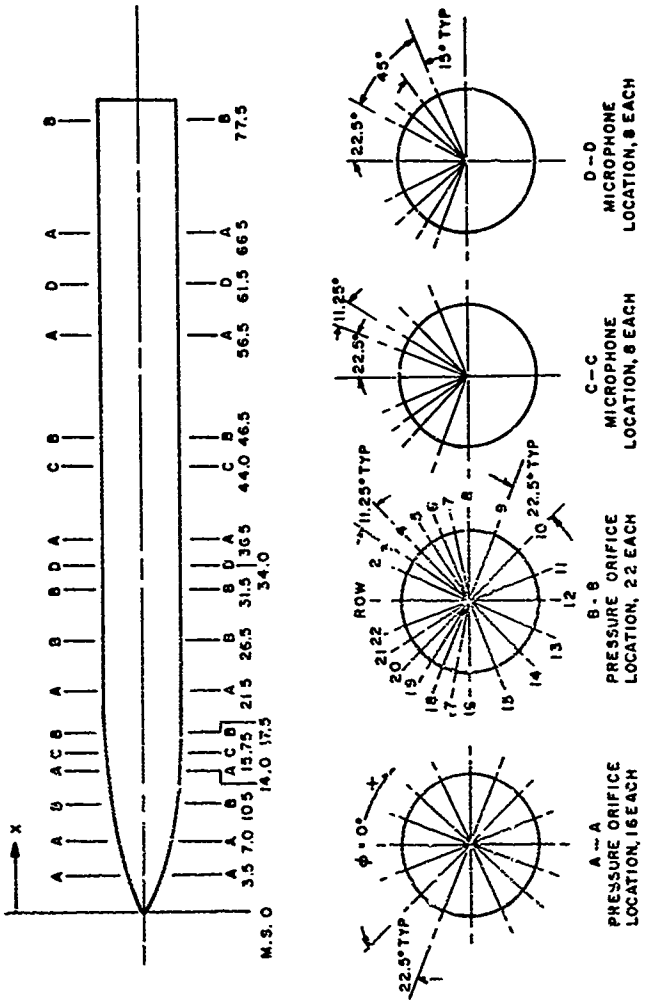

Figure 7. Pressure Orifice and Microphone Location, Configuration N2B1

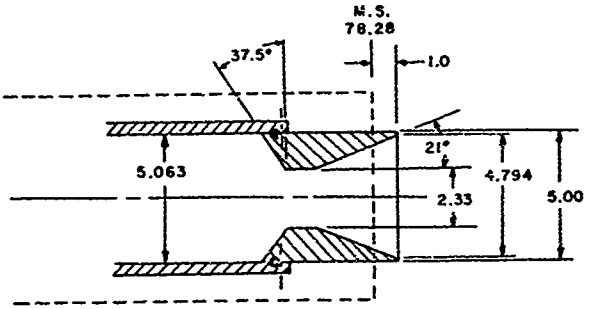

STRAIGHT NOZZLE

STATION AND DIMENSIONS IN INCHES

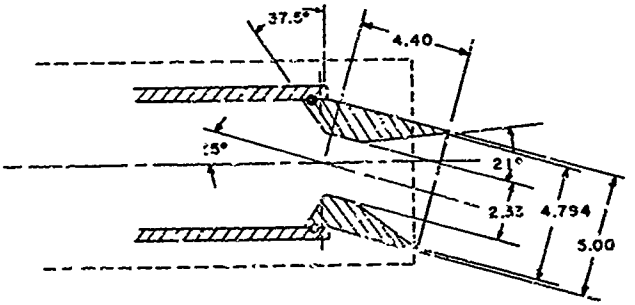

DEFLECTED NOZZLE

Figure 8. Exhaust Nozzle Details

of the sting-mounted force model was determined from an internally mounted angle-of-attack indicator, and the strut-mounted-model attitude was determined from an angle-of-attack indicator mounted on the pitch mechanism and corrected for balance deflections.

The model was mounted on a remotely controlled sting support system with a pitch range from -5° to 45°. To obtain model force and pressure data through an angle-of-attack range from 0 to 180 degrees, essentially two separate model support systems were required. A sketch showing the model support arrangement and associated angle-of-attack range is shown in Figure 9.

To obtain data through an angle-of-attack range from 0 to 45 degrees, the model was aft mounted on a straight sting support system, Figure 10. To obtain data through an angle-of-attack range from 45 to 180 degrees the model was strut mounted, Figure 10, and attached to a sting support with a clutch face arrangement. The clutch face allowed the model to be positioned at either 45, 90 or 135 degrees with respect to the main support system. High-pressure air was supplied through the sting and strut to an aft-mounted nozzle for cold-flow simulation of the nozzle exhaust plume during the pressure phase of the test.

A large number of the sting-mounted configurations were tested with a boundary-layer transition strip around the nose. The transition strip consisted of a 1/8-inch-wide ring of "grit" around the nose. The grit consisted of No. 70 (approximately .0083-inch-diameter) glass spheres glued on with polaroid print fixer. The chart in Figure 11 lists the location of the grit ring for each of the 14 nose configurations. The N1B1 configuration was also pressure tested with two lengthwise strips of grit located 30 degrees either side of the windward meridian for tripping the boundary layer when the model was at high angles-of-attack.

b. Flow Field Tests

The N2B1 configuration described in the previous section was used for a more detailed analysis of the wake characteristics. The missile model was floor mounted on a strut/sting arrangement with a pitch range from 0 to 70 degrees and a roll range of from -180 to 180 degrees.

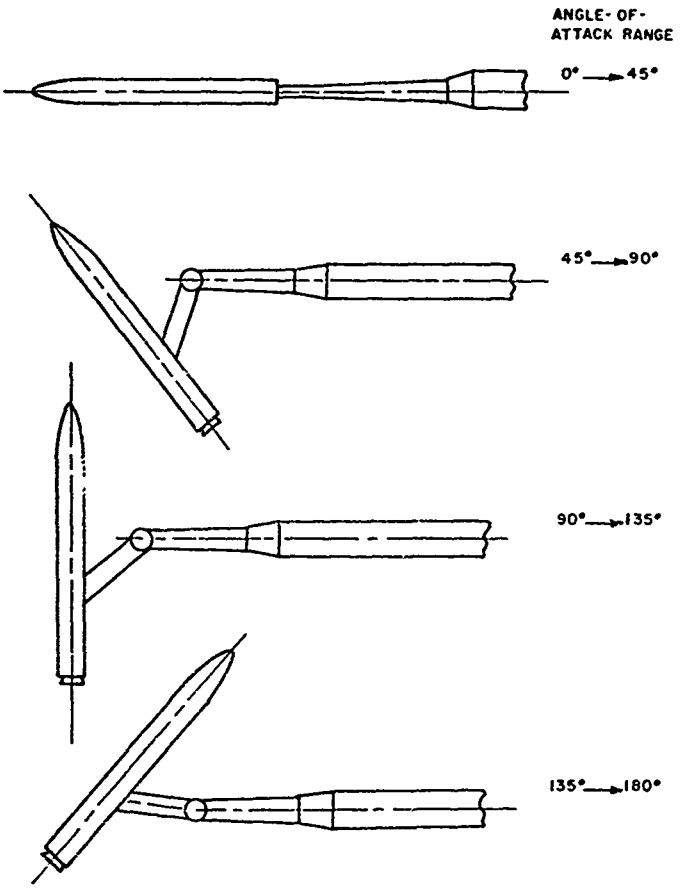

Figure 9. Model Support Arrangements

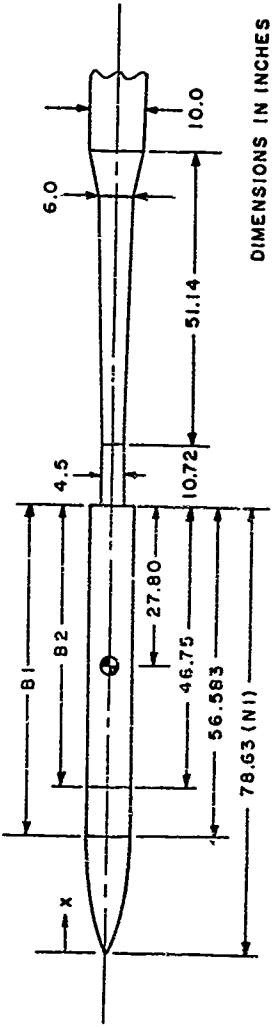

Figure 10. Model Support Dimensions

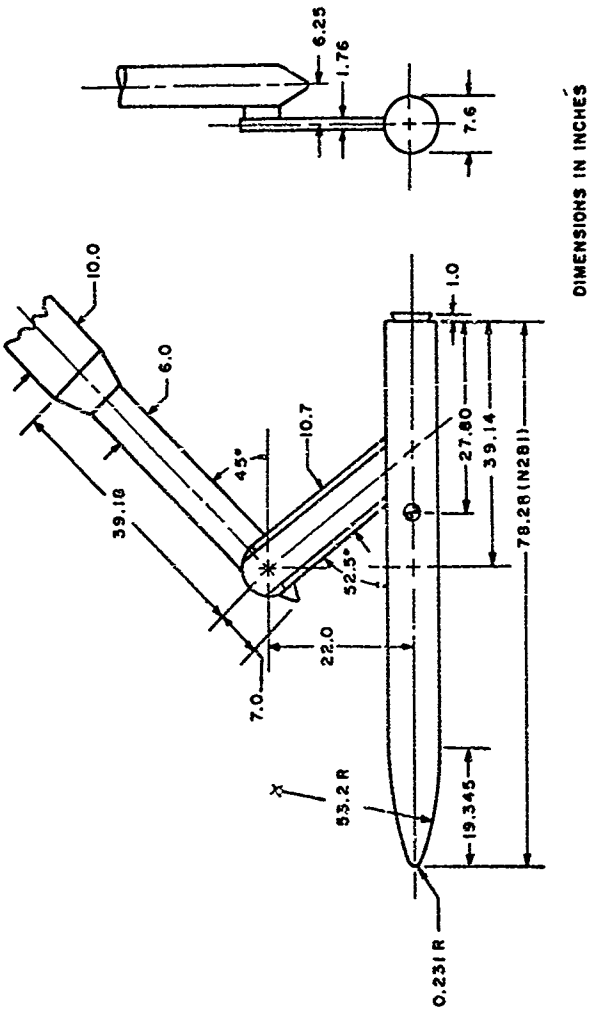

Figure 10 (Concluded)

The probe rake was sting mounted and positioned automatically under computer control. Figure 12 shows the model and the cone probe rake installed in the wind tunnel test section.

The wake data, consisting of steady state flow angularity and pressures, were obtained with a nine-probe rake, each probe having a conic tip with four static and one total pressure orifice. In addition, unsteady flow field data was obtained with a rake of the same geometric design, employing Kulite transducers in each probe. The geometrical details of the probe are shown in Figure 13.

The missile model was instrumented with 260 pressure taps as shown in Figure 7. Sixteen model pressures at station X/D = 7.4 were measured by the PWT digital pressure system to provide a continuous sampling of the data with respect to time. The purpose was to determine the steady or unsteady nature of the data being recorded. More information on the procedure will be provided in following sections. All other pressures were measured by 6 internally mounted 48-port Scanivalves and strain gage pressure transducers.

3. DATA REDUCTION

a. Pressure and Force Tests

The pressure and force data presented in this report were obtained at freestream Mach numbers from 0.30 to 1.50 and angles-of-attack from 0 to 180 degrees. The freestream Reynolds number per foot was varied from 0.50 to 5.00 x 10^6 at discrete Mach numbers as shown in Table 1.

The steady-state force, moment, and pressure coefficient data were obtained by setting the appropriate tunnel conditions and varying the angle-of-attack in 5-degree increments. The pressure coefficient data were also obtained both with and without simulated nozzle exhaust flow.

The force and moment data were corrected for weight tares and reduced to body axis coefficients by AEDC. Moment coefficients were referred to a location 27.8 inches forward of the base of the model.

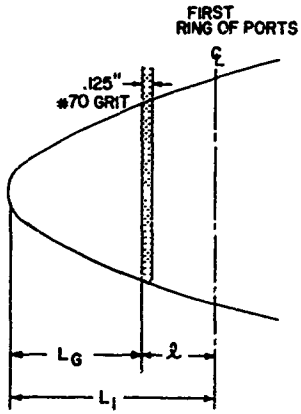

L_1 = Distance from nose to ℄ of first ring of pressure ports

L_G = Axial distance from nose to leading edge of grit ring

ℓ = Axial distance from leading edge of grit ring to ℄ of first ring of pressure ports

	NOSE CONFIGURATION	$\frac{r_n}{D}$	L_1 INCHES	L_G INCHES	ℓ INCHES
N_1	7-cal. ogive	0	3.90	2.80	1.10
N_2	"	.0304	3.50	2.40	1.10
N_3	5-cal. ogive	.0304	3.00	2.40	.60
N_4	3-cal. ogive	.0304	2.38	1.88	.50
N_5	5-cal. triconic	.040	4.63	2.40	2.23
N_6	"	.080	3.78	1.55	2.23
N_7	4-cal. triconic	.040	2.78	2.40	.50
N_8	"	.080	2.15	1.77	.50
N_9	"	.120	1.52	1.14	.50
N_{10}	3-cal. triconic	.040	3.58	2.50	1.08
N_{11}	"	.080	3.07	1.99	1.08
N_{12}	"	.120	2.56	1.48	1.08
N_{13}	"	.160	2.05	.97	1.08
N_{14}	3-cal. ogive	.150	--	1.00	--

Figure 11. Nose Ring Grit Patterns

PHOTOGRAPH OF MODEL INSTALLATION

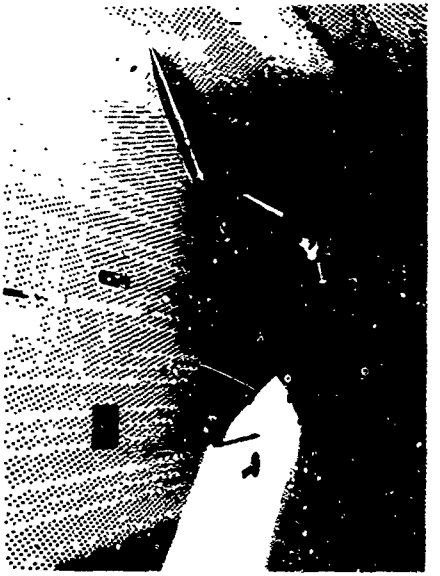

Figure 12. Model Installation for Flow Field Test

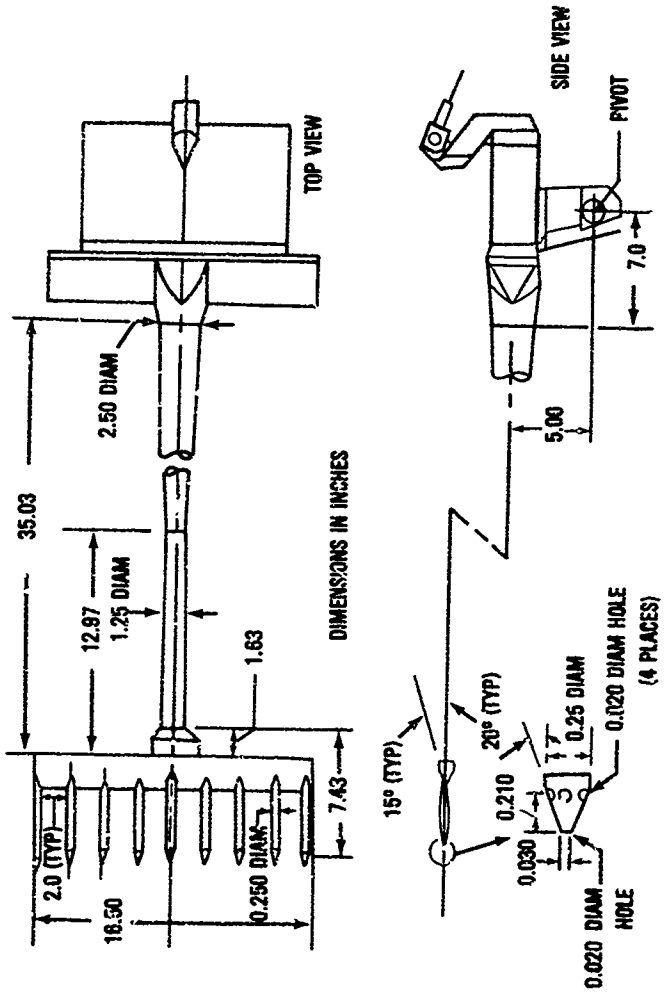

Figure 13. Sketch of Cone Probe Rake

The pressure data was received from AEDC in tabulated listings and on magnetic tape. The pressure coefficients were plotted and integrated to give running loads and total force and moment coefficients.

b. Flow Field Test

The flow field measurements were obtained at Mach 0.40 at 40- and 45-degree angle-of-attack, and at Mach 0.60 at 40-degree angle-of-attack. The freestream Reynolds number was 2.0×10^6 per foot at Mach 0.40 and 5.0×10^6 per foot at Mach 0.60. Wake data were obtained at three model stations at Mach 0.40 and 45-degree angle-of-attack, two model stations at Mach 0.40 and 40-degree angle-of-attack, and one model station at Mach 0.60 and 40-degree angle-of-attack. The first survey station was at X/D = 3.78. The two subsequent survey stations were at X/D = 7.4 and 8.8. The dynamic total pressure surveys were made parallel to the model centerline at about 1.0 diameter above the centerline. The wake velocities and flow angularities were calculated from the pressures based on calibrations of the cone probe rake.

The objective of this test was to obtain flow field velocity data with the model at a roll angle where the side force was high. To select this roll angle the model was rolled 180 degrees in 22.5-degree increments with the model pressure data recorded at each roll angle. It was surmised that the maximum side force would occur when the pressure differential between taps on opposite sides of the missile at $\phi = 90°$ was a maximum.

At Mach 0.40 and 45-degree angle-of-attack the objective was accomplished and a zero degree roll angle was selected. However, after this set of data was obtained, one of the taps at the survey station became plugged and remained undetected during the acquisition of the remaining test data. As a consequence, a roll angle was selected for the remaining sets of data which did not give the maximum side force.

Vortex switching did not occur for the present test conditions. This was determined by monitoring two pressure transducers at the same relative leeward position on each side of the body as a function of time. Had vortex switching occurred the relative reading between these two taps would have fluctuated from positive to negative. At Mach 0.40 the

difference between the two leeward taps was observed to be nearly constant with time, indicating steady flow conditions. At Mach 0.60 there were large differences between the two leeward taps with time, although the readings were always positive. Thus one may conclude that the flow field was unsteady at Mach 0.60 but vortex switching did not occur.

4. PRECISION OF MEASUREMENTS

a. Pressure and Force Tests

An estimate of the precision of the data at two standard deviation is presented below for Mach number 0.60 to 1.30.

Parameter	Mach No. = 0.60 Reynolds No. 0.5×10^6	Mach No. = 0.60 Reynolds No. 5.0×10^6	Mach No. = 1.30 Reynolds No. 3.6×10^6
C_m	± 0.711	± 0.077	± 0.093
C_N	± 0.226	± 0.039	± 0.150
C_n	± 0.586	± 0.065	± 0.02[illegible]
C_p	± 0.008	± 0.008	± 0.008
C_Y	± 0.312	± 0.031	± 0.026
M_∞	± 0.003	± 0.003	± 0.010
q_∞	± 3.0 psf	± 3.0 psf	± 3.0 psf
α	± 0.10°	± 0.10°	± 0.10°

At Mach 0.60 the estimates point out the loss of accuracy of the force and moment data at the low Reynolds numbers. The original test plan called for the maximum Reynolds number available and the balance was therefore sized and calibrated to accommodate the higher loads.

b. Flow Field Test

Estimates of the precision in certain test parameters at a 95-percent confidence level are as follows:

Parameter	Mach No. - 0.40	Mach No. - 0.60
M_∞	$\pm$ 0.004	$\pm$ 0.003
q_∞	$\pm$ 3.5 psf	$\pm$ 3.3 psf
p (Scanivalve)	$\pm$ 5.8 psf	$\pm$ 6.2 psf
p (PPB system)	$\pm$ 5.5 psf	$\pm$ 4.8 psf
α (model)	$\pm$ 0.15°	$\pm$ 0.15°
α (rake)	$\pm$ 0.05°	$\pm$ 0.05°
ϕ	$\pm$ 0.5°	$\pm$ 0.5°
x/D(rake)	$\pm$ 0.014	$\pm$ 0.014
y/D(rake)	$\pm$ 0.014	$\pm$ 0.014
z/D(rake)	$\pm$ 0.014	$\pm$ 0.014

SECTION IV

EXPERIMENTAL RESULTS OF THE PRESSURE AND FORCE TESTS

The effects of the major variables in the experimental program have been separated into sections. The intent is to show trends and sensitivities as functions of flow field and geometric variables. Two principal questions were identified as the test plan was developed. The application of the test data to flight conditions required more than a correction to the axial force coefficient to account for skin friction differences. All of the static force and moment coefficients would be sensitive to boundary layer separation at high angles of attack and some type of Reynolds number scaling description was required. The second question was the effect of the nose shape on the separated vortex pattern. The separated vortices induce forces and moments which affect flight characteristics. Both the force balance data and the surface pressure data were used to show the experimental trends.

1. PRESSURE INTEGRATION

The pressure data offered a unique opportunity to compare aerodynamic characteristics as measured from two independent sources. The pressure coefficients were integrated over the surface of the missile to obtain force and moment coefficients. The integrated values were then compared with the direct measurements of forces and moments. The comparison answered questions about the repeatability of data and instrumentation response to time dependent pressure fluctuations. Structural analysis requires data on running loads, and this could only be provided by the integrated pressure data. Analytical development was also dependent upon the measurements of running load patterns.

Pressure integration was accomplished using geometric data which describes the slope and location of each tap on the model. Direction cosines are computed at each tap. Experimental pressure coefficients are read from the data tape, multiplied by the appropriate direction cosines, and integrated with respect to location over the missile surface.

Figures 14 through 16 present comparisons between force data and integrated pressure data for the N2B1 and N6R2 configurations, which are typical. The normal force coefficients for both configurations show excellent agreement below 35-degree angle-of-attack but at 35 degrees and higher some differences are noted. The effect of the asymmetric flow on the aerodynamic coefficients above 35 degrees is probably the biggest factor causing these differences. Differences have been found in expected normal force levels for other cases and these differences invariably occur when the asymmetric forces are very large. The axial force coefficient plots show that with corrections for base axial force (Figure 15) and skin friction the integrated pressure data would agree quite well with the force data. The side force coefficient at 35-degree angle-of-attack is plotted versus Mach number for both configurations. These figures show that, in general, the magnitude of the side force coefficients is the same but that the signs may be different. This difference in signs, even with just small angle-of-attack differences, indicates that the flow pattern of shedding vortices and their frequencies and strengths are highly dependent on a large number of factors which must be systematically tested to improve analytical methods.

The pressure data can reveal much more about what is happening on the model as opposed to total forces and moments, and, as such, provides invaluable information for research on asymmetrical flow phenomena.

2. ASYMMETRIC FORCES

One of the primary objectives of this test effort was the investigation of asymmetric flow on slender bodies at angles-of-attack above 25 degrees. The large model at high Reynolds number combined with the large Mach number range and 13 nose configurations tested provide a wealth of useful data for this type of investigation.

Figure 17 presents the absolute value of the ratio of side force coefficient to normal force coefficient ($|C_Y/C_N|$) versus angle-of attack for eight of the configurations at Mach numbers 0.4, 0.6, and 0.8.

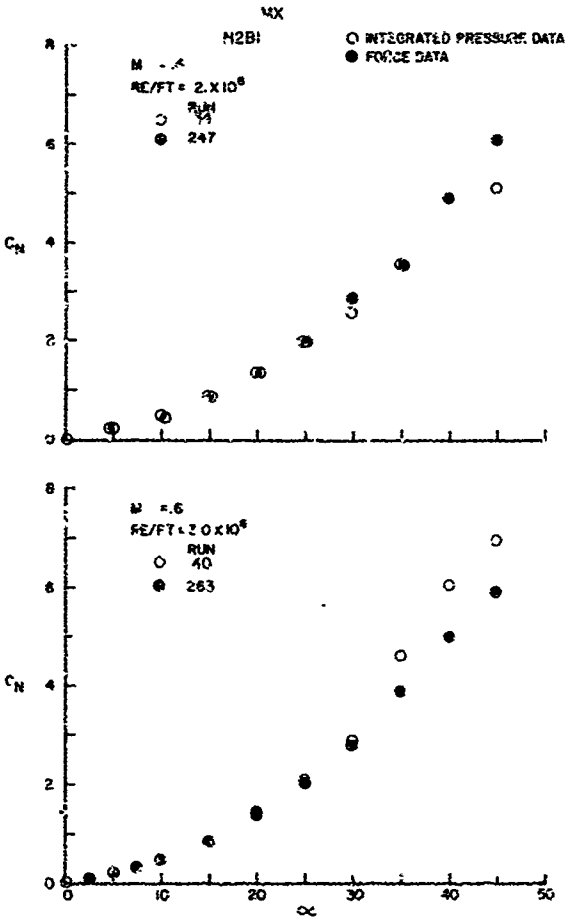

a. N2B1 Configuration

Figure 14. Comparison Between Integrated Pressure and Force Balance Data for Normal Force Coefficient

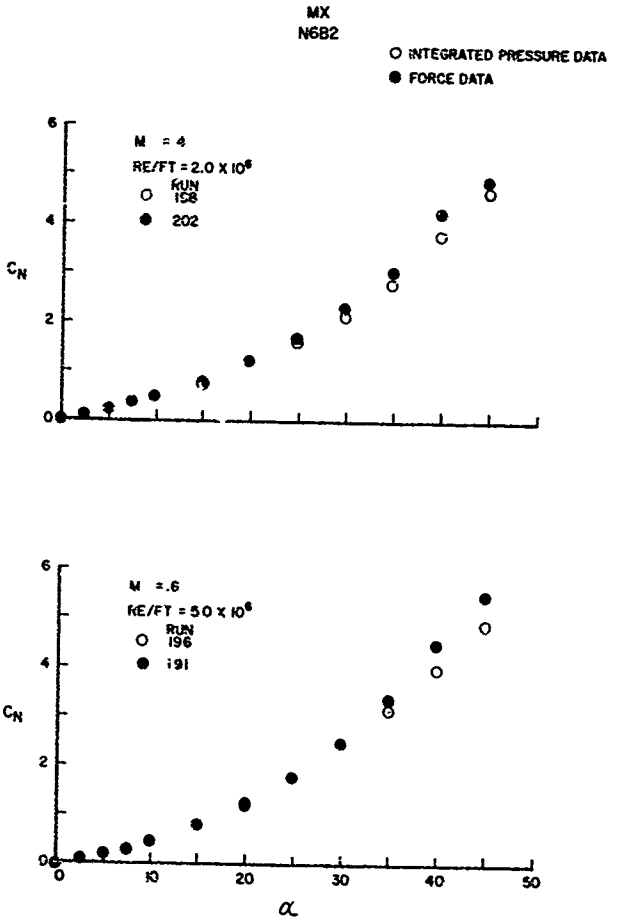

b. N6B2 Configuration

Figure 14 (Concluded)

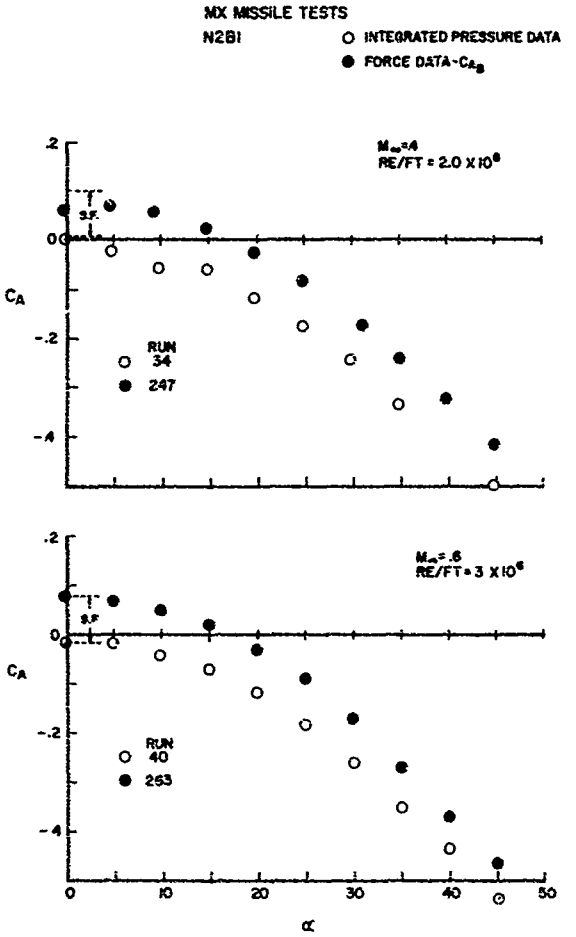

a. N2B1 Configuration

Figure 15. Comparison Between Integrated Pressure and Force Balance Data for Axial Force Coefficient

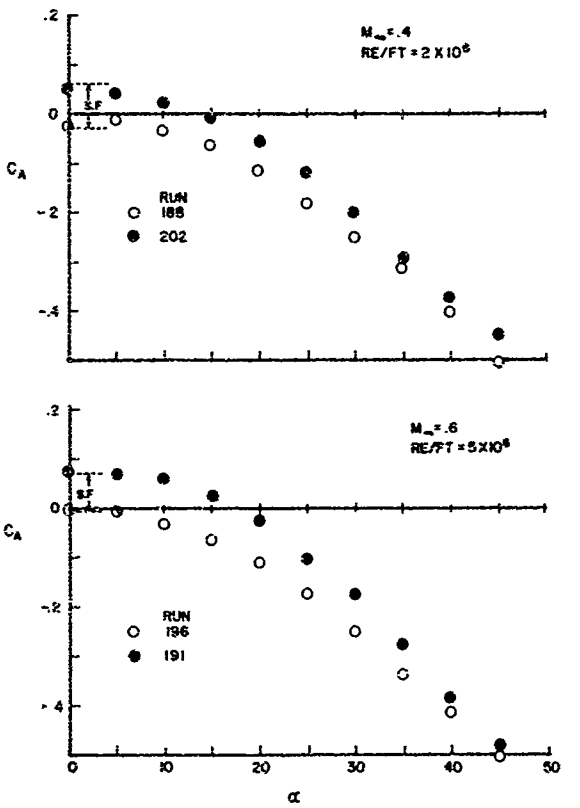

b. N682 Configuration

Figure 15 (Concluded)

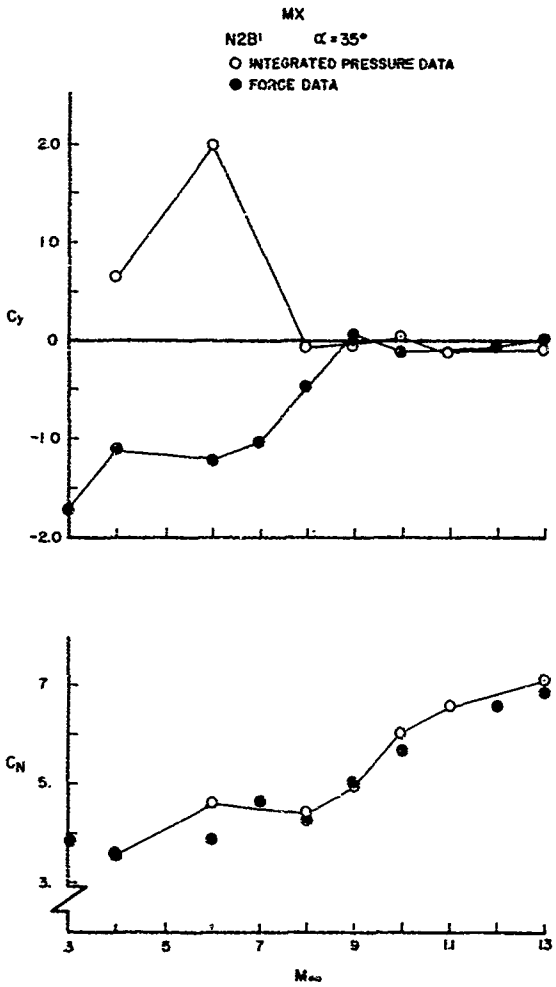

a. N2B1 Configuration

Figure 16. Comparison Between Integrated Pressure and Force Balance Data at Various Mach Numbers

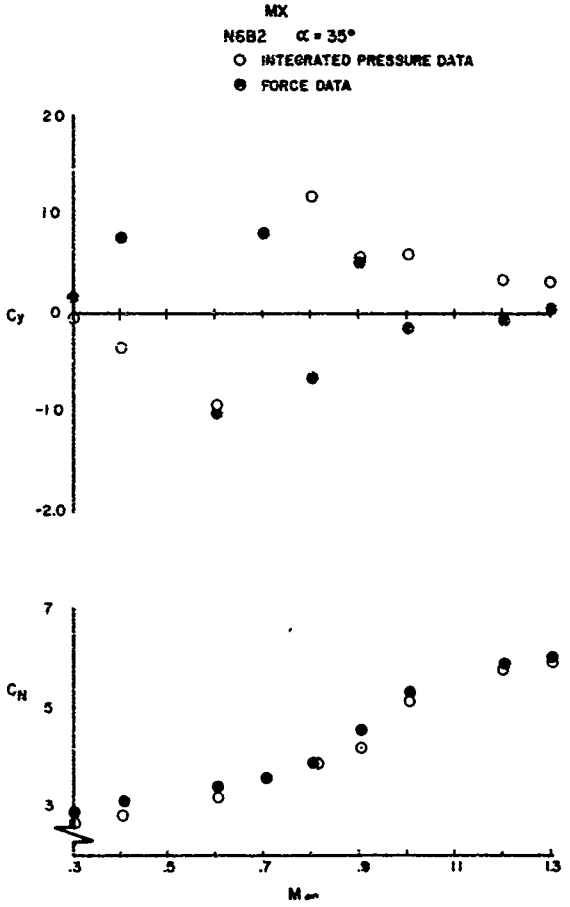

b. N6B2 Configuration

Figure 16 (Concluded)

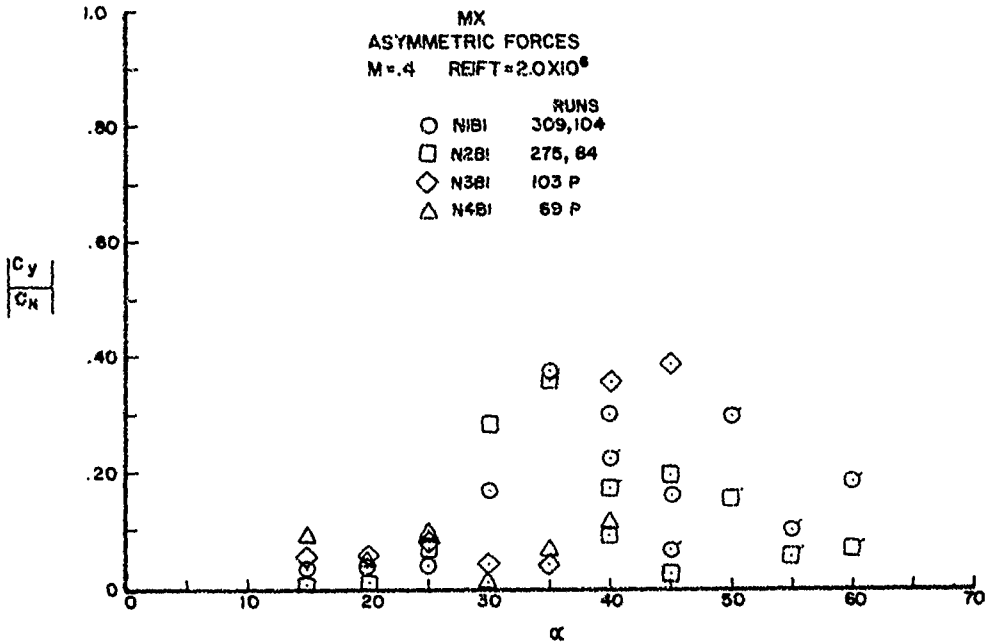

a. Mach 0.4, B1 Body

Figure 17. Effect of Angle-of-Attack and Configuration Geometry on the Ratio of Side Force to Normal Force Coefficient

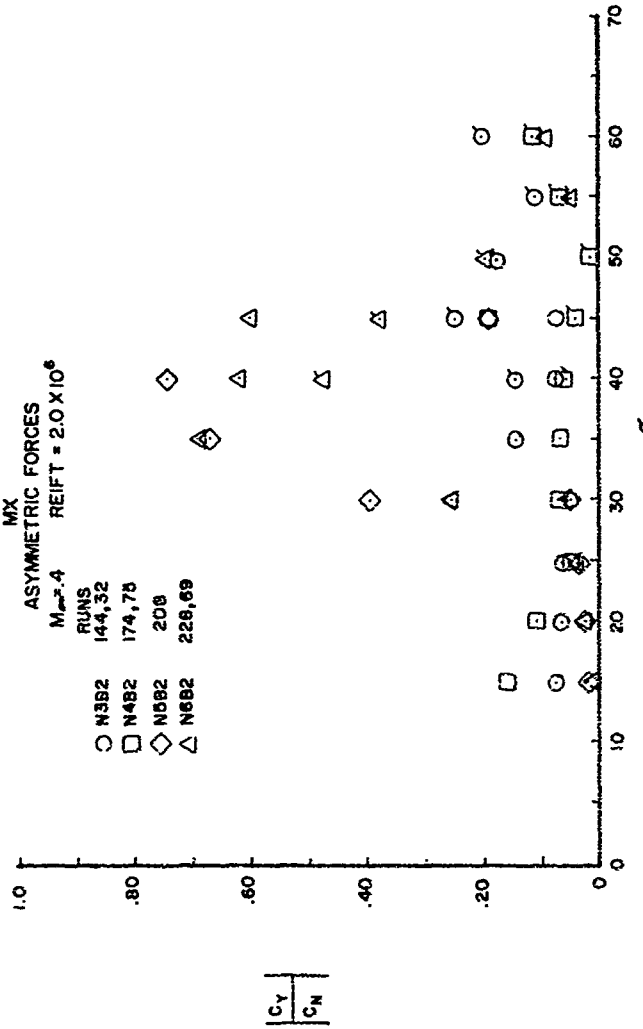

b. Mach 0.4, B2 Body
Figure 17 (Continued)

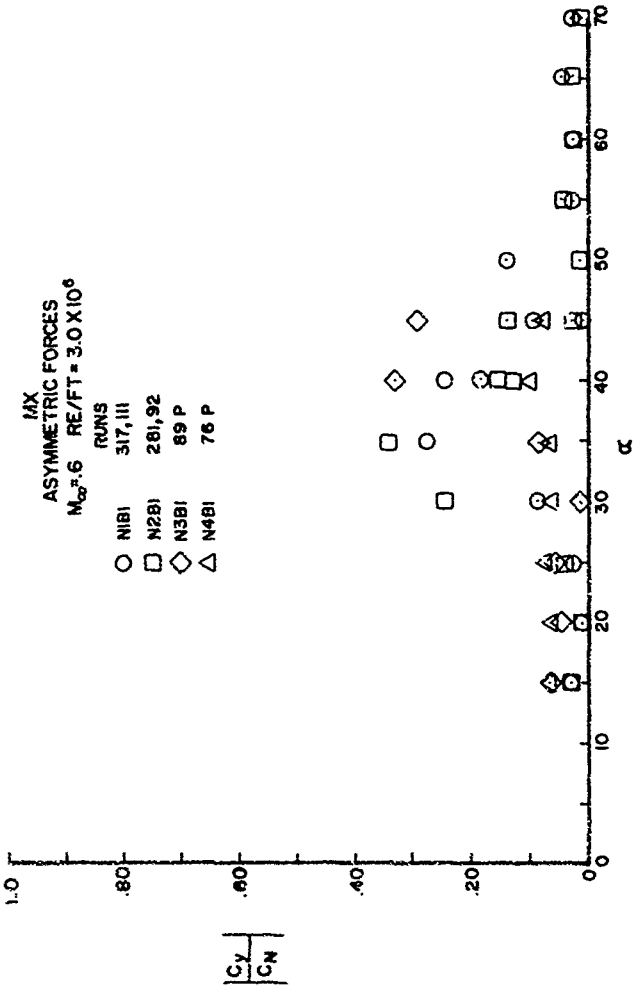

c. Mach 0.6, B1 Body

Figure 17 (Continued)

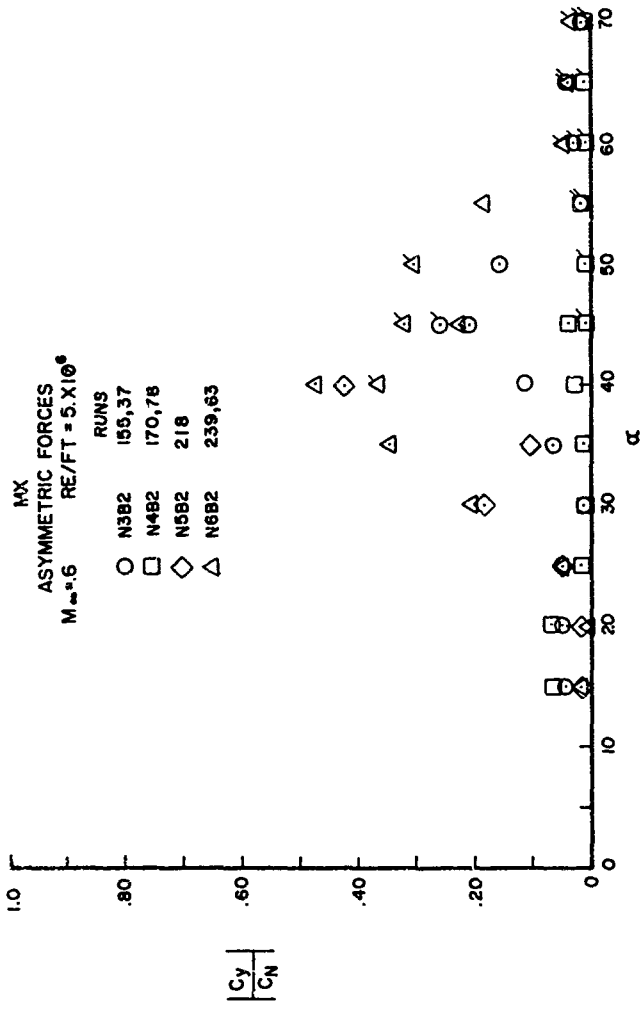

d. Mach 0.6, B2 Body

Figure 17 (Continued)

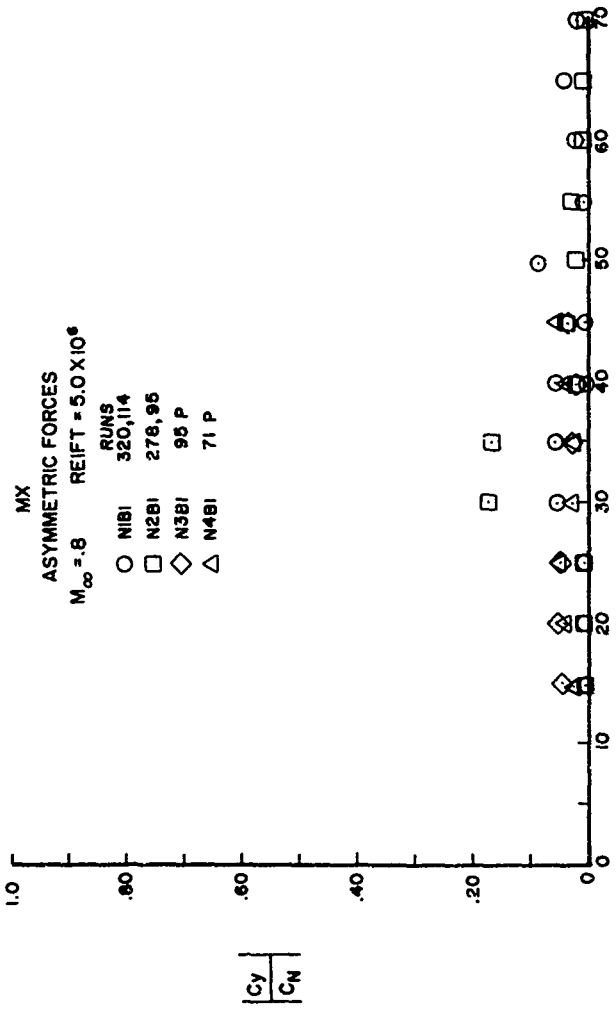

e. Mach 0.8, B1 Body

Figure 17 (Continued)

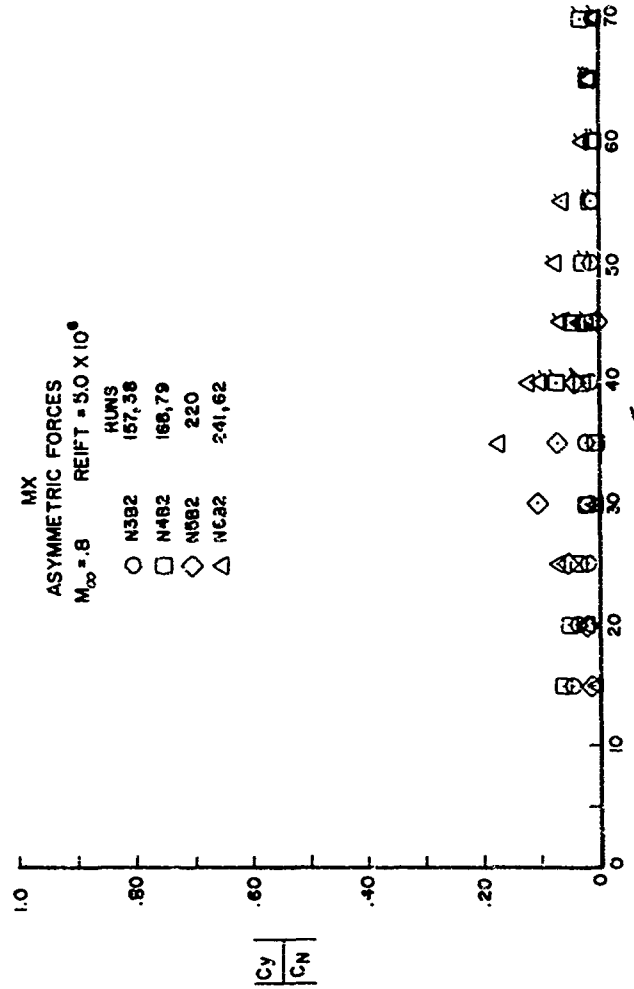

f. Mach 0.8, 82 Body
Figure 17 (Concluded)

One of the most interesting results is the effect of nose shape on the development of side force with increasing angle-of-attack above 25 degrees. The lowest fineness ratio nose (N4) is shown to have, in general, much lower side forces at all Mach numbers than the other configurations, while the triconic (N5B2, N6B2) nose configurations side forces are the highest. In fact at Mach 0.4, the N5B2 side force is seen to be as much as 73 percent of the normal force at α = 40 degrees, while the N4B2 is only about 6 or 7 percent. The ogive nose (N1, N2, N3 and N4) configurations side forces generally decrease with decreasing fineness ratio. The figures again show the side forces decreasing with increasing Mach number, dropping from 30 to 40 percent of normal force to about 5 percent -- going from Mach 0.4 to 0.8.

The section on Reynolds number effects will show that for all but the N4B2 the magnitudes of the forces and moments were sensitive to freestream Reynolds number once asymmetric flow had occurred. The trends with Reynolds number varied with configuration, and only generalized statements could be made concerning these effects. For the bluntest nose configuration, N4B2, the side forces and yawing moments stayed very small with Reynolds number variation; other nose configurations varied so much that there must be a point where decreased fineness ratio effects on the boundary layer are such that symmetrical shedding is continued to a much higher angle-of-attack. For other nose configurations the change in Reynolds number probably affects flow such that it changes the vortex shedding pattern in varying ways.

3. REYNOLDS NUMBER EFFECTS

The MX wind tunnel model was designed to as large a scale as possible for testing at maximum dynamic pressure in the 16T facility. The primary purpose for this was to test at the highest crossflow Reynolds number possible because of the very large angle-of-attack encountered by the MX air-launched missile, with possibilities of large side forces and yawing moments due to asymmetric vortex flow phenomena. Simulation of these phenomenon is a strong function of crossflow Reynolds number, R_{e_c}, and crossflow Mach number, M_c. The expected variation of full-scale R_{e_c} with M_c for the forward and rearward launch of the MX 3-80 missile

are shown in Figure 18 along with the wind tunnel values run during the MX testing program. Maximum R_{e_c} for full scale is 7.2×10^6 at $M_c = 0.4$ while wind tunnel R_{e_c} was 2.35×10^6. Although the mismatch of Reynolds number is apparent, these data still represent some of the highest Reynolds number testing at very high angles-of-attack to date and, as such, should aid in understanding the asymmetric vortex shedding problem area. Figure 19 shows the range of crossflow Reynolds numbers covered during these tests with respect to crossflow drag coefficient.

Since the primary purpose of the high Reynolds number was to investigate the asymmetric flow phenomena the emphasis in looking at the data was concentrated on angles-of-attack between 30 and 45 degrees. The very high angle-of-attack data were obtained on the strut model support. A data shift was observed when strut data were compared with sting data, indicating support interference effects due to the forward swept strut. For this reason the sting-mounted model data were primarily used.

Pressure coefficient data for the N2B1 configuration at $M = 0.6$, $\alpha = 45°$ and Reynolds numbers of 0.5, 1.0, 3.0 and 5.6×10^6 are shown in Figure 20a through f. A scrutiny of each station reveals that the effect of Reynolds number on the pressure distribution varies considerably. Each station has its own variations with meridian angle, and few definite trends could be noted. The positive C_p values are virtually unaffected by the changing Reynolds number, while the negative C_p's fluctuate with the Reynolds number. At station 10.5, for example, the pressure distribution is symmetrical with the largest negative C_p on the far leeward side being for the lowest Reynolds number. At station 17.5 the distribution is slightly unsymmetrical, with the highest Reynolds number run showing the largest negative C_p on the far leeward side. For meridian angles of 60 to 110 degrees, the increasing negative C_p corresponds to increasing Reynolds number in most cases. A noteworthy effect was the increasingly unsymmetrical pressure distribution, particularly at the higher Reynolds numbers, with only a short change in body length. At station 17.5 the distribution is already slightly unsymmetrical, and at $X = 26.5$ the distribution is quite unsymmetrical. At $X = 46.5$ the distribution is fairly symmetrical again, and at $X = 66.5$ the distribution is unsymmetrical, with the larger

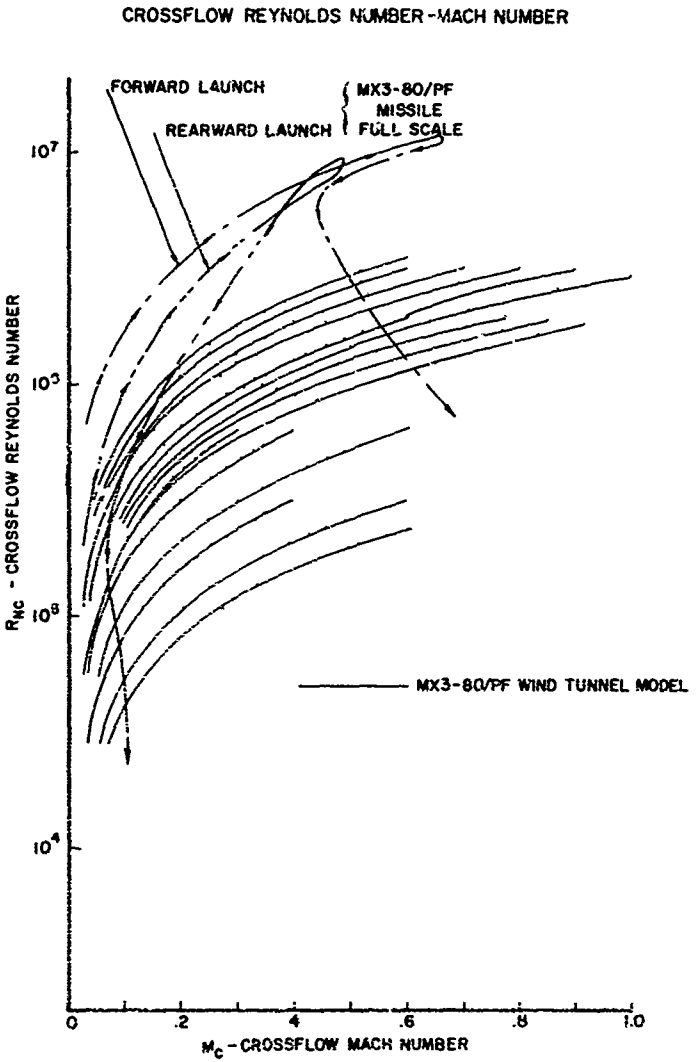

Figure 18. Variation of Crossflow Reynolds Number with Crossflow Mach Number

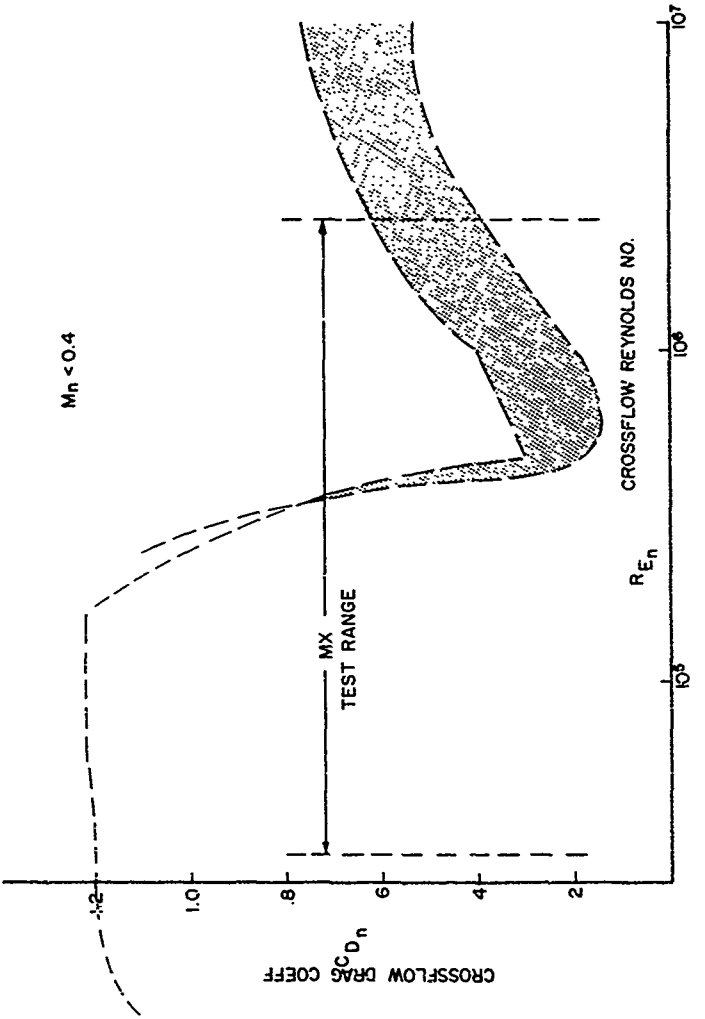

Figure 19. Variation of Crossflow Drag Coefficient with Crossflow Reynolds Number

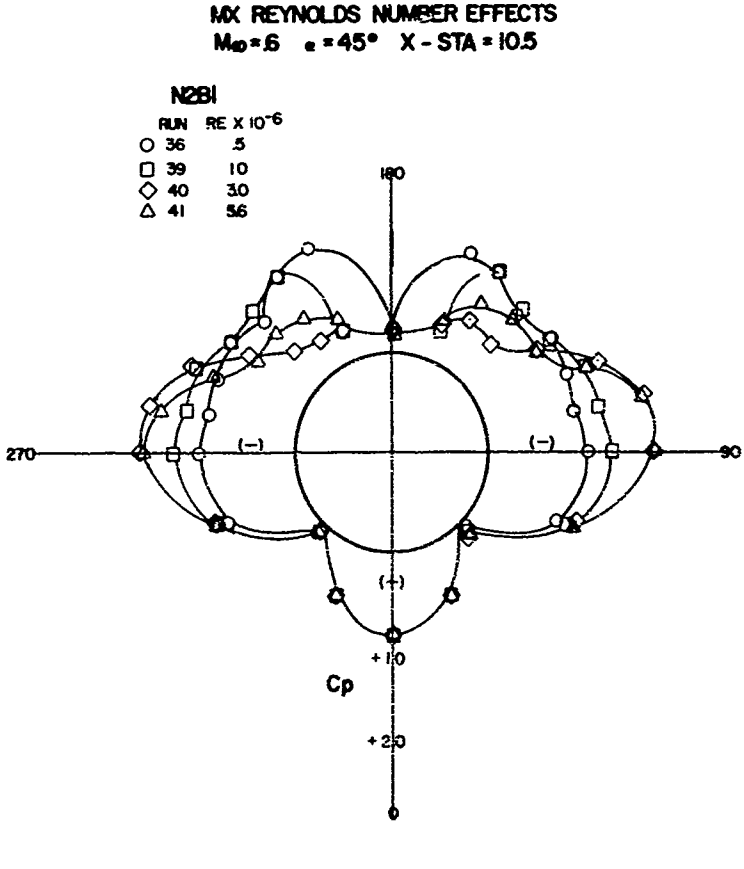

a. X = 10.5

Figure 20. Effect of Reynolds Number on Local Pressure Coefficient Distribution

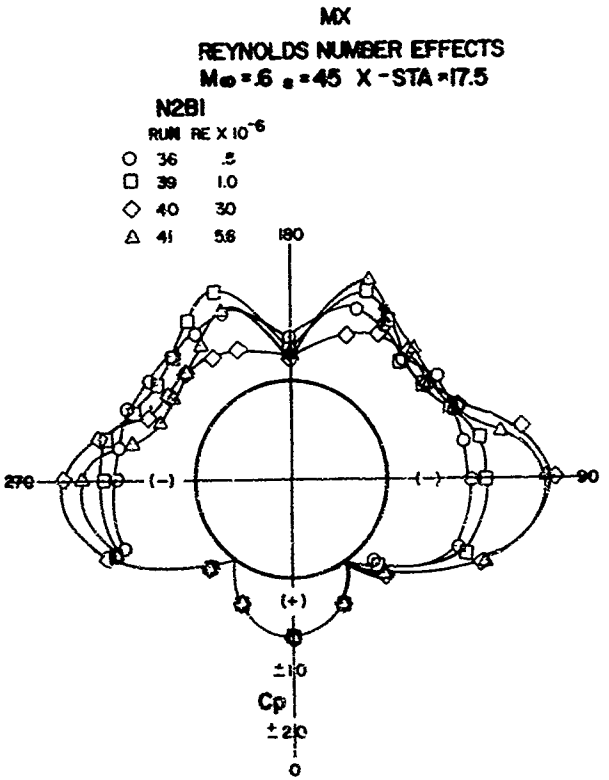

b. x = 17.5

Figure 20 (Continued)

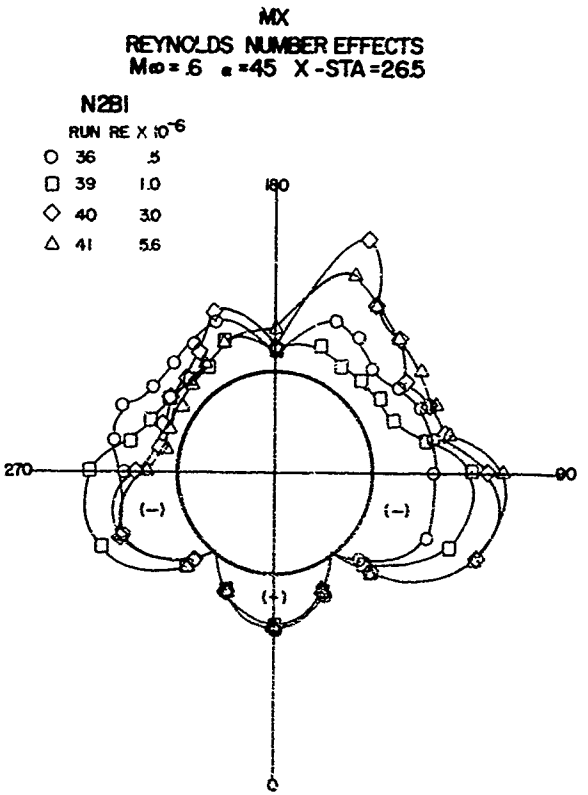

c. X = 26.5

Figure 20 (Continued)

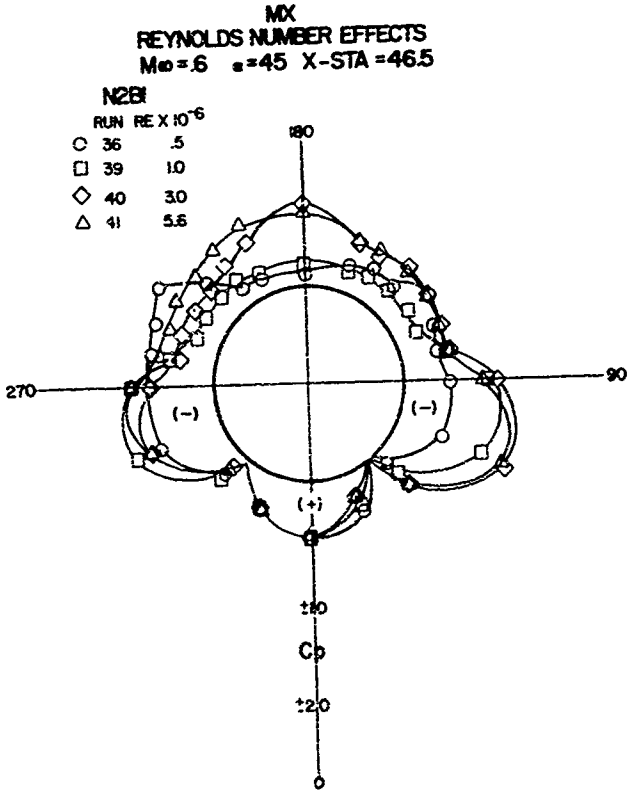

d. X = 46.5

Figure 20 (Continued)

MX

REYNOLDS NUMBER EFFECTS

$M_\infty = .6$ $\alpha = 45$ X-STA = 66.5

N2BN

RUN	RE X 10^{-6}
○ 36	.5
□ 39	1.0
◇ 40	3.0
△ 41	5.6

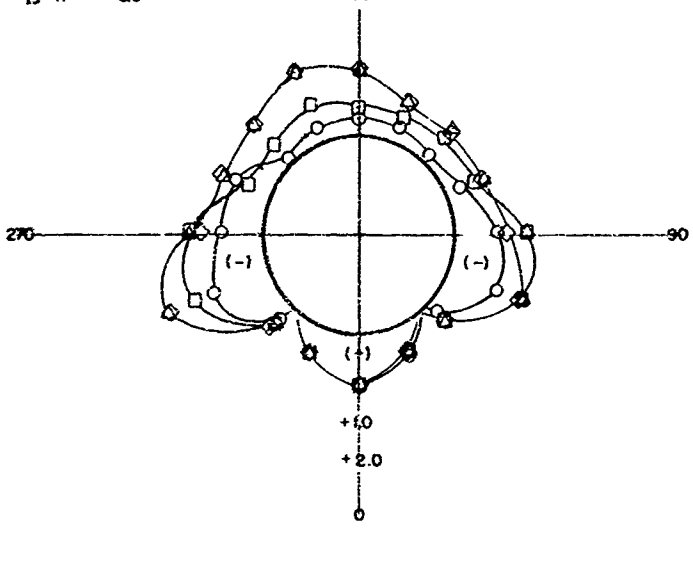

e X = 66.5

Figure 20 (Continued)

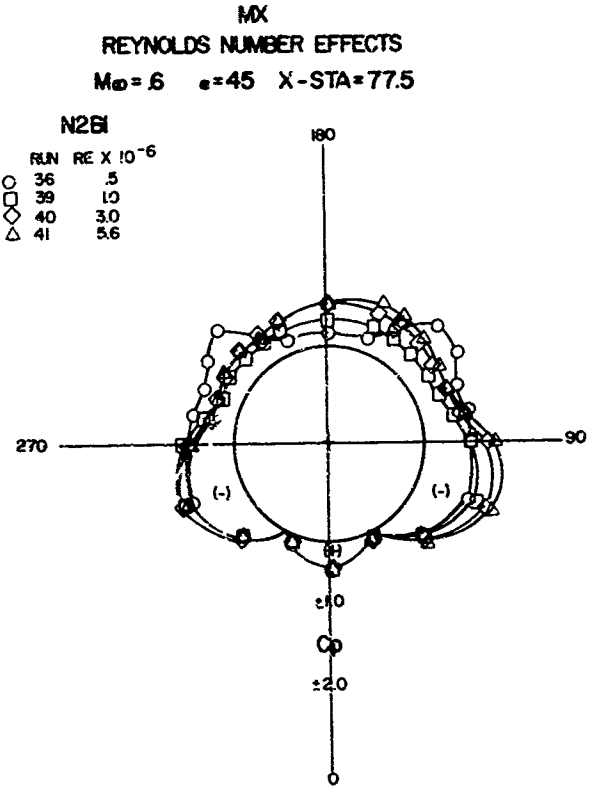

f. X = 77.5

Figure 20 (Concluded)

negative values to the opposite side of the X = 26.5 values. The systematic variation of side force values from side to side is apparent from the pressure data. Depending on the pattern, the integrated side forces could give a small summation force; whereas with the unsymmetrical pattern starting so far forward, the yawing moments could still be very large.

The force and moment balance data for various Reynolds numbers on the N2B1, N3B2, N4B2 and N6B2 configurations was so inconsistent that no definite trends could be established. Figures 21 through 22 show the C_N, C_Y and C_n aerodynamic coefficients plotted versus angle-of-attack for the N2B1 and N3B2 configurations at M_∞ = 0.6 for four different Reynolds numbers. Initial conclusions from these figures would indicate that the highest Reynolds number would have the largest normal force, side force, and yawing moment coefficients at the higher angles of-attack. Unfortunately, the balance data for other Mach numbers and configurations did not always show these same trends. Crossplots of C_N, C_A, C_y and C_n with Reynolds number for the N2B1, N3B2 and N6B2 configuration at angles-of-attack between 25 and 45 degrees (shown in Figure 23) demonstrate that even at a constant Mach number of 0.6 the trends are not completely consistent. Generally, increasing the Reynolds number increased the magnitude of the side force and yawing moment coefficients and increased normal force coefficients over the medium Reynolds number values.

The strut data for the N3B2 configuration was also cross plotted (Figure 24) to see if the trends noted above for the angles-of-attack, 40 and 45 degrees on the sting, remained the same. The side force and yawing moment were of different values but showed the same trends. The integrated pressure data for the N2B1 configuration was also plotted (Figure 25) to see if the pressure data trends were similar. These plots show a different shape to the curves with the increases in coefficients leveling off above a Reynolds number of 3.0×10^6.

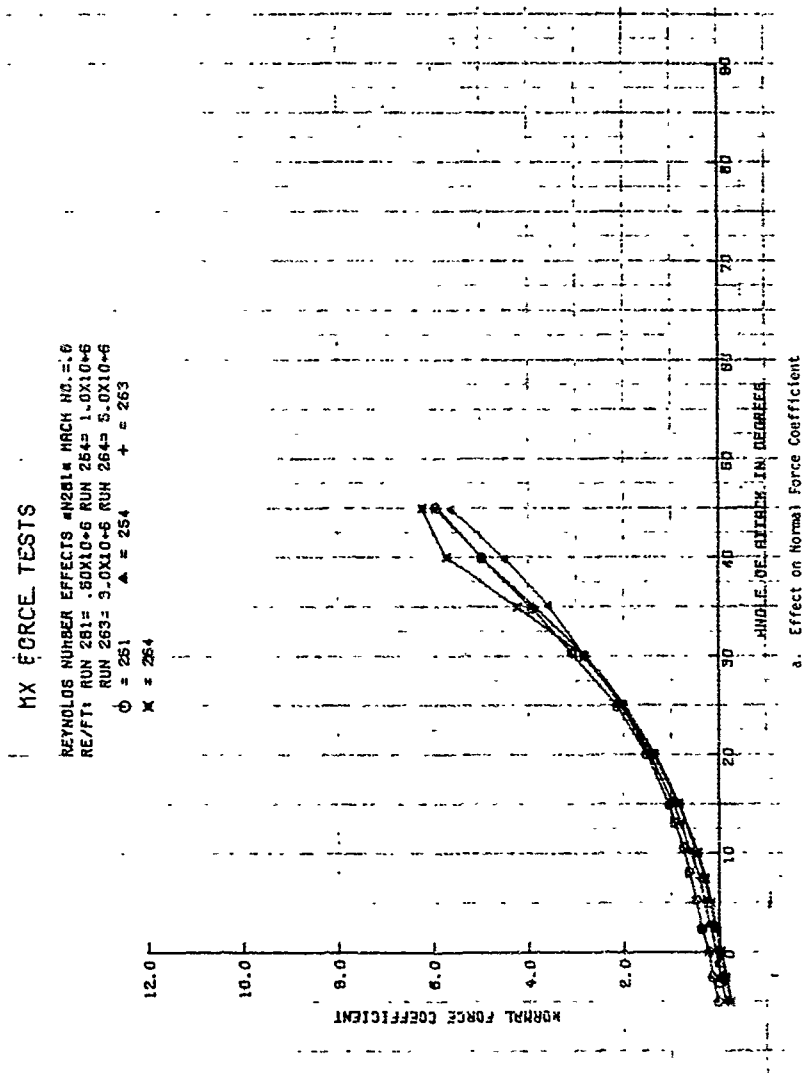

a. Effect on Normal Force Coefficient

Figure 21. Effect of Reynolds Number on Force and Moment Coefficients. N281 Configuration.

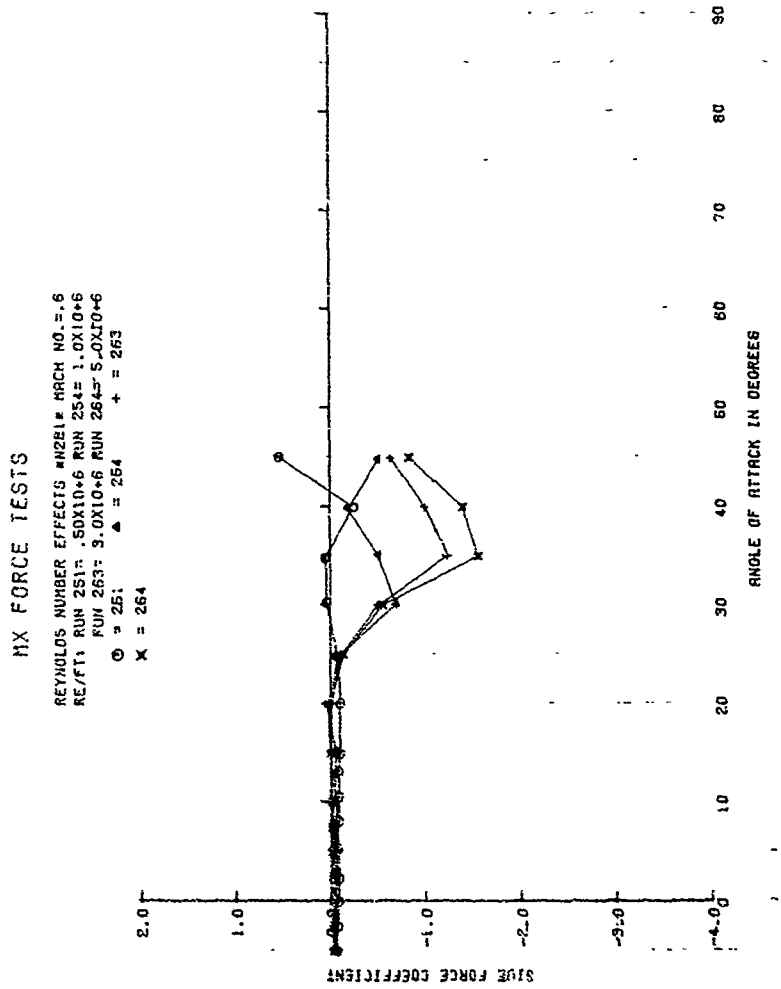

b. Effect on Side Force Coefficient

Figure 21 (Continued)

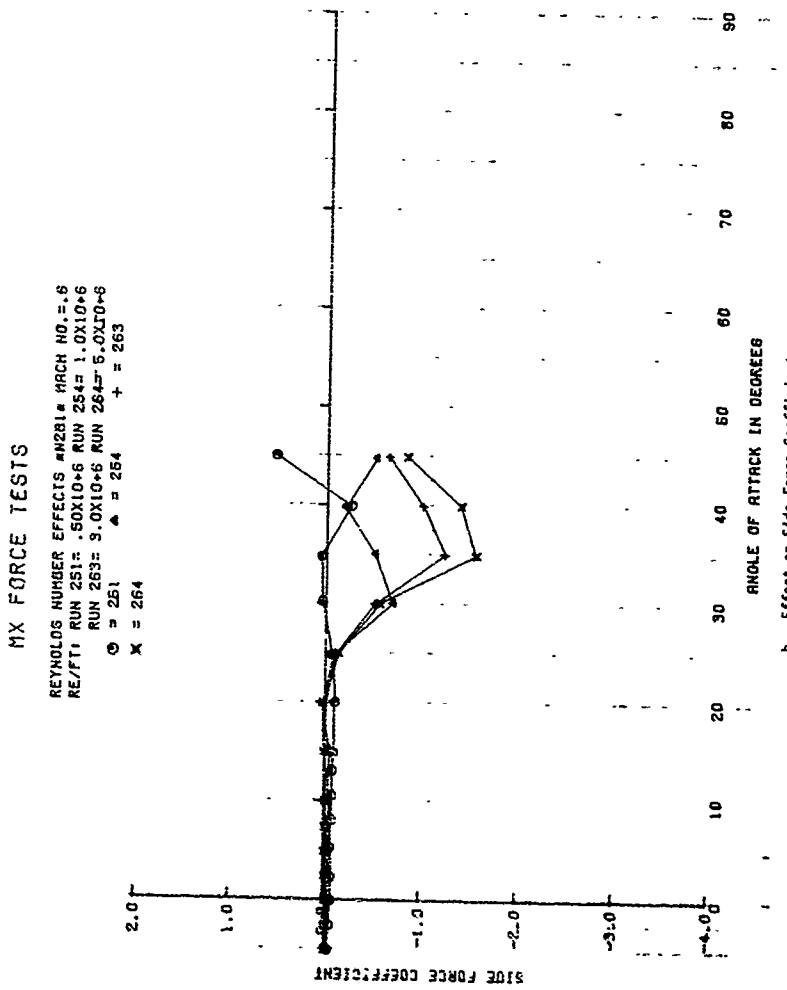

b. Effect on Side Force Coefficient

Figure 21 (Continued)

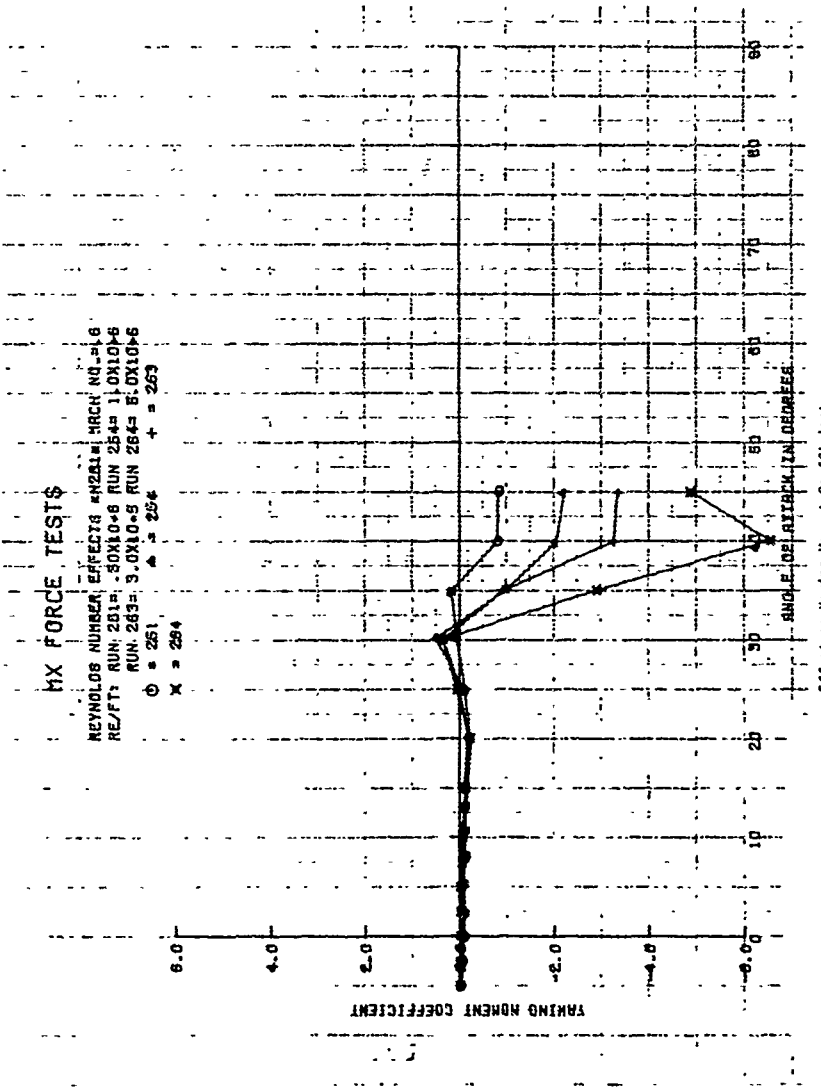

c. Effect on Yawing Moment Coefficient

Figure 21 (Concluded)

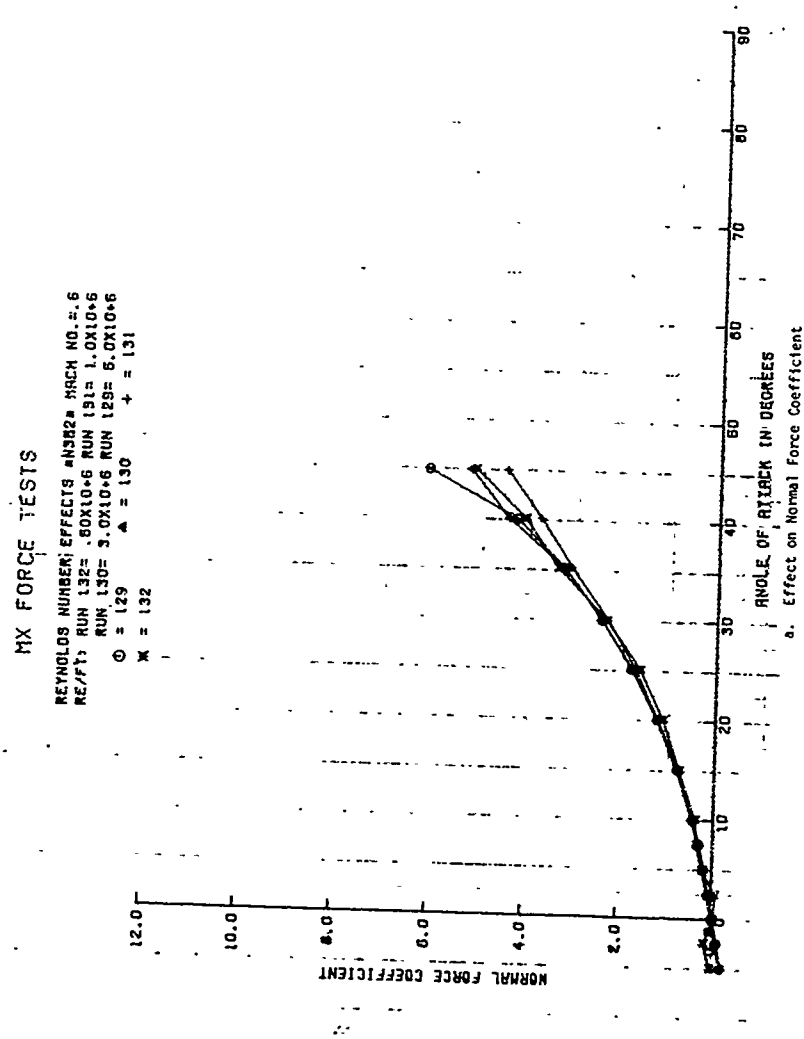

a. Effect on Normal Force Coefficient

Figure 22. Effect of Reynolds Number on Force and Moment Coefficients. N382 Configuration.

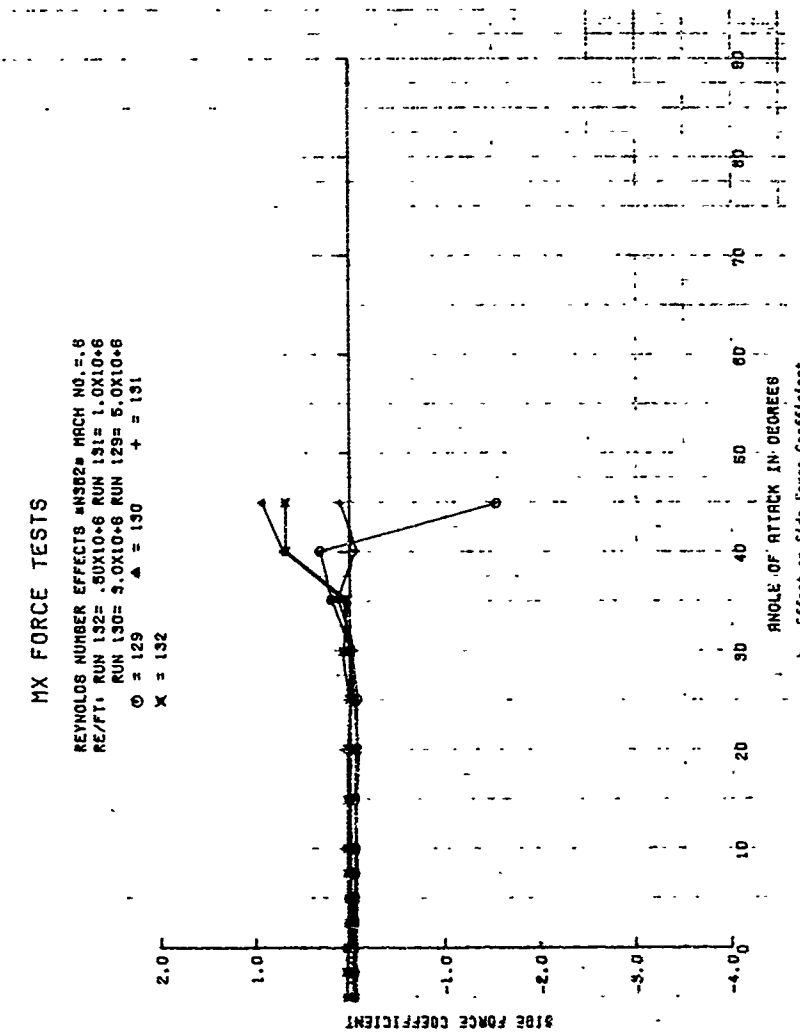

b. Effect on Side Force Coefficient

Figure 22 (Continued)

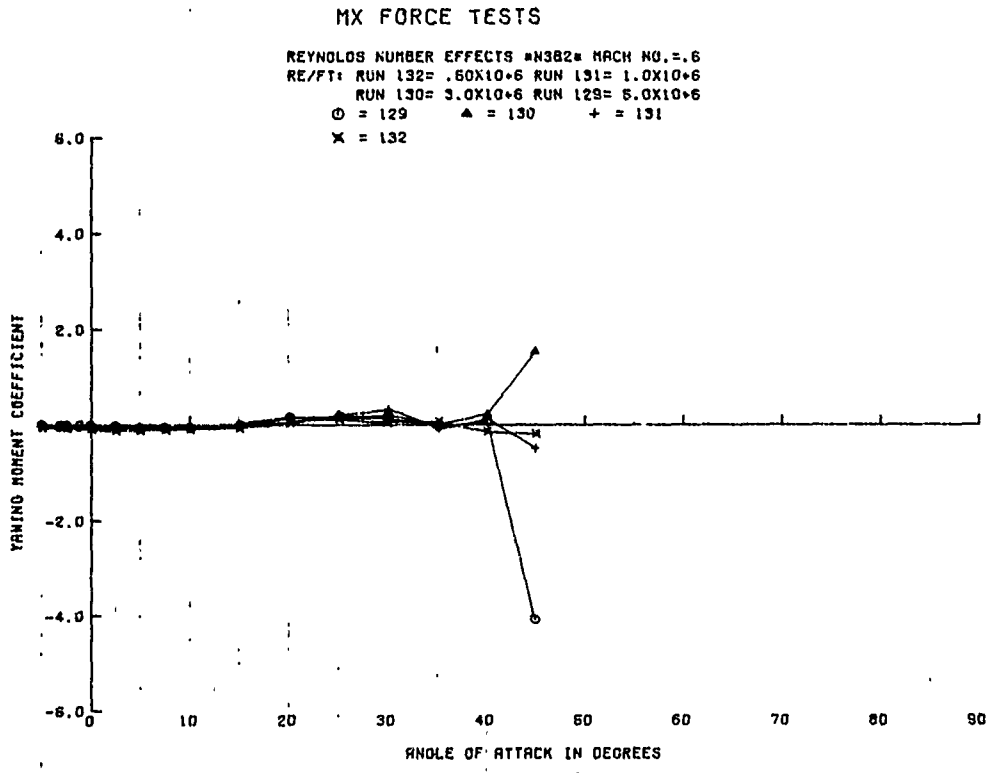

c. Effect on Yawing Moment Coefficient

Figure 22 (Concluded)

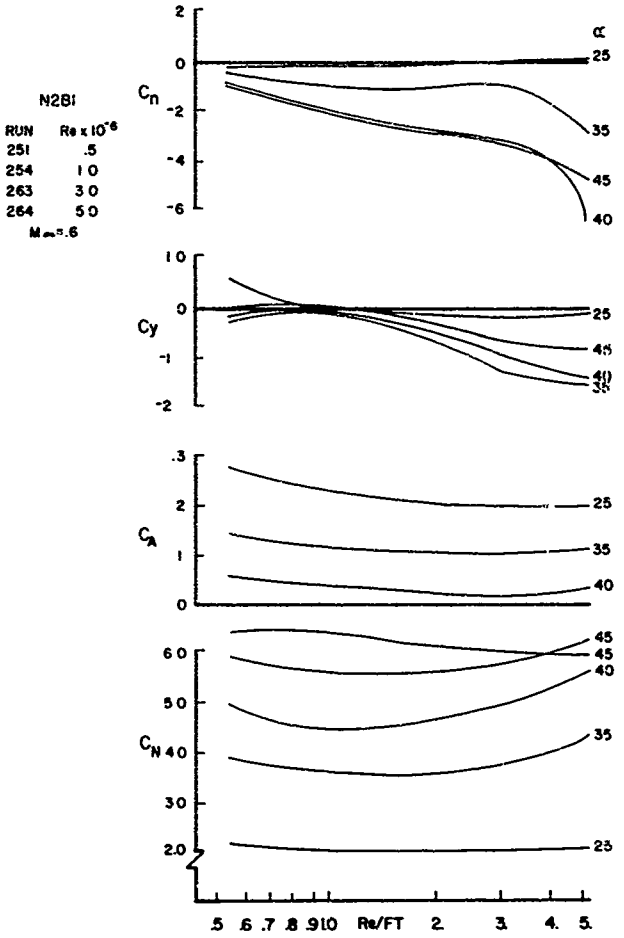

a. N281 Configuration

Figure 23. Force and Moment Coefficients vs Unit Reynolds Number - Sting-Mounted Data

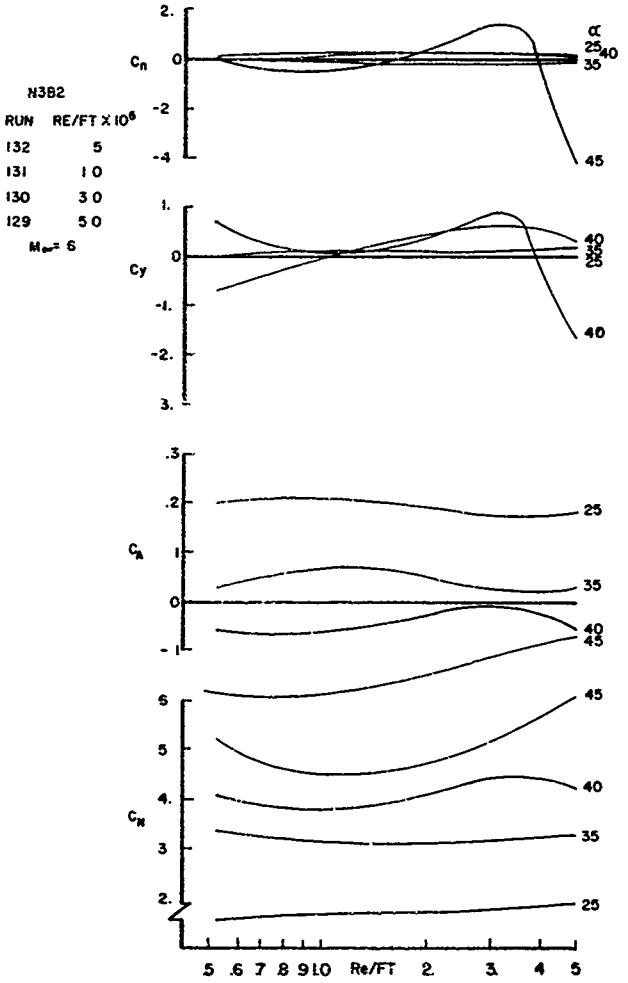

b. N3B2 Configuration

Figure 23 (Continued)

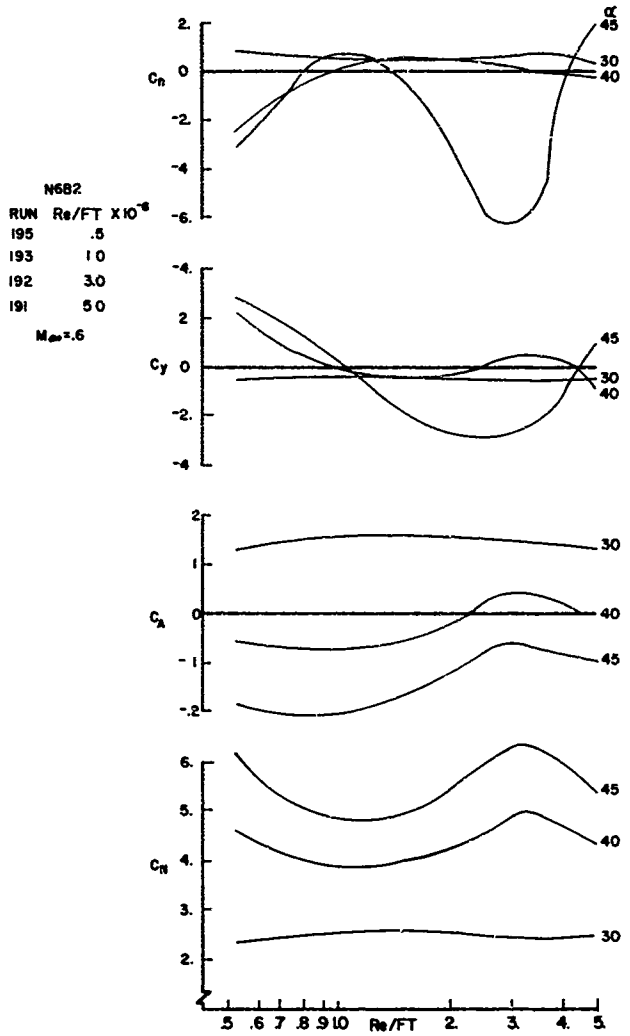

c. N6B2 Configuration

Figure 23 (Continued)

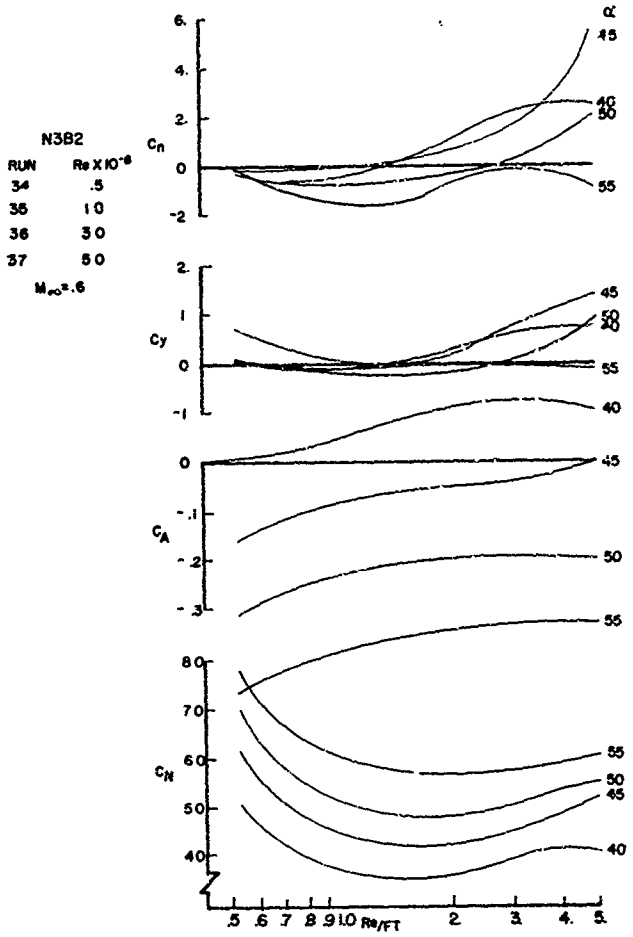

Figure 24. Force and Moment Coefficients vs Unit Reynolds Number for the N3B2 Configuration - Strut-Mounted Data

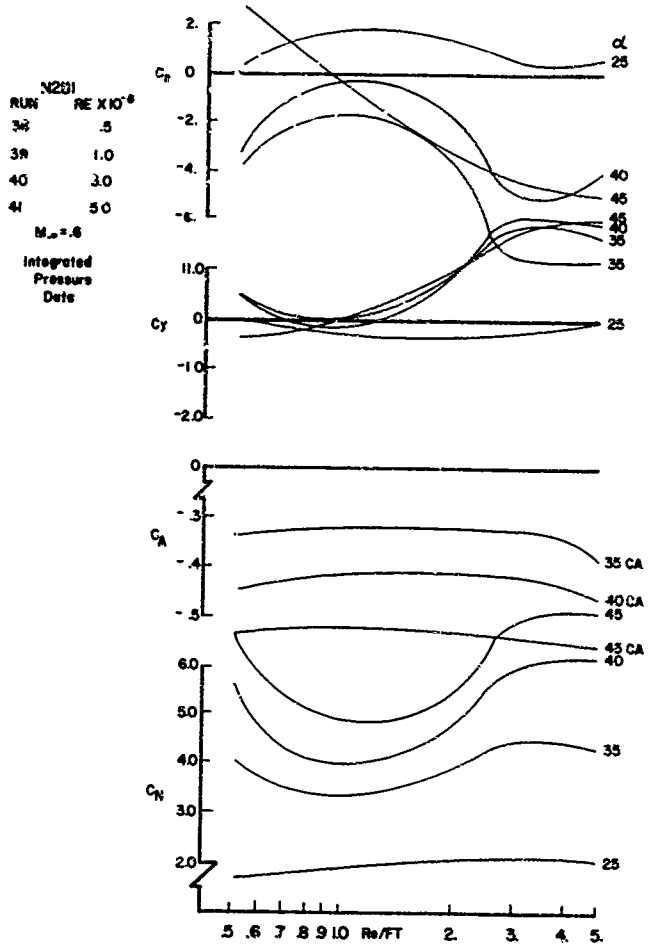

Figure 25. Integrated Pressure Force and Moment Coefficients vs Unit Reynolds Number - N2B1 Configuration

4. MACH NUMBER EFFECTS

Testing spanned Mach numbers from 0.3 to 1.5 for most of the model configurations. Figures 26 and 27 present some of the higher angle-of-attack aerodynamic coefficient data showing the effect of increasing Mach number. Figure 26 shows the increasing normal force coefficient with increasing Mach number for seven different configurations at an angle-of-attack of 35 degrees. Figure 27 shows the decreasing side force and yawing moment coefficients with increasing Mach number. These plots clearly demonstrate that asymmetric force phenomena is essentially associated with subsonic Mach numbers.

5. NOSE SHAPE EFFECTS

Figure 28 shows sketches of all 14 nose shapes which were built for wind tunnel testing. Figures 29 to 31 compare the N1, N2, N3 and N4 noses (with B1 body length) aerodynamic coefficients for Mach numbers of 0.4, 0.6 and 0.8. The N3B1 and N4B1 data are integrated pressure results. At Mach number 0.4 the normal force coefficient for the N4B1 configuration is noted to be somewhat lower than the others for angles-of-attack above 30 degrees. The N1B1, N2B1 and N3B1 C_N values are very close and all increase rapidly from 35 to 45 degrees. The side force and yawing moment coefficients are quite small until angles-of-attack increase above 25 degrees. The side force increases rapidly for all configurations, but much less with the N4B1 than with the other three. The yawing moment stays relatively small until 40 degrees, meaning that, although the side forces are large, the distribution is such that they cancel out as moments, then increase dramatically for the N1B1, N2B1 and N3B1 configurations. Again the N4B1 asymmetric forces are much less than the other three. At Mach number 0.6 the plots show similar trends with the exception of the jump in normal force coefficient of the N3B1 configuration. It is of interest to note that this occurs at the angle-of-attack where the N3B1 configuration has large asymmetric forces, in fact, much larger than the other three configurations. The Mach number 0.8 data show little difference in C_N and only small asymmetric forces for all configurations.

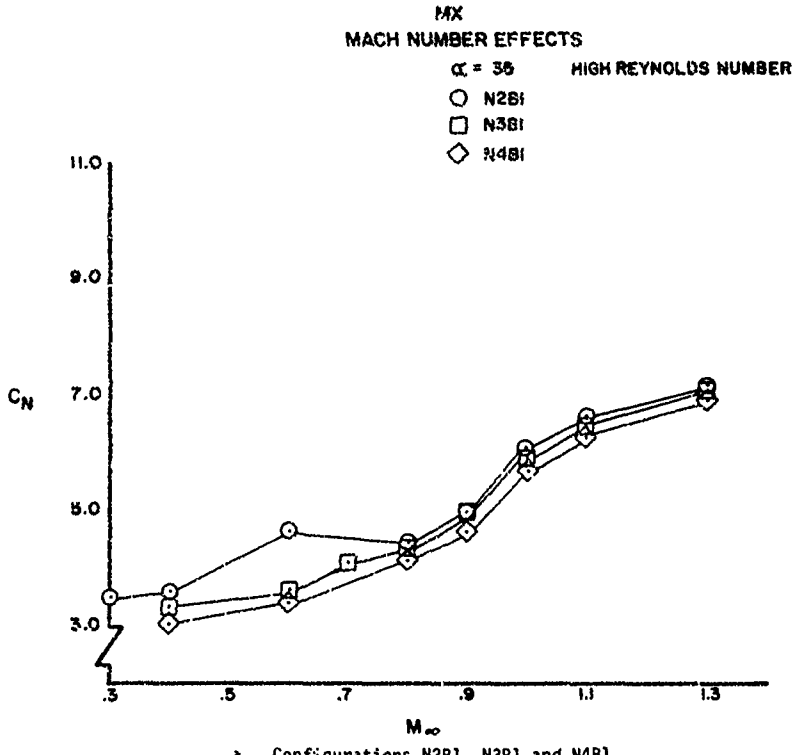

a. Configurations N2B1, N3B1 and N4B1

Figure 26. Normal Force Coefficient vs Mach Number at α = 35

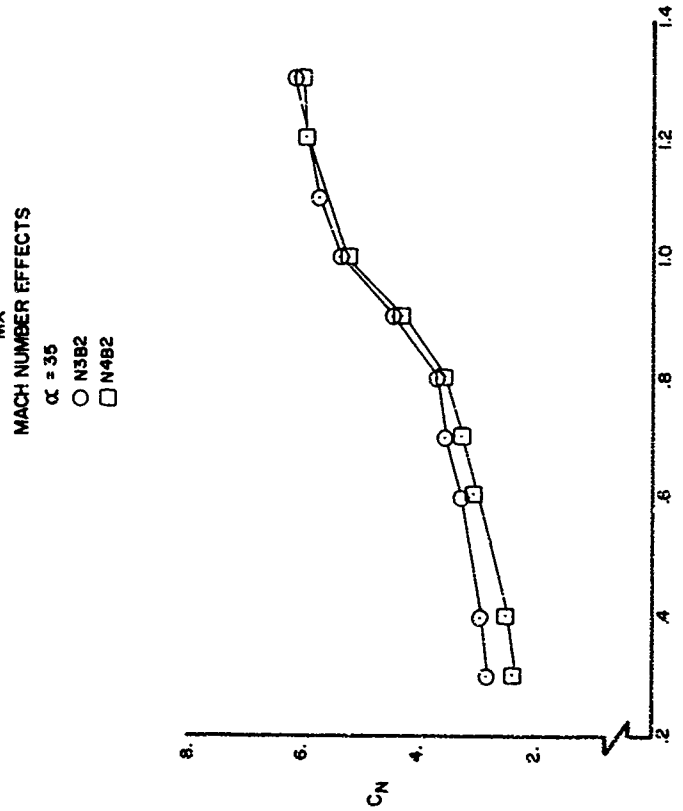

b. Configurations N3B2 and N4B2

Figure 26 (Continued)

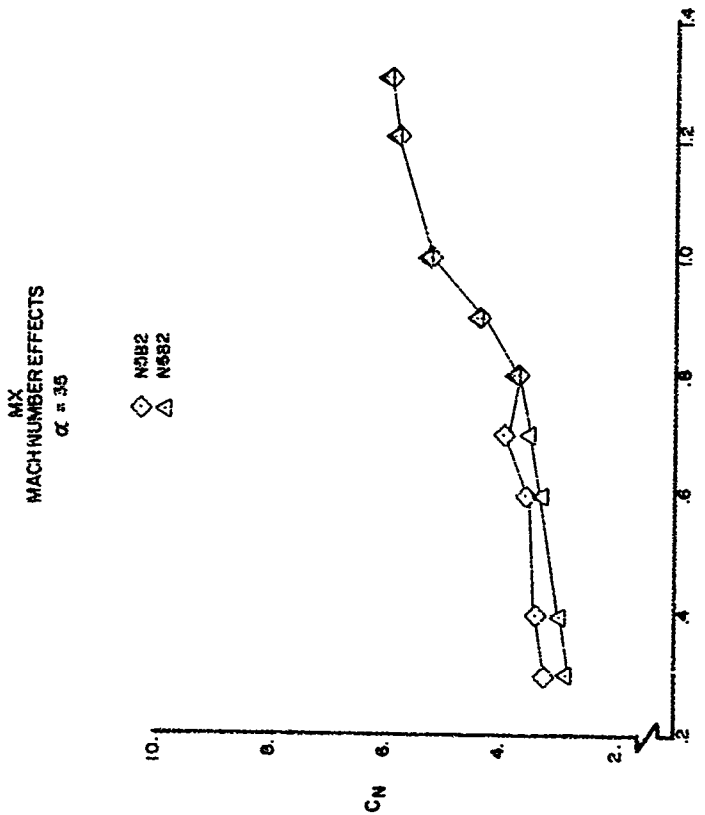

c. Configurations N5B2 and N6B2
Figure 26 (Concluded)

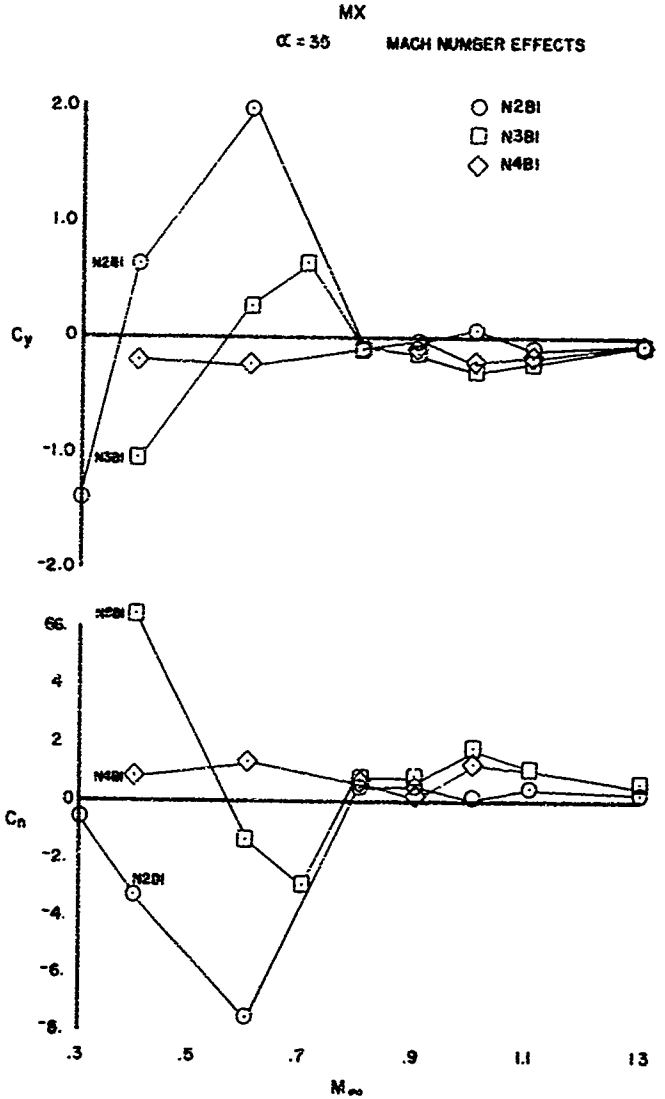

a. Configurations N2B1, N3B1 and N4B1 at α = 35°

Figure 27. Side Force and Yawing Moment Coefficients vs Mach Number

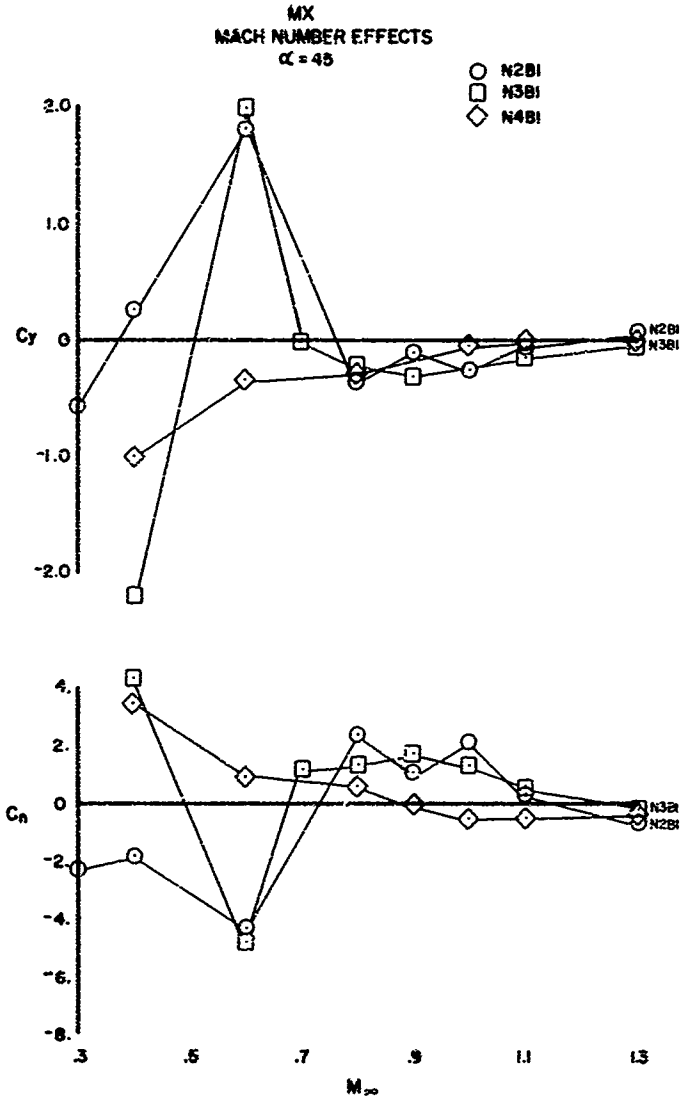

b. Configurations N2B1, N3B1 and N4B1 at α = 45°

Figure 27 (Continued)

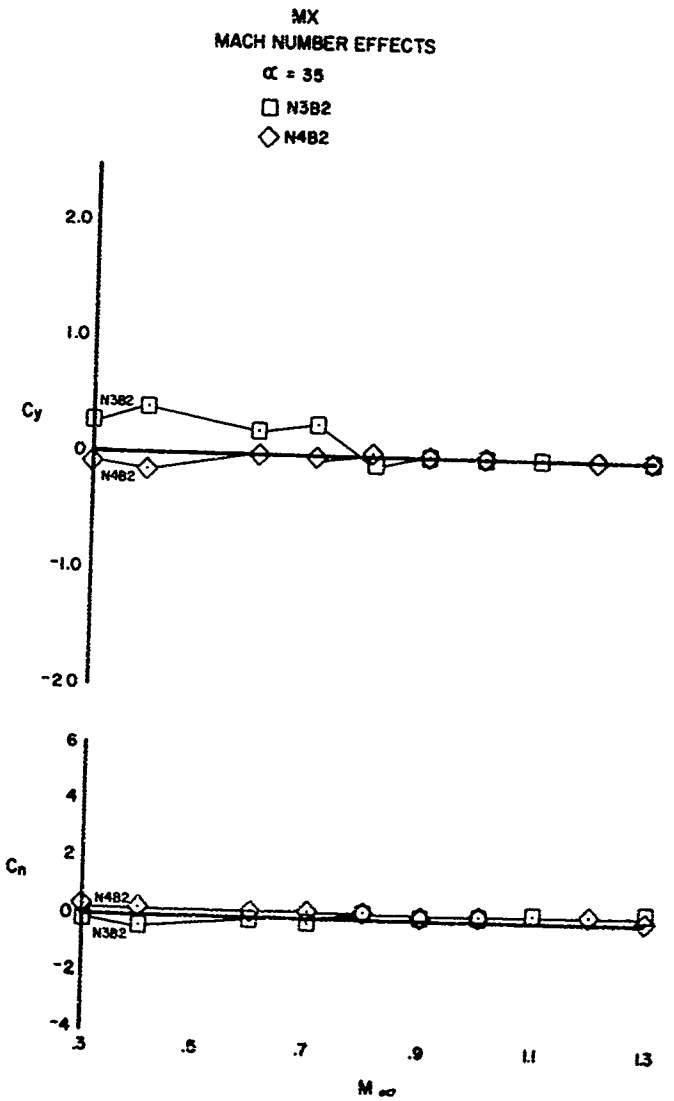

c. Configurations N3B2 and N4B2 at α = 35°

Figure 27 (Continued)

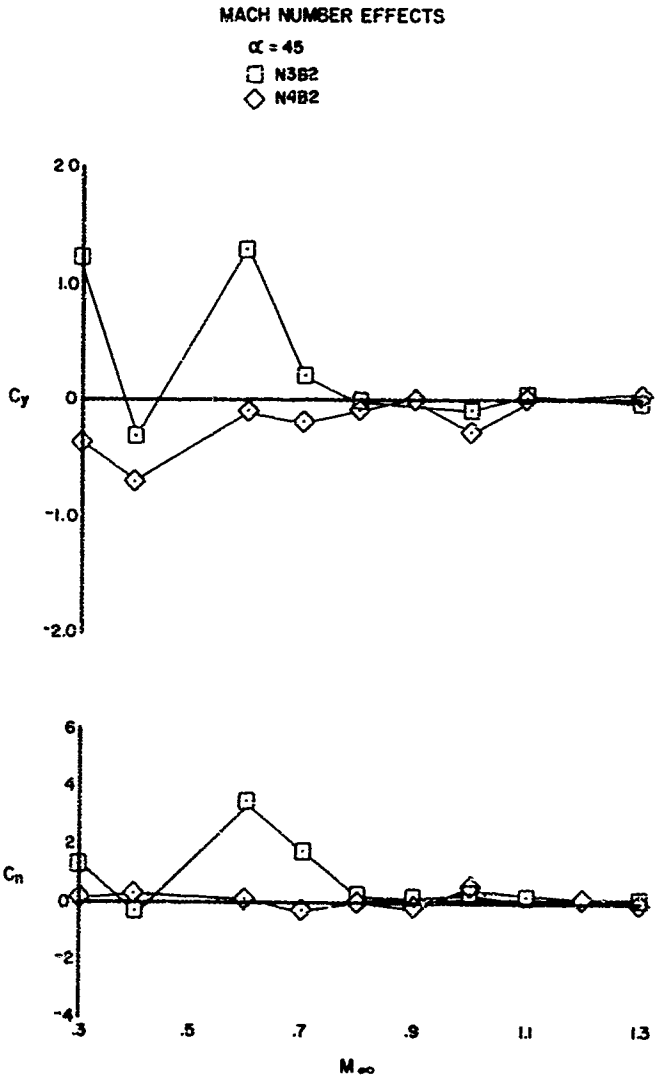

d. Configurations N3B2 and N4B2 at α = 45°

Figure 27 (Continued)

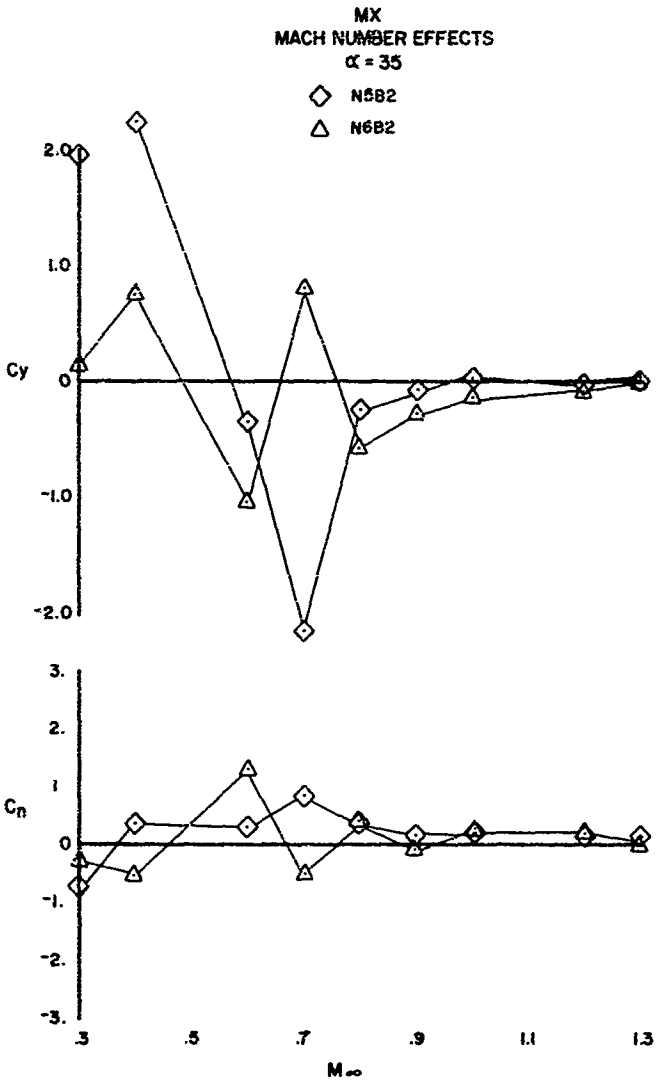

e. Configurations N5B2 and N6B2 at α = 35°

Figure 27 (Continued)

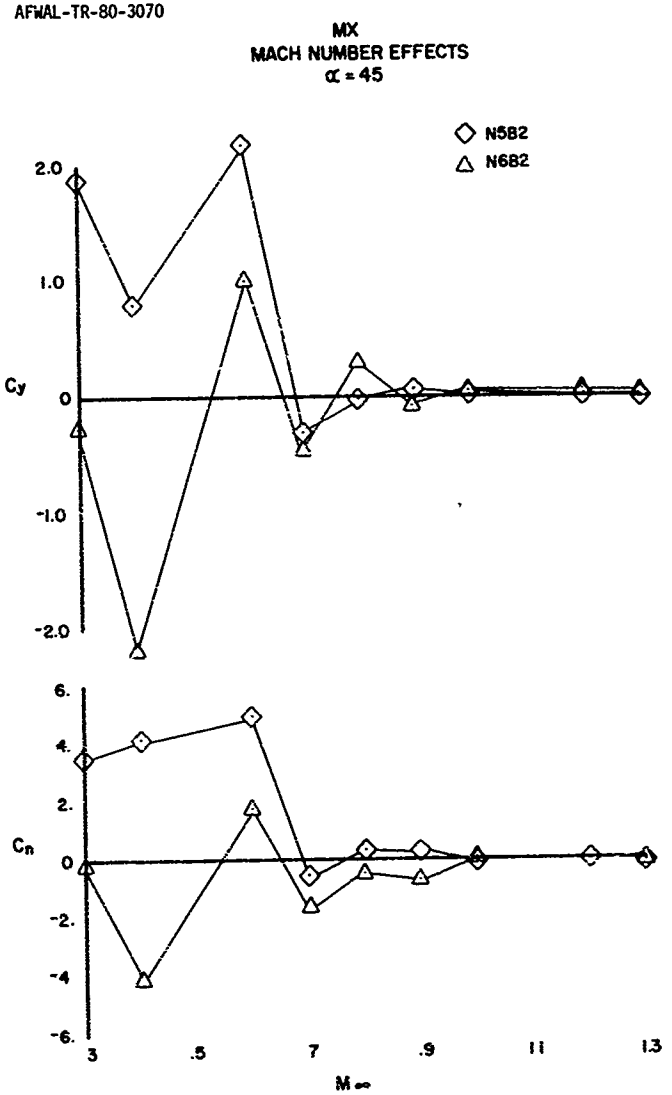

f. Configurations N5B2 and N6B2 at α = 45°

Figure 27 (Concluded)

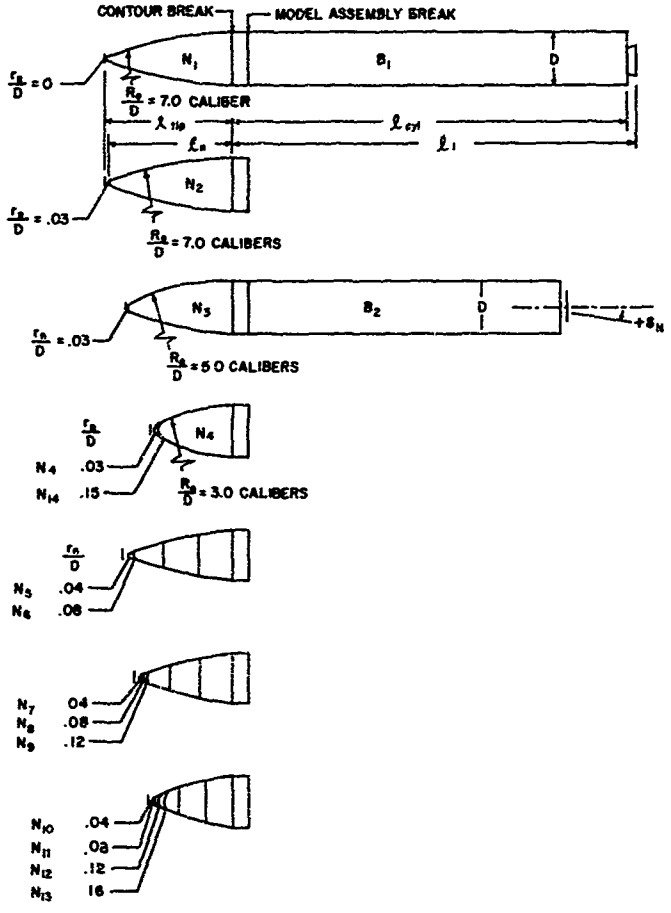

Figure 28. Model Configurations and Nomenclature

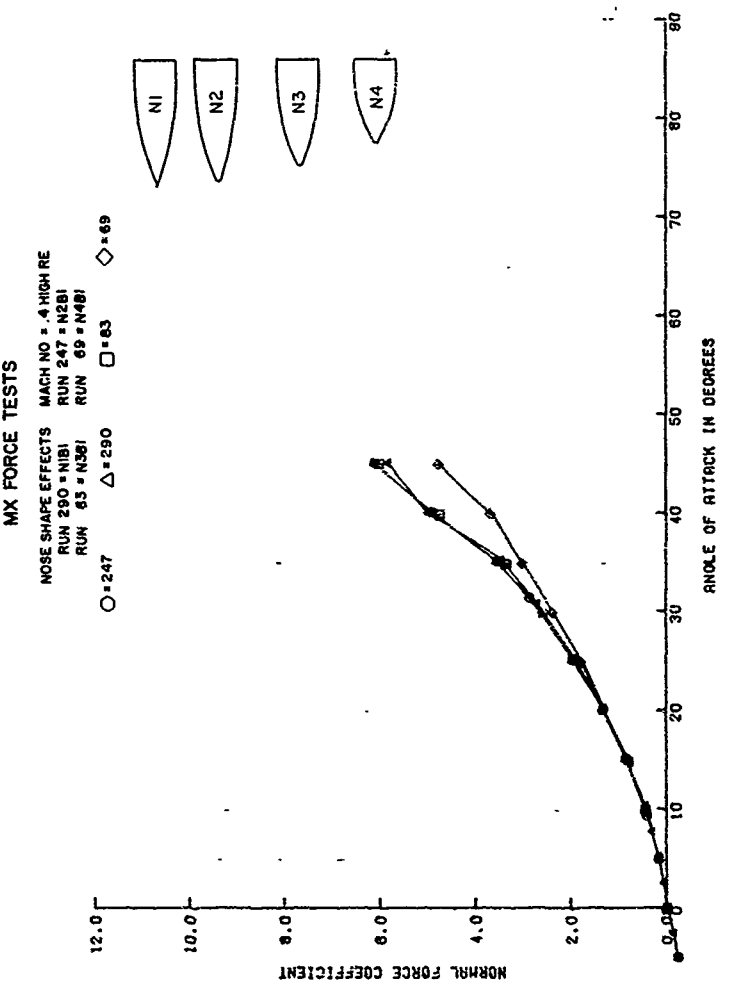

a. M = 0.4

Figure 29. Effect of Nose Shape on Normal Force Coefficient, B1 Body

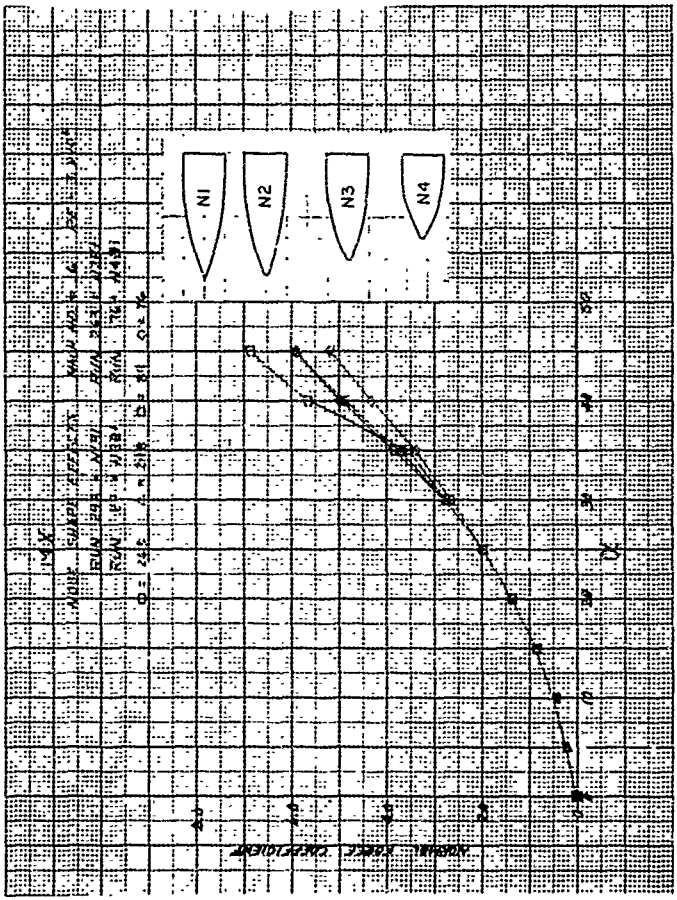

b. M = 0.6

Figure 29 (Continued)

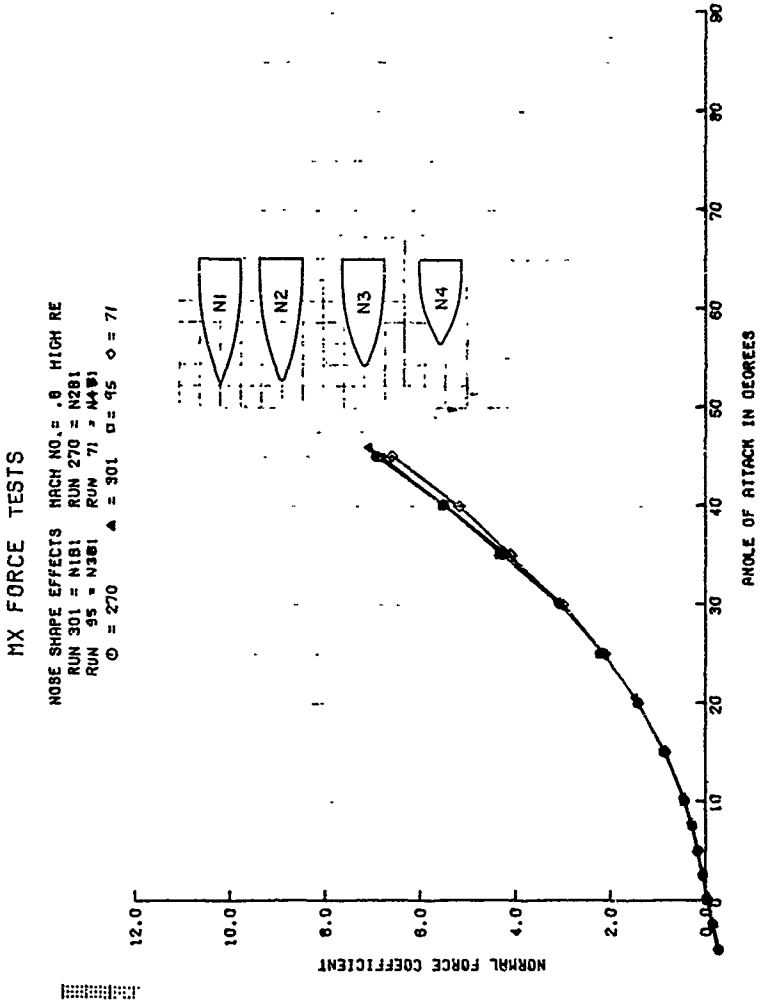

c. M = 3.0

Figure 29 (Concluded)

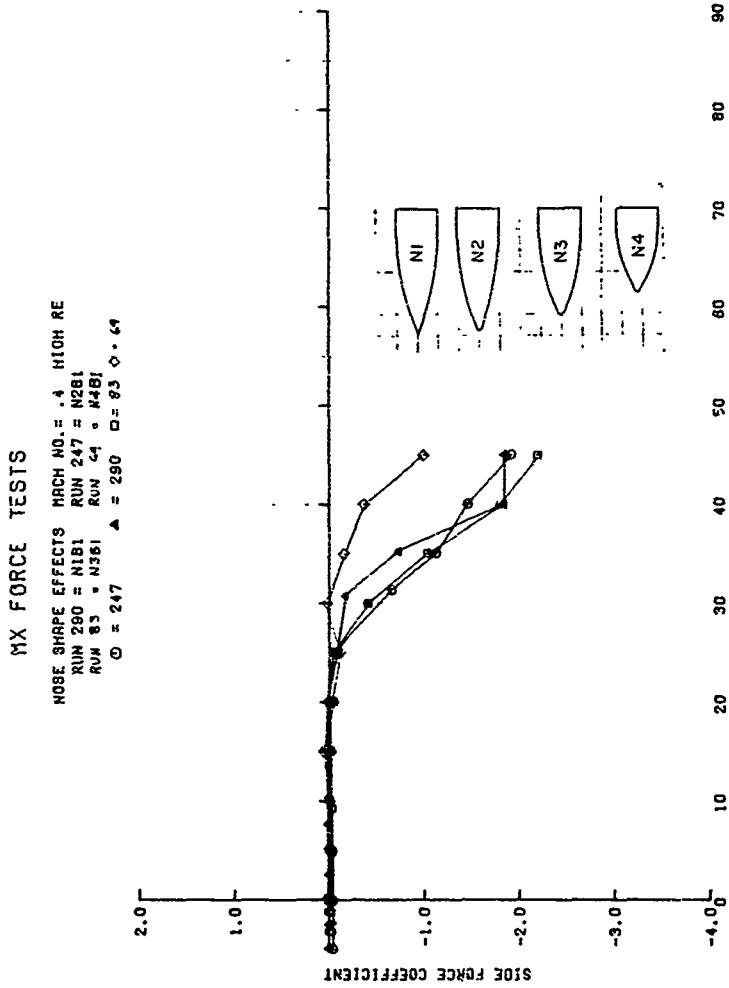

4. M = 0.4

Figure 30. Effect of Nose Shape on Side Force Coefficient, B1 Body

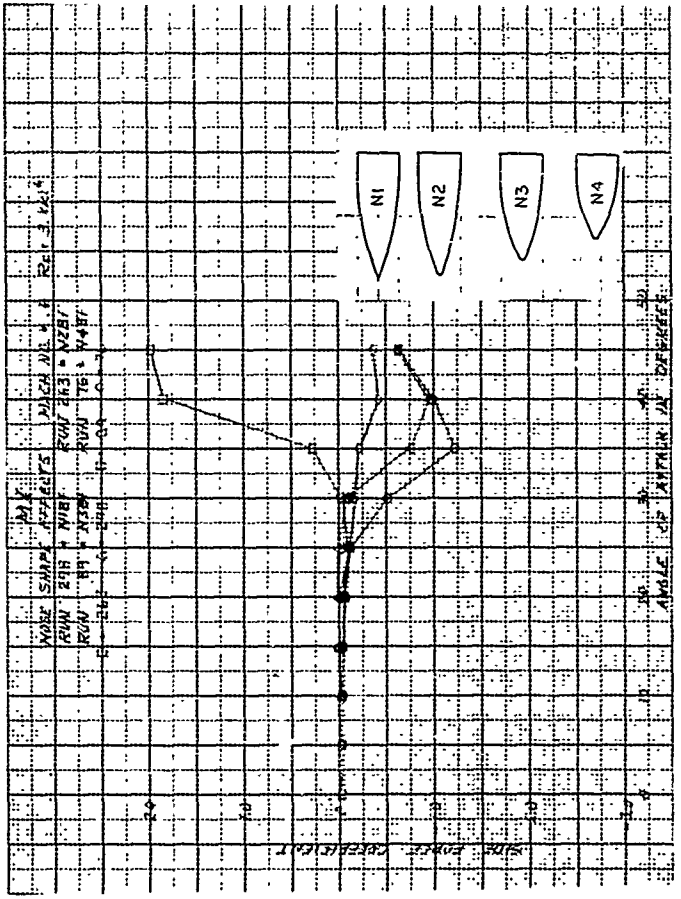

b. M = 0.6

Figure 30 (Continued)

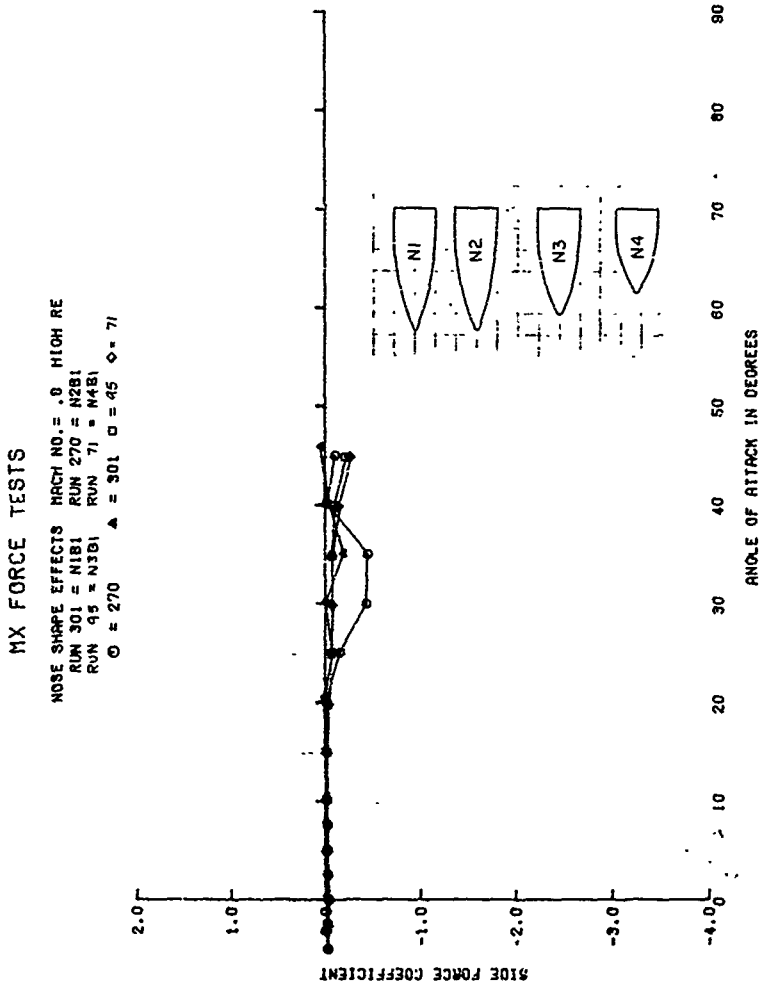

c. M = 0.8

Figure 30 (Concluded)

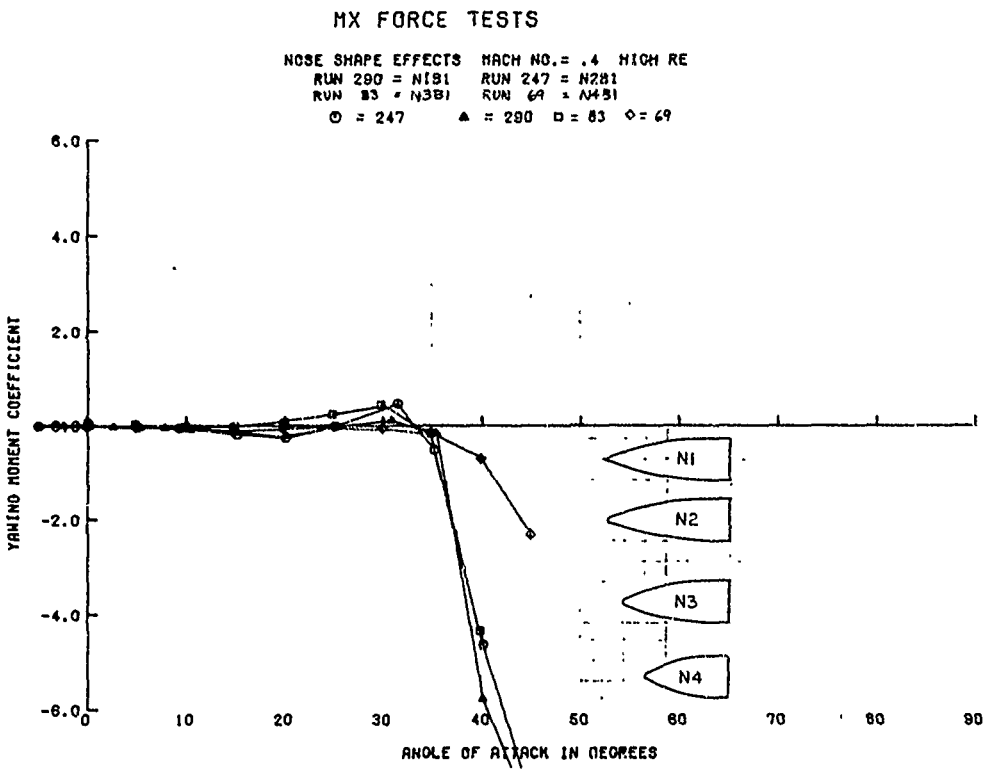

a. M = 0.4

Figure 31. Effect of Nose Shape on Yawing Moment Coefficient, B1 Body

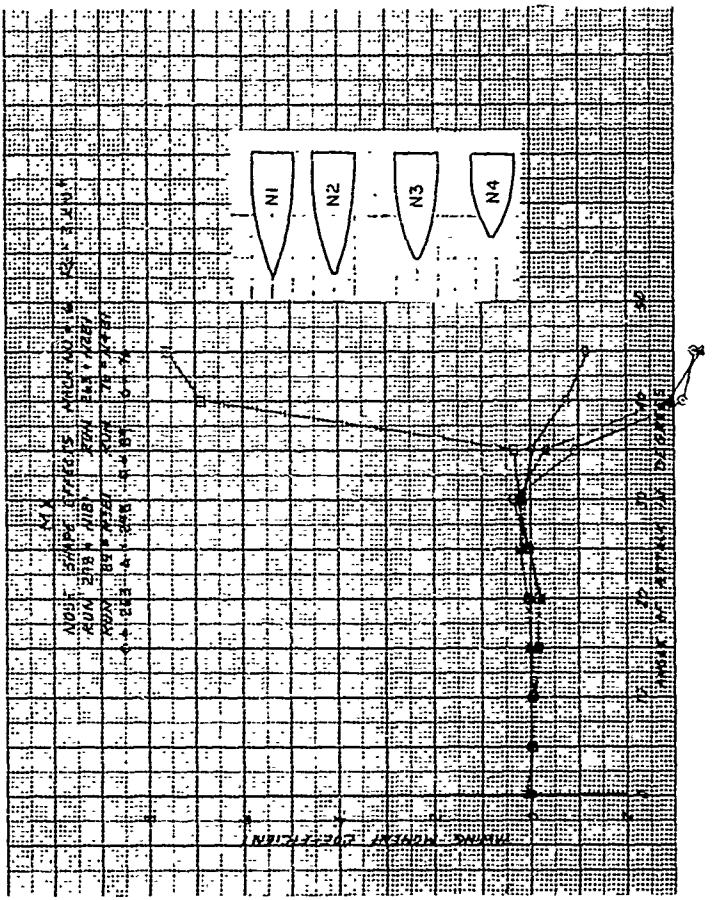

b. M = 0.6

Figure 31 (Continued)

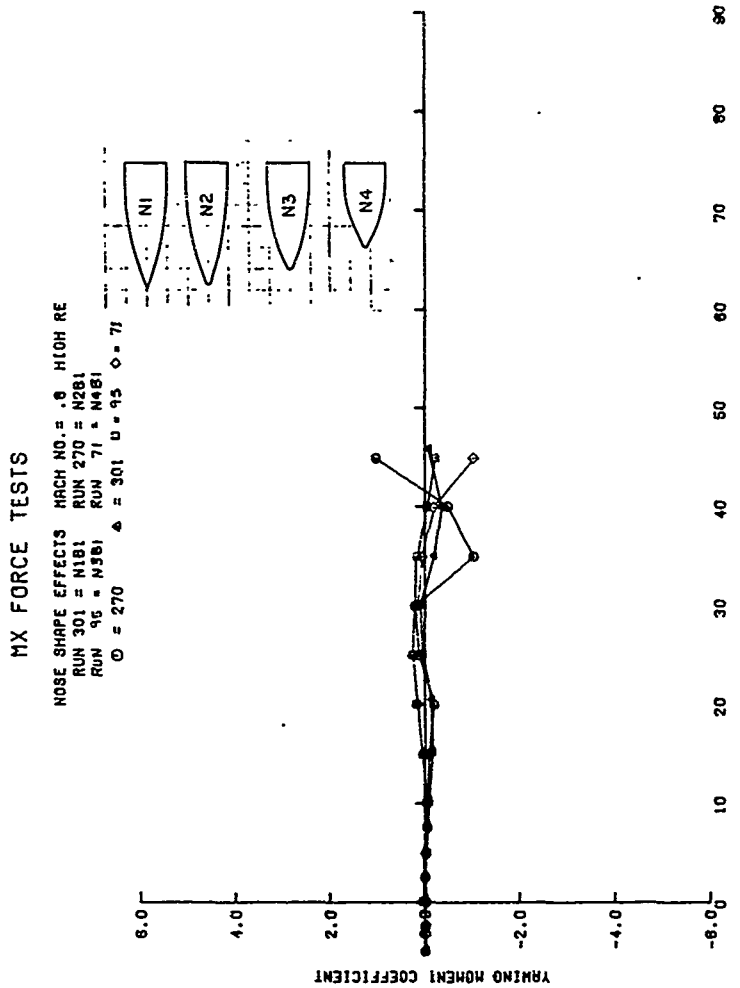

c. M = 0.8

Figure 31 (Concluded)

Figures 32 to 34 show similar results for the N2B2, N3B2, N4B2 and N14B2 configurations at Mach numbers of 0.4, 0.6 and 0.8. The N2B2 configuration shows much larger asymmetric forces and moments than the lower fineness ratio nose configurations. The increased tip bluntness on N14 compared to N4 showed a reduction in normal force coefficient but with no additional reduction in the asymmetric forces and moments.

Figures 35 through 37 compare the two 5-caliber triconic noses N5 and N6. The nose tip bluntness on N6 is twice that of N5. Both noses are seen to have large side force and yawing moment coefficients at the lower Mach numbers and that no advantage was gained from the increased bluntness.

The effect of nose tip bluntness on the aerodynamic coefficients of the 4-caliber triconic noses for Mach numbers 0.4, 0.6 and 0.8 is shown in Figures 38 through 40. N77 is the N7 nose removed from the cylindrical body, rotated 180 degrees, and re-attached. At the lower Mach numbers the sharpest nose has the larger normal force and side force coefficients at the higher angles-of-attack but the N9 nose configuration with its increased bluntness shows no additional reduction over the N8 nose configuration.

Similar data are shown in Figures 41 through 43 for the 3-caliber triconic nose configurations N10, N11 and N13. The N12 configuration nose button was built but never tested. For this fineness ratio (3) basic nose shape, increasing the bluntness reduced the asymmetric forces and moments only at Mach 0.4.

The effect of fineness ratio on the triconic-type noses is shown in Figures 44 to 46 comparing N5B2, N77B2 and N10B2 configurations. These are the smallest nose tip bluntness (.04 D) noses for fineness ratio 5.0, 4.0 and 3.0 triconic configurations. At Mach 0.4 all three noses exhibit large side force and yawing moment coefficients at the high angles-of-attack with corresponding fluctuations in normal force coefficients. At Mach 0.6 the two slender nose configurations exhibit large asymmetric forces and moments. At Mach 0.8 the largest fineness ratio (5.0) configuration still shows a relatively large side force

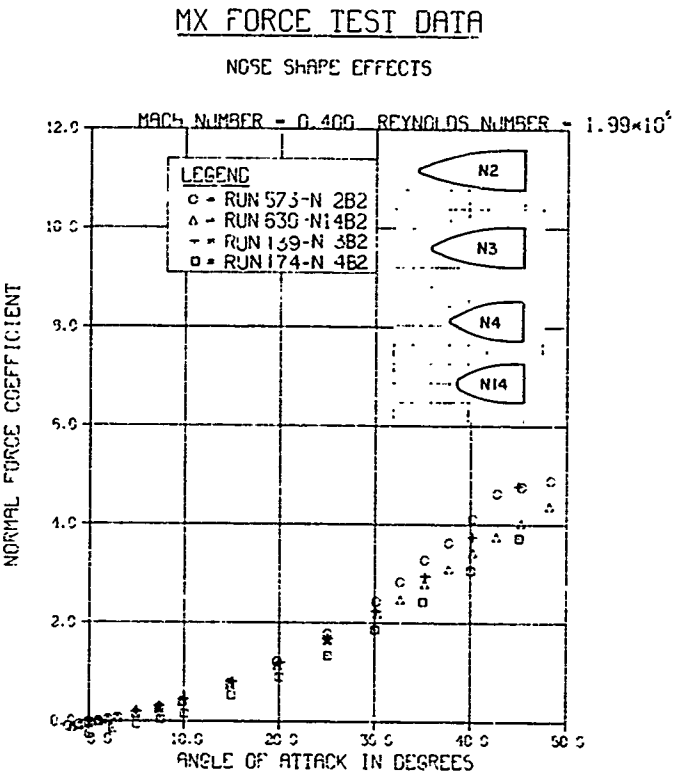

a. M = 0.4

Figure 32. Effect of Nose Shape on Normal Force Coefficient, B2 Body

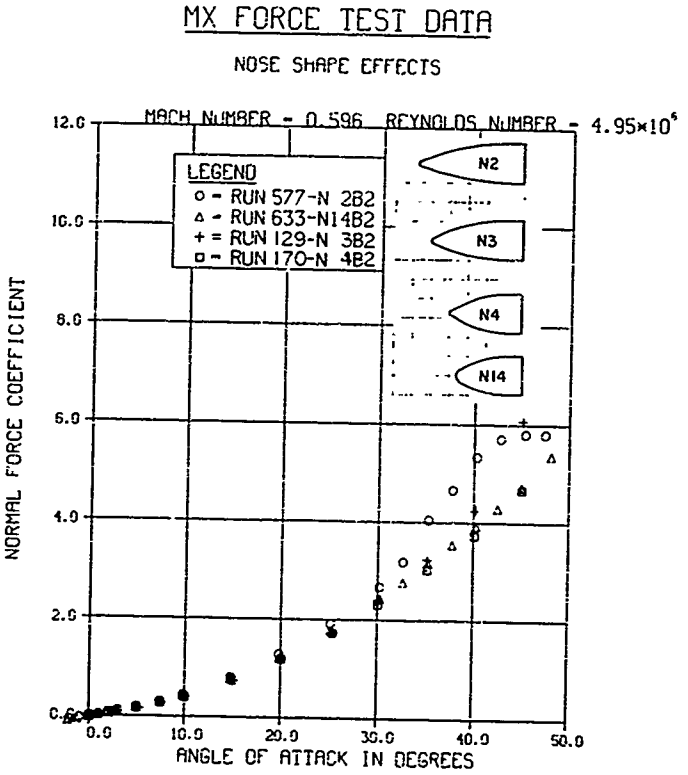

b. M = 0.6

Figure 32 (Concluded)

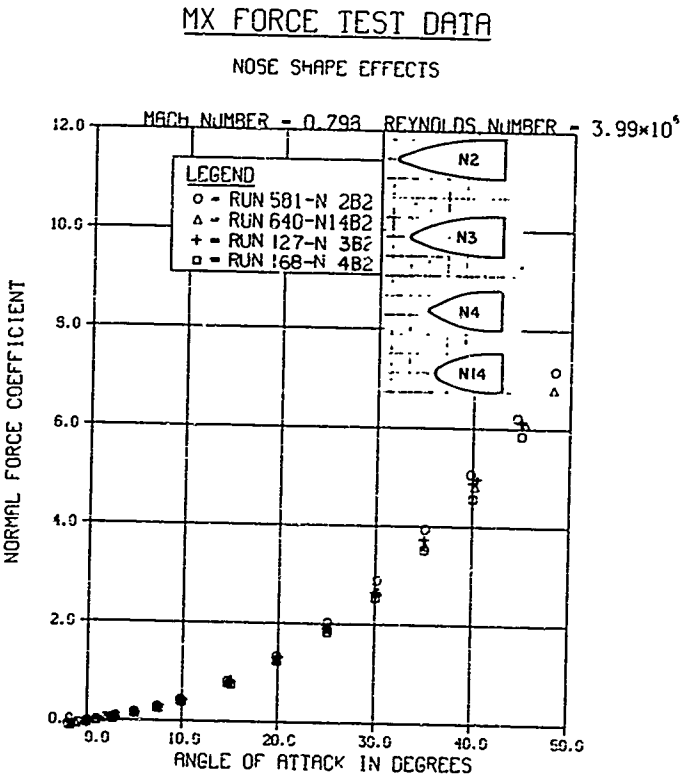

c. M = 0.8

Figure 32 (Continued)

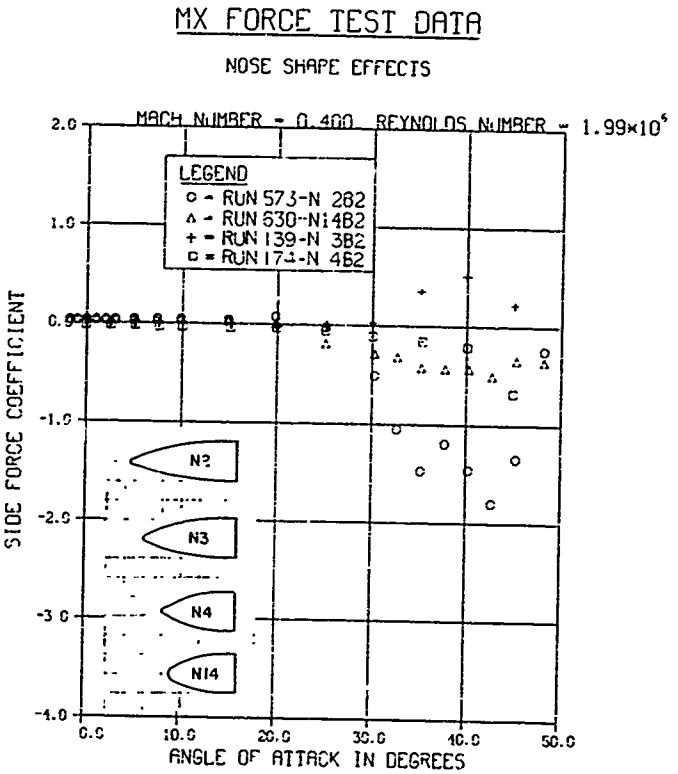

a. M = 0.4

Figure 33. Effect of Nose Shape on Side Force Coefficient, B2 Body

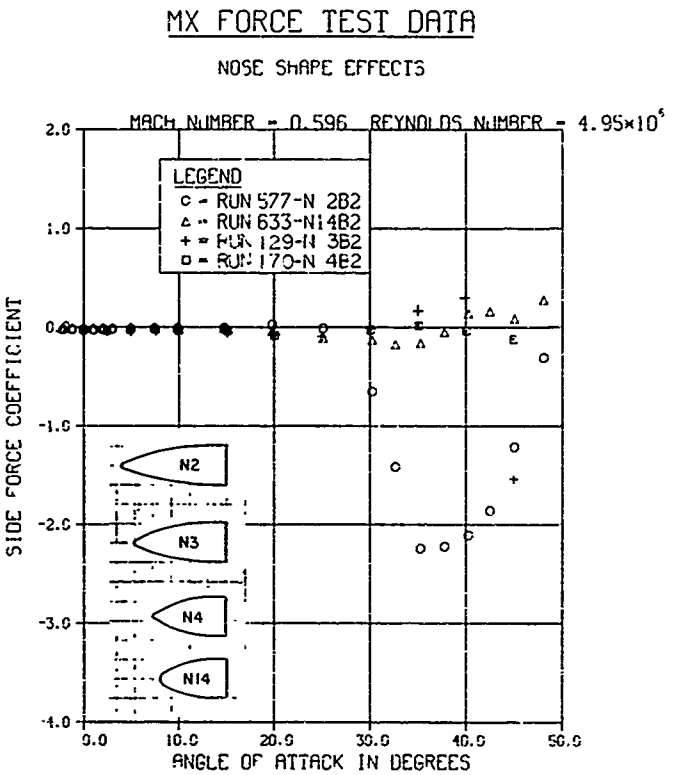

b. M = 0.6

Figure 33 (Continued)

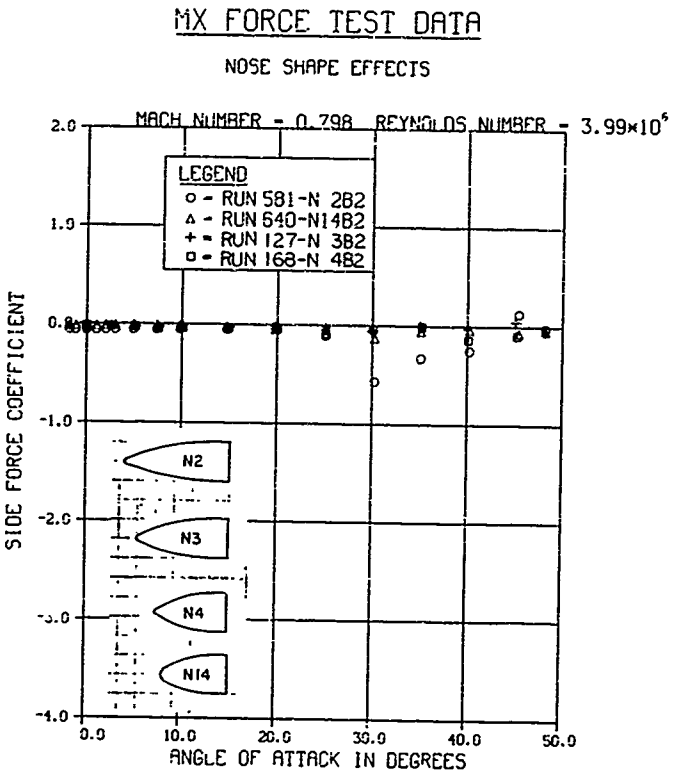

c. M = 0.8

Figure 33 (Concluded)

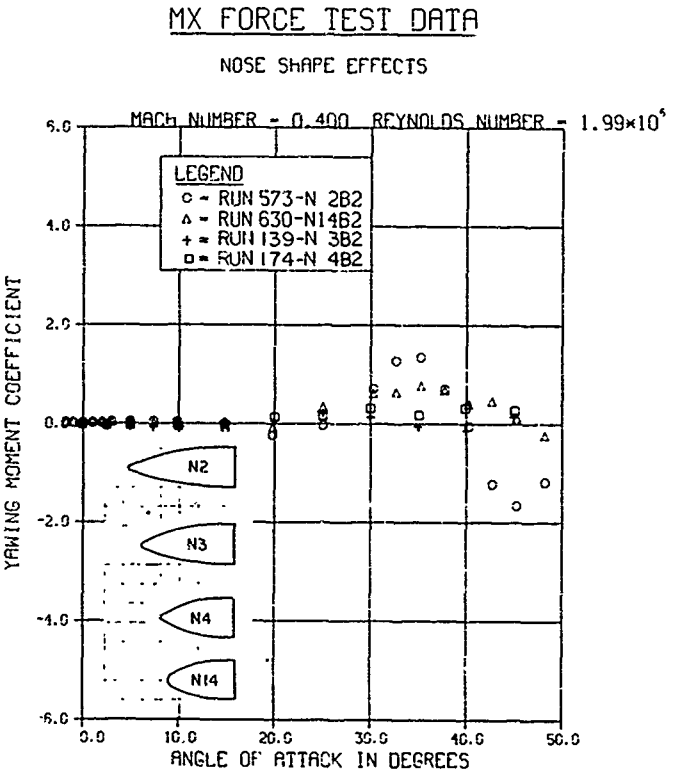

a: M = 0.4

Figure 34. Effect of Nose Shape on Yawing Moment Coefficient, B2 Body

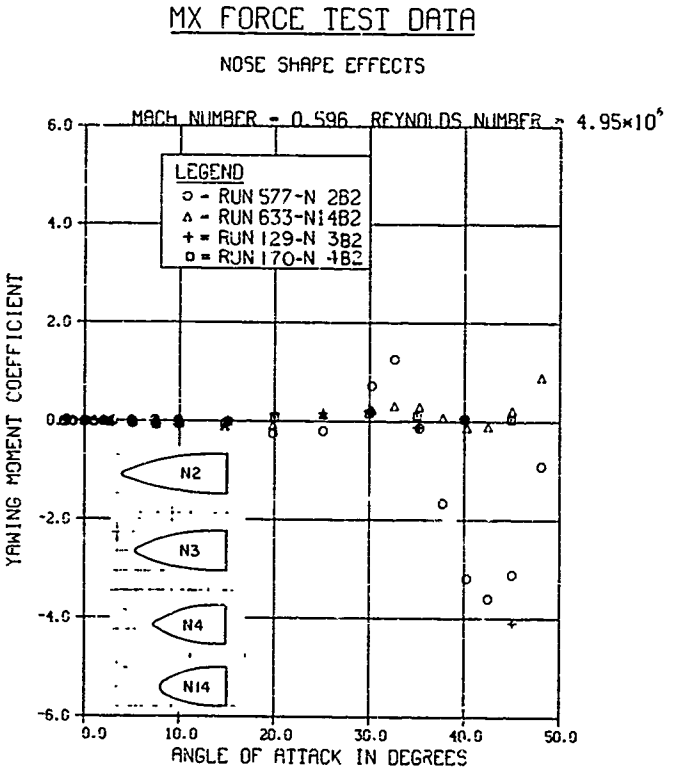

b. M = 0.6

Figure 34 (Continued)

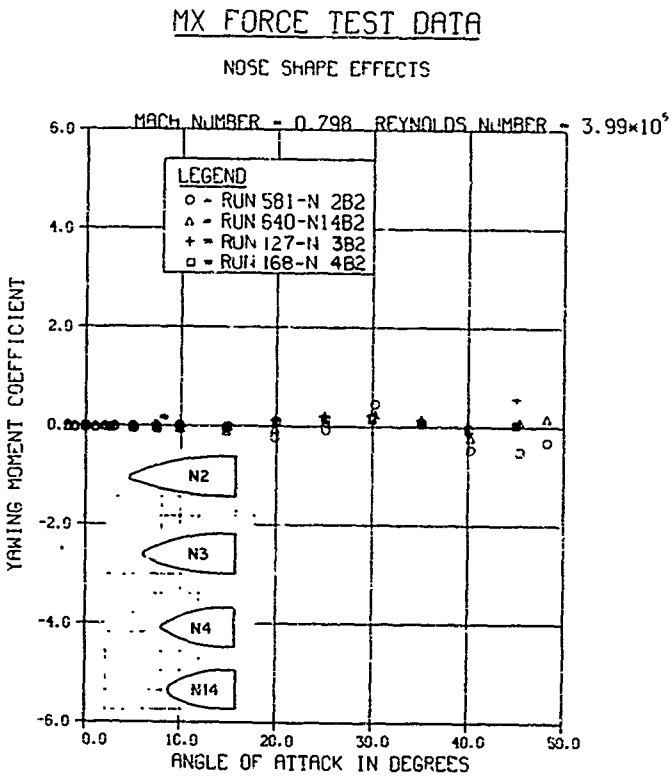

c. M = 0.8

Figure 34 (Concluded)

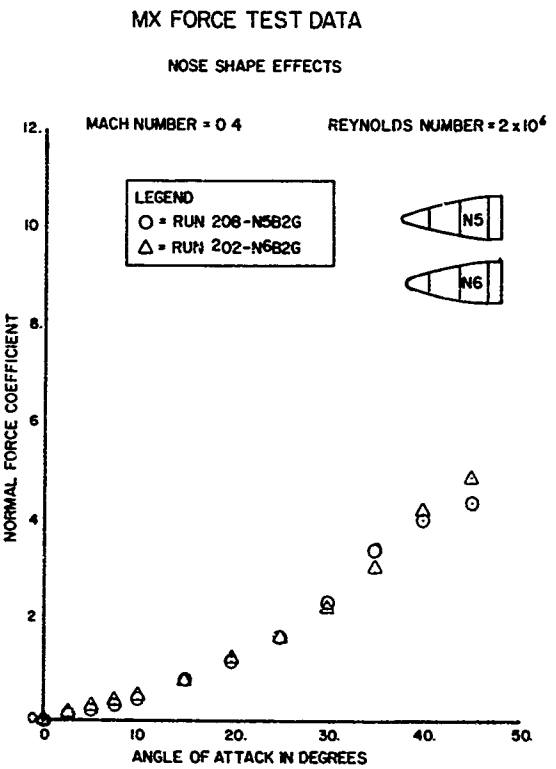

a. M = 0.4

Figure 35. Comparisons of the 5-Caliber Triconic Nose Shapes - Normal Force Coefficient

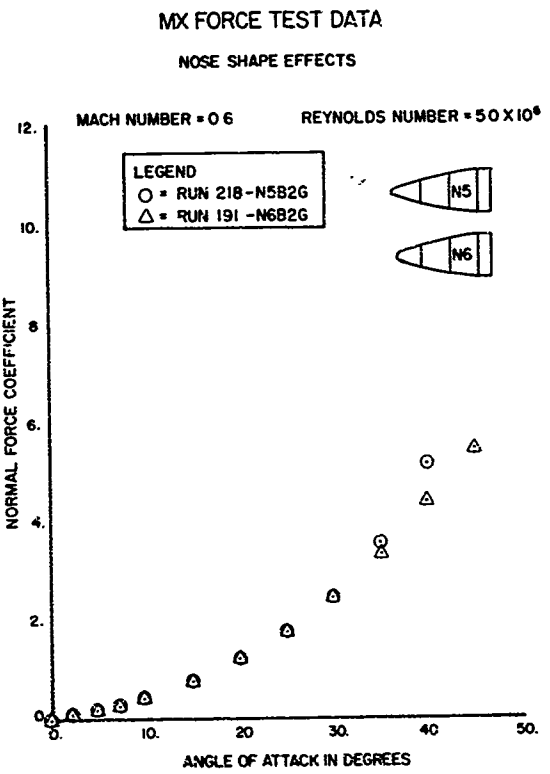

b. M = 0.6

Figure 35 (Continued)

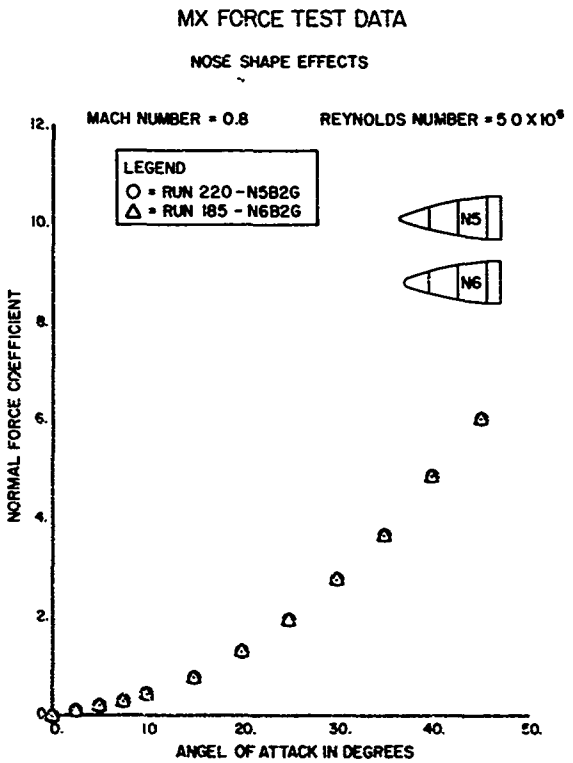

c. M = 0.8

Figure 35 (Concluded)

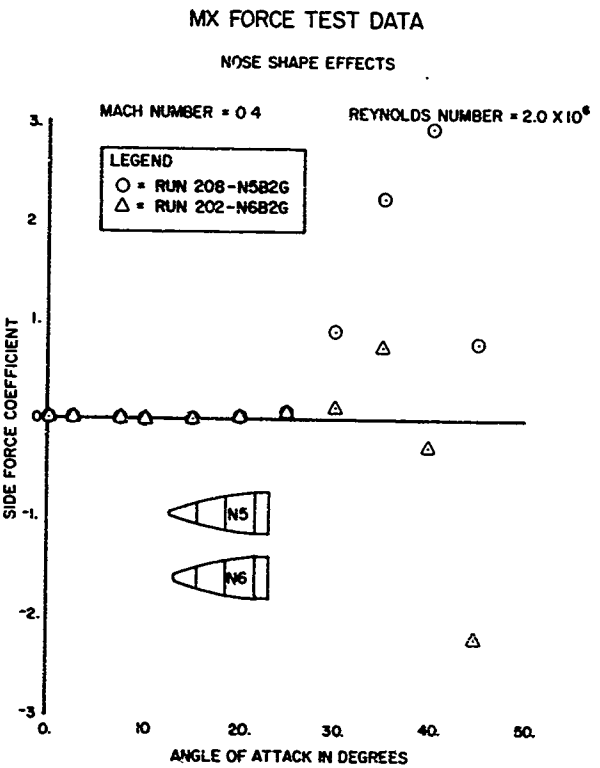

a. M = 0.4

Figure 36. Comparisons of the 5-Caliber Triconic Nose Shapes - Side Force Coefficient

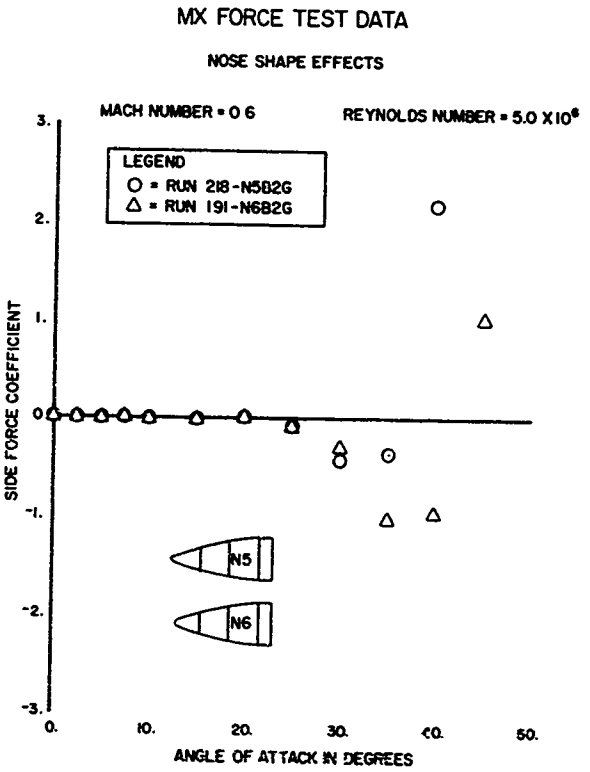

b. M = 0.6

Figure 36 (Continued)

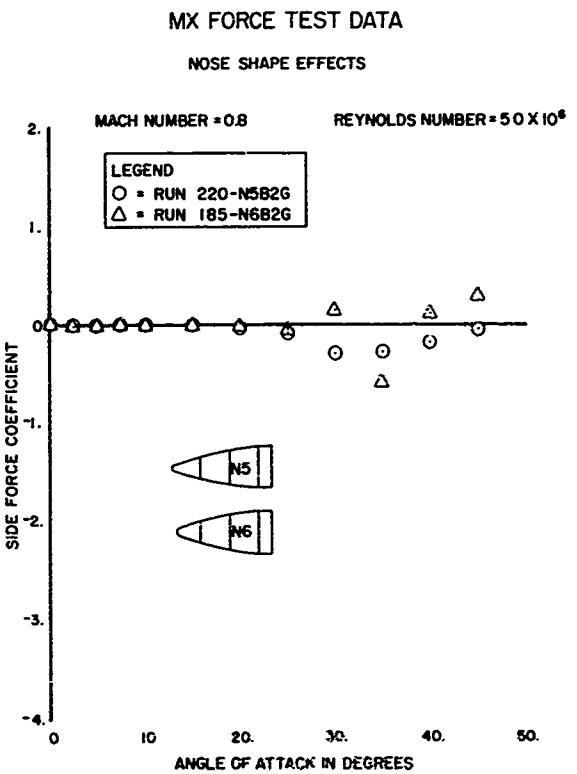

c. M = 0.8

Figure 36 (Concluded)

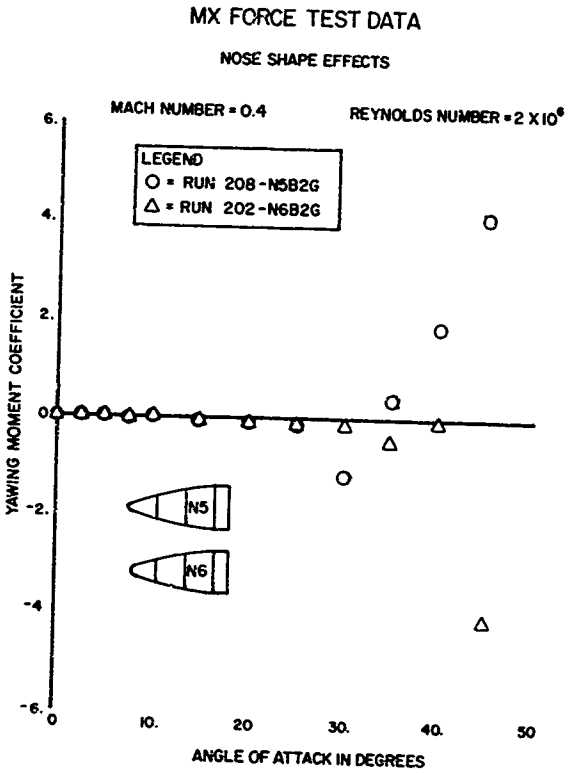

a. M = 0.4

Figure 37. Comparisons of the 5-Caliber Triconic Nose Shapes - Yawing Moment Coefficient

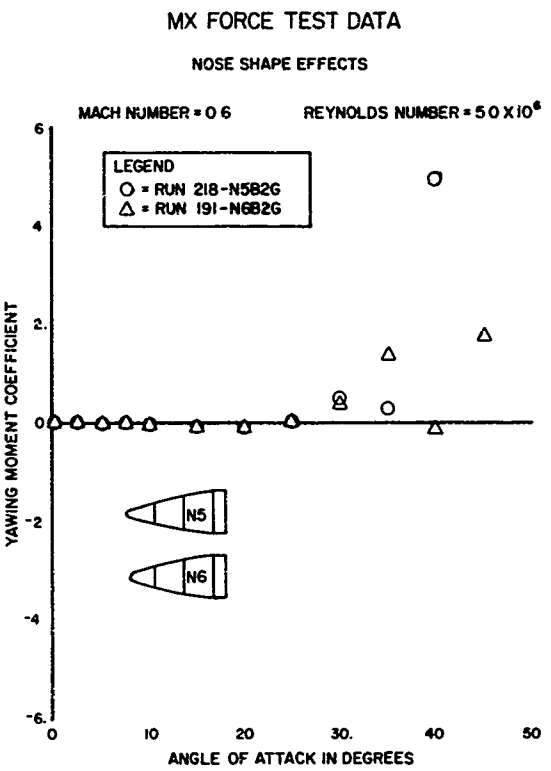

b. M = 0.6

Figure 37 (Continued)

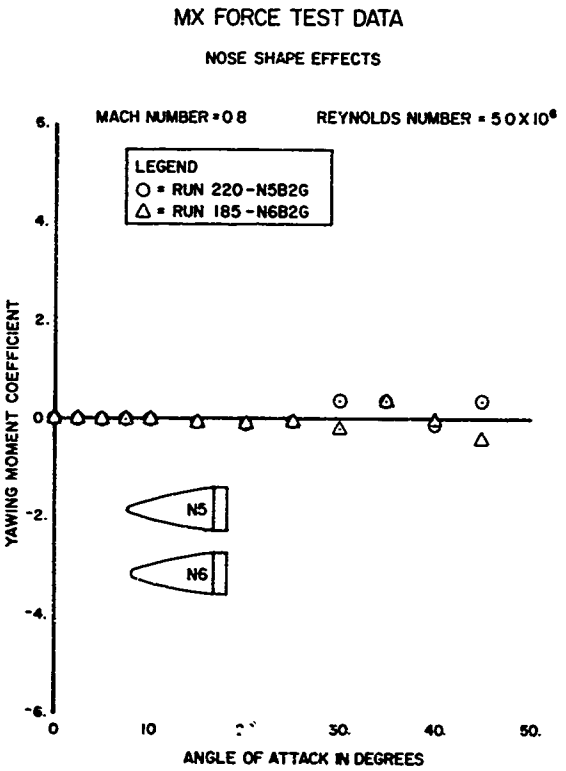

c. M = 0.8

Figure 37 (Concluded)

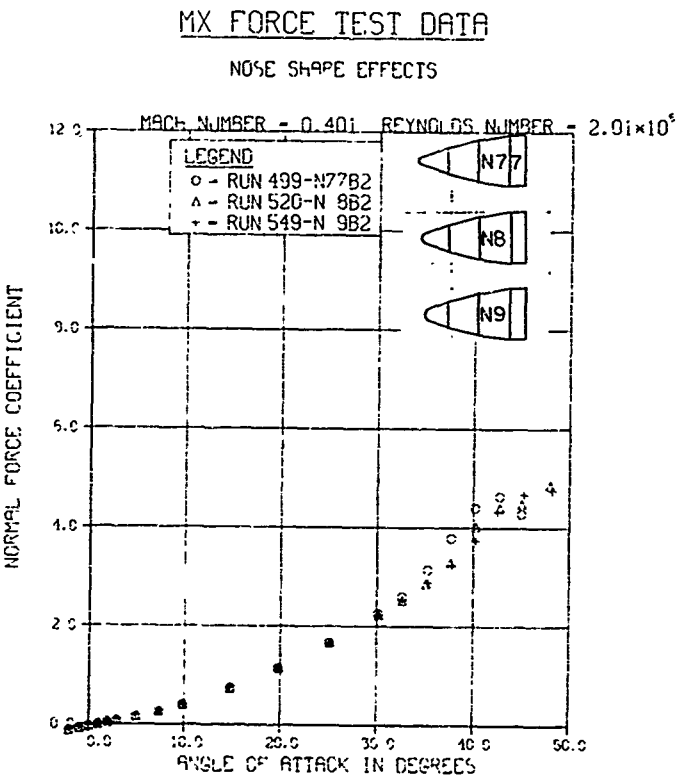

a. $M_\infty = 0.4$

Figure 38. Comparisons of the 4-Caliber Triconic Nose Shape - Normal Force Coefficient

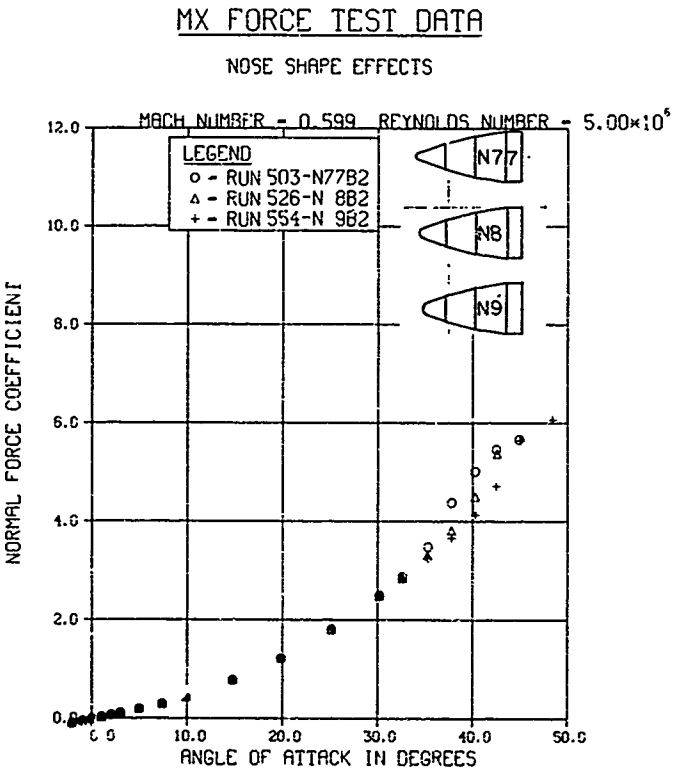

b. $M_\infty = 0.6$

Figure 38 (Continued)

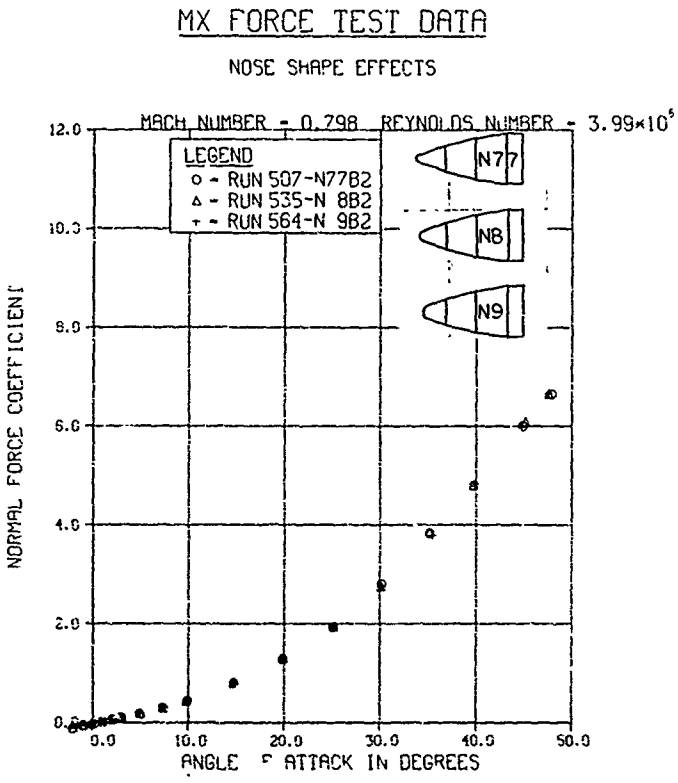

c. $M_\infty = 0.8$

Figure 38 (Concluded)

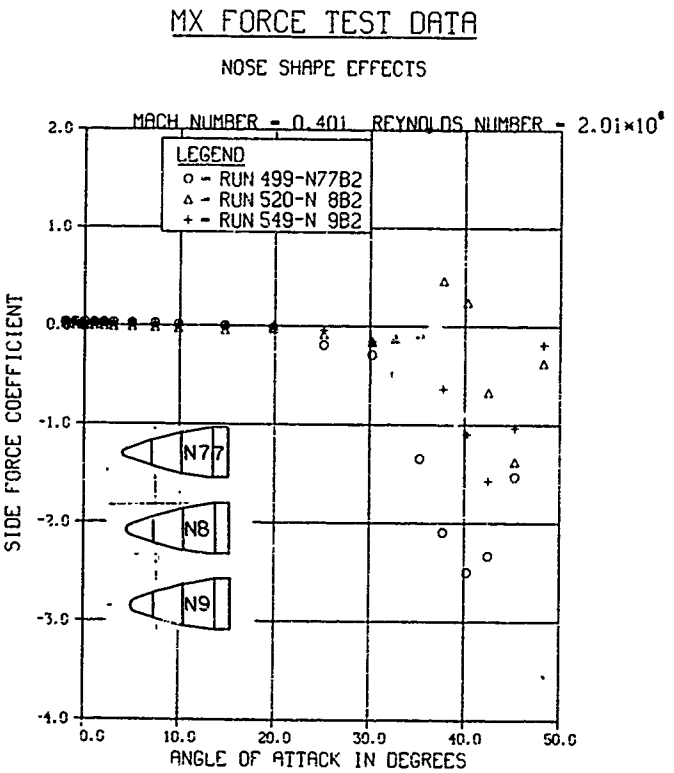

a. $M_\infty = 0.4$

Figure 39. Comparisons of the 4-Caliber Triconic Nose Shapes - Side Force Coefficient

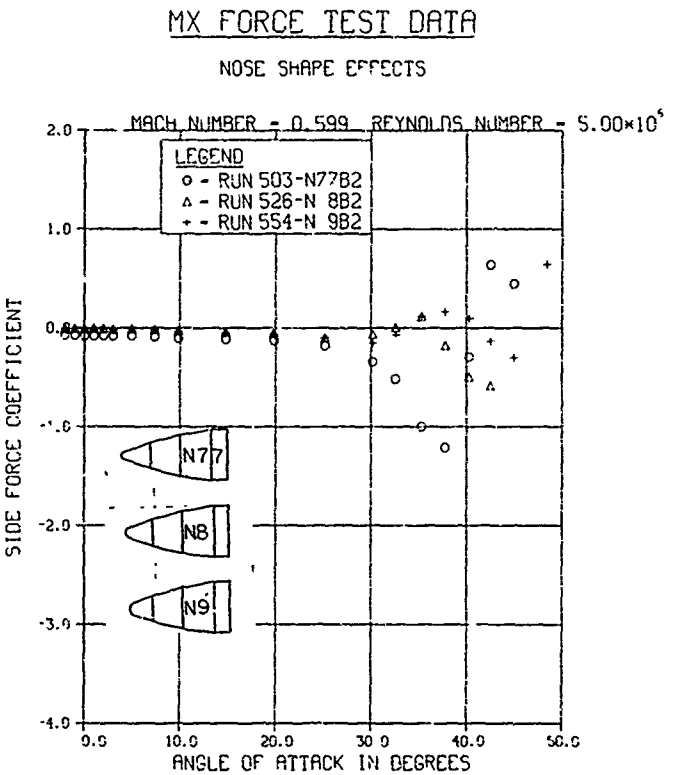

b. $M_\infty = 0.6$

Figure 39 (Continued)

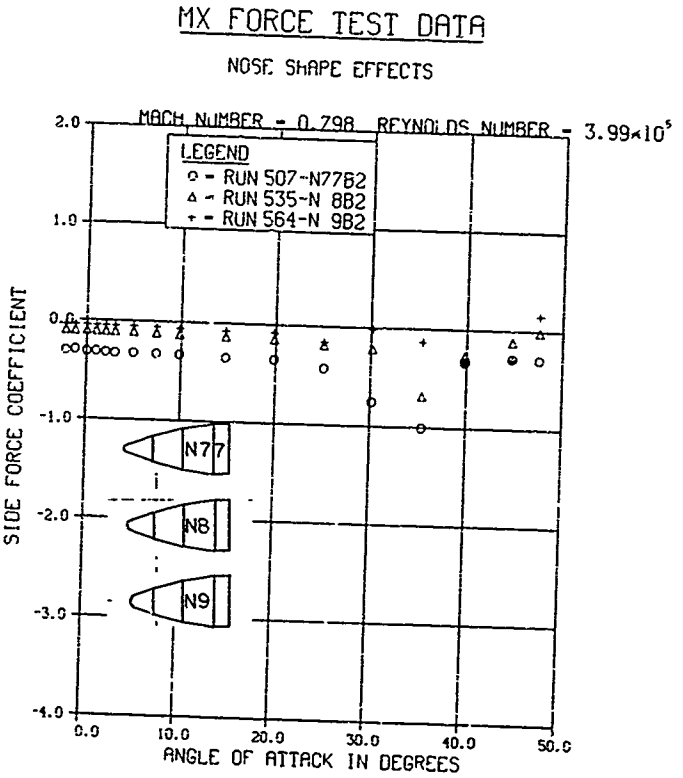

c. $M_\infty = 0.8$

Figure 39 (Concluded)

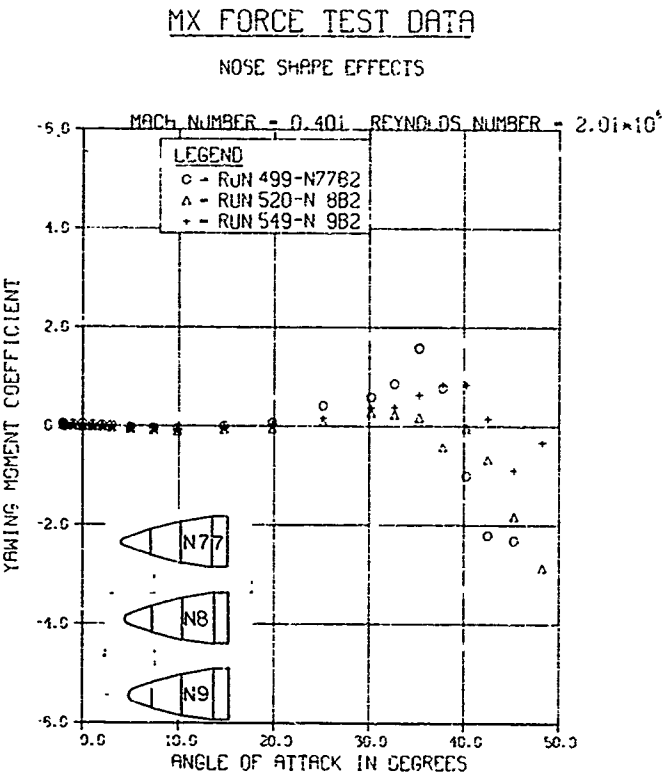

a. $M_\infty = 0.4$

Figure 40. Comparisons of the 4-Caliber Triconic Nose Shapes - Yawing Moment Coefficient

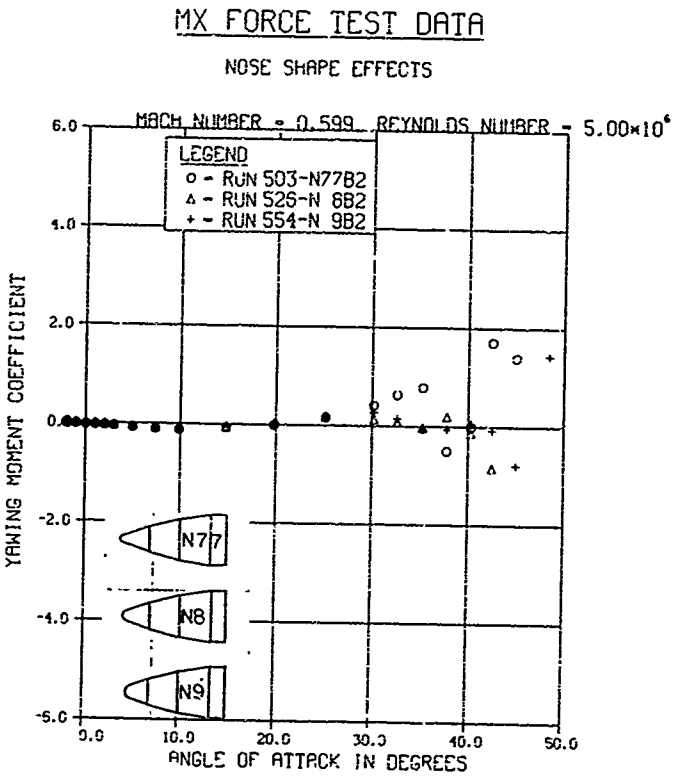

b. $M_\infty = 0.6$

Figure 40 (Continued)

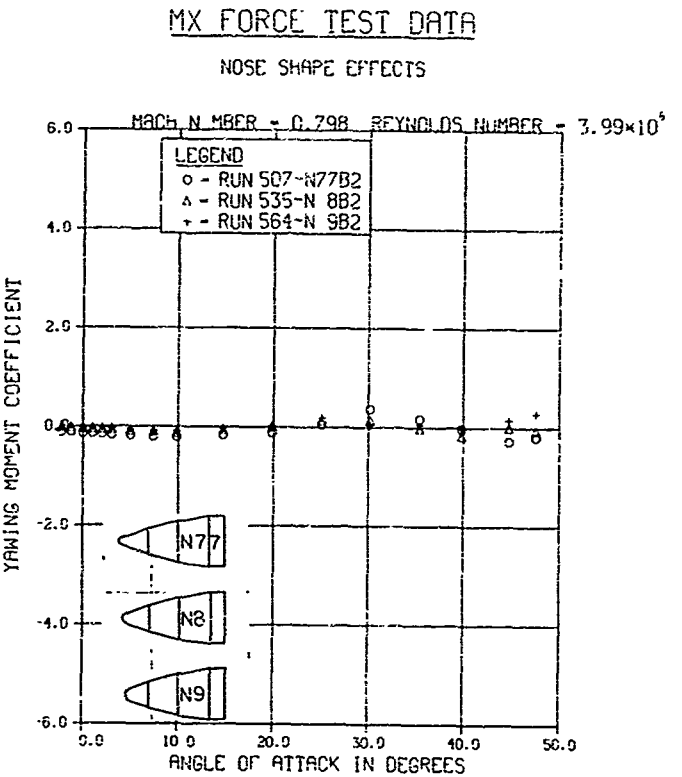

c. $M_\infty = 0.8$

Figure 40 (Concluded)

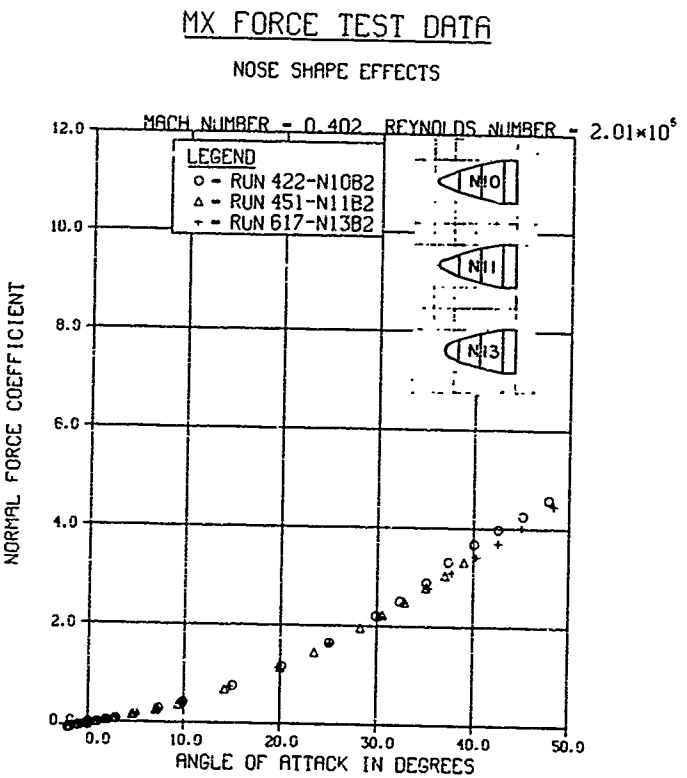

a. M = 0.4

Figure 41. Comparisons of the Normal Force Coefficient for 3-Caliber Nose Shapes

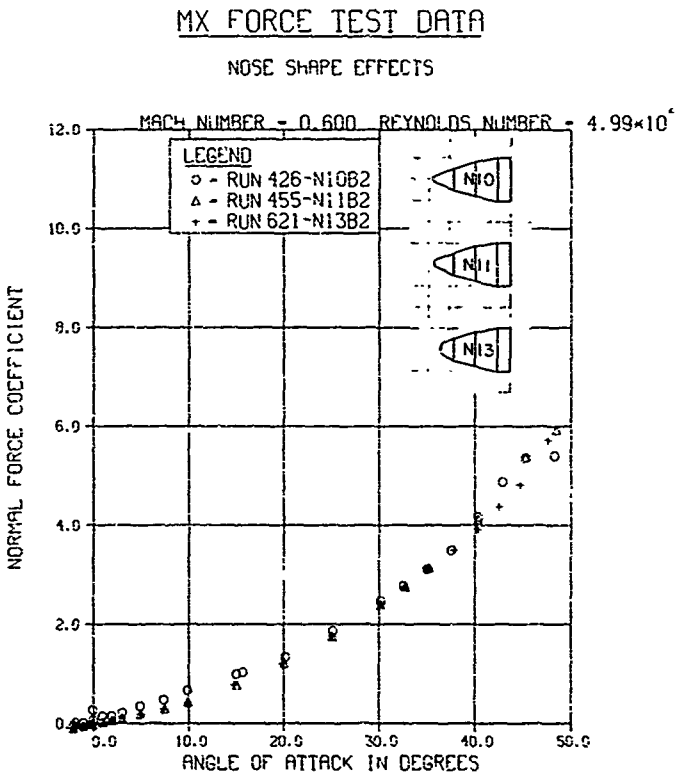

b. M = 0.6

Figure 41 (Continued)

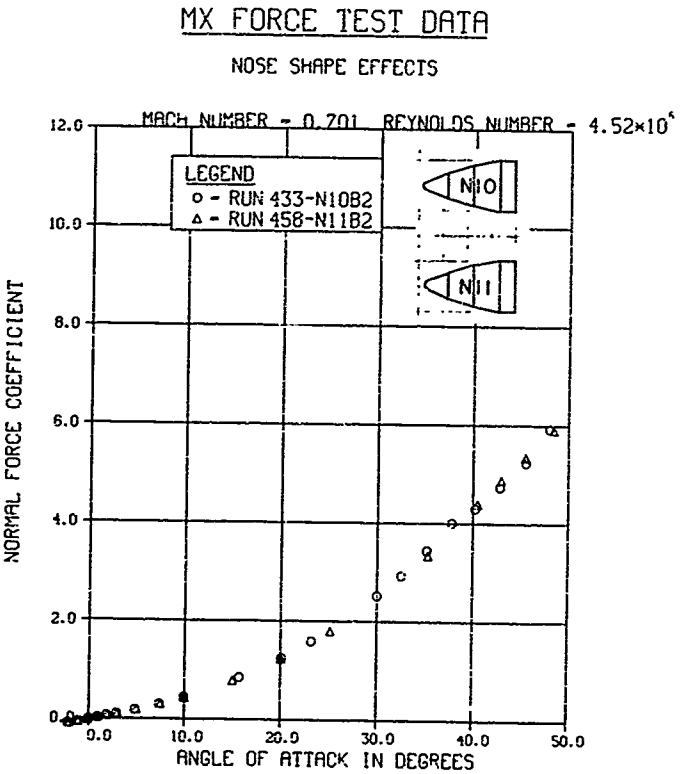

c. M = 0.7

Figure 41 (Concluded)

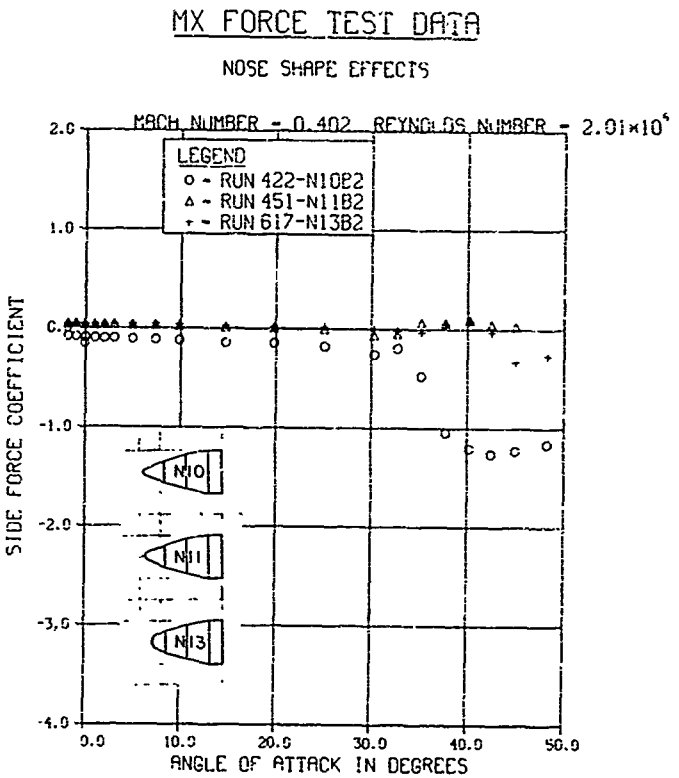

a. M = 0.4

Figure 42. Comparisons of the Side Force Coefficient for 3-Caliber Nose Shapes

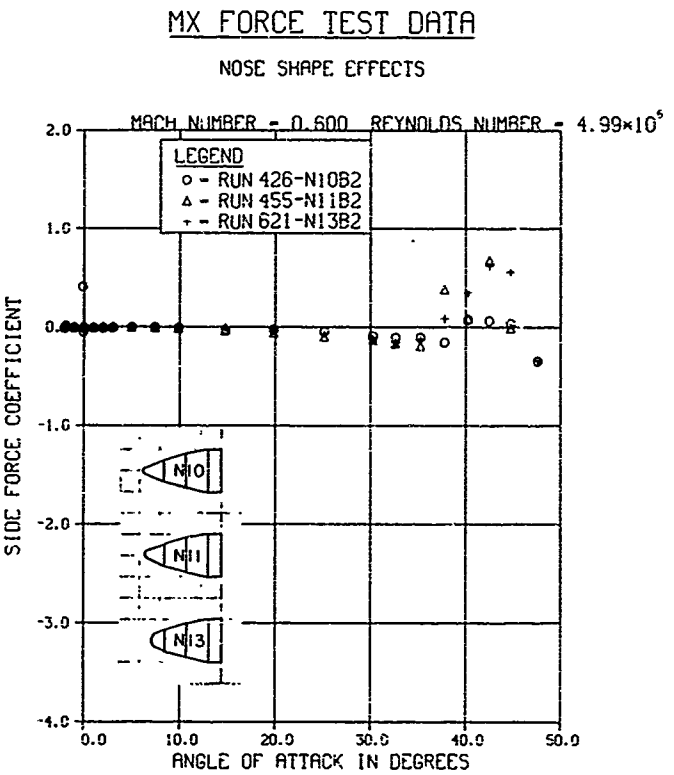

b. M = 0.6

Figure 42 (Continued)

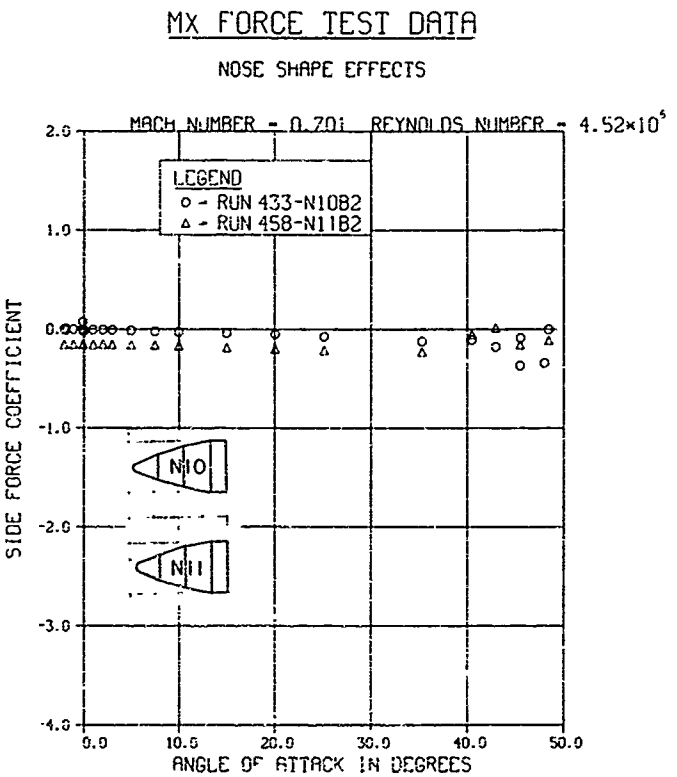

c. M = 0.7

Figure 42 (Concluded)

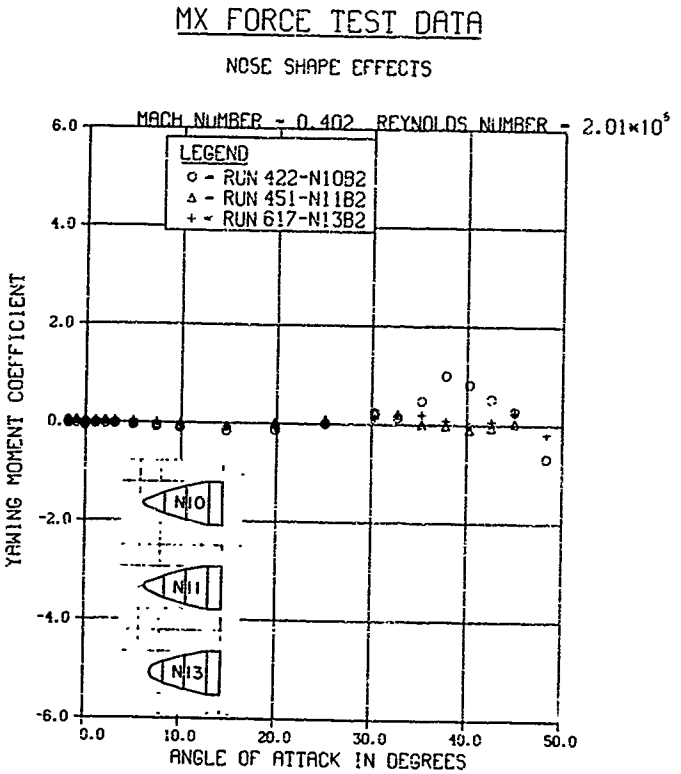

a. $M_\infty = 0.4$

Figure 43. Comparisons of the Yawing Moment Coefficient for 3-Caliber Nose Shapes

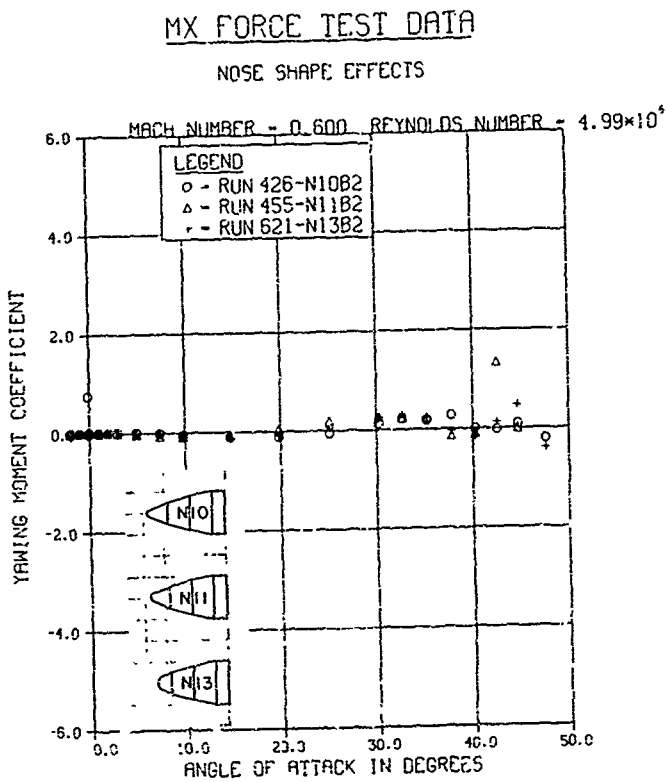

b. $M_\infty = 0.6$

Figure 43 (Continued)

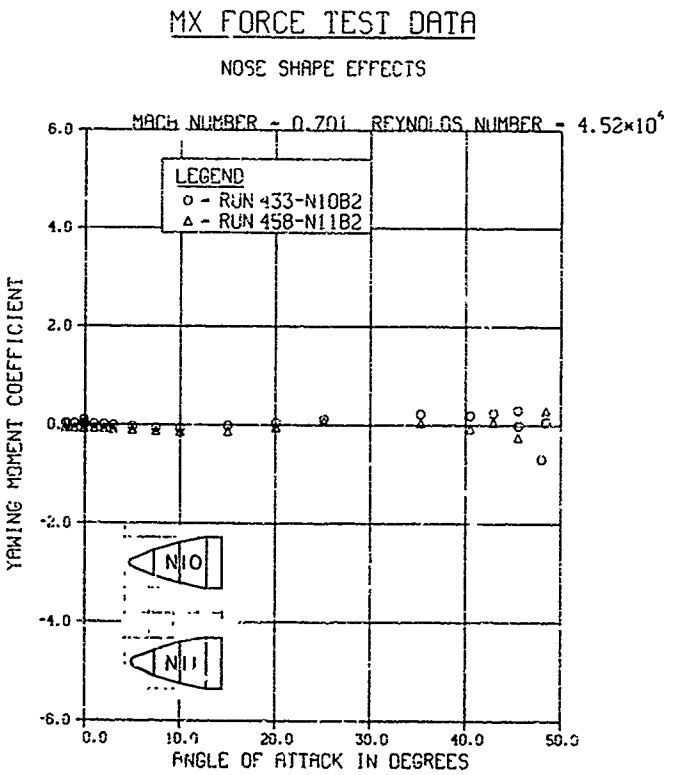

c. $M_\infty = 0.7$

Figure 43 (Concluded

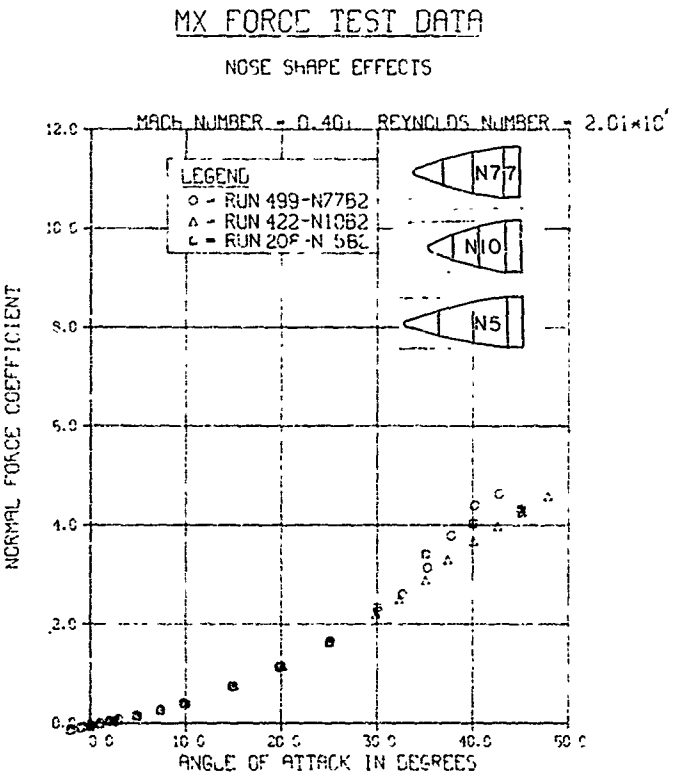

a. $M_\infty = 0.4$

Figure 44. Effect of Fineness Ratio of the Tricnic Nose Shapes on Normal Force Coefficient, Bluntness Ratio = 0.040

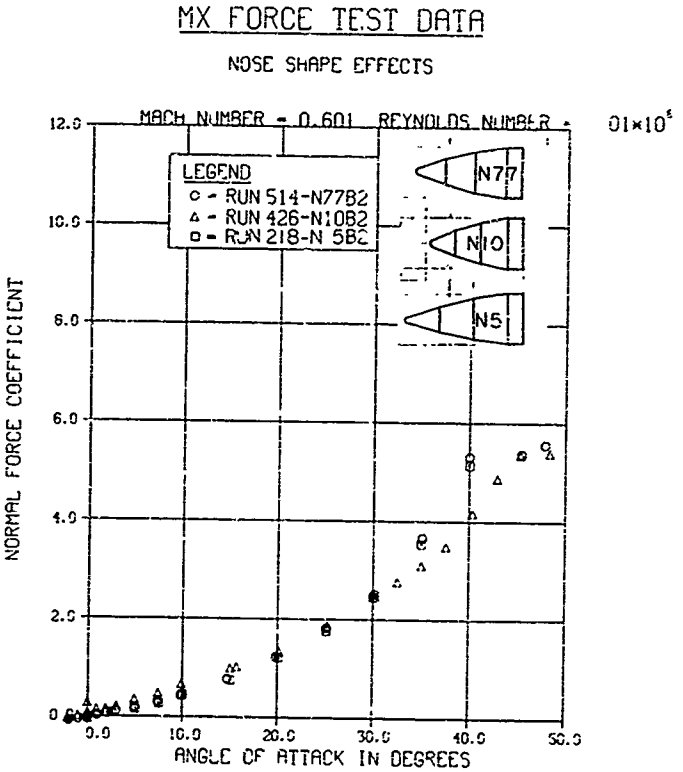

b. $M_\infty = 0.6$

Figure 44 (Continued)

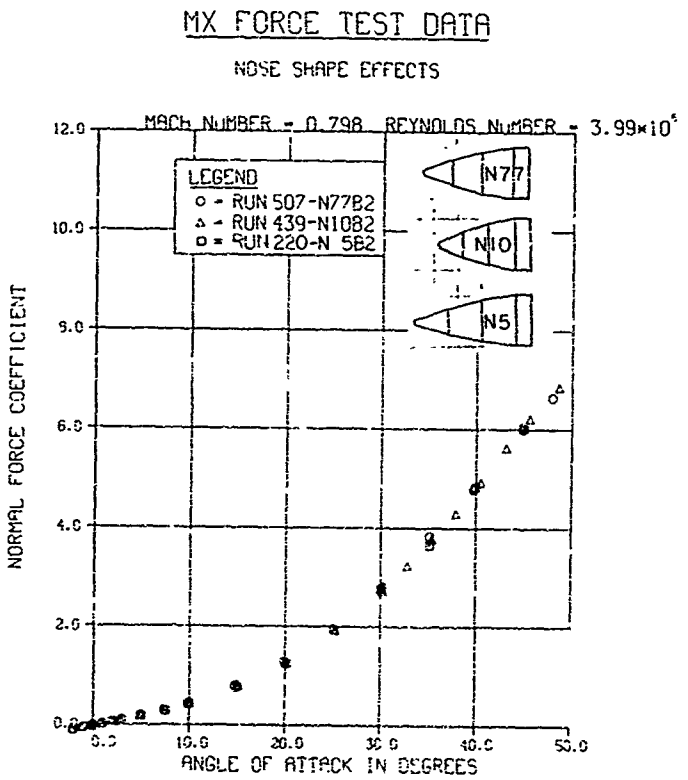

c. $M_\infty = 0.8$

Figure 44 (Concluded)

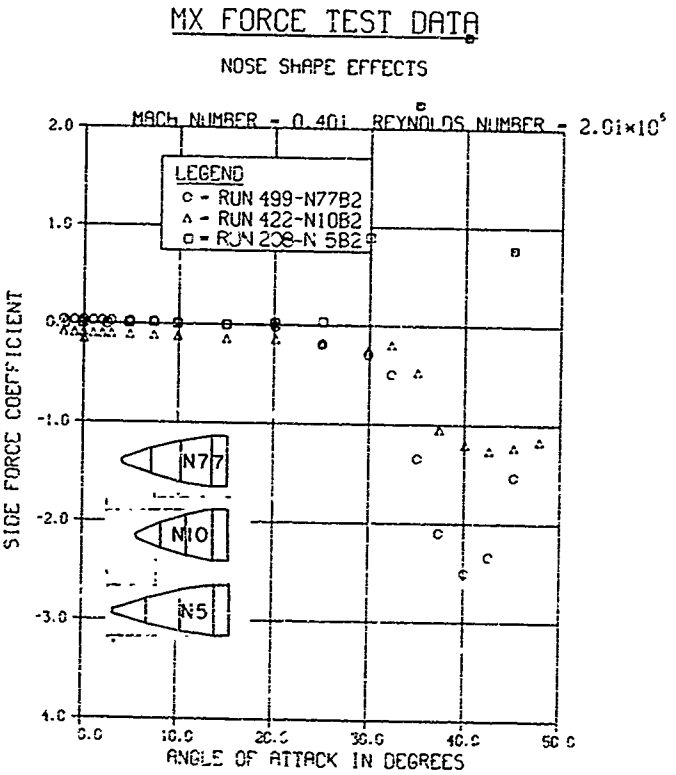

a. $M_\infty = 0.4$

Figure 45. Effect of Fineness Ratio of the Triconic Nose Shapes on Side Force Coefficient, Bluntness Ratio = 0.040

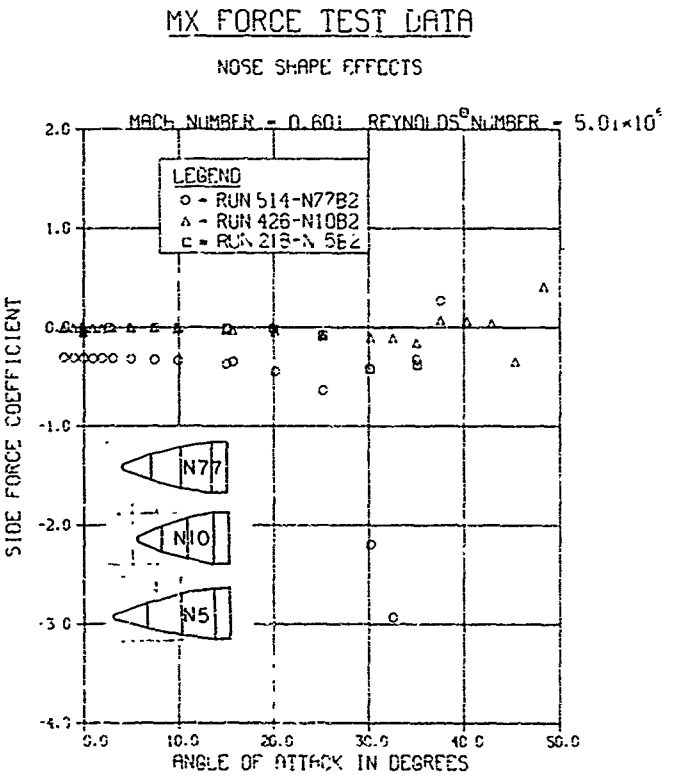

b. $M_\infty = 0.6$

Figure 45 (Continued)

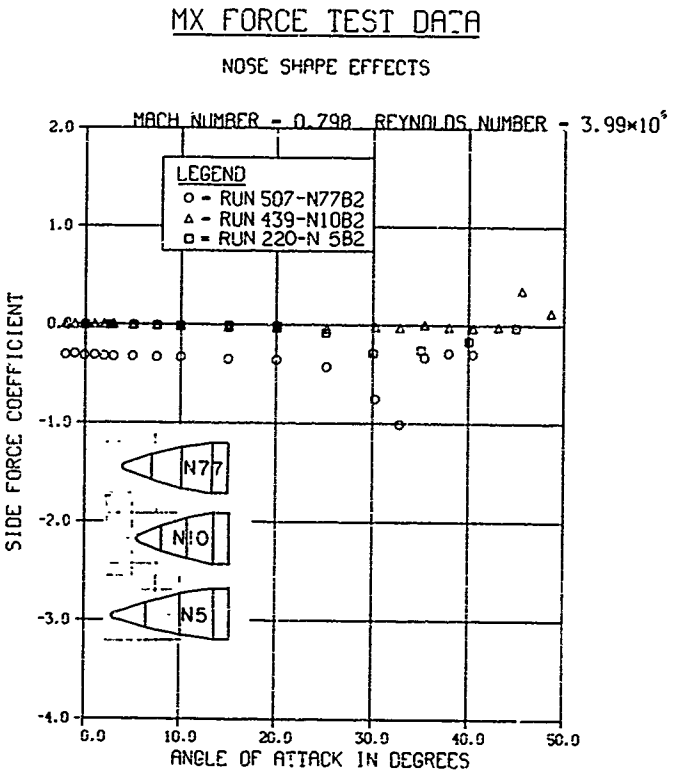

c. $M_\infty = 0.8$

Figure 45 (Concluded)

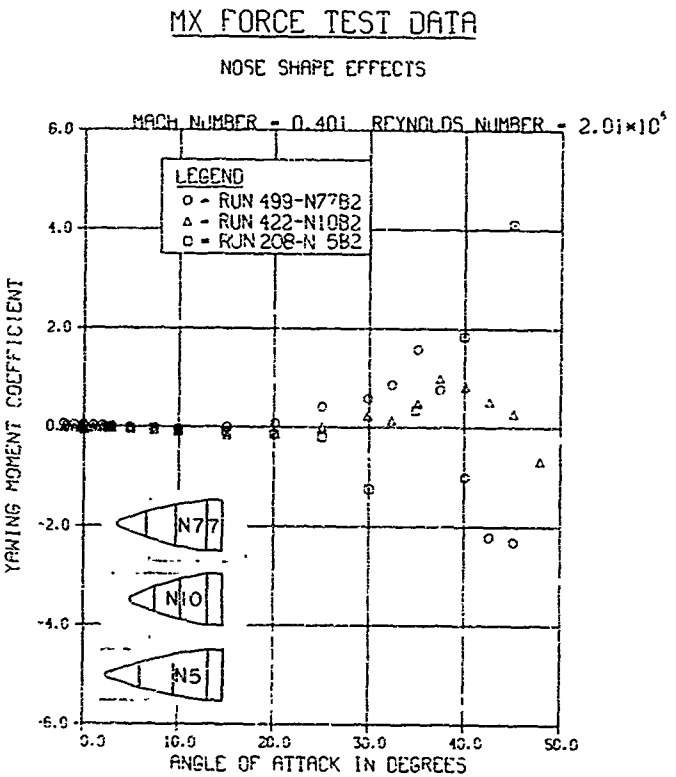

a. $M_\infty = 0.4$

Figure 46. Effect of Fineness Ratio of the Triconic Nose Shapes on Yawing Moment Coefficient, Bluntness = 0.040

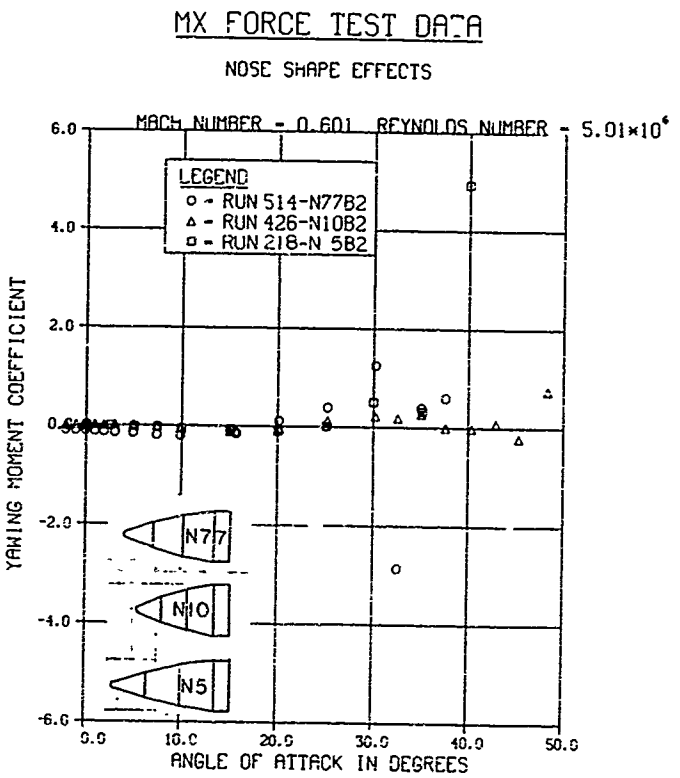

b. $M_\infty = 0.6$

Figure 46 (Continued)

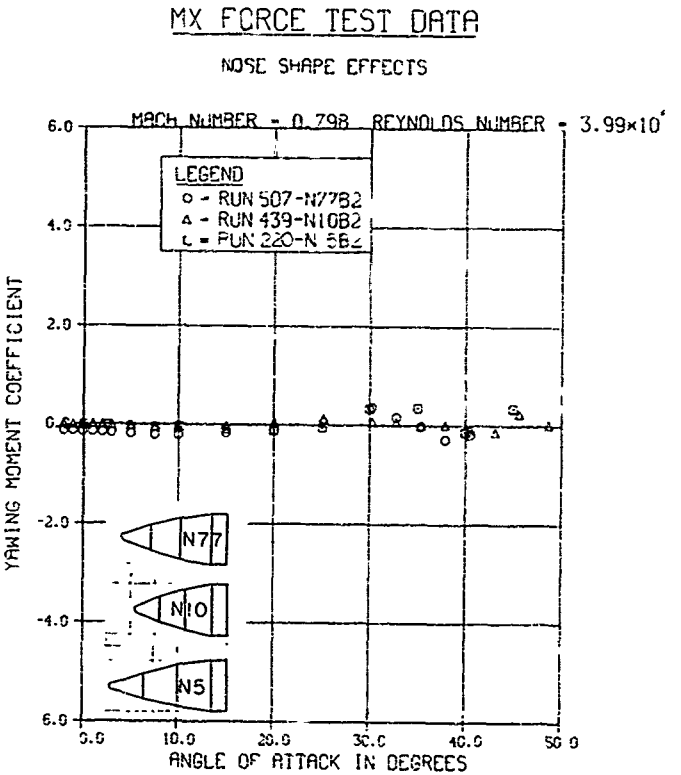

c. $M_\infty = 0.8$

Figure 46 (Concluded)

coefficient at angles-of-attack above 30 degrees even though there appears to be a shift in the data.

Several of the previous figures show offsets in the side force coefficient curves, with fairly large values at low angles of attack and no sideslip angle. No explanation is readily available as to the reason for this. Since the offset was not constant with Mach number and no corresponding yawing moment coefficient was shown, the shift in side force coefficient is apparently not real and should be disregarded.

Figures 47 through 49 compare the largest tip bluntness triconic nose configurations for effects of fineness ratio at Mach numbers 0.4, 0.6 and 0.7. These plots indicate that with reduced fineness ratios less than 4.0 calibers the asymmetric forces and moments are greatly reduced. The 5.0 and 4.0 caliber fineness ratio nose configurations both exhibit large side force and yawing moment coefficients of about the same magnitude.

The final plots on nose shape effects compare the ogive nose (N3) and triconic nose (N5) configurations of comparable fineness ratio at Mach numbers 0.4, 0.6 and 0.8 (Figures 50 through 52). The ogive nose configuration has smaller asymmetric forces and moments than the triconic nose configuration particularly at Mach number 0.4.

The data show that the smallest length to diameter nose (N4, l/d = 1.6333) had much lower asymmetric forces and moments than any of the other nose shapes. As the l/d of the ogive shape nose was decreased, there was generally a decrease in the asymmetric forces and moments. The triconic nose configurations generally had, as large or larger asymmetric side forces and yawing moment coefficients as the ogive nose configuration of the same length-to-diameter ratio.

6. BODY LENGTH EFFECTS

The N2 nose configuration was the only one that was force tested with and without the 9.8333-inch-long body insert in the 0 to 45 degrees angle-of-attack region. Plots of the aerodynamic coefficients comparing the N2B1 and N2B2 configurations at Mach numbers 0.4, 0.6 and 0.8 are shown in Figure 53. The figures show the expected resulting effects of increased planform area. Base Area of 45.36 in.^{2} was kept constant.

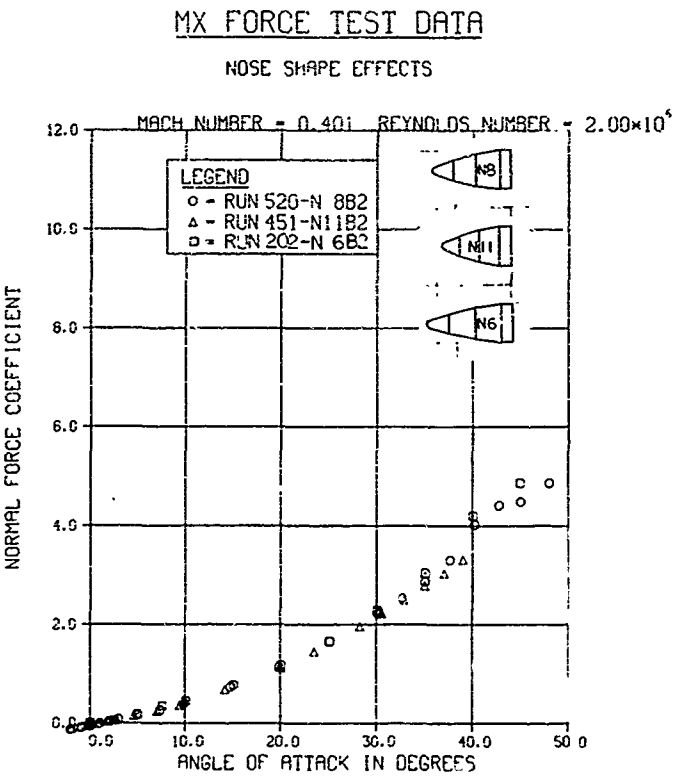

a. $M_\infty = 0.4$

Figure 47. Effect of Fineness Ratio of the Triconic Nose Shapes on Normal Force Coefficient, Bluntness Ratio = 0.080

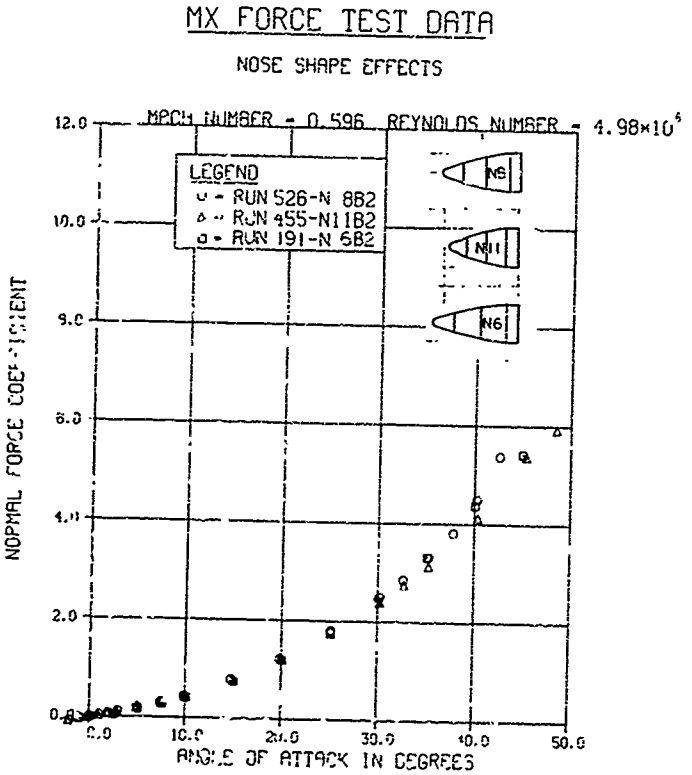

b. $M_\infty = 0.6$

Figure 4.7 (Continued)

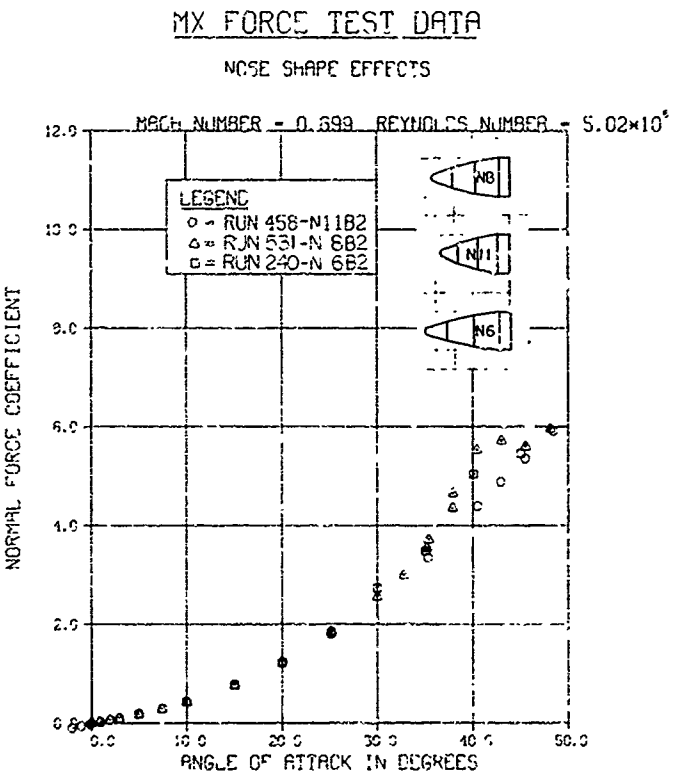

c. $M_\infty = 0.7$

Figure 47 (Concluded)

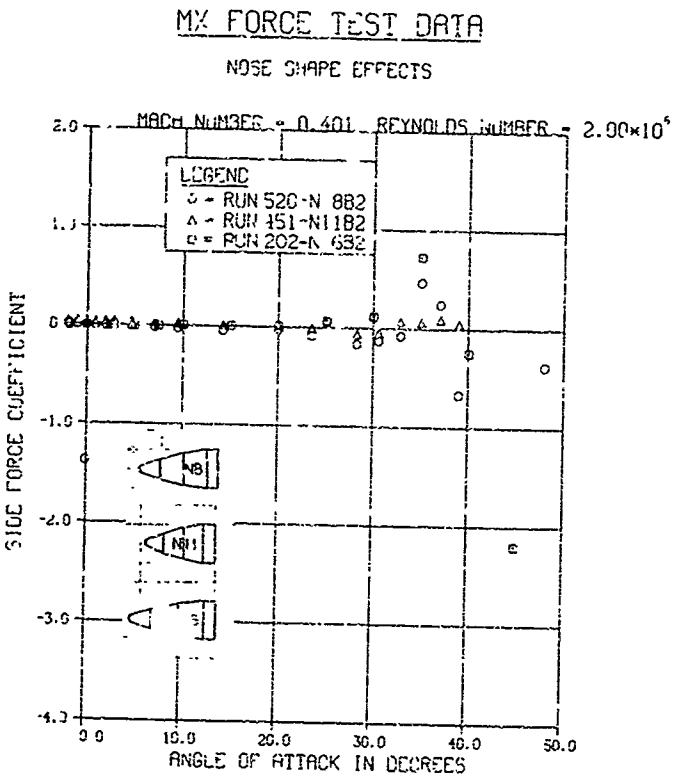

a. $M_\infty = 0.4$

Figure 48. Effect of Fineness Ratio of the Triconic Nose Shapes on Side Force Coefficient, Bluntness Ratio = 0.060

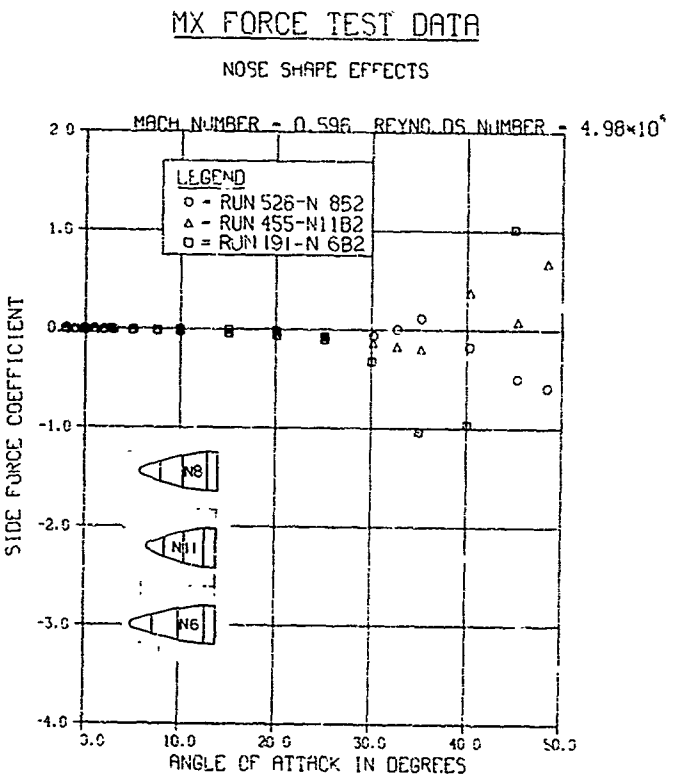

b. $M_\infty = 0.6$

Figure 48 (Continued)

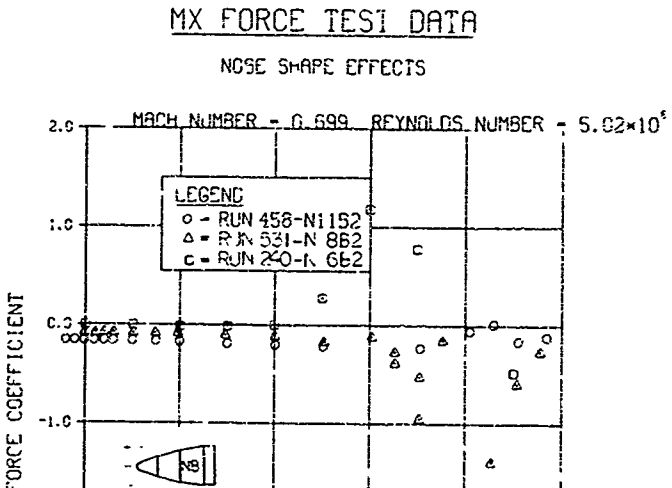

c. $M_\infty = 0.7$

Figure 48 (Concluded)

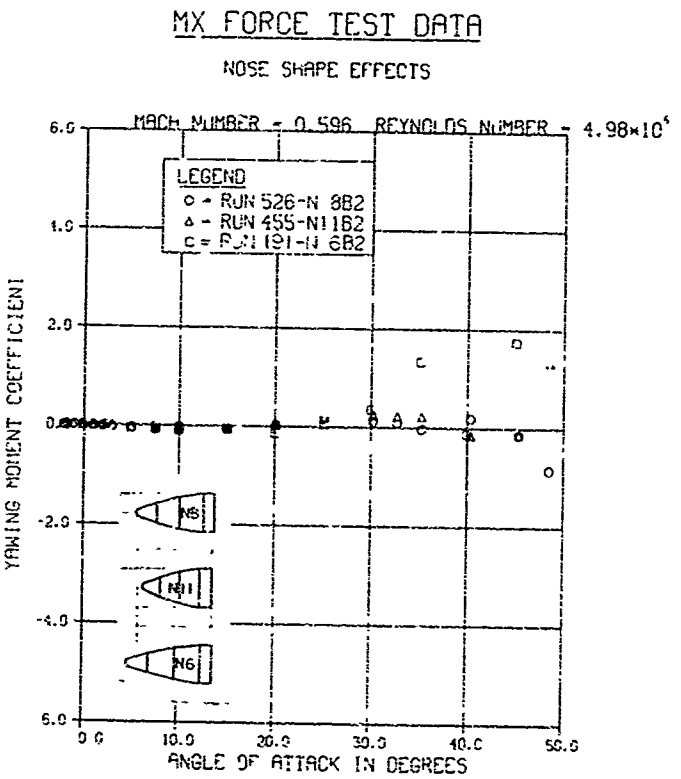

b. $M_\infty = 0.6$

Figure 49 (Continued)

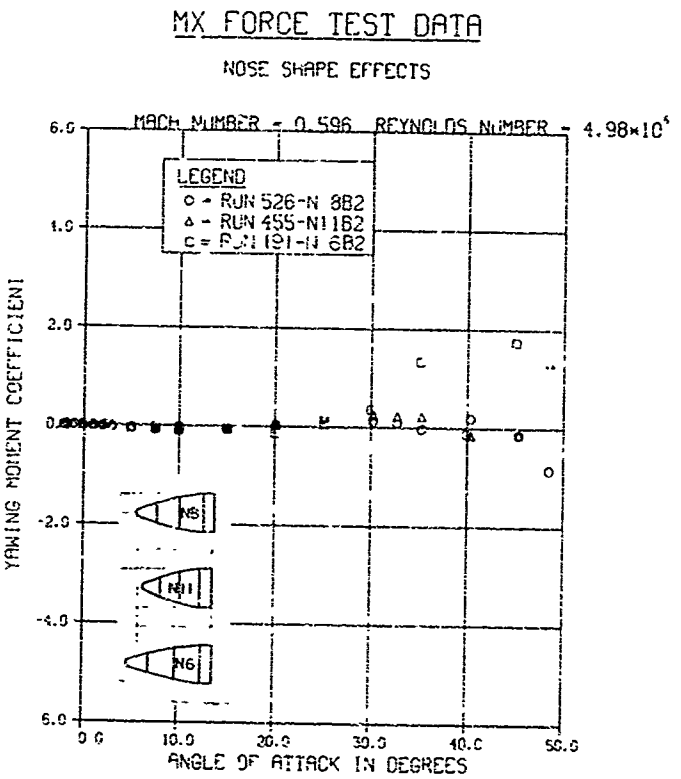

b. $M_\infty = 0.6$

Figure 49 (Continued)

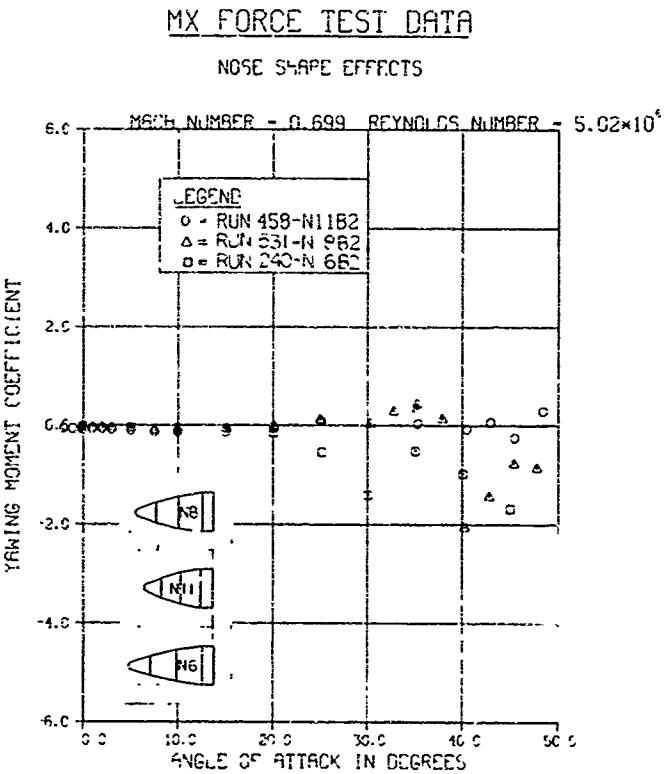

c. $R_m = 0.7$

Figure 49 (Concluded)

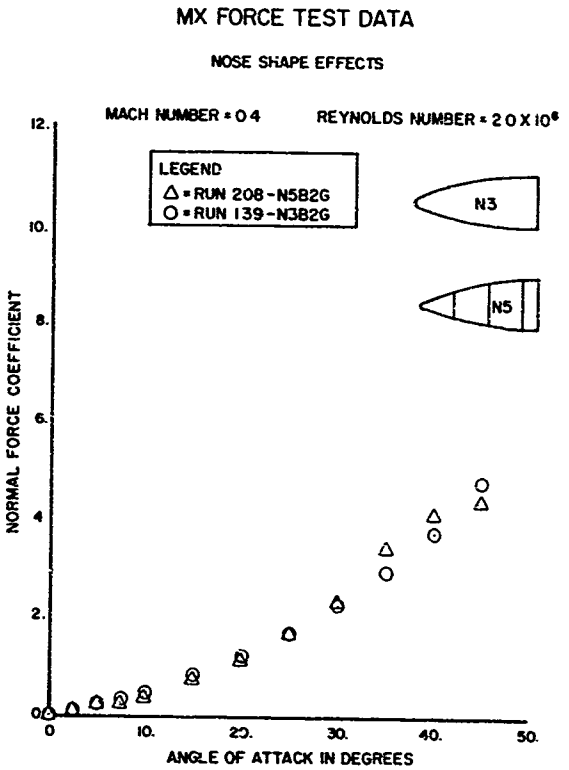

a. $M_\infty = 0.4$

Figure 50. Comparison of the N3 Ogive Nose and the N5 Triconic Nose, Normal Force Coefficient

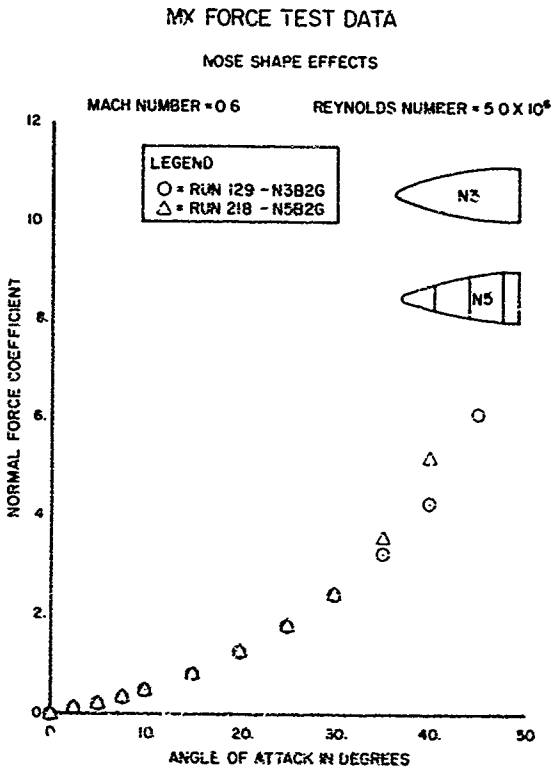

b. $M_\infty = 0.6$

Figure 50 (Continued)

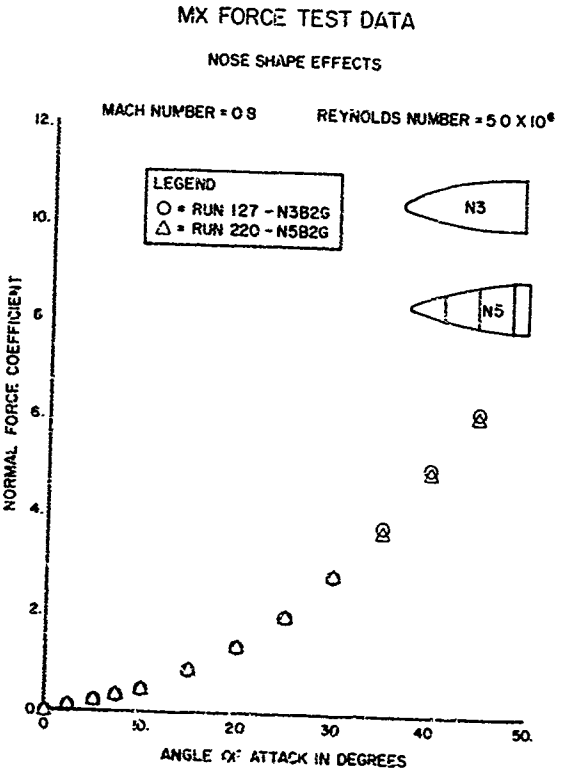

c. $M_\infty = 0.8$

Figure 50 (Concluded)

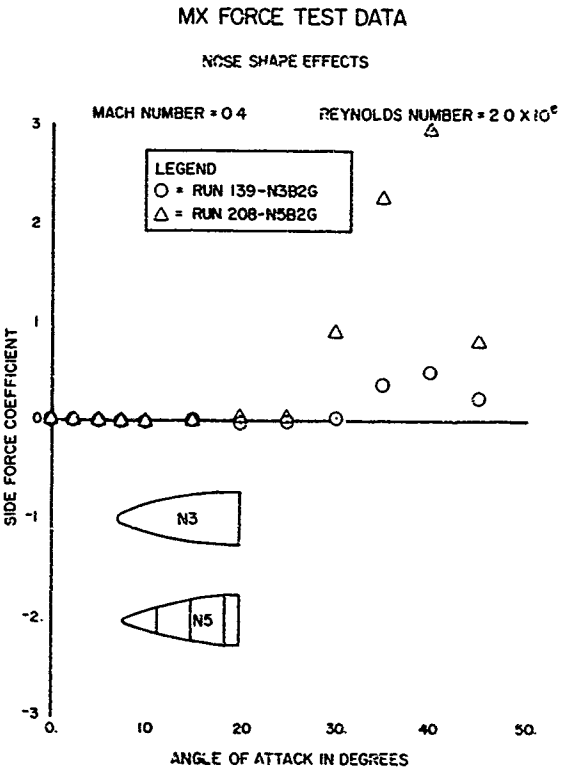

a. M = 0.4

Figure 51. Comparison of the N3 Ogive Nose and the N5 Tricomic Nose, Side Force Coefficient

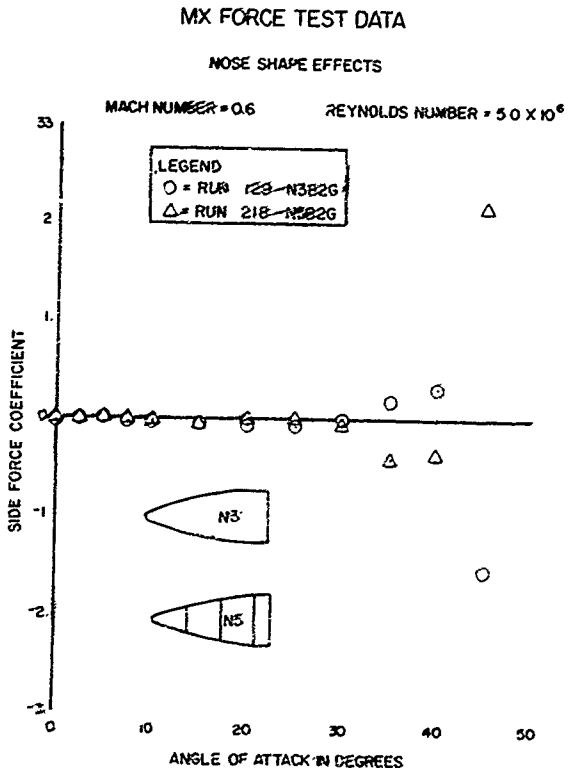

b M = 2.6

Figure 51 (Continued)

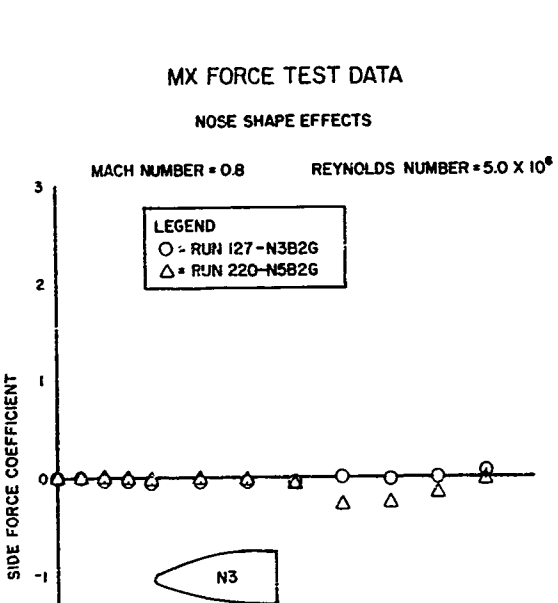

c. M = 0.8

Figure 51 (Concluded)

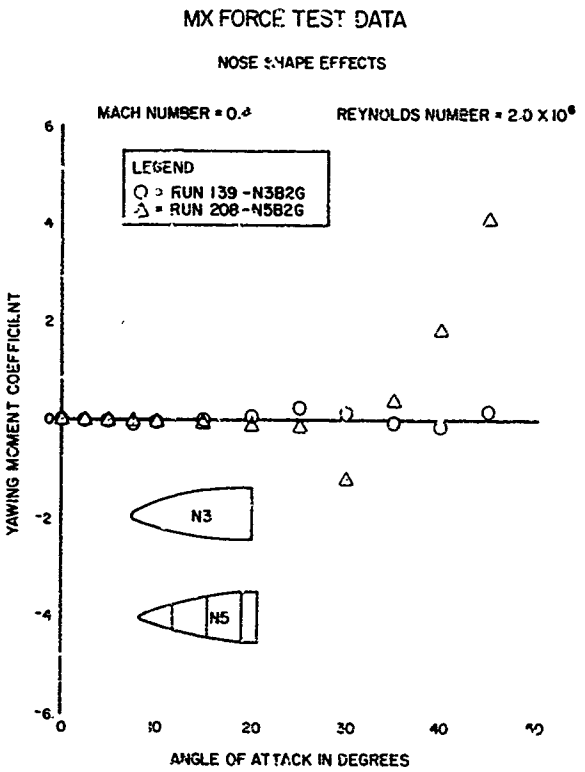

a. M = 0.4

Figure 52. Comparisons of the N3 Ogive Nose and the N5 Triconic Nose, Yawing Moment Coefficient

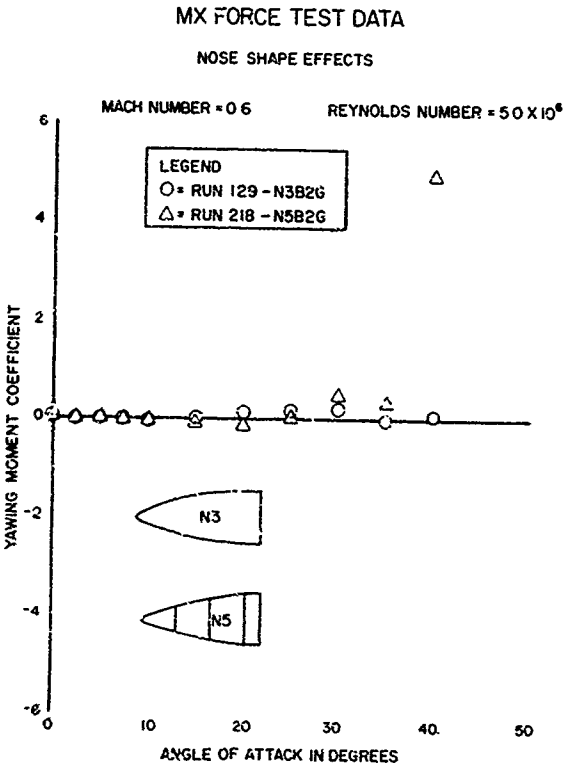

b. M = 0.6

Figure 52 (Continued)

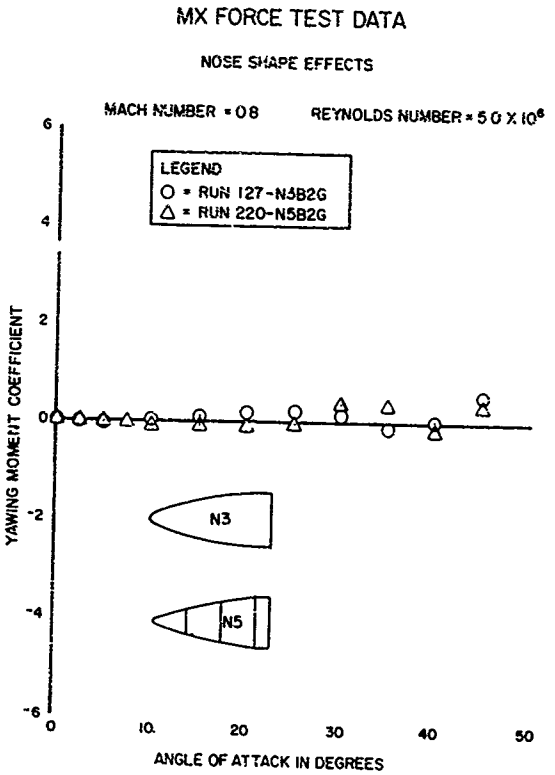

c. M = 0.8

Figure 52 (Concluded)

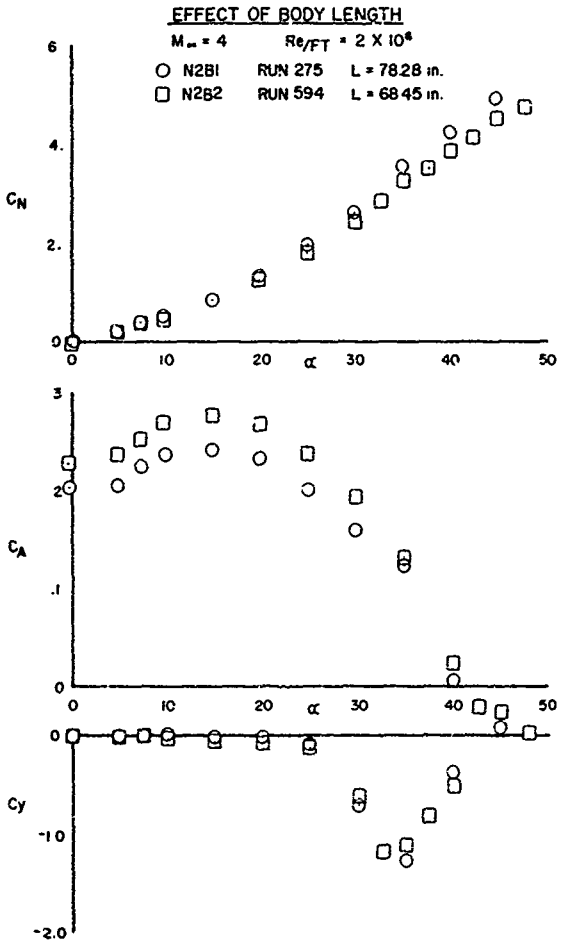

a. M = 0.4

Figure 53. Effect of Body Length on Force Coefficients

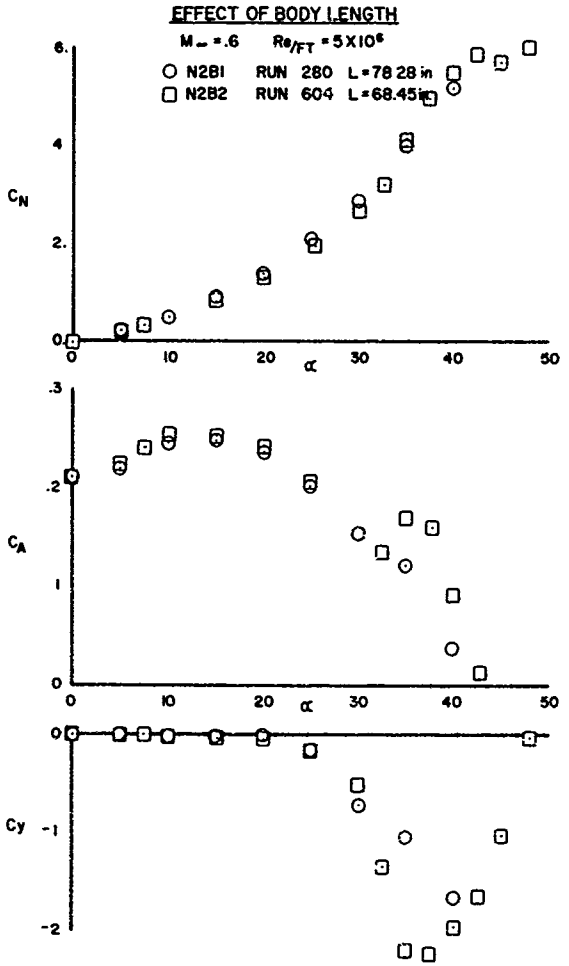

b. $M_\infty = 0.6$

Figure 53 (Continued)

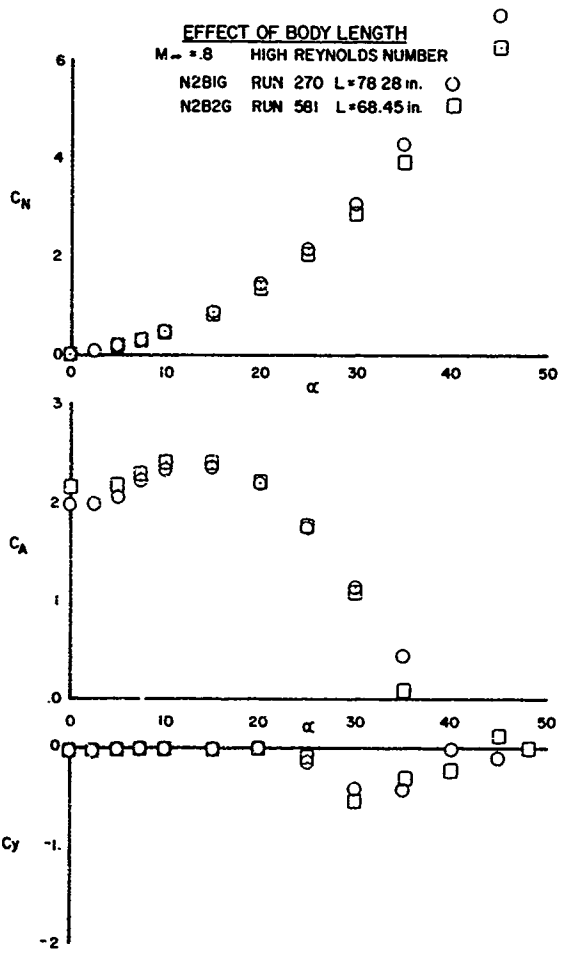

c. M = .0 8

Figure 53 (Concluded)

Of particular interest is the effect of increased length on the running loads patterns. Figure 54 shows the N4B1 and N4B2 normal force and side force coefficients at each pressure station at Mach number 0.4, and an angle of attack of 40 degrees. The patterns shown are very similar, with the exception of the dropoff in C_N at the aft end of N4B2, caused by base effects. The next figure (Figure 55) compares the running loads for the N3B1 and N3B2 configurations at Mach number 0.6 and an angle-of-attack of 40 degrees. Again the patterns are similar. These results indicate that the extended body continues the running load pattern of the shorter body length.

Body length effects on asymmetric forces were also studied in Reference 20, which contains test data on nose configurations without an afterbody and with a detached afterbody. The research found that no changes in the nose asymmetric forces and moments occurred due to the presence of an afterbody.

7. ROLL ANGLE EFFECTS

During the second force-and-moment test entry, which was the last of the five entries in 16T for this test series, roll angles were varied from -10 to 190 degrees at several high angles-of-attack at Mach numbers of from 0.4 to 0.7 to investigate the effect of roll angle on the asymmetric forces. Repeatability of the continuous-roll data was checked by recording data from -10 to 190 degrees and from 190 to -10 degrees. Good repeatability was found on several different configurations so the remaining roll runs were made in only one direction. The model was rolled at a rate of 2 degrees per second. Data were recorded at a rate of 100 samples per second on magnetic tape for off-line analysis (Reference 43). As a check on the validity of the continuous-roll procedure, data were taken using manual roll settings with the model held stationary. Excellent agreement was obtained as shown in Figures 56 (a) and 57 (a). Figures 56 through 57 show the effect of roll angle on C_N and C_Y for the N2B2 configuration at Mach numbers 0.4, 0.6 and 0.7. These plots indicated the necessity of rolling the model to

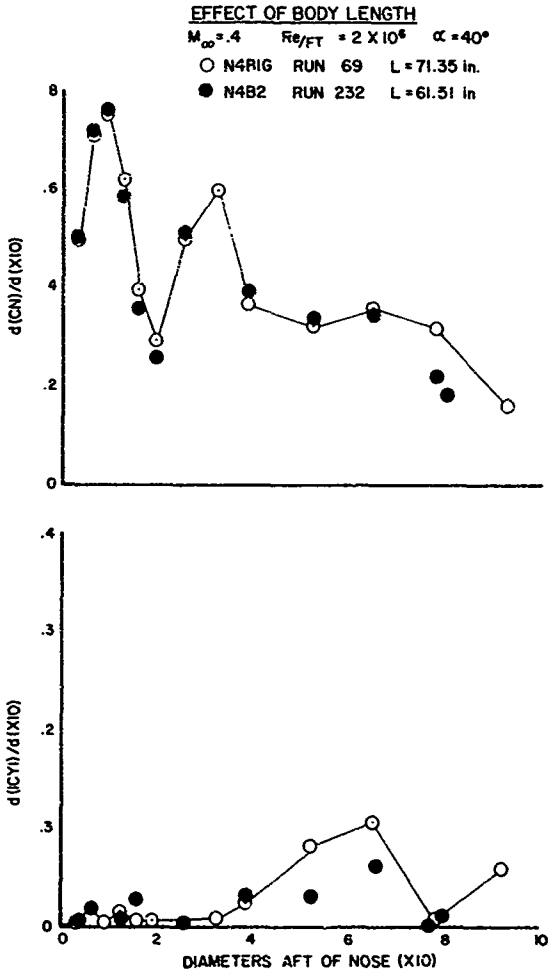

Figure 54. Effect of Body Length on the Distributed Force Coefficients at Mach 0.4

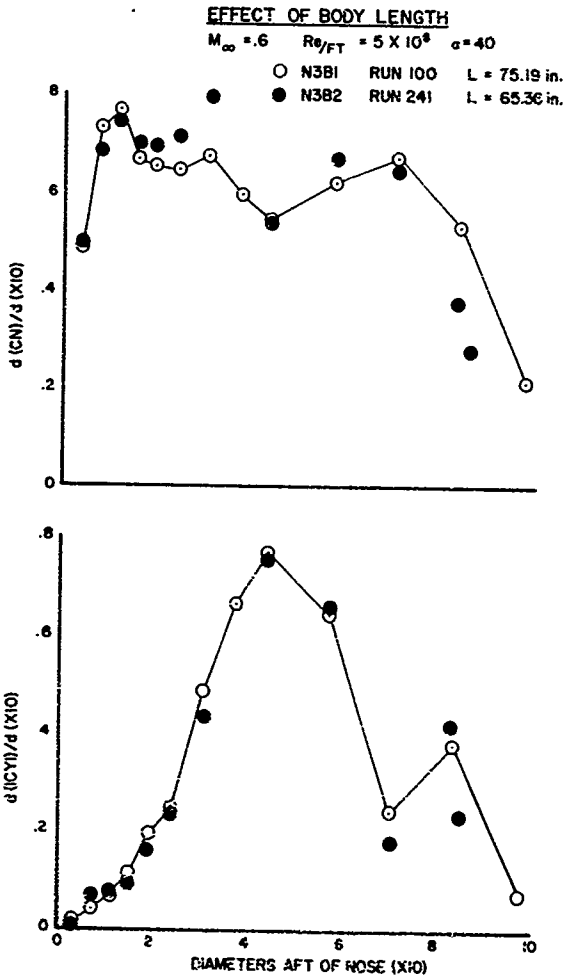

Figure 55. Effect of Body Length on the Distributed Force Coefficients at Mach 0.6

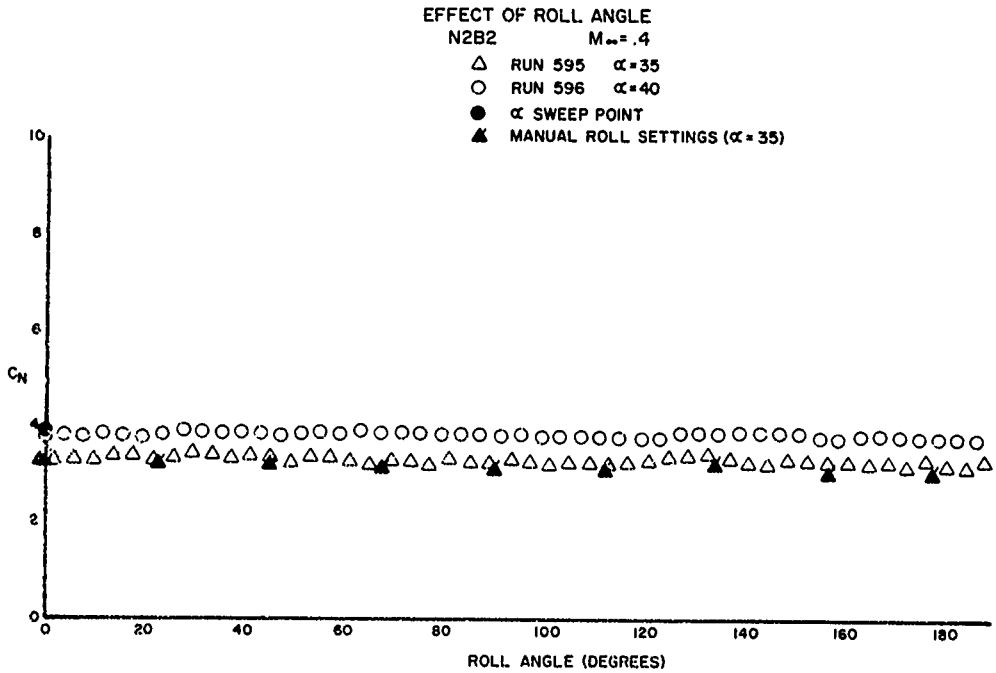

a. M = 0.4

Figure 56. Effect of Roll Angle on Normal Force Coefficient/N2B2 Configuration

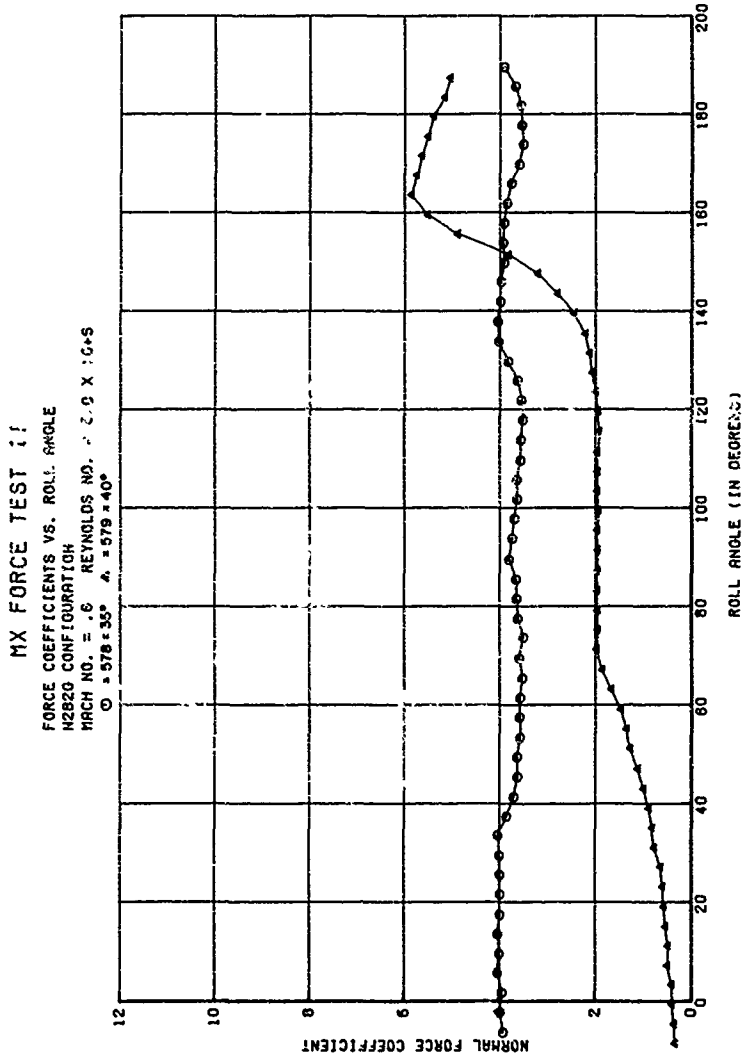

b. M = 0.6

Figure 56 (Continued)

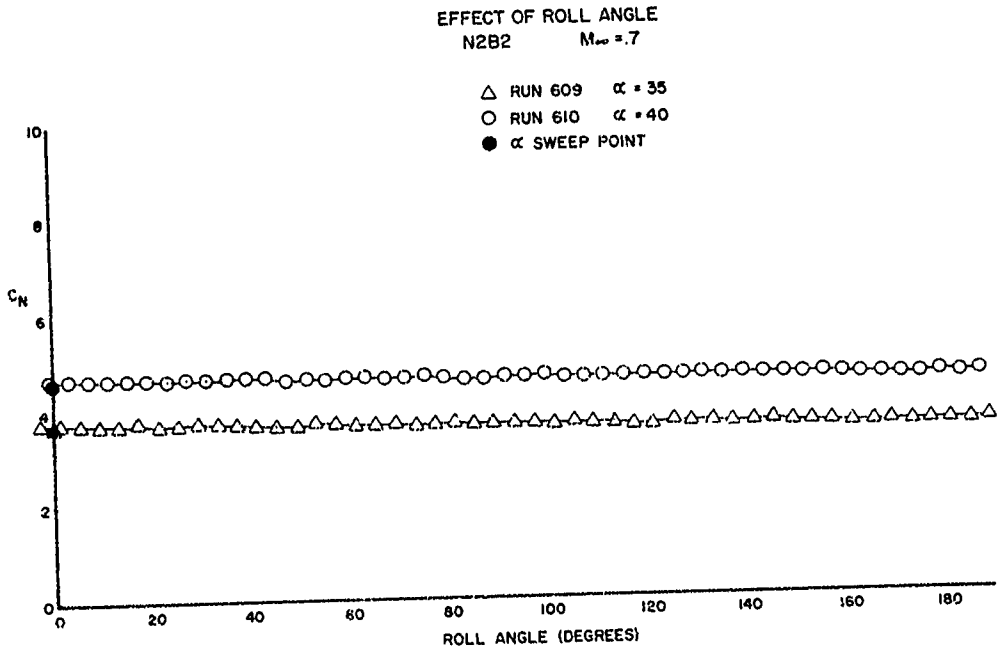

c. M = 0.7

Figure 56 (Concluded)

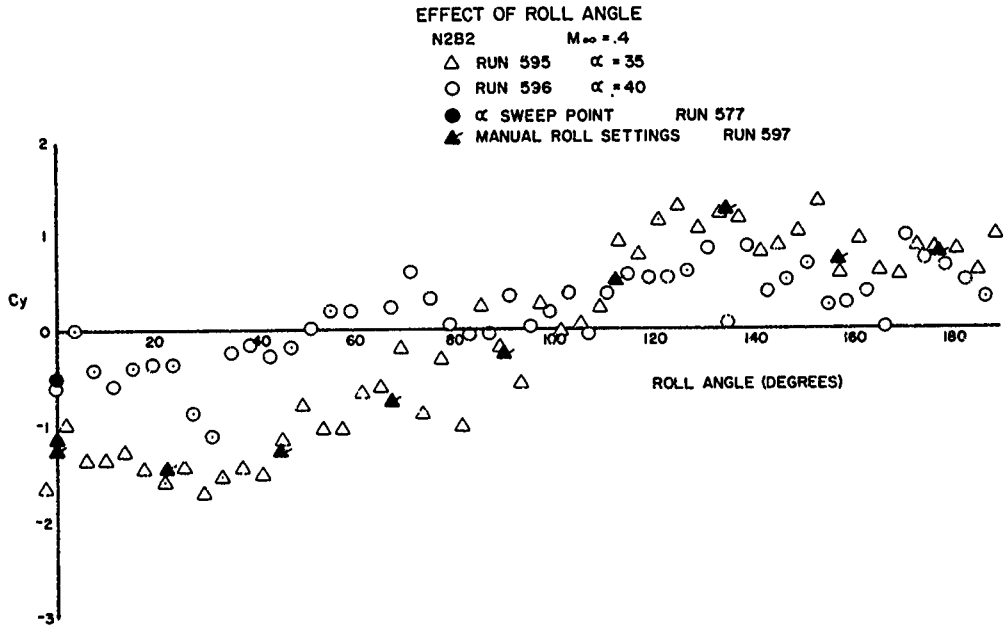

a. M = 0.4

Figure 57. Effect of Roll Angle on Side Force Coefficient/N2B2 Configuration

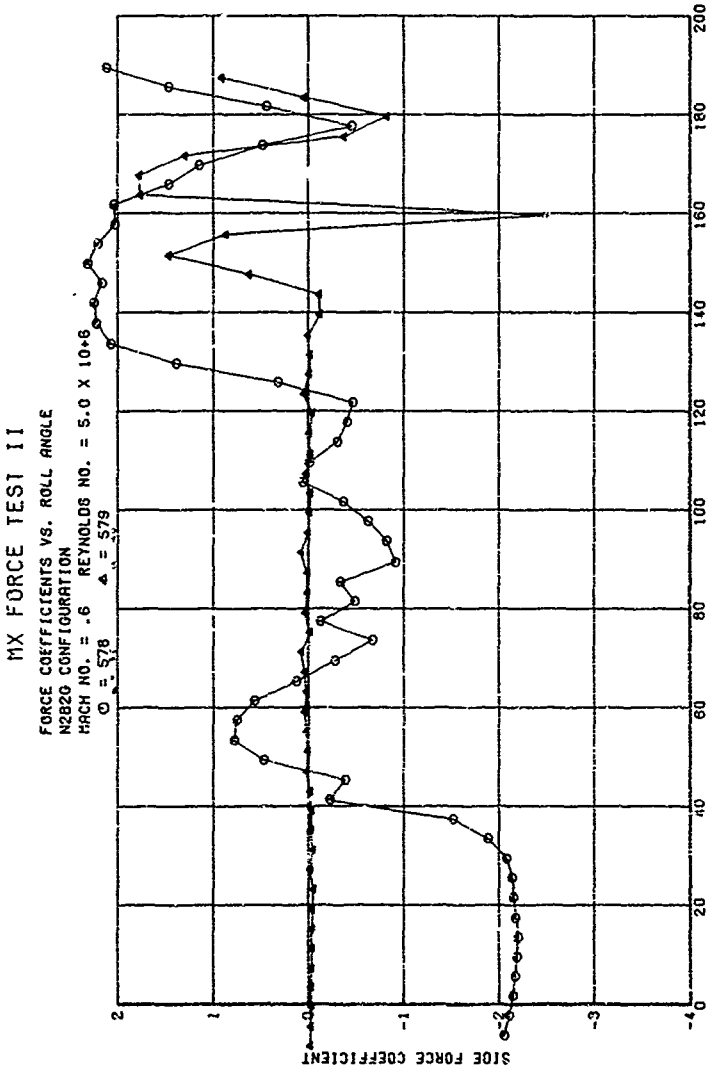

b. M = 0.6

Figure 57 (Continued)

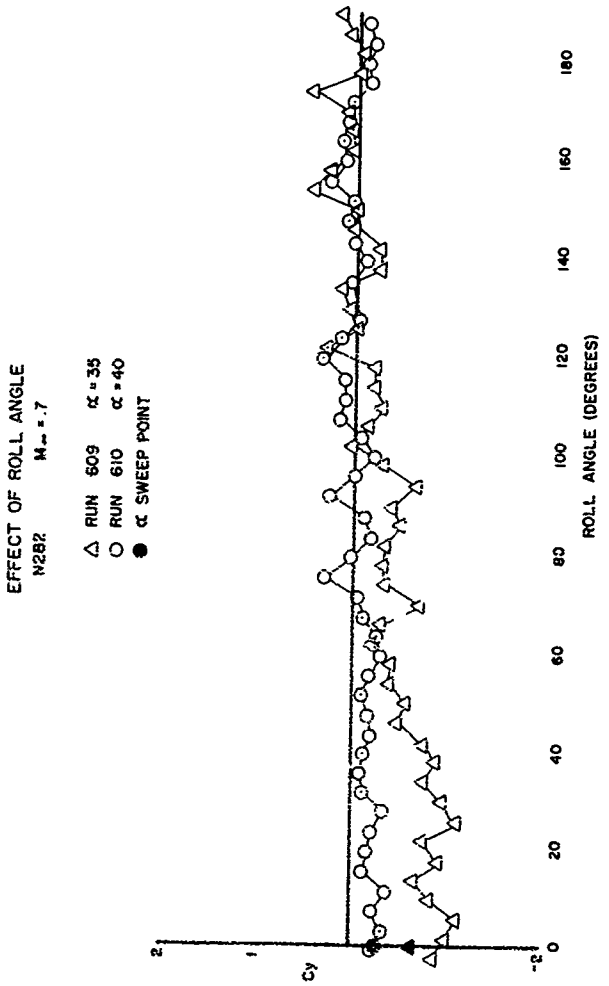

c. M = 0.7

Figure 57 (Concluded)

determine the maximum side force. Figures 56 (a) and 57 (a) include the manual roll settings and angle-of-attack sweep points which indicate the repeatability of the test data.

Figures 58 through 59 show the effect of roll angle on the N14B2 configuration for Mach numbers from 0.4 to 0.7. The side force coefficient is seen to vary between -1.0 and 1.7 at Mach number 0.4, depending on the roll angle.

To shed some light on the effect of possible nose asymmetrics on the asymmetric forces, the triconic nose N7 was removed from the B2 body and reinstalled 180 degrees from its original position (and designated N77). Theoretically if the nose asymmetrics caused the asymmetric flow pattern the data should now be shifted 180 degrees. Figures 60 and 61 show the results, which reveal a lack of repeatability at roll angles of 0 degrees and 180 degrees. This may have been caused by a change in the asymmetry of nose to body alignment when the nose was reinstalled.

8. GRIT EFFECTS

A large number of the sting-mounted configurations were tested with a boundary-layer transition strip around the nose. The transition strip consisted of a 1/8-inch-wide ring of "grit" around the nose. The grit consisted of No. 70 (approximately .0083-inch-diameter) glass spheres glued on with polaroid print fixer. The chart in Figure 62 lists the location of the grit ring for each of the 14 nose configurations. The N1B1 configuration was also pressure tested with two lengthwise strips of grit located 30 degrees either side of the windward meridian for tripping the boundary layer when the model was at high angles-of-attack.

Plots were generated comparing grit ring on and off results of the higher Reynolds number runs. Typical normal and axial force coefficient results are shown in Figure 63. No regular trends were apparent in these data. To isolate the grit effects, if any, on the aerodynamics at higher Reynolds numbers, the differences between C_N, C_A, C_n and C_y, with and without grit, for the N3B2 were plotted for Mach numbers of 0.3 to 0.9.

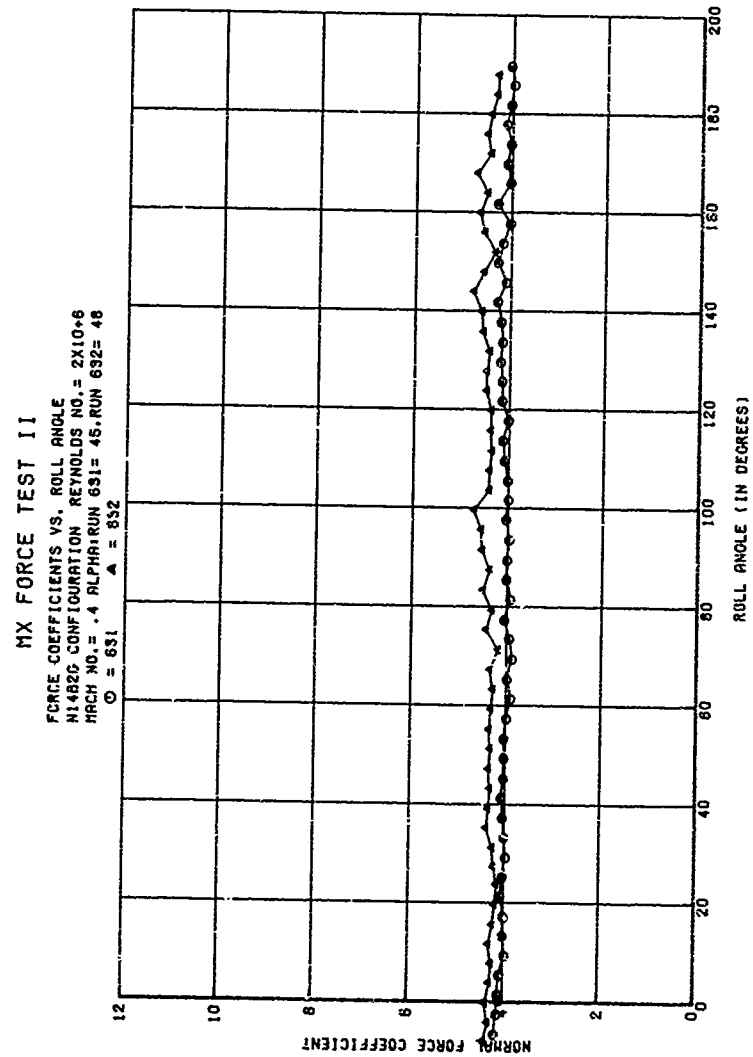

a. M = 0.4

Figure 58. Effect of Roll Angle on Normal Force Coefficient for the N1482 Configuration

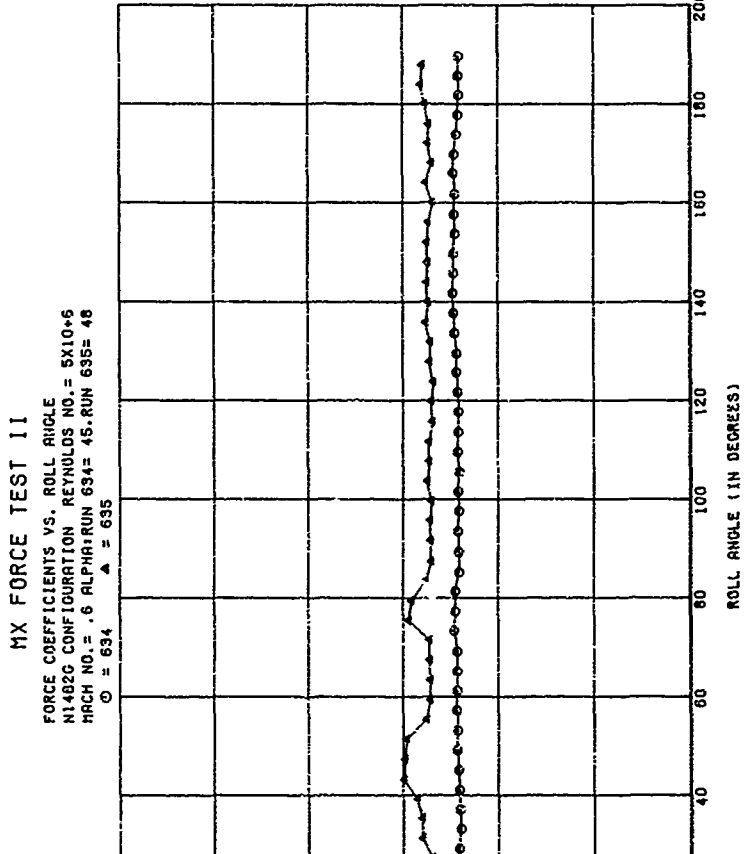

b. M = 0.6

Figure 58 (Continued)

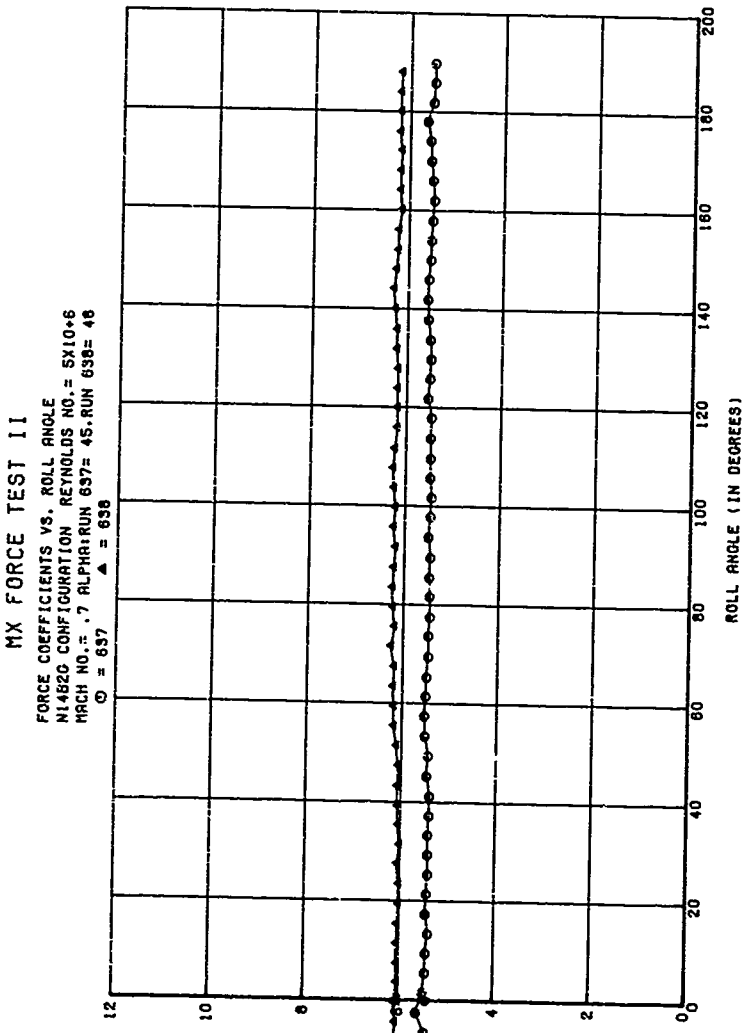

c. M = 0.7

Figure 58 (Concluded)

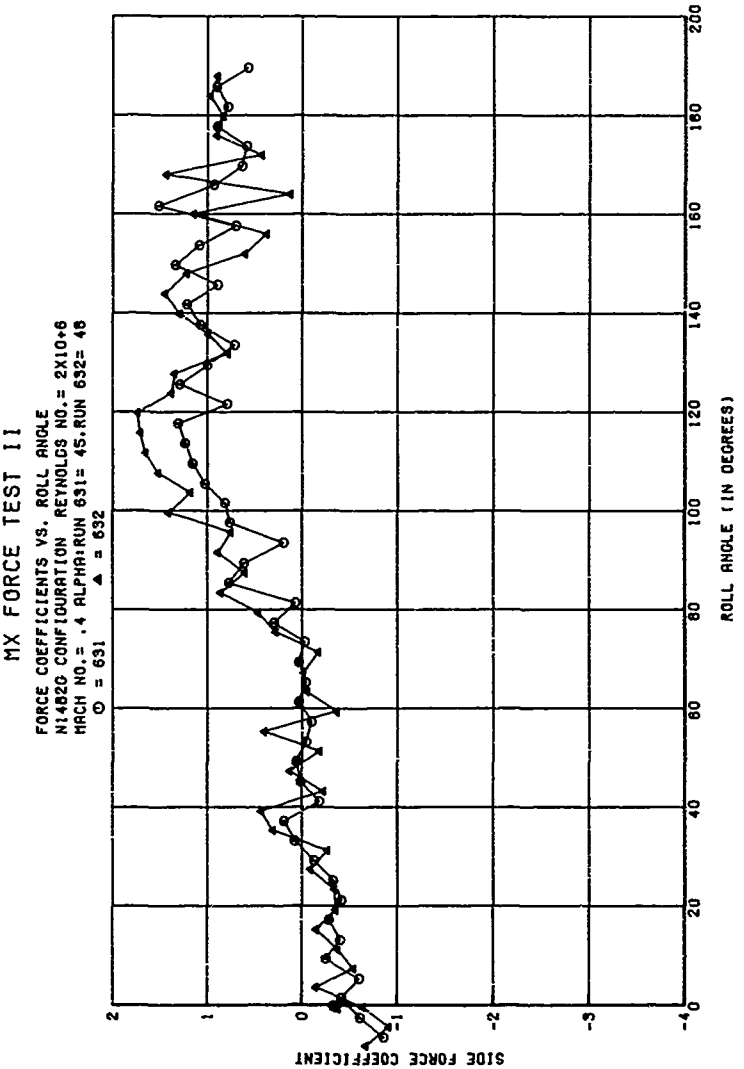

a. M = 0.4

Figure 59. Effect of Roll Angle on the Side Force Coefficient for the N1482 Configuration

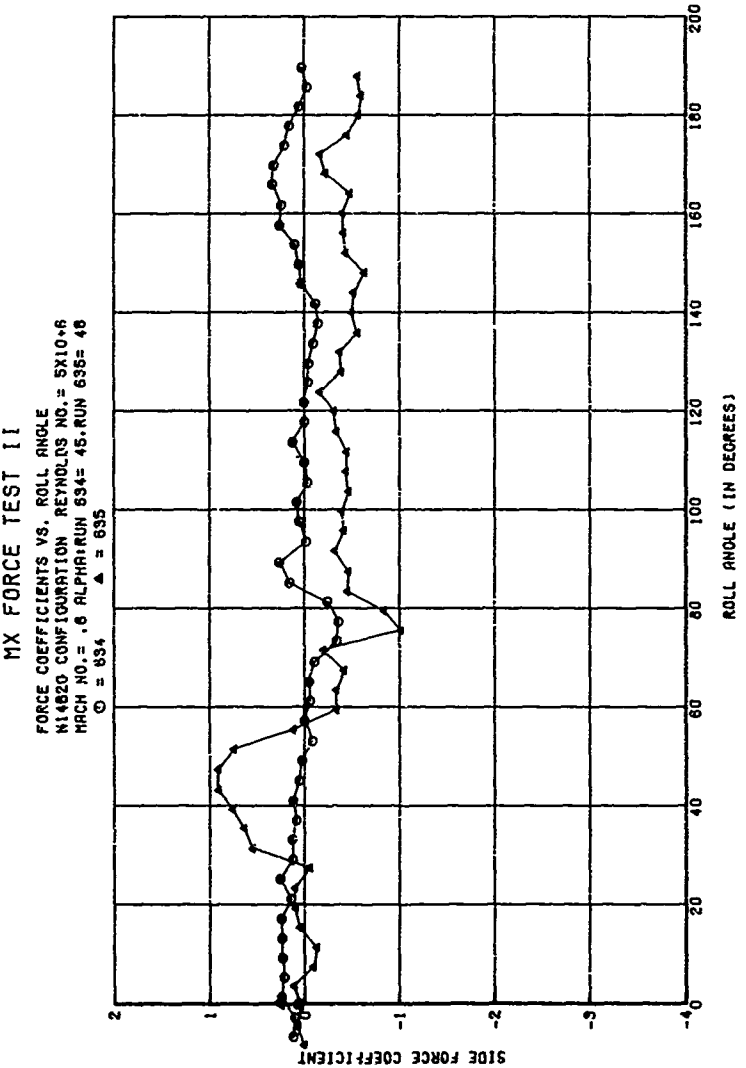

b. M = 0.6

Figure 59 (Continued)

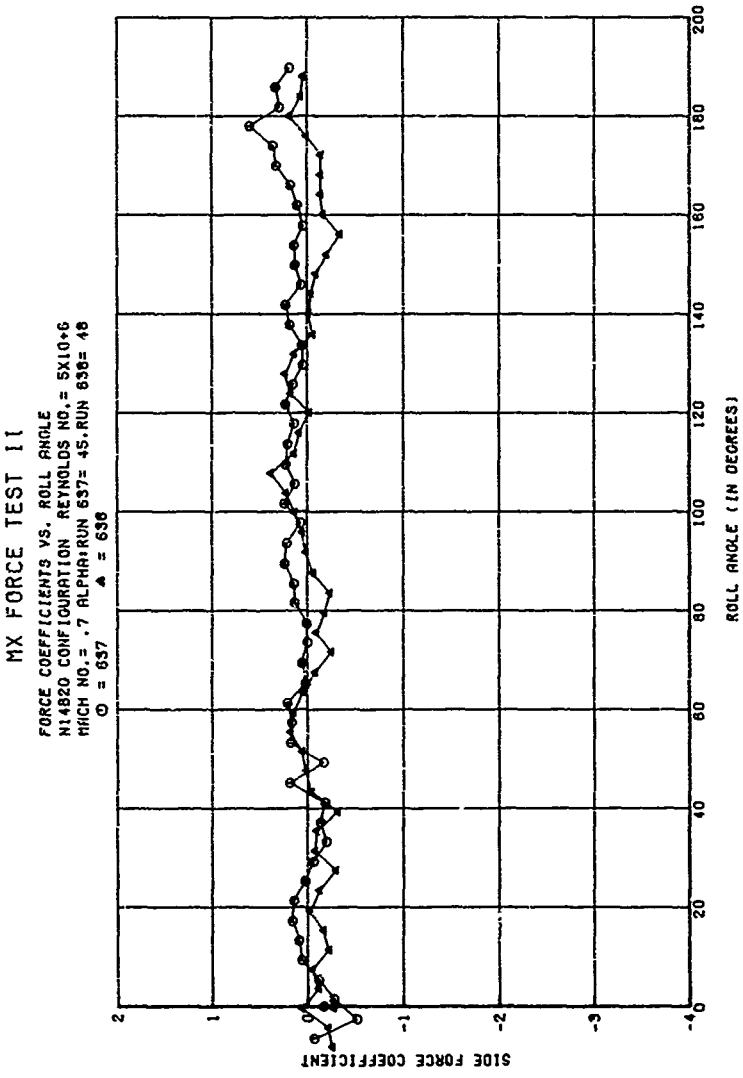

c. M = 0.7

Figure 59 (Concluded)

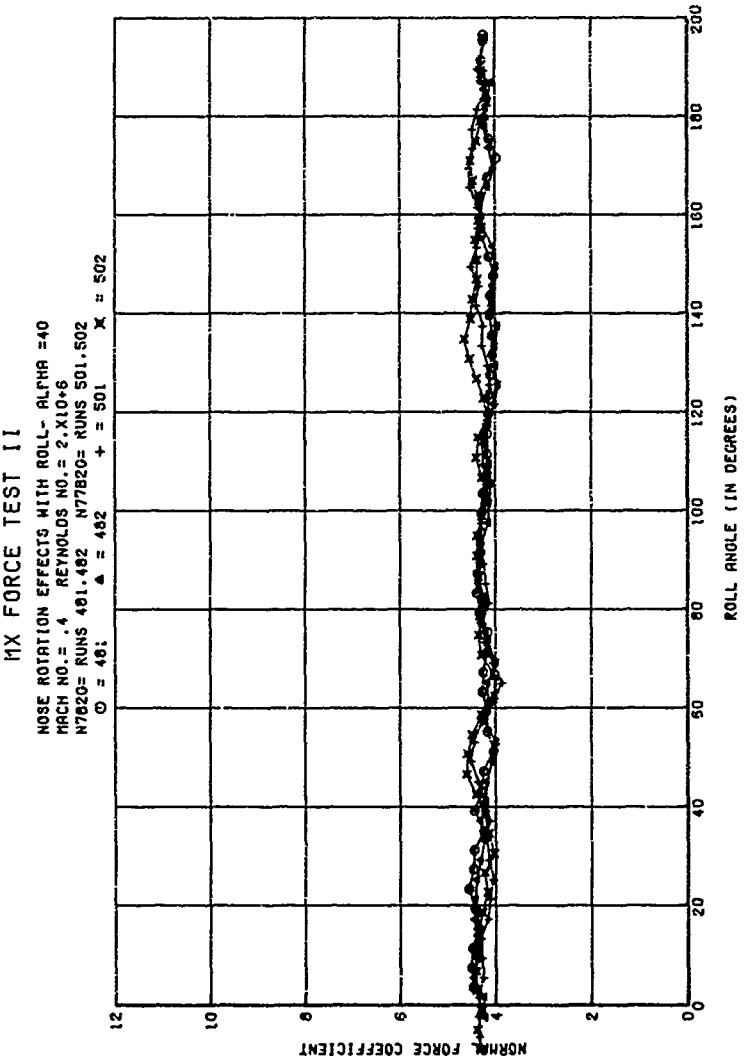

Figure 60. Effect of Nose Geometry and Roll on the Normal Force Coefficient

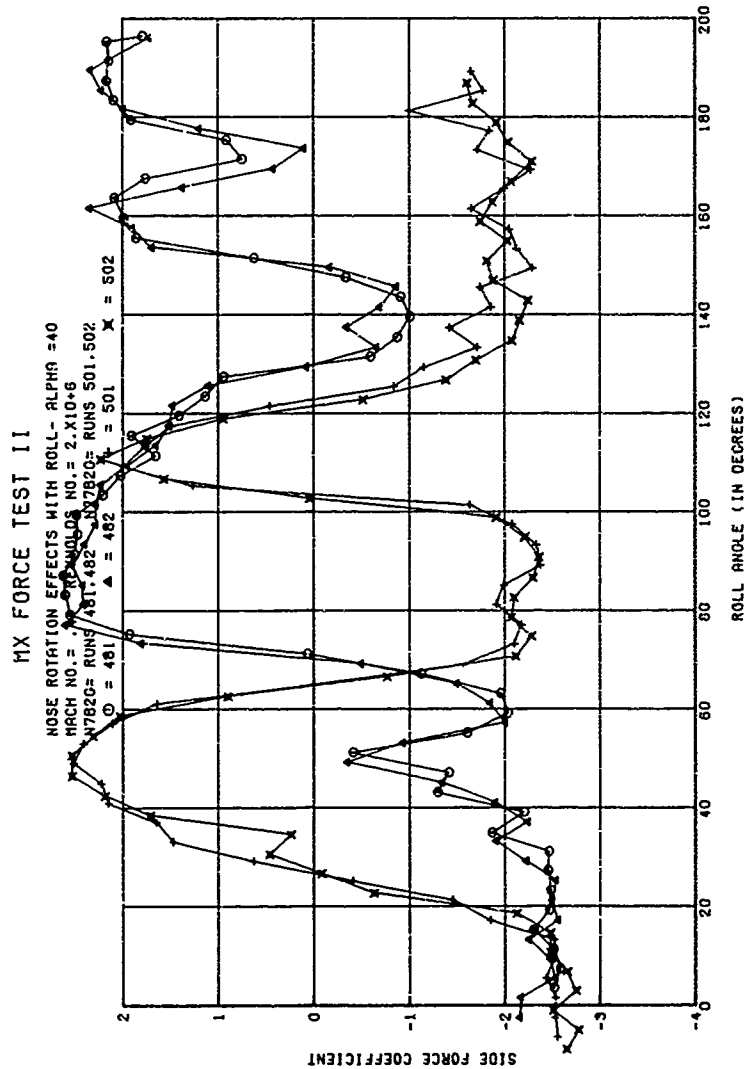

Figure 61. Effect of Nose Geometry and Roll on the Side Force Coefficient

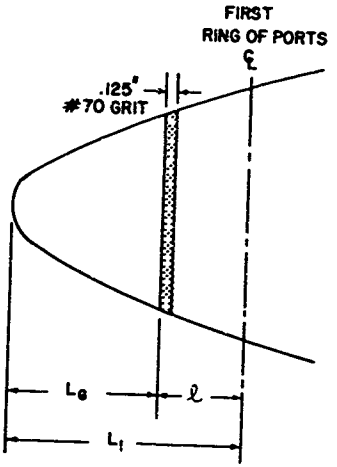

L_1 = Distance from nose to ℄ of first ring of pressure ports

L_G = Axial distance from nose to leading edge of grit ring

ℓ = Axial distance from leading edge of grit ring to ℄ of first ring of pressure ports

	NOSE CONFIGURATION	$\frac{r_n}{D}$	L_1 INCHES	L_G INCHES	ℓ INCHES
N_1	7-cal. ogive	0	3.90	2.80	1.10
N_2	"	.0304	3.50	2.40	1.10
N_3	5-cal. ogive	.0304	3.00	2.40	.60
N_4	3-cal. ogive	.0304	2.38	1.88	.50
N_5	5-cal. triconic	.040	4.63	2.40	2.23
N_6	"	.080	3.78	1.55	2.23
N_7	4-cal. triconic	.040	2.78	2.40	.50
N_8	"	.080	2.15	1.77	.50
N_9	"	.120	1.52	1.14	.50
N_{10}	3-cal. triconic	.040	3.58	2.50	1.08
N_{11}	"	.080	3.07	1.99	1.08
N_{12}	"	.120	2.56	1.48	1.08
N_{13}	"	.160	2.05	.97	1.08
N_{14}	3-cal. ogive	.150	--	1.00	--

Figure 62. Nose Ring Grit Patterns

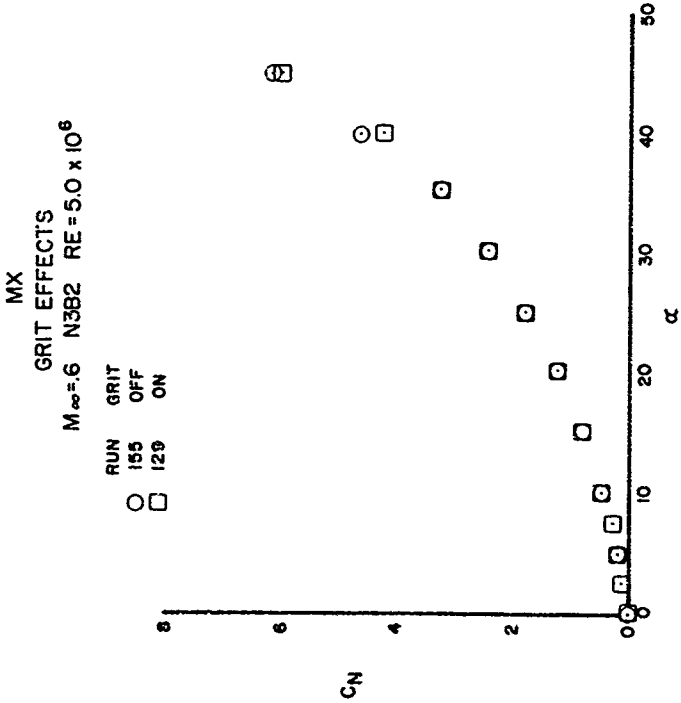

a. Normal Force Coefficient

Figure 63. Grit Effects on Normal Force and Axial Force Coefficient

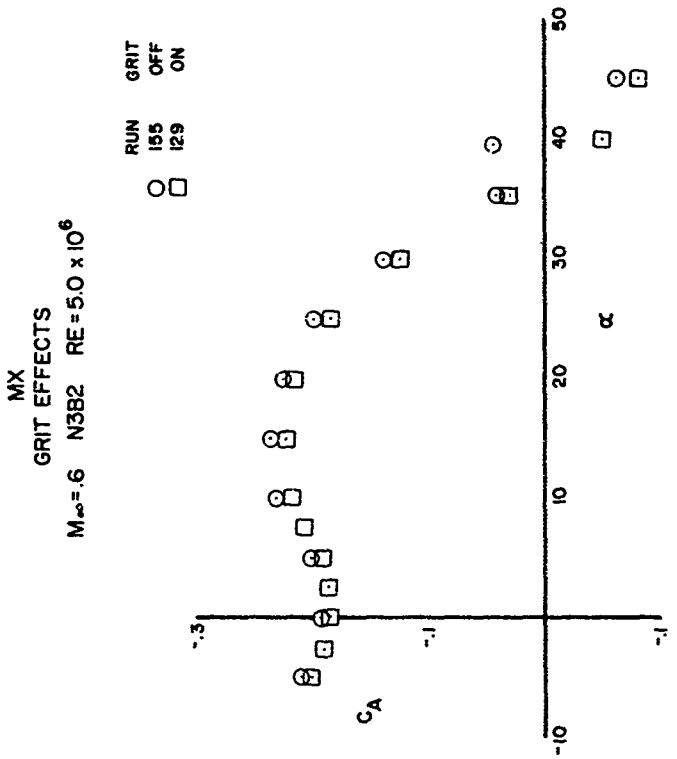

b. Axial Force Coefficient
Figure 63 (Concluded)

Figures 64(a through d) show typical results. The C_N plots show very small differences, less than ± 3 percent, for angles-of-attack less than 30 degrees. Above 30 degrees the differences were larger but, again, both positive and negative. The C_A differences are also very small and the values graph on both sides of zero. Since the expected effect of roughness would be to increase axial force, the changing sign indicates the differences are probably within the accuracy of the balance. Side force coefficients and yawing moment coefficients, C_y, and C_n, have very small differences for angles-of-attack less than 35 degrees. The differences become large above 30 degrees, but this is due more to the nature of the asymmetric flow field (i.e. large forces of opposite signs) and model dynamics than can be contributed to grit effect.

Figure 65 shows typical pressure coefficients for the N2B1 configuration 3.5-inch station plotted for grit ring "on" and "off." No difference could be seen, lending strength to the conclusion that the grit ring at the higher Reynolds number (3.0×10^6 per foot) had no regular effect on the aerodynamics.

The N1B1 configuration without grit, with a grit ring on the nose and with both the grit ring and lengthwise grit strips (N1B1, N1B1G, N1B1GS respectively) aerodynamic coefficients are compared in Figures 66 and 67 for Mach numbers 0.4 and 0.6 at high Reynolds numbers. The grit affects the asymmetric force values at angles-of-attack greater than 20 degrees. The grit strips tend to increase the normal force coefficient and yawing moments at angles-of-attack as low as 25 degrees. The maximum yawing moments are encountered with the grit strips for these conditions.

To determine if the addition of the grit ring plus grit strips improved Reynolds number simulation, the N1B1 and N1B1GS data for low Reynolds number was compared with the data of N1B1 for high Reynolds number at Mach number 0.6. No benefits from adding the grit could be found. In fact, the no-grit run matched the high Reynolds number data better than did the configuration with grit ring and strips. This is shown in Figure 68. The low Reynolds number data are subject to a much greater uncertainty due to the low dynamic pressures and resulting forces

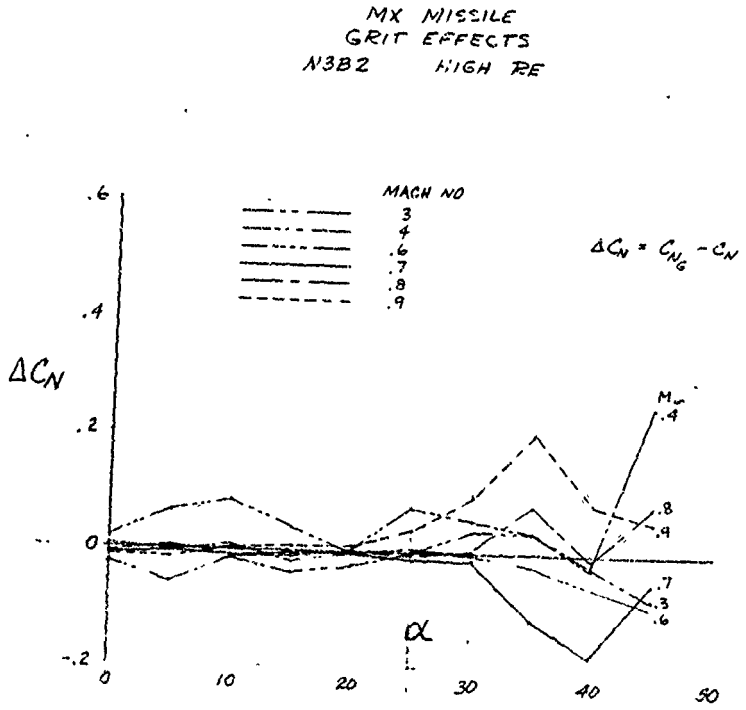

a. Incremental Normal Force Coefficient

Figure 64. Incremental Differences Between Force and Moment Coefficient With and Without Grit

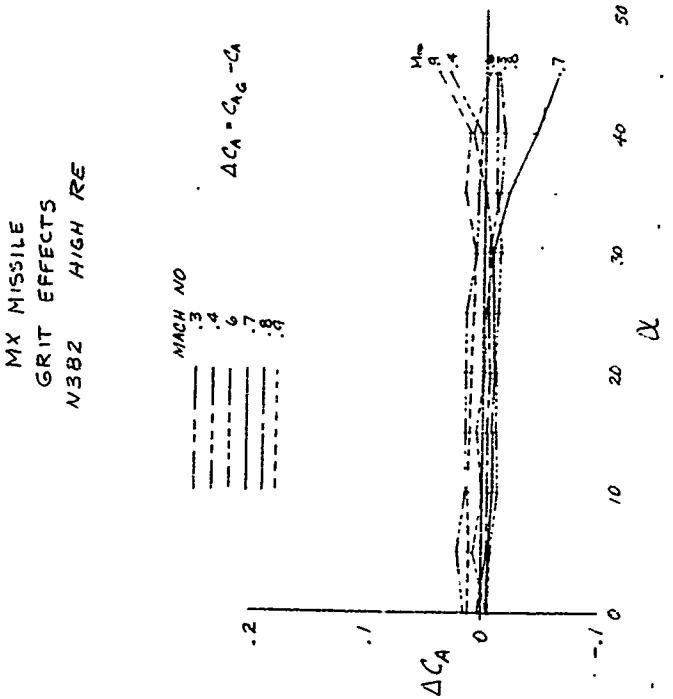

b. Incremental Axial Force Coefficient

Figure 64 (Continued)

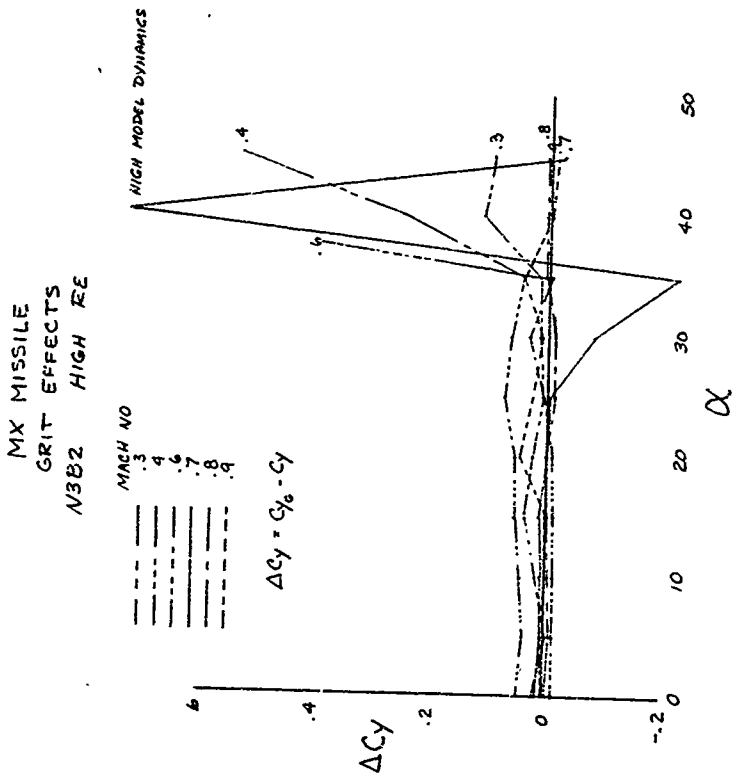

c. Incremental Side Force Coefficient
Figure 64 (Continued)

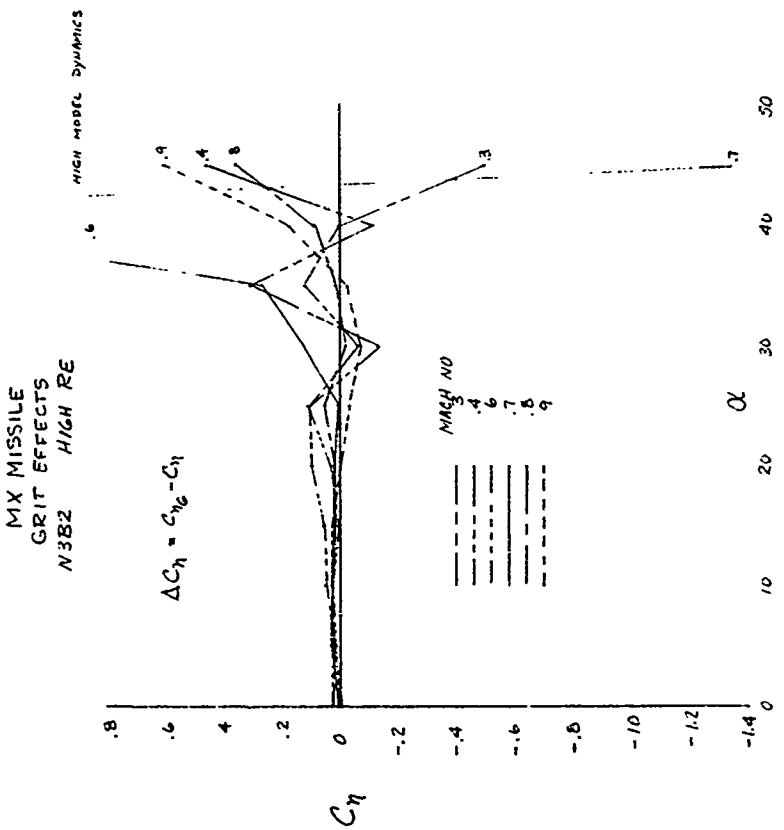

d. Incremental Yawing Moment Coefficient

Figure 64 (Concluded)

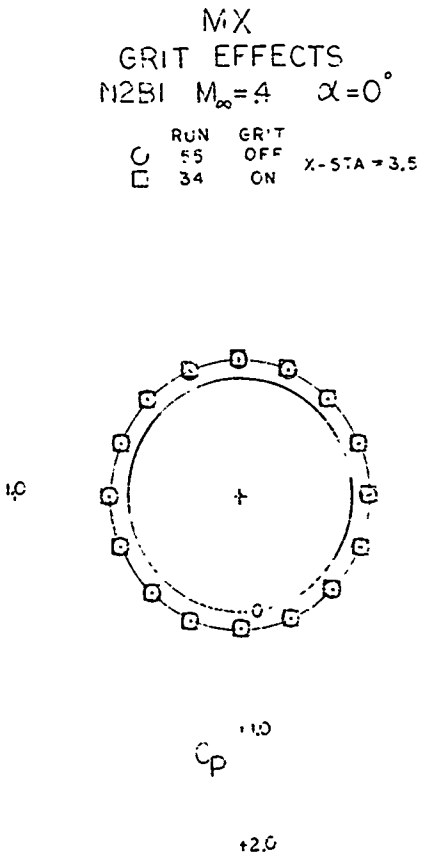

Figure 65. Grit Effect on Pressure Distribution at x = 3.5

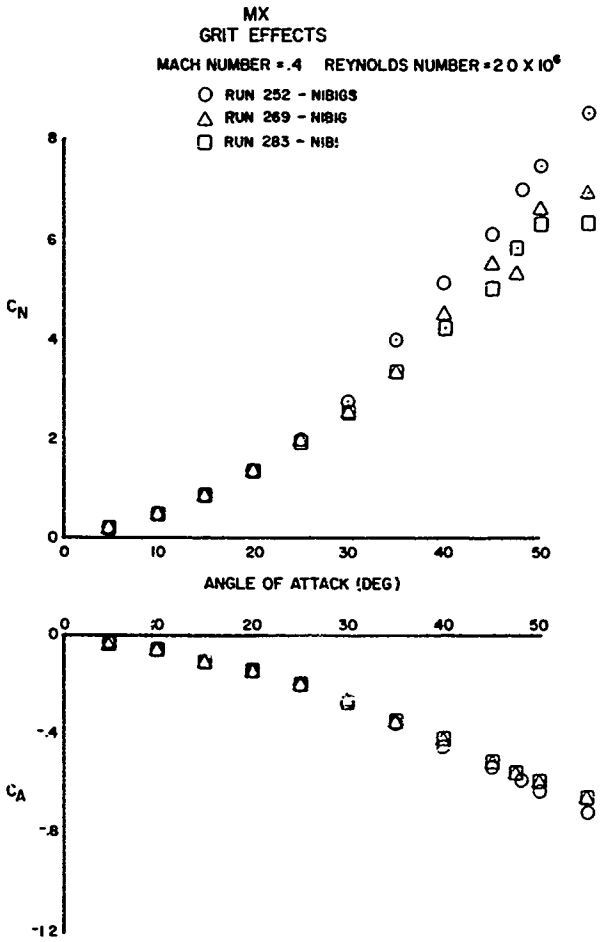

a. M = 0.4

Figure 66. Comparison Between Grit Strips and Grit Rings Effects and Axial Force Coefficient

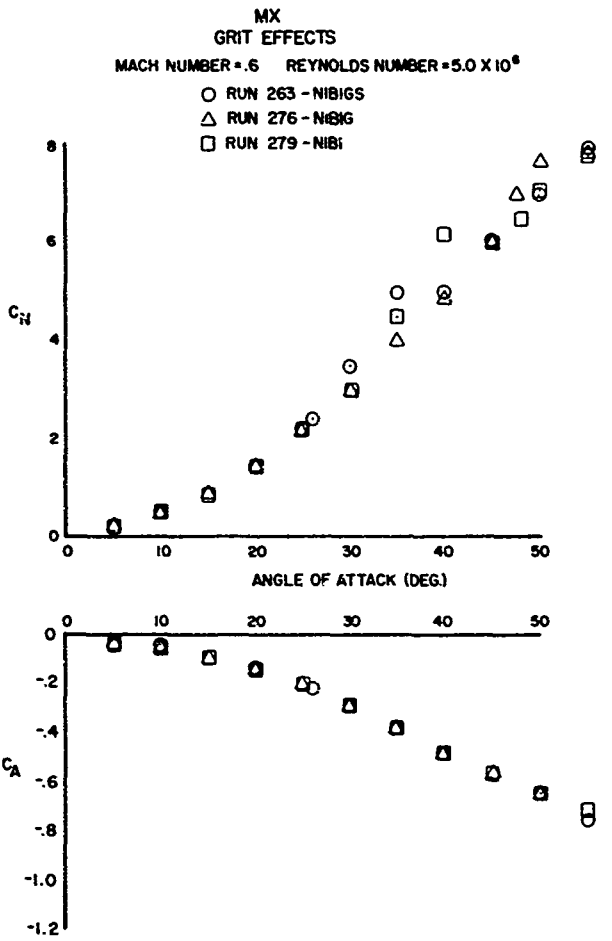

b. M = 0.6

Figure 66 (Continued)

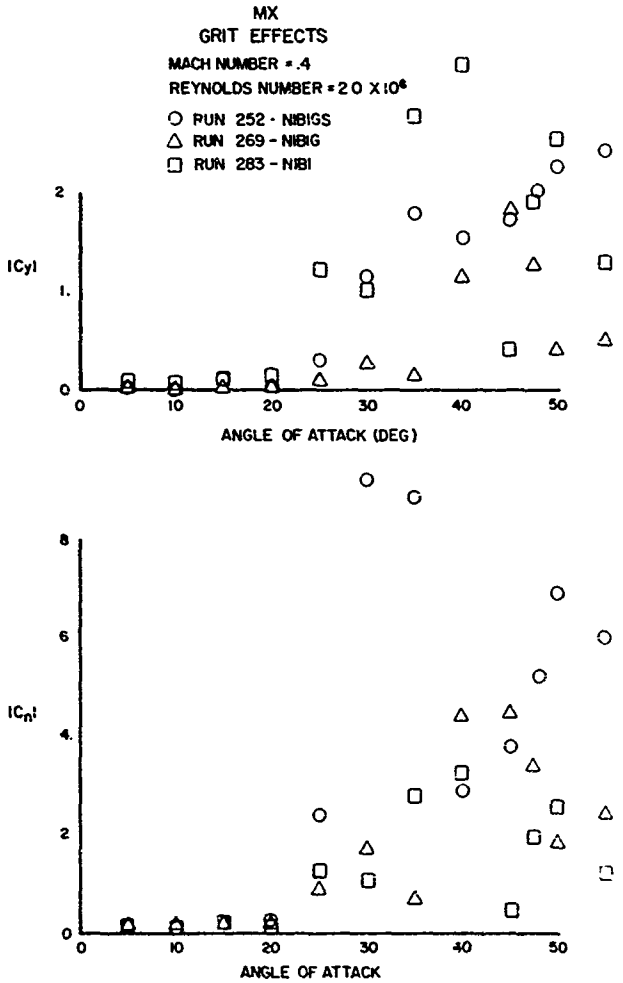

a. M = 0.4

Figure 67. Comparison Between Grit Strips and Grit Rings Effects on Side Force and Yawing Moment Coefficient

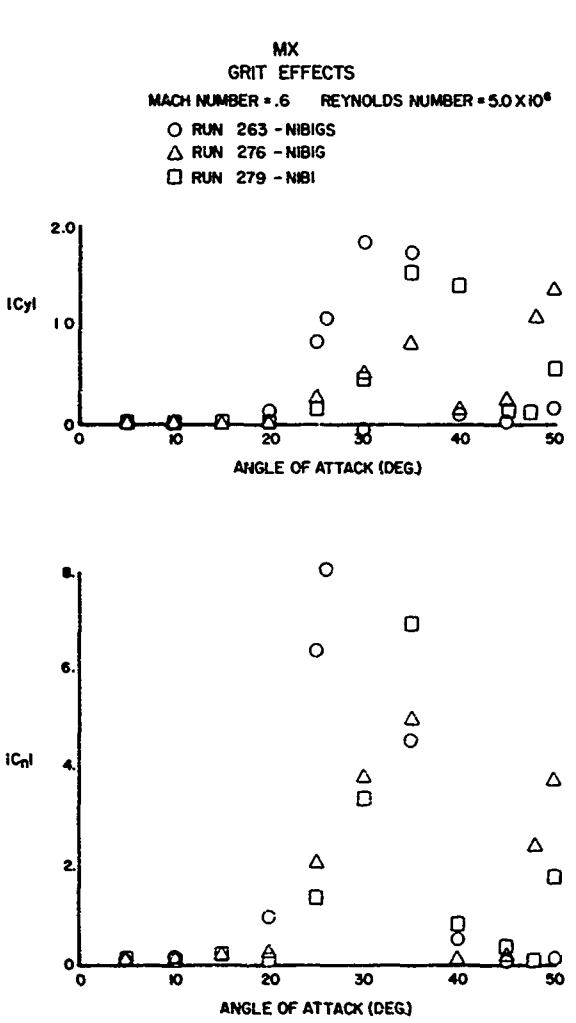

b. M = 0.6

Figure 67 (Continued)

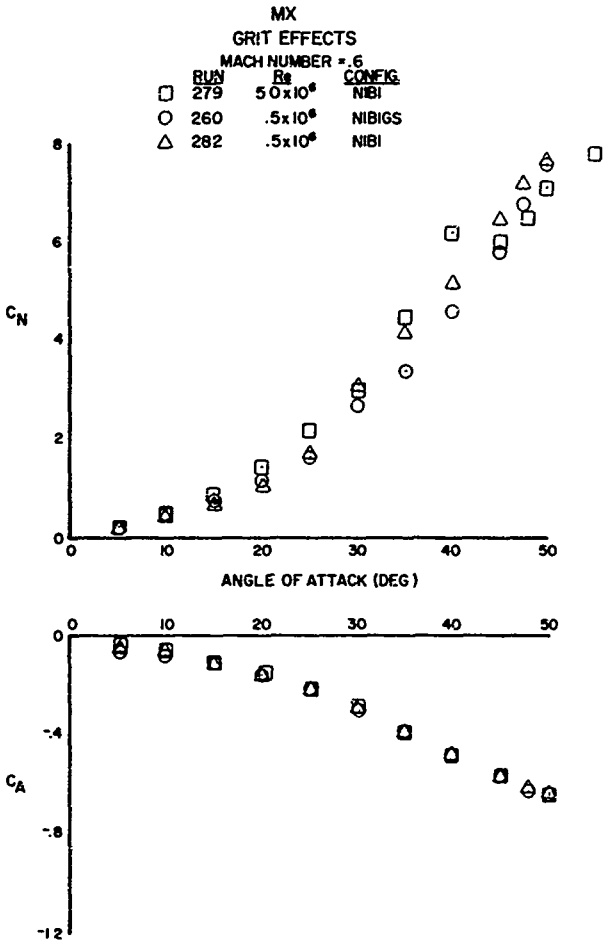

a. Normal and Axial Force Coefficients

Figure 68. Effect of Grit with Reynolds Number Variation on Force Moment Coefficients

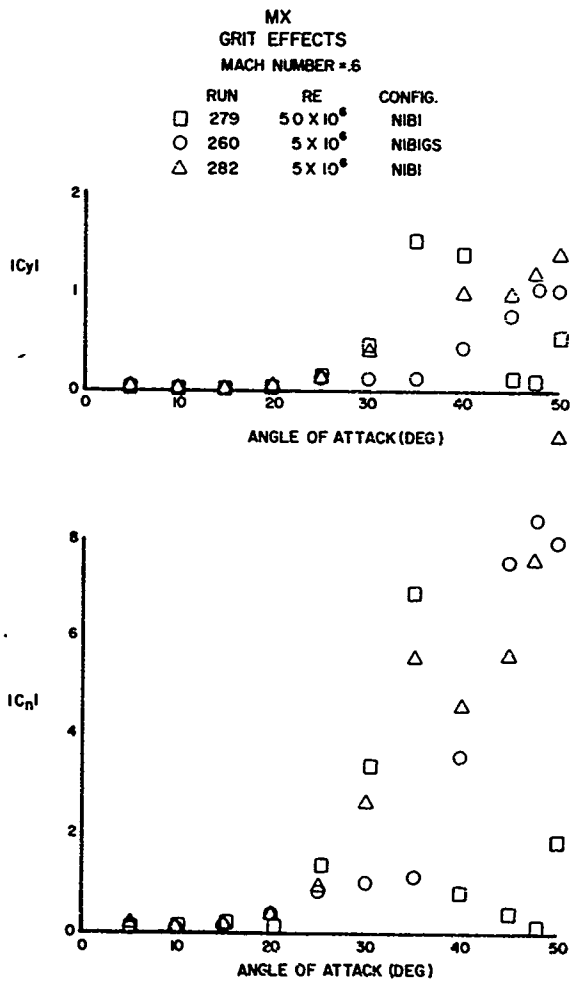

b. Side Force and Yawing Moment Coefficients

Figure 68 (Concluded)

on a balance designed for very large loads. The large Reynolds number effects discussed in another section indicates that the wind tunnel testing should be done at the highest possible Reynolds number and that grit, at least of this size and patterns, will not improve Reynolds number simulation. Leland Jorgensen (Reference 22) also conducted tests with a ring of glass spheres about the nose. These tests also show negligible effects of small-type grit on aerodynamics at high Reynolds numbers.

9. STRUT/STING EFFECTS

The use of a large model with resulting large aerodynamic loads imposed large bending loads on the knuckle joint of the support system. The strut was swept forward to reduce the bending loads but this increased strut support interference, causing some compromise of the very high angle-of-attack data.

Plotted data show sizeable offsets between strut angle-of-attack range sectors as well as between sting-to-strut data. Figures 69 and 70 show the N3B2 force and moment data for angles-of-attack of from 0 to 180 degrees at M = 0.4 and 0.6 respectively. Obvious mismatches are shown, particularly at 45- and 90-degree overlap points. These data results are typical of other plotted results. The low Mach number dip in normal force coefficient at about 70 degrees angle-of-attack (shown in Figure 69(a)) occurred in both integrated pressure and force plotted data.

Figure 71 shows integrated pressure data and force data for the N3B2 configuration at Mach number 0.6 for the 5- to 80-degree angle-of-attack range. Again some mismatch is apparent. The same types of data are shown in Figures 72 and 73 for the N2B1 configuration at Mach numbers 0.4 and 0.6. The normal force coefficient overlap agreement is better, but the side force coefficients are quite different. It is difficult to determine which differences are due to sting or strut and which are due to the unpredictability of the asymmetric forces, since they are functions of many variables, e.g., roughness, model asymmetries, Mach number, angle-of-attack and roll angle.

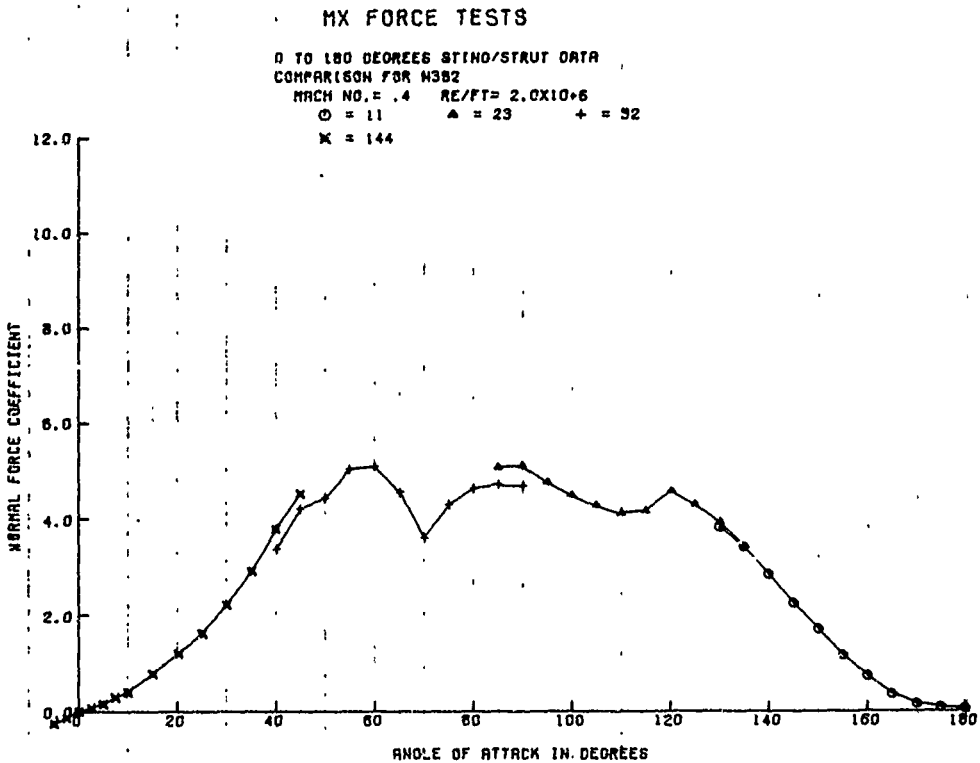

a. Normal Force Coefficient

Figure 69. Comparisons Between Strut and Sting Force and Moment Coefficients at Mach 0.4

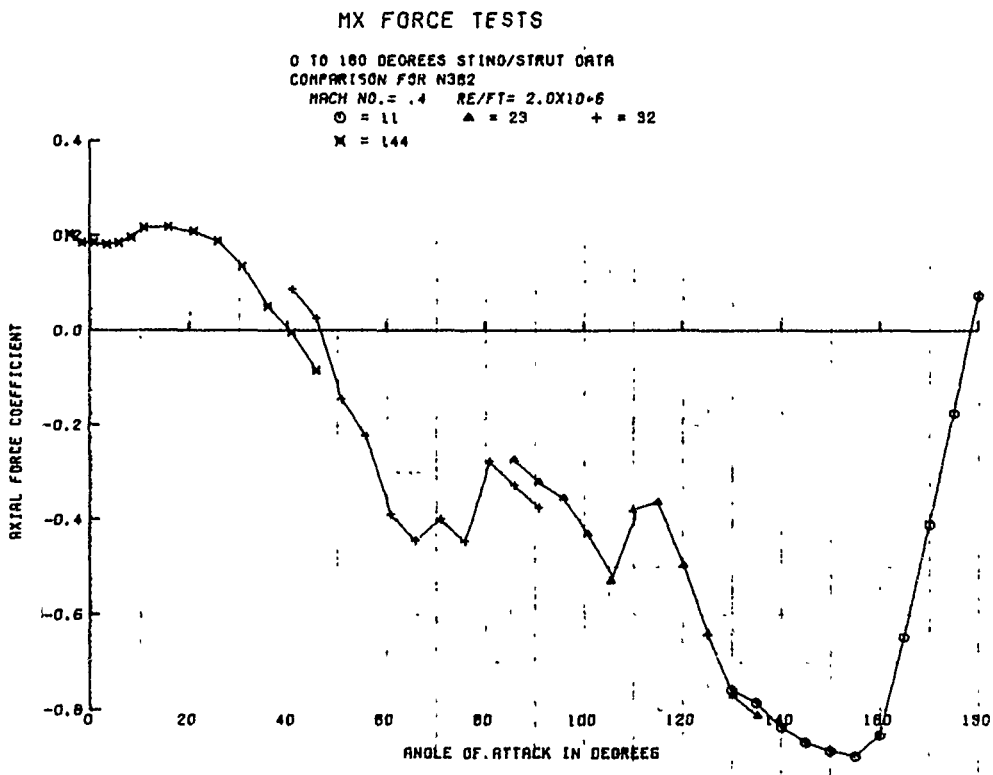

b. Axial Force Coefficient

Figure 69 (Continued)

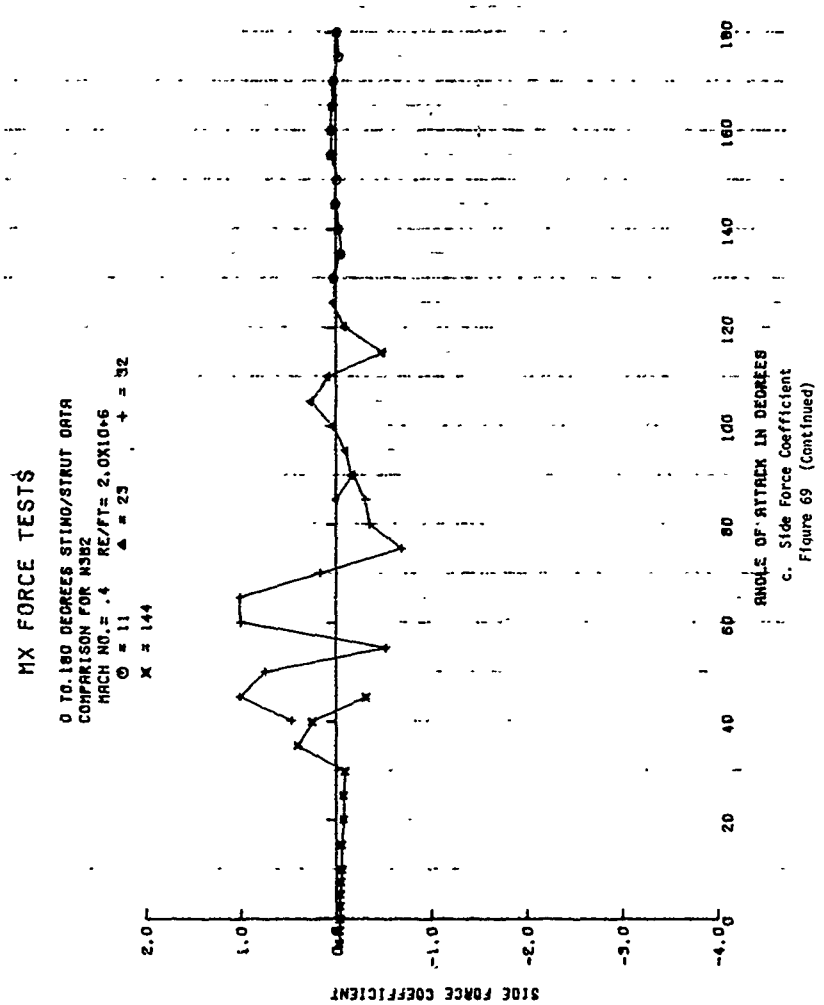

c. Side Force Coefficient
Figure 69 (Continued)

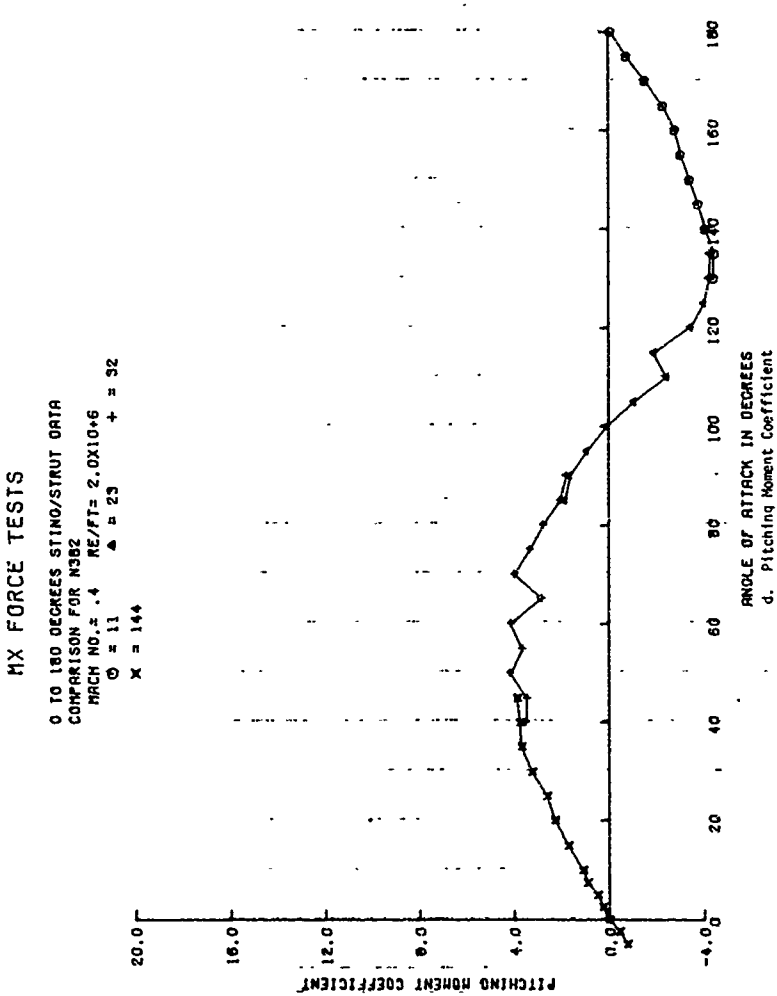

d. Pitching Moment Coefficient
Figure 69 (Continued)

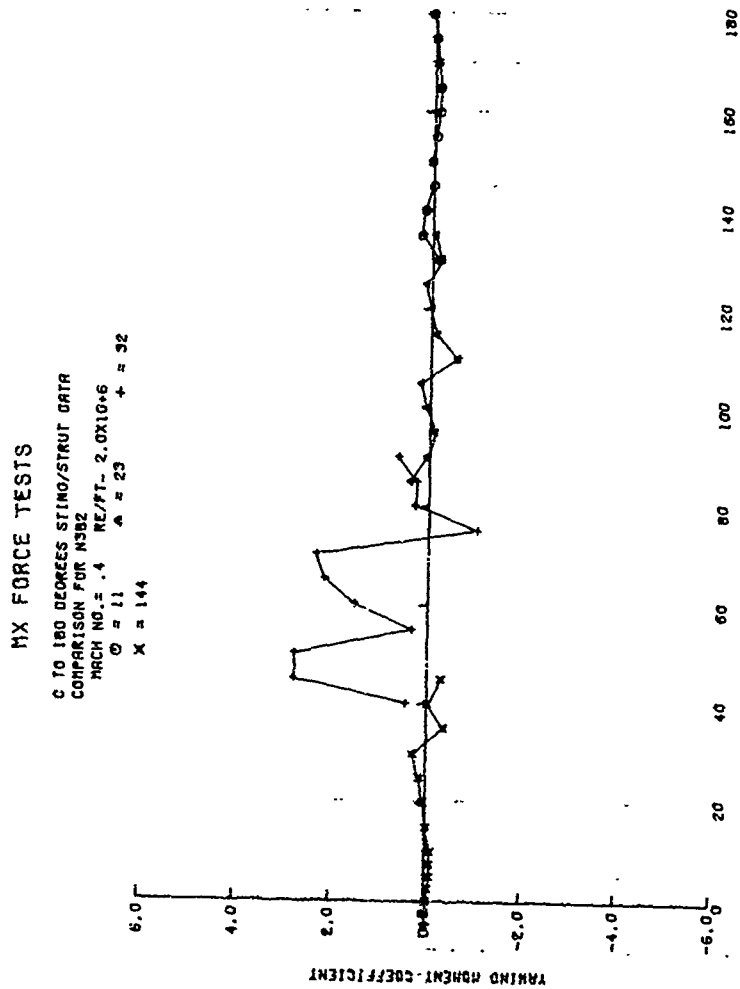

c. Yawing Moment Coefficient
Figure 69 (Concluded)

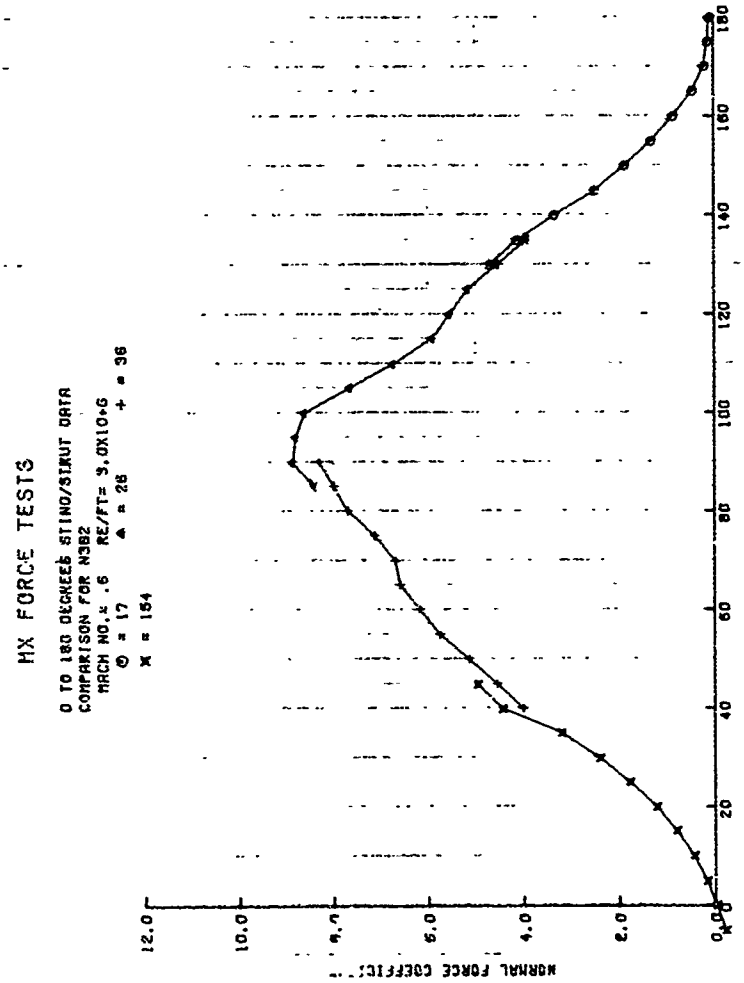

a. Normal Force Coefficient

Figure 70. Comparisons Between Strut and Sting Force and Moment Coefficients at Mach 0.6

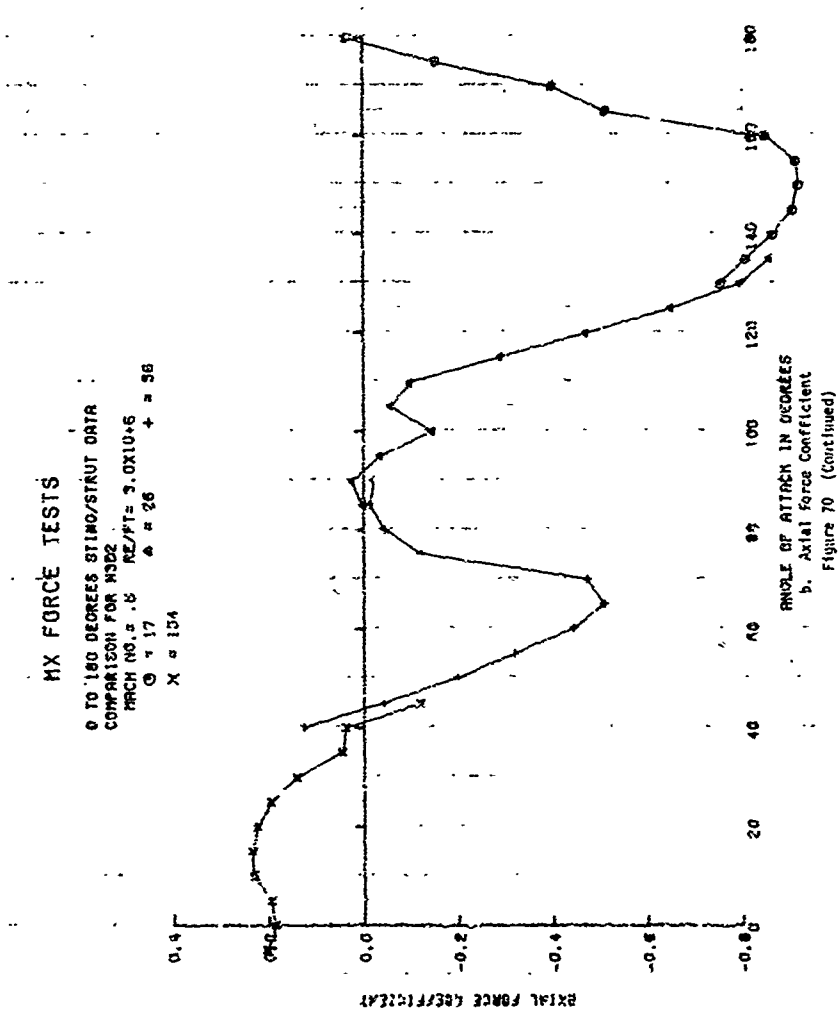

b. Axial Force Coefficient
Figure 70 (Continued)

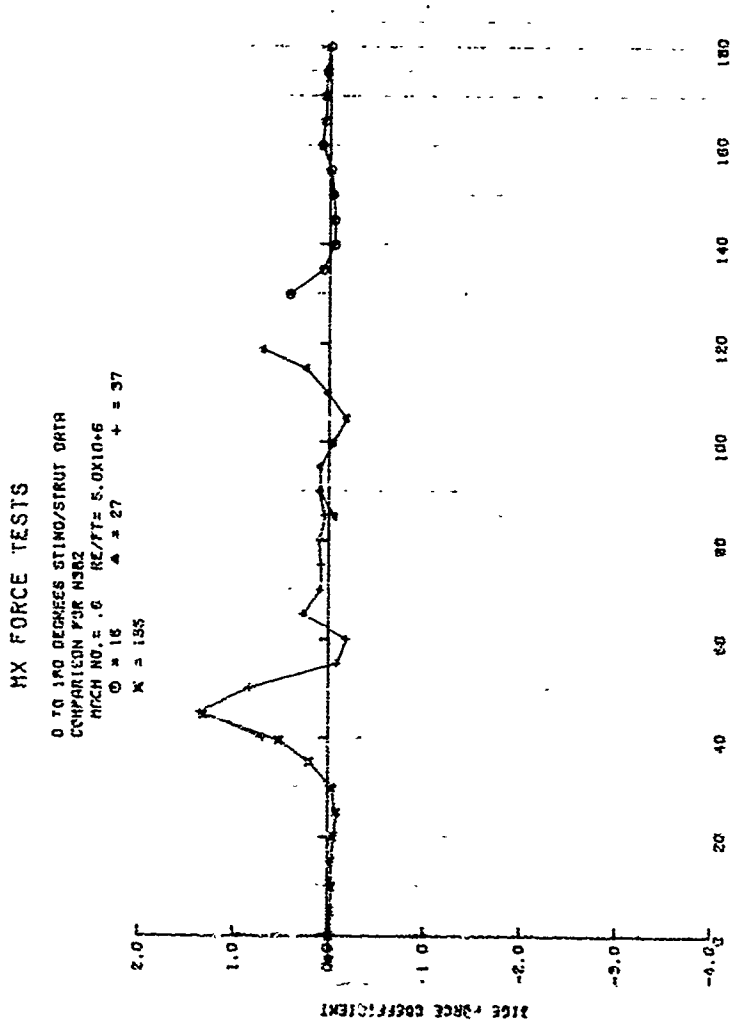

c. Side Force Coefficient
Figure 70 (Continued)

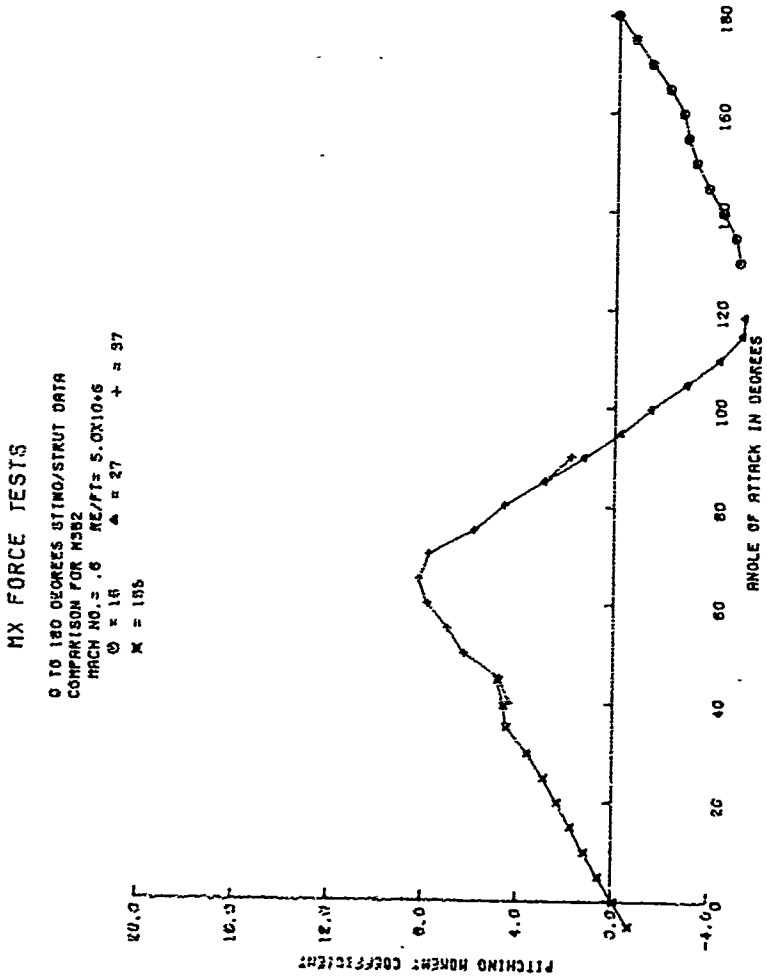

d. Pitching Moment Coefficient
Figure 70 (Continued)

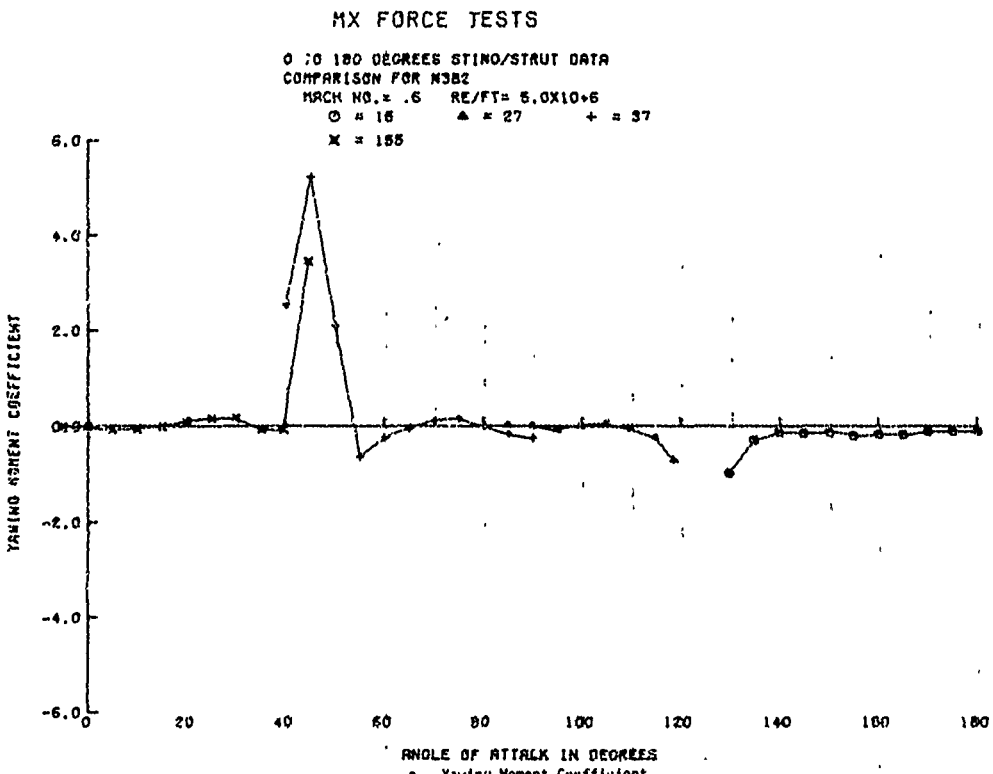

e. Yawing Moment Coefficient

Figure 70 (Concluded)

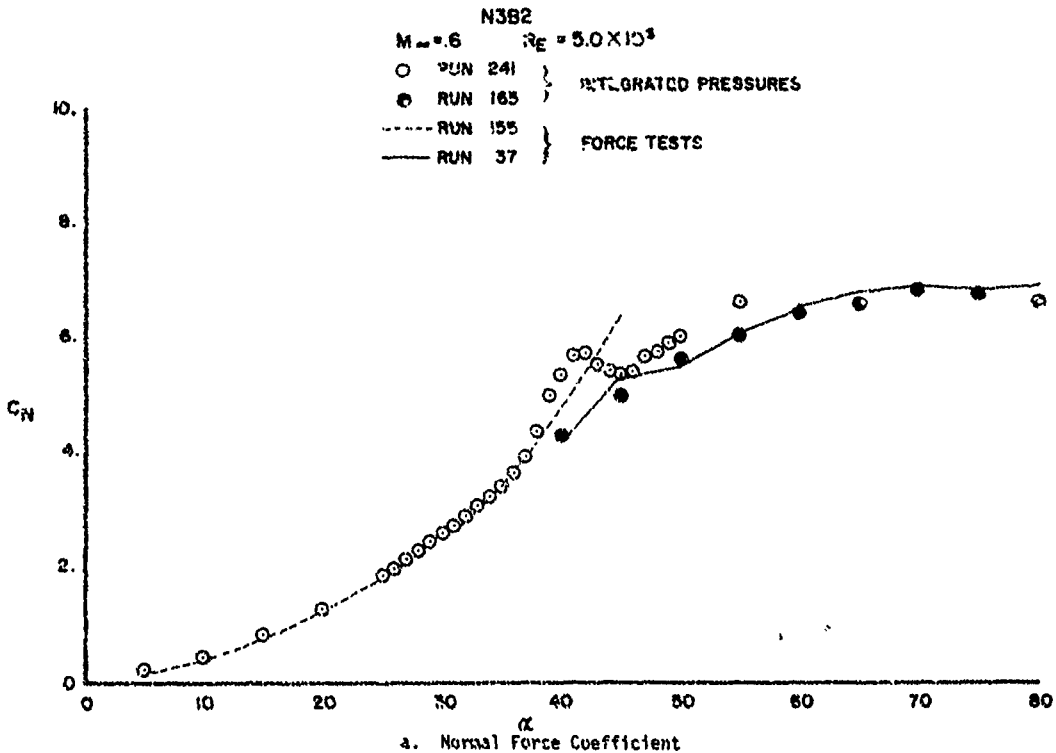

a. Normal Force Coefficient

Figure 71. Comparisons Between the Integrated Pressure Data and Balance Data at Mach 0.6/N382 Configuration

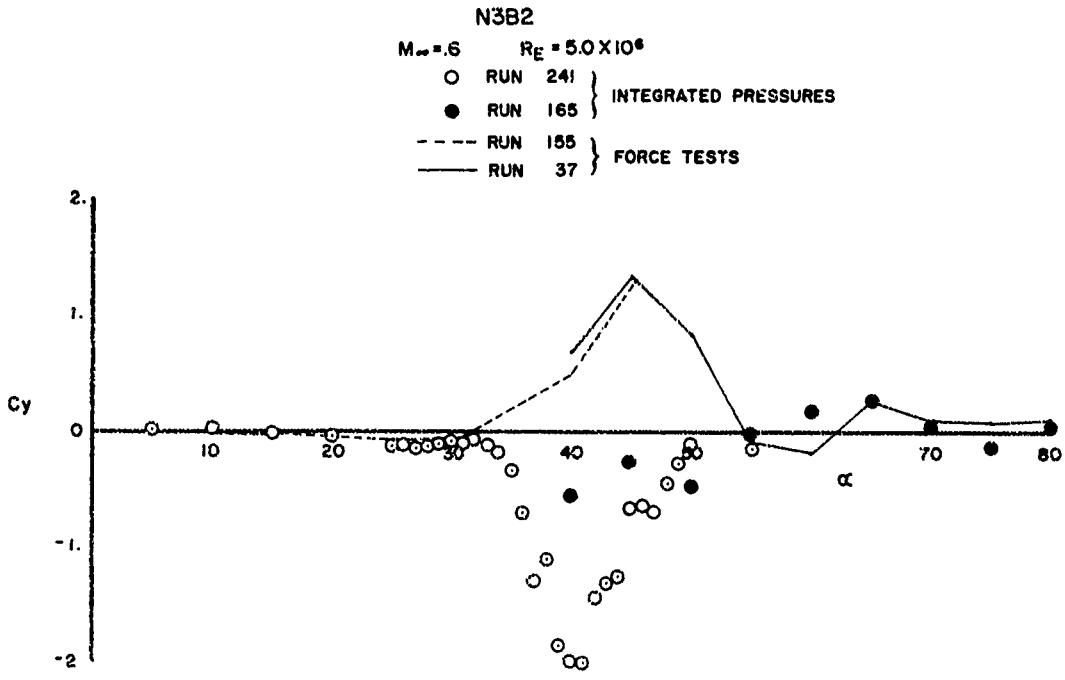

b. Side Force Coefficient
Figure 71 (Continued)

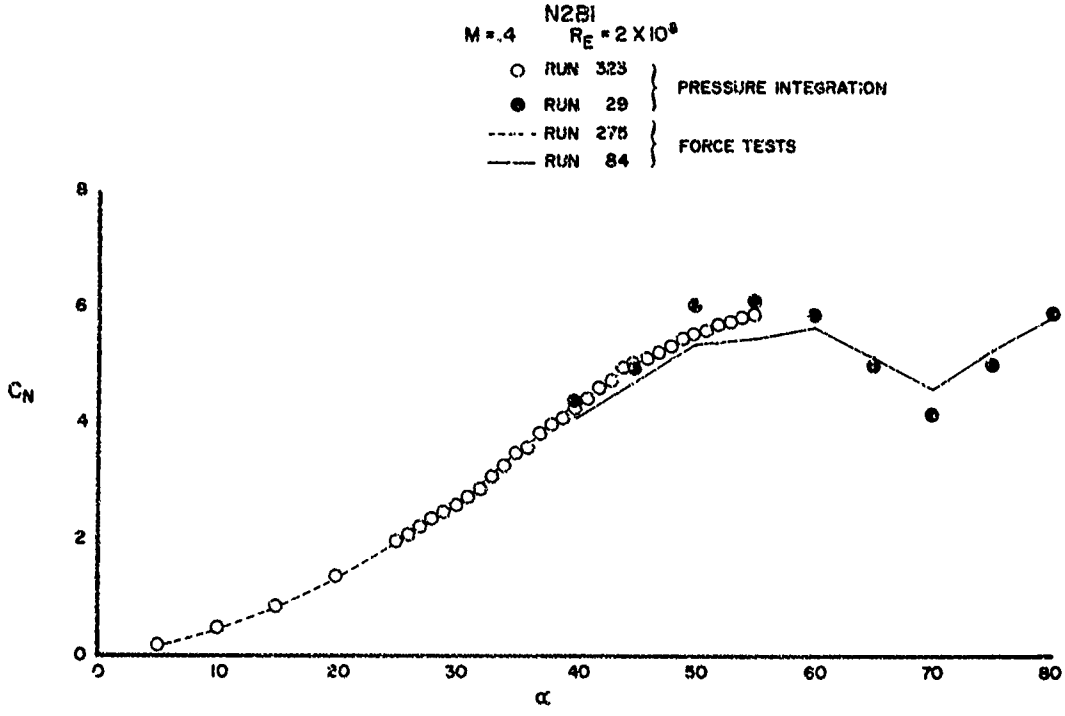

a. M = 0.4

Figure 72. Comparisons Between Integrated Pressure and Balance Normal Force Coefficient/N2B1 Configuration

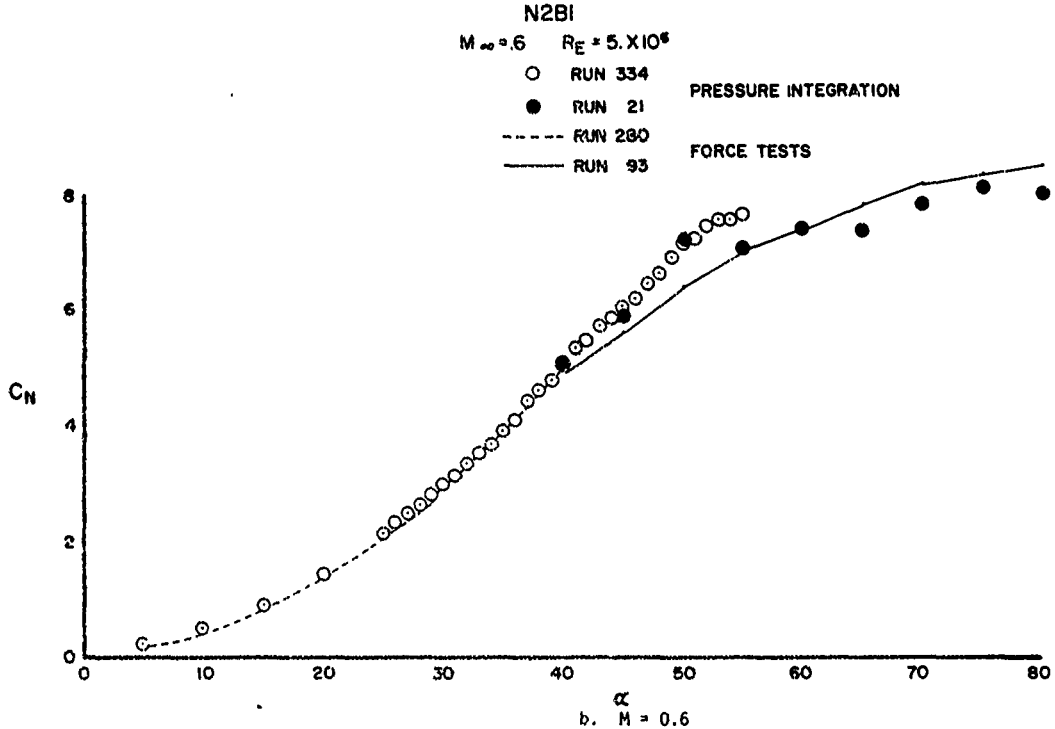

b. M = 0.6

Figure 72 (Concluded)

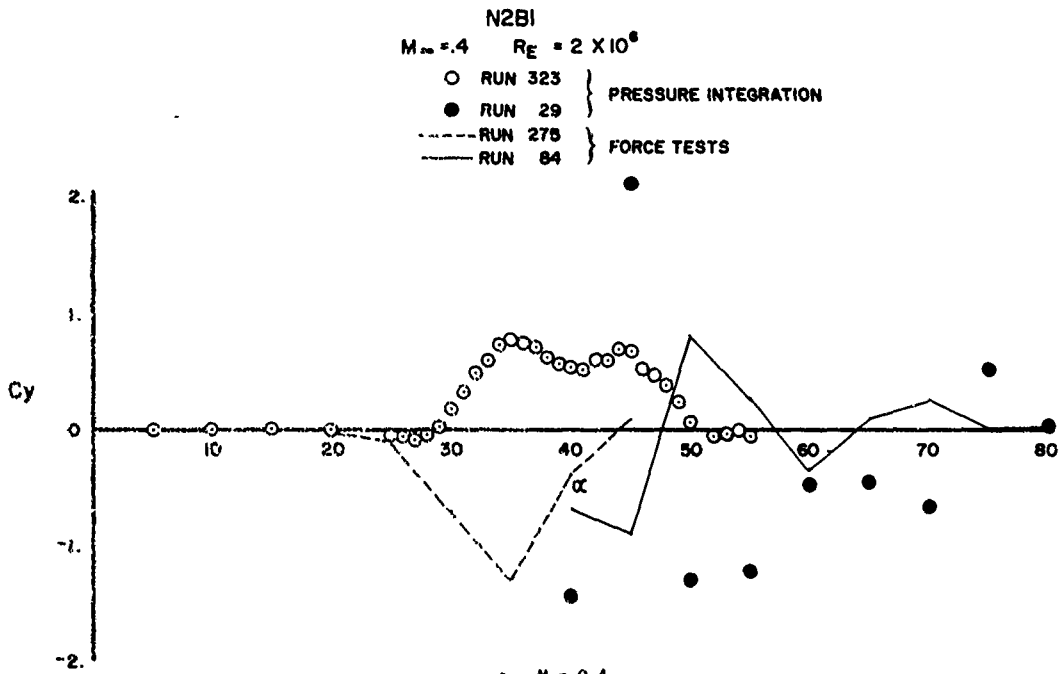

z. M = 0.4

Figure 73. Comparison Between Integrated Pressure and Balance Side Force Coefficient/N2B1 Configuration

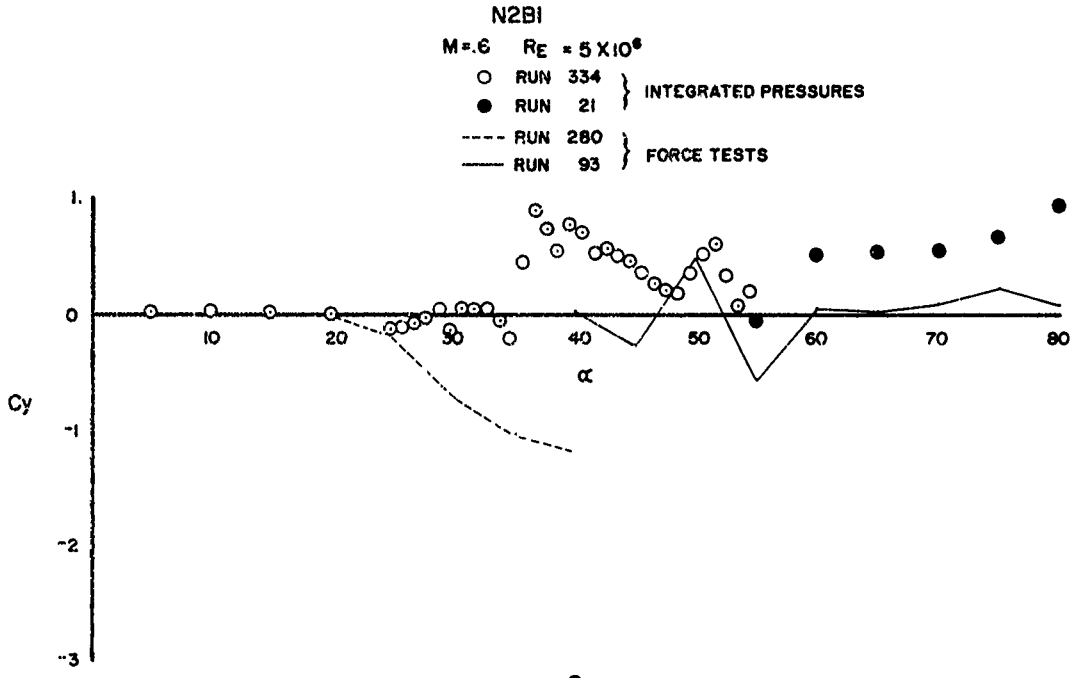

b. M = 0.6

Figure 73 (Concluded)

Figure 74 shows the percentage difference in normal force coefficient at angles-of-attack of 40 and 45 degrees between the sting- and strut-mounted N3B2 configuration. The difference is seen to decrease with increasing Mach number.

10. ROCKET EXHAUST EFFECTS

Simulation of exhaust in these wind tunnel tests is based on using high-pressure room temperature air with the scaling of several matching parameters. For the MX test program the primary objective was to obtain as high a Reynolds number as possible, which meant testing as large a model as feasible. The model scale selected, combined with the MX rocket characteristics, prevented full simulation of the desired parameters, i.e. momentum flux ($PeVe^2Ae/P_\infty V_\infty^2 A_c$) and the ratio of exit static pressure to freestream static pressure. Calculations of the free-flight values of these parameters were based on engine specifications and system performances analysis data provided by SAMSO/TRW. A flight Mach number of 0.74 at 29,600-foot altitude for the MX = 3/80 missile was used to calculate freestream free-flight conditions. An exit Mach number of 3.0 was selected for model scaling as compared to a full-scale exit Mach number of 4.38. Even though the maximum weight flow, 40 #/sec, available for tests in the PWT 16T facility and geometric scaling of the exit area was used, neither of the desired parameters could be matched without a tremendous increase in weight flow rates (Figure 75). Even with the mismatch between parameters it was felt that the simulation would still give some indications of the effects of the plume on the MX missile and was obviously better than no simulation at all. Data from the Air Slew Missile tests with jet "on" and "off" showed large jet effects at high angles-of-attack ($\alpha > 45$) but also showed that P_{t_c} values of 1/2 matching conditions gave about the same increments in forces.

It was originally planned that Jet-on testing for angles-of-attack greater than 45 degrees would be conducted during both pressure test entries and a force data entry. During the early runs of the first pressure entry, severe model dynamics were encountered at Mach number 0.6 and a Reynolds number of 5.6×10^6, resulting in reduced Reynolds number

MX
STING/STRUT MISMATCH WITH INCREASING MACH NUMBER
N3B2

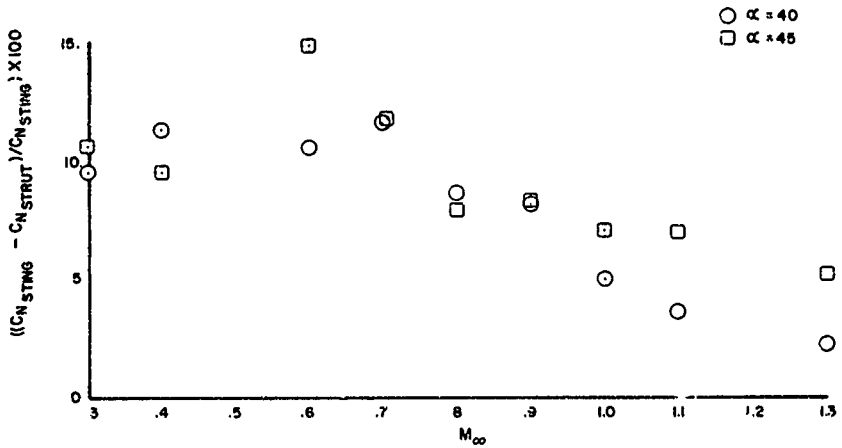

Figure 74. Percentage Difference Between Sting and Strut Normal Force Coefficient for the N3B2 Configuration vs Mach Number

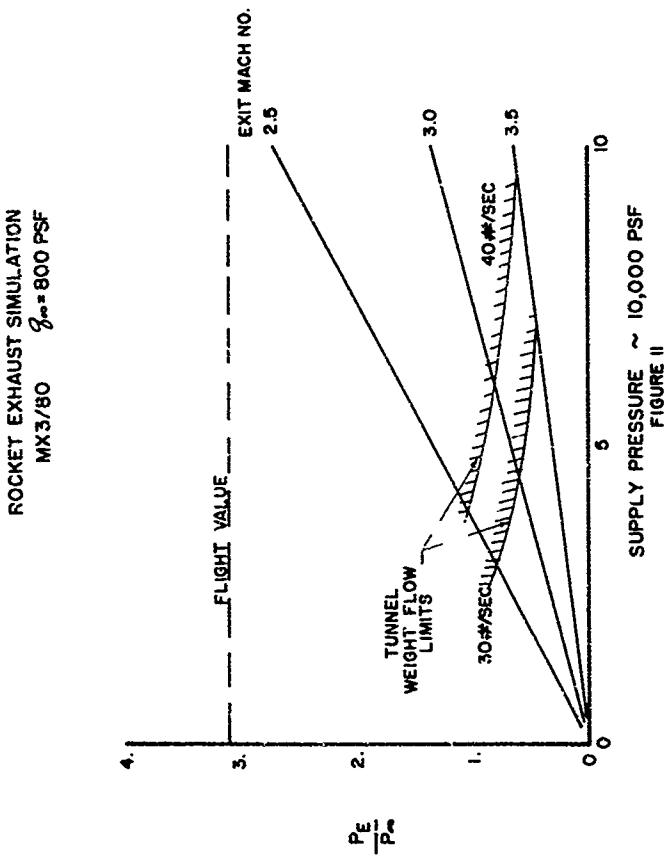

FIGURE 11

a. Exit Pressure Ratio

Figure 75. Comparison Between Simulated and Flight Nozzle Parameters

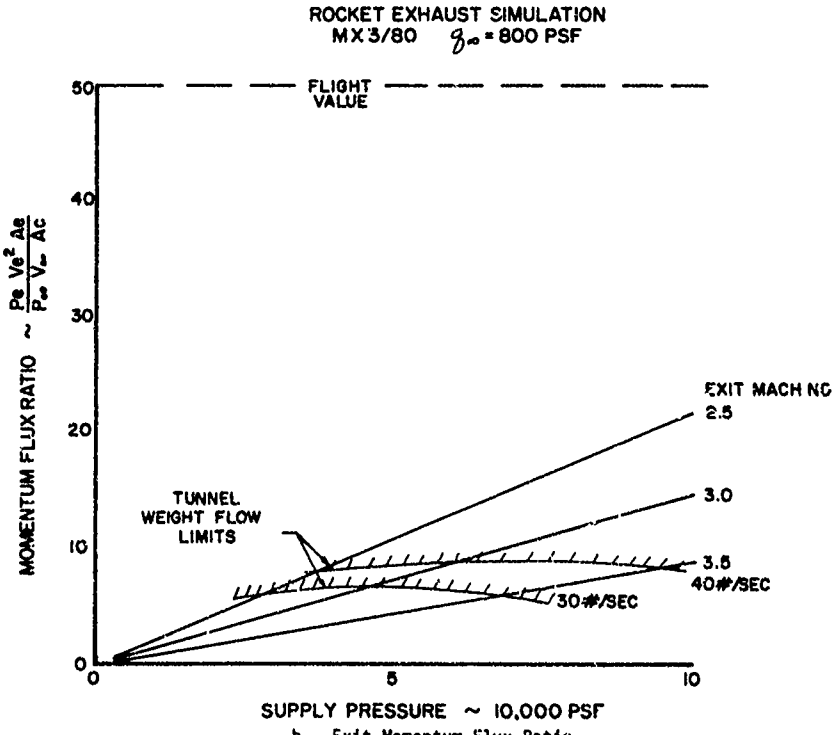

b. Exit Momentum Flux Ratio
Figure 75 (Concluded)

testing for later entries. After the first entry was completed, cracks were found in the weld joints in the leading and trailing edges of the strut high-pressure air plenum. The jet-on data for the first entry is, therefore, questionable due to what may have been considerable leakage of high pressure air from the strut. The strut could not be properly repaired in time for the subsequent force testing, thus no jet-on force data was obtained. After the force data testing, the model strut was electron-beam welded and successfully used in the second pressure entry in testing of the N3B2 (MX 3/15C) model.

Figure 76 shows the pressure distribution about the N3B2 configuration at 90-degree angles-of-attack and Mach number 0.6, starting at the most aft station forward to station 23.58 for jet-off, jet-on, and jet-on deflected 15 degrees. The positive pressure is only affected at the most rearward station; whereas the negative pressure coefficients are still effected at X = 23.58. The deflected jet-on added only a small effect to the non-deflected jet-on pressure increment. The jet-on increased the negative pressures at all of the stations shown.

Figures 77 and 78 show the integrated pressure data of N3B2 at Mach numbers 0.6 and 0.8, respectively, for jet-off, jet-on and deflected jet-on for angles-of-attack of from 40 to 90 degrees. For angles-of-attack above 60 degrees the effects of the rocket exhaust plume on missile aerodynamics become increasingly important. The impact of what was shown in the pressure coefficient plots is reflected in the integrated forces, i.e., increasingly negative pressure coefficients as proximity to nozzle increases, gives a normal force coefficient increment (ΔC_N) which increases and a pitching moment coefficient increment (ΔC_m) increasingly negative as angle-of-attack increased. The deflected nozzle integrated data show only a small additional increment in C_N and C_m. Note that the pressure data was integrated using the nose (X = 0) station as the moment reference center.

Figure 79 shows the integrated pressure normal force coefficient for the N2B1 configuration from the first pressure entry. The increments are about the same as N3B2 with Jet-on, which indicates that the strut leaks were either small or had little influence on the pressure measurements.

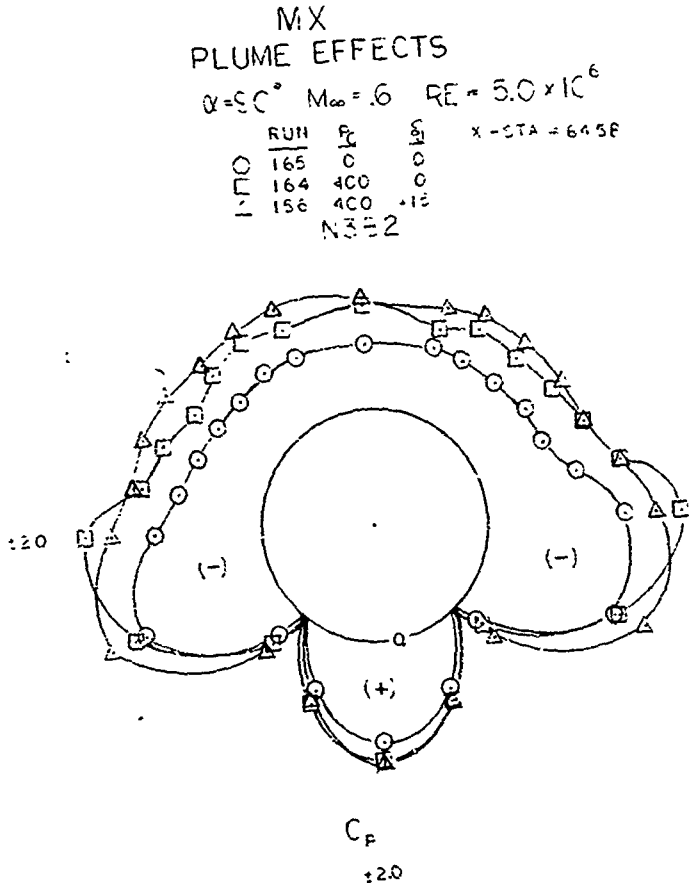

a. X = 64.58

Figure 76. Effect of Jet Plume on Local Pressure Coefficient Distribution

MX
PLUME EFFECTS
$\alpha = 90^\circ$ $M_\infty = .6$ $RE = 5.0 \times 10^6$

	RUN	P_c	δ_j
○	165	0	0
□	164	400	0
△	156	400	+15

X_STA. = 53.58

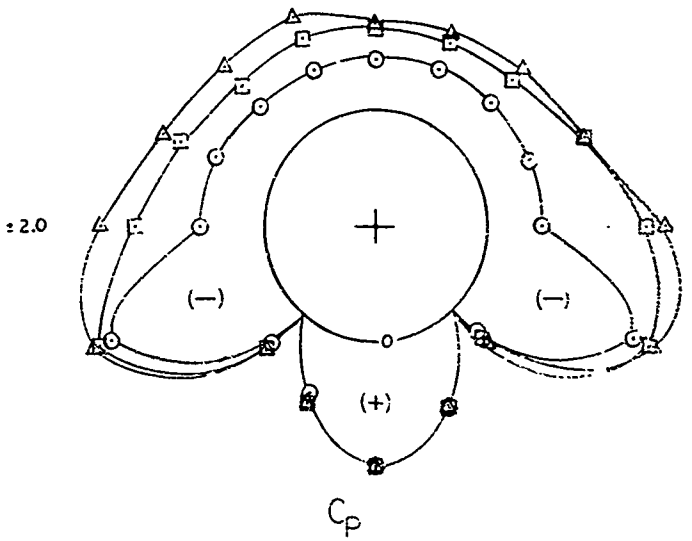

b. X = 53.58

Figure 67 (Concluded)

MX
PLUME EFFECTS
$\alpha = 90^\circ$ $M_\infty = .6$ $RE = 5.0 \times 10^6$

	RUN	F_C	δ_J
○	185	0	0
□	164	400	0
△	156	400	+15

X-STA = 43.58

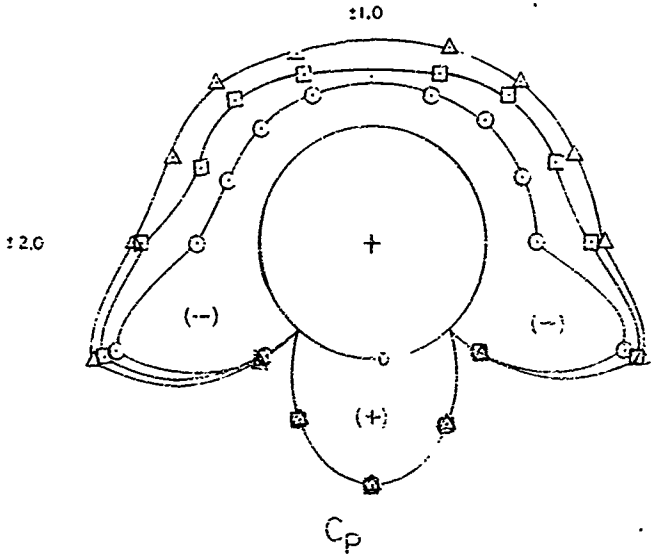

c. X = 43.58

Figure 76 (Continued)

MX
PLUME EFFECTS
$\alpha = 90^\circ$ $M_\infty = .6$ $RE = 5.0 \times 10^6$

	RUN	P_c	δ_j
○	165	0	0
□	164	400	0
△	156	400	+15

X-STA = 33.58

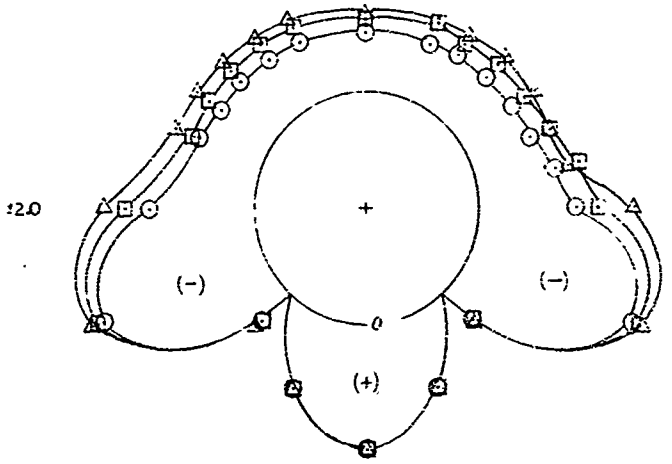

C_P

±2.0

d. X = 33.58

Figure 76 (Continued)

MX
PLUME EFFECTS
$\alpha = 90^0$ $M_\infty = .6$ $RE = 5.0 \times 10^6$

RUN	P_c	δ_j
165	0	0
164	400	0
156	400	+15

X-STA = 23.58

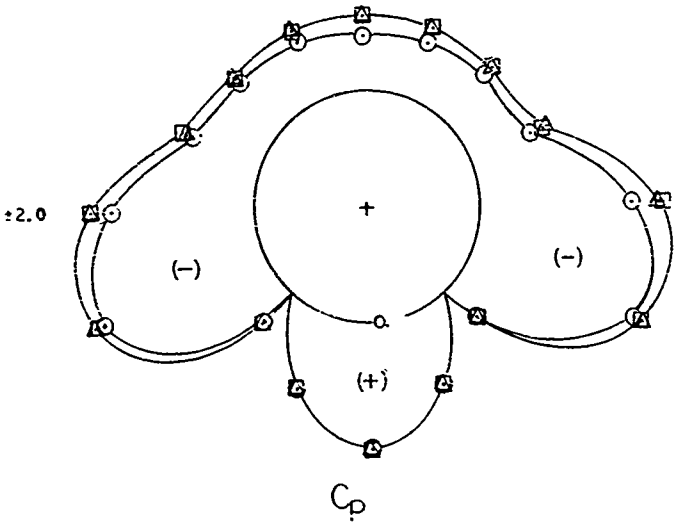

e. X = 23.58

Figure 76 (Continued)

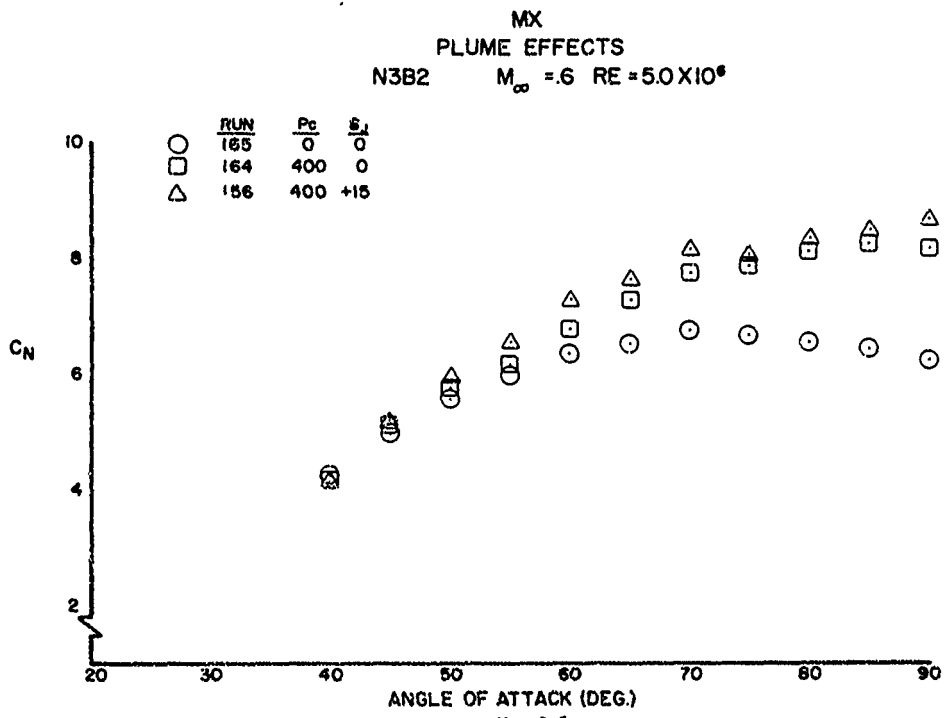

a. M = 0.6

Figure 77. Effect of Jet Plume on the Normal Force Coefficient

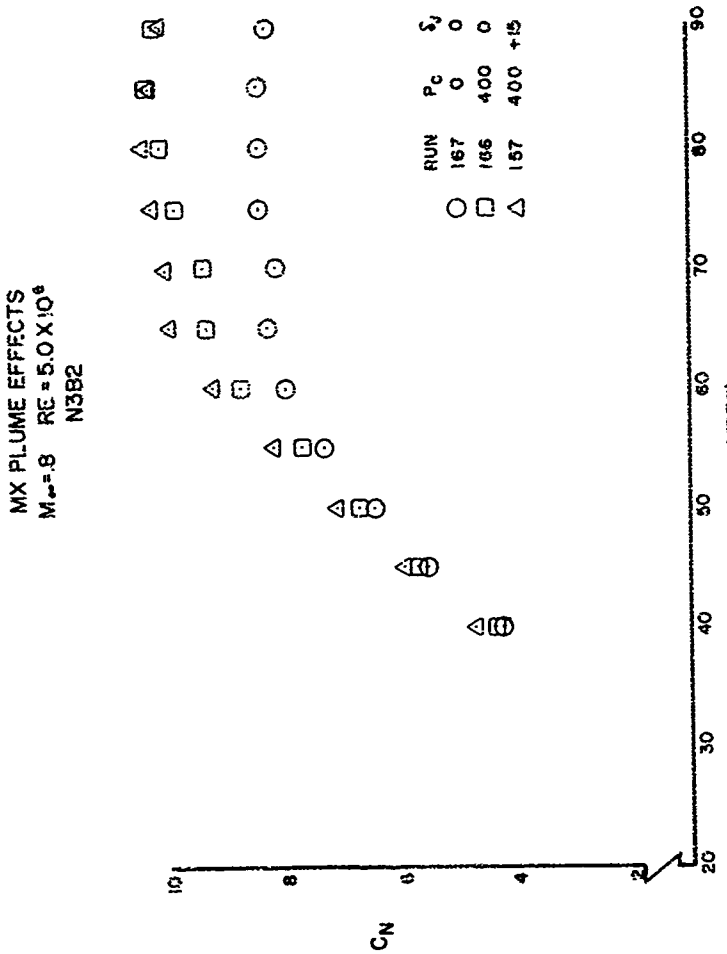

b. M = 0.8

Figure 77 (Concluded)

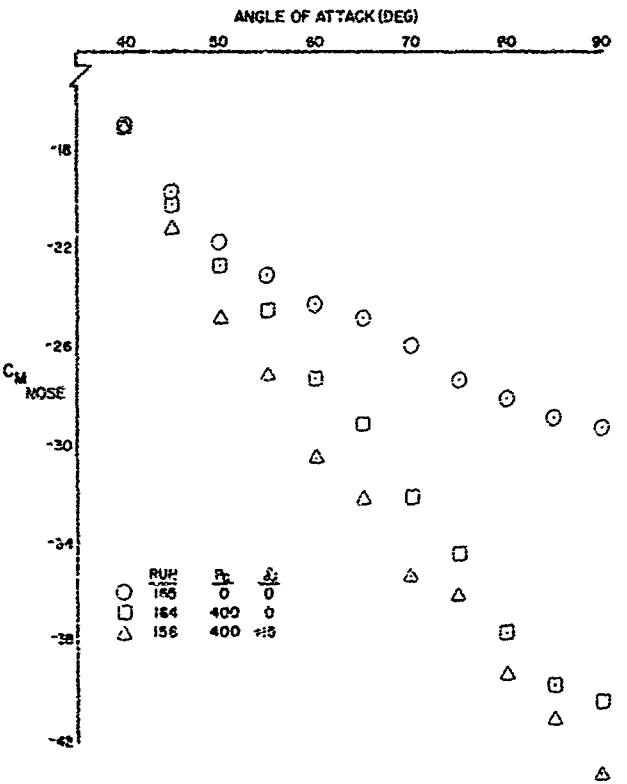

a. M = 0.6

Figure 78. Effect of Jet Plume on Pitching Moment Coefficient

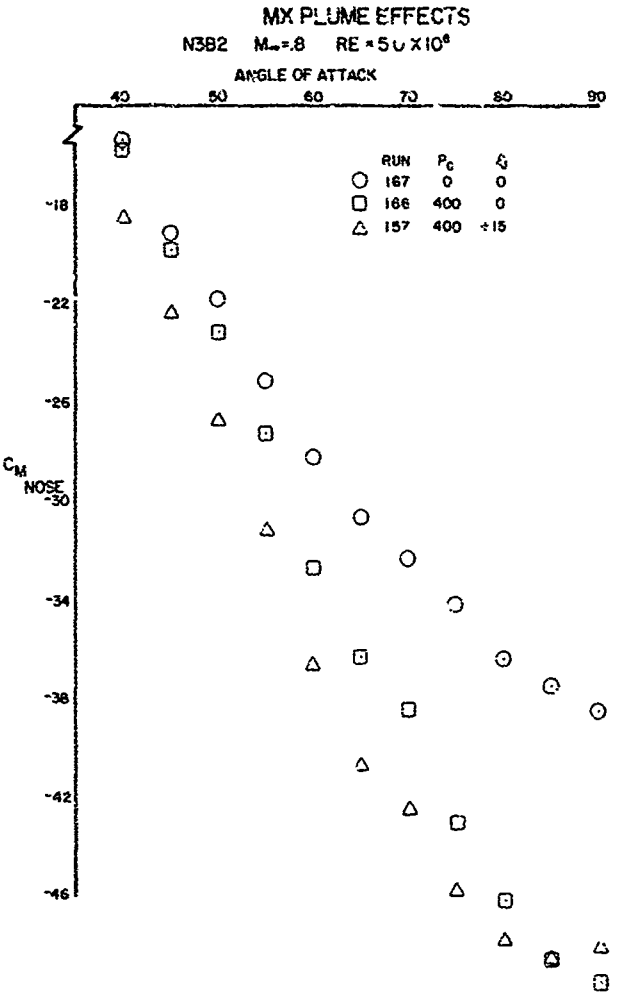

b. M = 0.8

Figure 78 (Concluded)

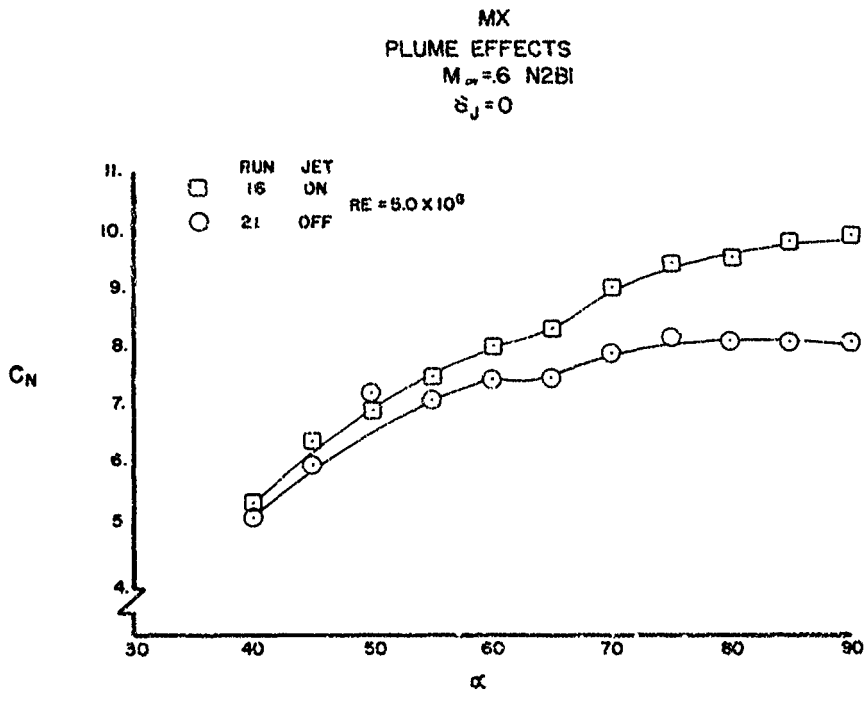

Figure 79. Integrated Pressure Results Showing Jet Plume Effects on Normal Force Coefficient at M = 0.6

Reynolds number effect on jet-on integrated coefficients were similar to jet-off at lower angles-of-attack; but in the 130- to 180-degree angle-of-attack range, the increments in coefficients for the jet-on were much less than for jet-off, indicating that the plume is one of the dominating factors for very high angles-of-attack aerodynamics.

SECTION V

EXPERIMENTAL FLOW FIELD RESULTS

To gain additional insight into the data characteristics from SECTION IV, attention was focused on the N2Bi configuration previously described. For this configuration the experimental test results from References 43 through 45 were supplemented with experimental wake flow data obtained in the 16T wind tunnel at AEDC. The data are representative of flight conditions where the maximum out-of-plane (side) forces were observed to occur.

In the following paragraphs the crossflow velocity data will be shown for all of the test conditions. A limited analysis of the data will be made for the Mach 0.4 data at alpha 40 and 45 degrees. No analysis was made for the Mach 0.6 data however because of its unsteady nature. In a later section a more detailed analysis is made using presently available analytical procedures. In the more detailed analysis, however, only the Mach 0.4 data at 45 degrees alpha were used because it is representative of maximum side force conditions. Experimental results from other references were used to aid the analysis.

1. CROSS FLOW VELOCITY

The velocity field in the body axis system may be written

$$U = U_\infty \cos \alpha + u$$

$$V = v$$

$$W = U_\infty \sin \alpha + w \qquad (4)$$

where U_∞ is the freestream velocity and u, v and w are the induced or "perturbation" velocity components. In the present test, the 9-cone probe rake was positioned parallel to the tunnel centerline and the missile was pitched to angle-of-attack. Thus the rake measured the perturbation components. Figures 80 through 82 show the crossflow

"perturbation" velocity component measurements in the crossflow plane and have been nondimensionalized by the freestream velocity, i.e.

$$\vec{V} = \frac{u}{U_\infty}\vec{j} + \frac{w}{U_\infty}\vec{k} \qquad (5)$$

Note also, that the Z/D = 0.5 location for the velocity plots corresponds to the top of the model surface. For the Mach 0.4 data at 45-degree angle-of-attack (Figure 80) the only discernible vortex center is the one at X/D = 7.4 appearing on the left (looking upstream from the rear of the model) at about 1.5 diameters above the model centerline. The absence of distinct vortex centers near the model nose (X/D = 3.78) is probably a result of not obtaining data close to the model surface (due to time limitations for the test). This conclusion is also supported for example in References 15, 46, and 47 which indicate that near the nose body juncture the vortices lie very close to the model surface. The lack of distinct vortex cores in the remaining data at Mach 0.4 and 45-degree angle-of-attack indicates the presence of a shear layer, which results in diffused velocity distributions with no clearly defined vortex centers evident.

As previously mentioned, the selected roll angle at 40-degree angle-of-attack at Mach 0.4 and 0.6 did not result in maximum side force loads. It is instructive, however, to observe the data at these conditions. The velocity vectors at X/D = 7.4 indicate the presence of nearly two symmetrical vortex cores. At Mach 0.4 and 40-degree angle-of-attack, the vortex center on the left at station X/D = 7.4 lies approximately 1.1 diameters above the model centerline, and the vortex center on the right is at 0.8 diameters above the model centerline. At Mach 0.6, two symmetrical vortices appear at approximately 1.1 diameters above the model centerline.

The absence of data in the center regions of flow field (i.e. in the neighborhood of the X/D = 0 axis) is the result of the total flow angularity exceeding the probe calibration limits. This unfortunate loss of

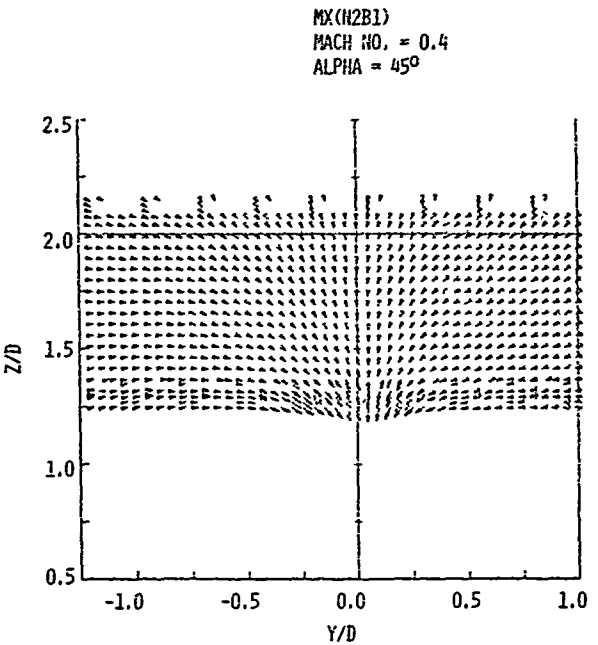

a. X/D = 3.78

Figure 80. Experimental Crossflow Perturbation Velocities at Mach 0.4 and 45-Degree Angle-of-Attack

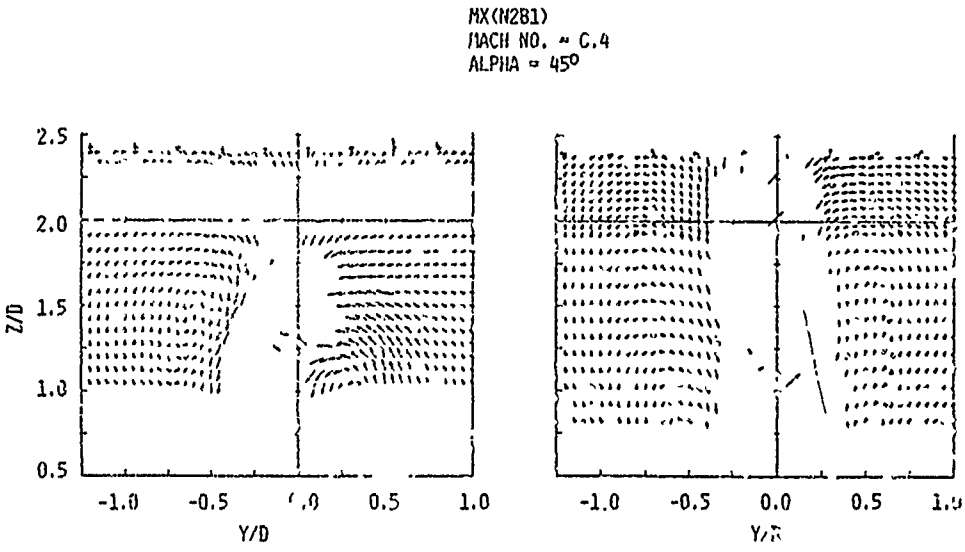

b. X/D = 7.4

c. X/D = 8.8

Figure 80 (Concluded)

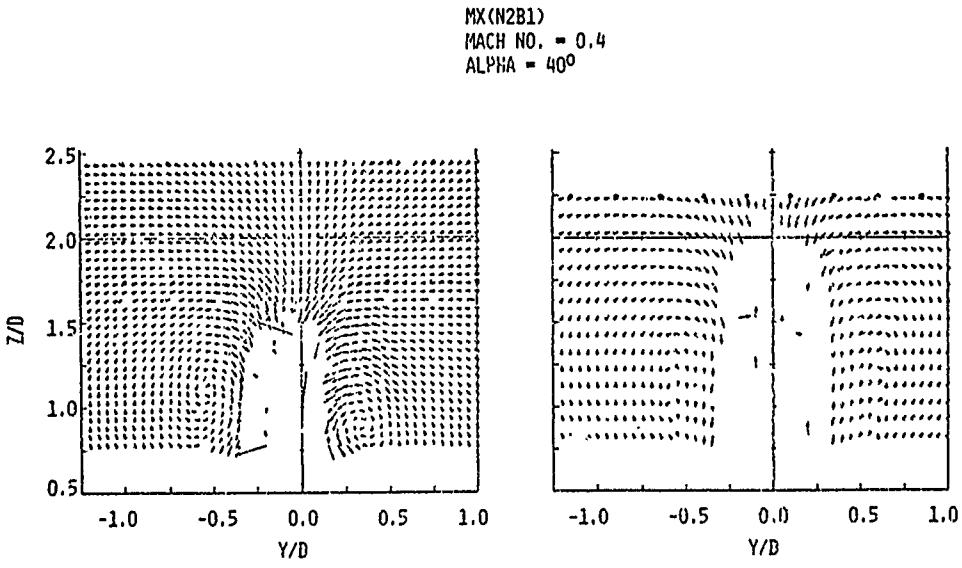

a. X/D = 7.4

b. X/D = 8.8

Figure 81. Experimental Crossflow Perturbation Velocities at Mach 0.4 and 40-Degree Angle-of-Attack

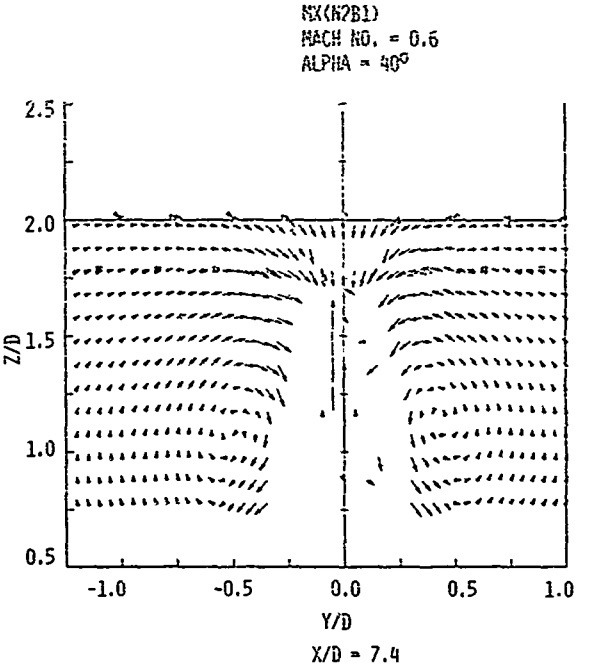

Figure 82. Experimental Crossflow Perturbation Velocities at Mach 0.6 and 40-Degree Angle-of-Attack

data precludes the determination of the vortex strengths from this set of data. Estimates of the vortex shedding locations may be deduced as described in the following paragraphs.

2. SEPARATION LOCATIONS

The data from the present test only provided visible vortex cores at one axial location, X/D = 7.4. To estimate the position where the vortices leave the body (i.e. the separation locations), it becomes necessary to rely on the results of previous experiments as well as engineering judgement. Nearly all experiments where data were obtained very close to the model surface (refer for example to References 15, 46 and 47) indicated that the first vortex shed was near the nose tip. Furthermore, Reference 15 indicates that the asymmetric vortices shed at parallel lines and that the vertical distance between vortices of unlike sign correlate as:

$$z/d = \frac{\tan\xi}{\tan\alpha} \cdot \frac{0.5}{S} \qquad (6)$$

where ξ = Angle between the vortex lines and the body axis, and S = Strouhal number.

References 15, 46 and 47 show that the Strouhal number is a function of crossflow Mach number and, for the present test condition, is approximately 0.2. If it is assumed that the vortex center farthest from the missile centerline at station X/D = 7.4 (the one on the left for the present set of data) is the one shed from the nose tip, then Equation 6 yields the apparent location of successive vortex centers. This cannot be verified from the present set of flowfield data because of the diffused nature of the crossflow velocities downstream of X/D = 7.4. Referring to Figure 83, the circle symbol denoted the measured vortex at station X/D = 7.4 that was clearly visible in the experiment and was assumed to be the one shed from the nose tip. An additional simplification was to assume that vortex centers can be extrapolated back to the

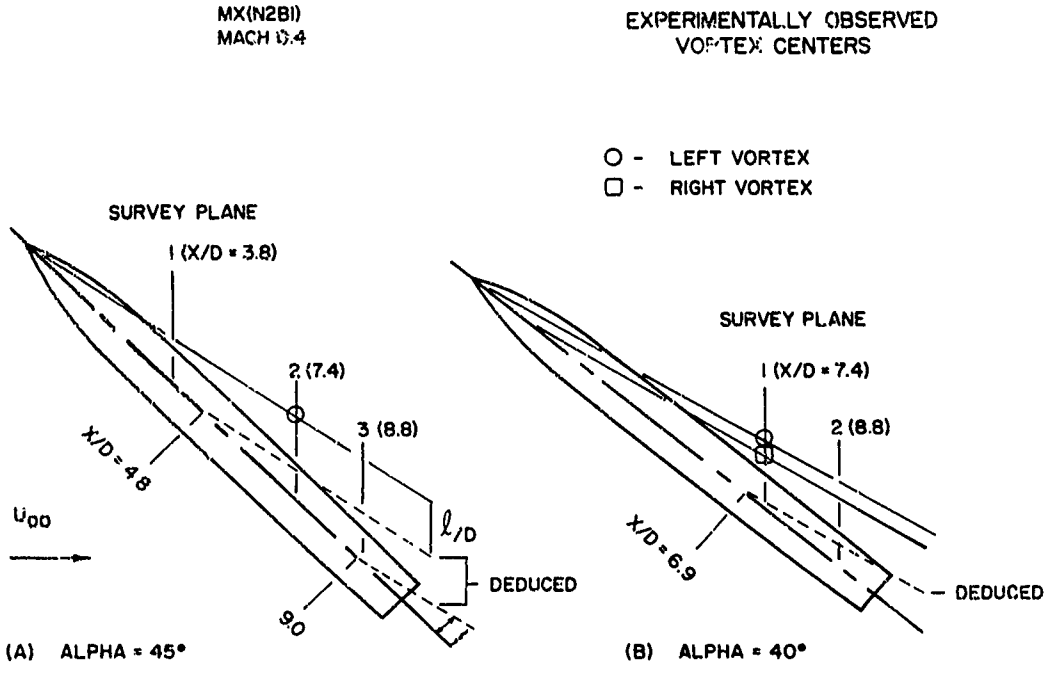

Figure 83. Deduced Vortex Separation Locations

body in a straight-line fashion to locate the apparent separation locations. Thus the deduced location of the vortex on the right was obtained from Equation 6, and the apparent separation location was deduced by extrapolating back to the body along a vortex line parallel to the one originating at the nose tip and connected with the measured vortex core evident in the experiment.

3. SIDE FORCE COEFFICIENT DISTRIBUTION

The local side force coefficient distribution along the missile axis was obtained by integrating the missile surface pressure data. The results are presented in Figure 84. It is of interest to compare the estimated vortex separation locations as determined from the previous section with the local side force coefficient distribution. Note that the sinusoidal peaks in the side force coefficients occur in the vicinity of the estimated vortex separation location. Due to the uncertainty in determining the vortex separation location, no direct correlation with maximum local side force can be firmly established. However, in Section VI of this report a more detailed analysis gave the same result; i.e., the maximum local side force coefficients correspond to the separation location of the shed vortices from the model surface.

4. UNSTEADY WAKE-PRESSURE DATA

A second phase of the test program was to measure the unsteady pressure data in the missile wake near the model surface. This was accomplished with a 9-probe rake of identical dimensions as the one used for the static pressure wake data. Each probe on the rake was instrumented with Kulite transducers. The rake was positioned approximately 0.5 diameters above the missile surface and was traversed parallel to the model centerline in the axial direction The most forward position was limited by the test hardware for a given angle-of-attack, but data were generally obtained at axial locations in the

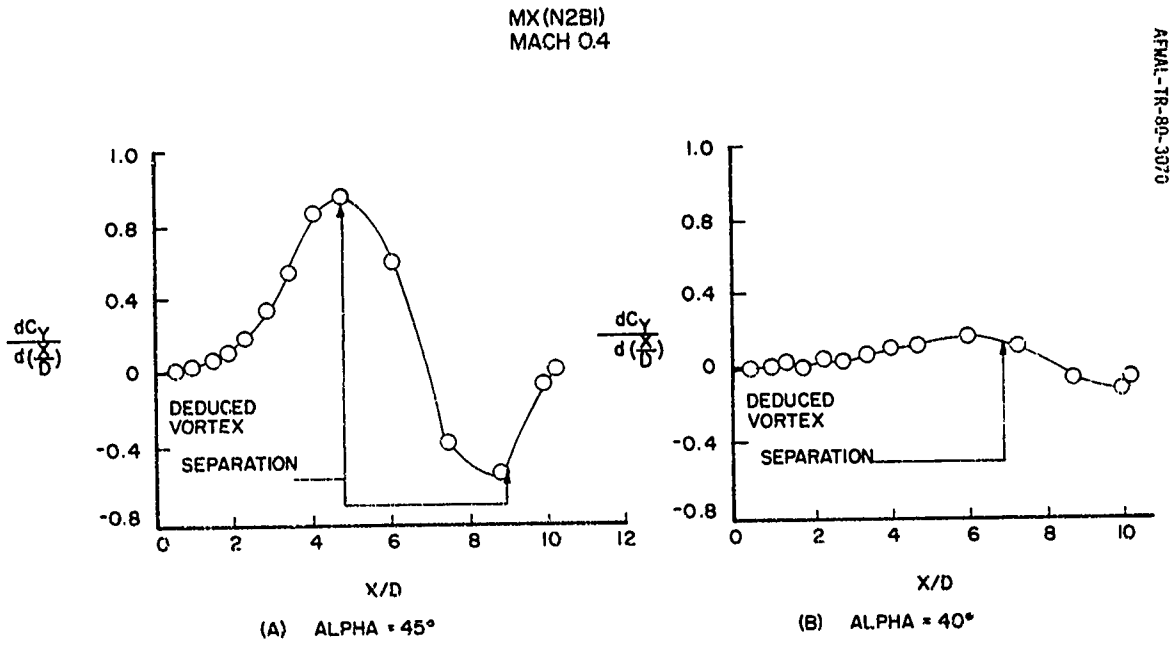

Figure 84. Axial Distribution of Local Side Force Coefficient

neighborhood of the peak side forces. The pressure coefficient based on RMS pressure of each probe is defined as:

$$C_{P_{RMS}} = \frac{P_{T_{RMS}} - P_\infty}{q_\infty} \qquad (7)$$

where $P_{T_{RMS}}$ = RMS total pressure of the unsteady Kulite probe data

- P_∞ = Tunnel static pressure

  q_∞ = Tunnel static dynamic pressure

The results near the missile centerline is presented in Figure 85. No correlation with the deduced separation from the previous section could be established. At alpha 45 degrees a minimum occurs in $C_{P_{RMS}}$ at the estimated vortex separation location (X/D = 4.8). However, at alpha 40 degrees a maximum occurs in $C_{P_{RMS}}$ at the estimated vortex separation location (X/D = 6.9).

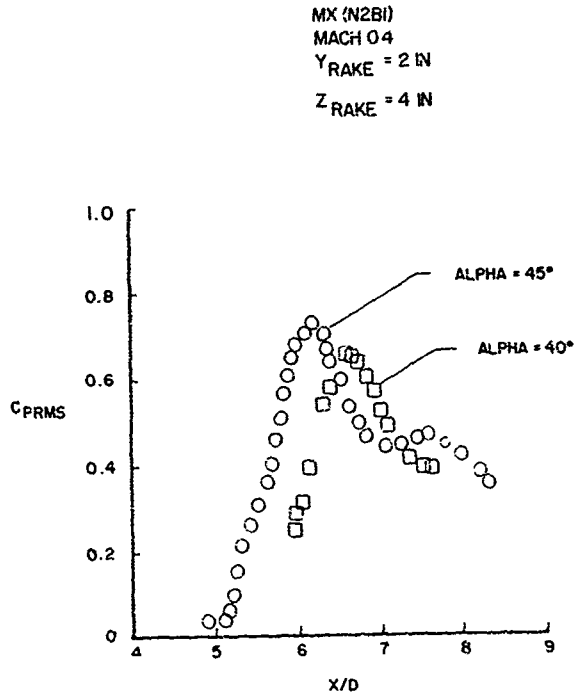

Figure 85. Axial Distribution of Unsteady Wake Pressure Coefficient

SECTION VI

ANALYSIS OF THE WAKE FLOW FIELD AND MISSILE AERODYNAMICS USING DISCRETE VORTEX THEORY

This section presents additional analysis of the experimental flow field data from Section V, in conjuncture with the model surface pressure data from Reference 44. Certain aspects of a currently existing discrete vortex theoretical model developed by Wardlaw (Reference 48) was utilized. The analysis method was extended to include the determination of the detailed model surface pressures. Vortex strengths from previous experimental studies were used in the theoretical model, and the vortex paths were determined empirically to result in reasonable comparisons with detailed model surface pressure data and flow field data.

Earlier examinations (Reference 49) using the analysis of Reference 48 showed that the calculated vortex paths did not provide good comparisons with the local normal and side force coefficients distributed along the missile axis. To improve on the results from Reference 49, the present investigation used the shed vortex strengths as a function of crossflow Mach number (which varies with angle-of-attack) as reported in Reference 15. The vortex paths were deduced from the measured wake data at Mach 0.4 and 45-degree angle-of-attack (as discussed in Section V.2 (see Figure 83)). At other Mach numbers and angles-of-attack, the vortex paths were determined in an iterative procedure by comparing the experimental pressure data with the calculated values. The vortex paths that resulted in reasonable comparisons with the experimental pressure data were selected as the representative paths in the analytical study. The calculations used concentrated vortex theory to model the wake. Details of the theoretical model and comparisons with the wake flow measurements and model surface pressure distributions are described in the following sections.

1. THEORETICAL MODEL

The three-dimensional vortex wake which develops due to separated flow over a missile at high angles-of-attack is the result of a complex

interaction between the inviscid vortex flow in the wake and the boundary layer on the lee side of the missile surface. At very low Reynolds numbers the flow is characterized by a nearly pure Von Karman idealization with nearly constant periodic shedding of constant strength vortices in a laminar wake. The basic parameter for describing the period of the vortex shedding is Strouhal number S, which is defined as:

$$S = nd/U \tag{8}$$

where n is the frequency of shedding of vortices of like sign, d is the diameter of the cylinder and U is the normal component of free stream velocity (Reference 15). As the crossflow Reynolds number increases beyond the critical range of $10^5 < R_{e_d} < 3.5 \times 10^6$, the wake narrows and becomes turbulent while the flow ahead of separation on the missile surface is still laminar. Further increases in Reynolds number beyond 3.5×10^6 results in transition to turbulent flow on the front face of the missile cross section and generally an unsteady wake. A rigorous procedure to describe the flow field above the critical Reynolds number has not been developed. It was decided, therefore, to rely on a predictive technique which had been developed using Karman vortex street theory with the sweepback principle employed as used by Wardlaw (Reference 48). In this method, the crossflow field is swept down the length of the body at the rate $U_\infty \cos \alpha$.

At each axial station the flow field is taken to be analogous to flow about a circular cylinder whose velocity is $U_\infty \sin \alpha$, and whose radius is equal to the body radius at that axial location. The wake is modeled by concentrated vortices trailing from the body. The necessary parameters to calculate the flow field velocities, and thus the pressures on the missile surface, are the concentrated vortex strengths and their locations in the wake. Figure 86 shows a schematic illustrating the flow field model. A typical side force distribution resulting from the experiments is also illustrated. The calculated pressure distributions in the present study relied on the measured and deduced vortex strengths and positions as a function of both Mach number and angle-of-attack.

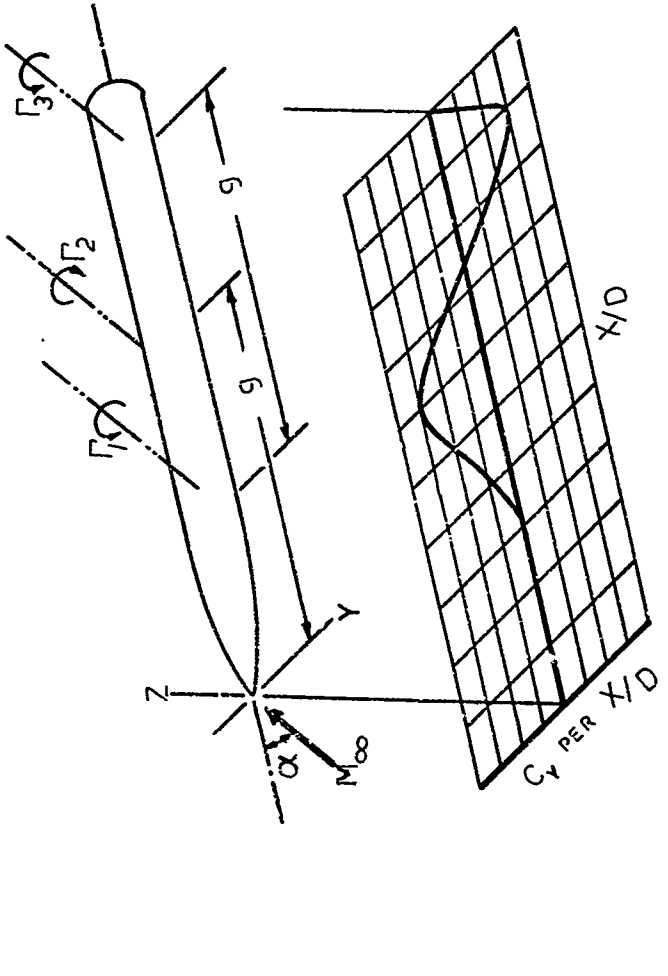

Figure 86. Flow Field Model for the Concentrated Vortex Analysis

In this sense the analysis is not rigorous and depends entirely on intuitive interpretation of the scatter and at times lacks empirical evidence.

a. Velocity Relationships

The coordinate system for the following analysis is defined in Figures 86 and 87. The analysis relies on the complex velocity potential developed by Wardlaw (Reference 48) for concentrated vortices which is:

$$\phi = U\left[-i\left(\xi-\frac{r^2}{\xi}\right) - \frac{i}{2\pi U}\sum_{j=1}^{K}\Gamma_j\,\ln\left\{\frac{\xi-\xi_j}{\xi-r^2/\bar{\xi}_j}\right\} + \frac{r}{\tan\alpha}\frac{dr}{dx}\ln\xi\right] \quad (9)$$

where $U = U_\infty \sin\alpha$ and $\xi = y + iz$

The real part of the complex velocity potential is:

$$\mathrm{REAL}|\phi| = U\left[z\left(1+\frac{r^2}{y^2+z^2}\right) + \frac{1}{2\pi U}\sum_{j=1}^{K}\Gamma_j\left\{\tan^{-1}\left(\frac{z-z_j}{y-y_j}\right) - \tan^{-1}\left(\frac{z-r^2/r_j^2 z_j}{y-r^2/r_j^2 y_j}\right)\right\} + \frac{r}{\tan\alpha}\frac{dr}{dx}\ln\sqrt{y^2+z^2}\right] \quad (10)$$

The velocity components u, v and w are obtained through the partial differentiation of the real part of the complex potential with respect to x, y and z.

Letting $f_j = z - z_j$

$g_j = y - y_j$

$\bar{f}_j = z - R_j^2 z_j, \quad R_j = \frac{r}{r_j}$

$\bar{g}_j = y - R_j^2 y_j$

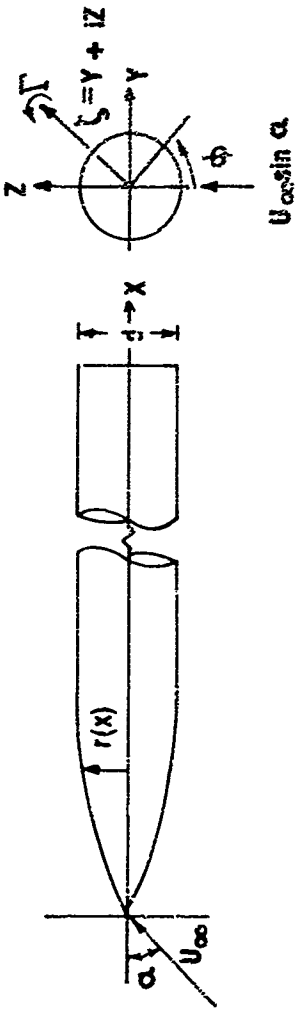

Figure 87. Coordinate System

$$u/U = \frac{2zrr'}{y^2+z^2} + \frac{1}{2\pi U} \sum_{j=1}^{K} \left[\Gamma_j' \left\{ \tan^{-1}\frac{f_j}{g_j} - \tan^{-1}\frac{\bar{f}_j}{\bar{g}_j} \right\} \right.$$

$$\left. + \Gamma_j \left\{ \frac{-g_j z_j' + f_j y_j'}{g_j^2+f_j^2} - \frac{\bar{f}_j \left[R_j^2 y_j' + 2y_j r/r_j^2 (r' - R_j r_j') \right] - \bar{g}_j \left[R_j^2 z_j' + 2z_j r/r_j^2 (r' - R_j r_j') \right]}{\bar{g}_j^2 + \bar{f}_j^2} \right\} \right]$$

$$+ \frac{\ln\sqrt{y^2+z^2}}{\tan\alpha} \left[(r')^2 + rr'' \right] \tag{11}$$

where the prime notation denotes differenation with respect to x. The differenation of the above terms with respect to x is obtained in the following manner:

$$\text{From } r_j = \sqrt{y_j^2+z_j^2}$$

$$\frac{dr_j}{dx} = \frac{y_j \frac{dy_j}{dx} + z_j \frac{dz_j}{dx}}{\sqrt{y_j^2+z_j^2}}$$

$$\frac{dy_j}{dx} = \frac{dy_j}{dt} \cdot \frac{dt}{dx} = v_j \cdot \frac{dt}{dx} \tag{12}$$

$$\text{From crossflow theory } t = \frac{x}{U_\infty \cos\alpha}, \quad \frac{dt}{dx} = \frac{1}{U_\infty \cos\alpha}$$

$$\frac{dy_j}{dx} = v_j \cdot \frac{1}{U_\infty \cos\alpha} = \frac{v_j}{U_\infty \sin\alpha} = \frac{v_j}{U} \cdot \tan\alpha$$

$$\text{Similarly } \frac{dz_j}{dx} = \frac{w_j}{U} \cdot \tan\alpha$$

$$\text{Thus } \frac{dr_j}{dx} = \frac{y_j \frac{v_j}{U} \tan\alpha + z_j \frac{w_j}{U} \tan\alpha}{r_j} \tag{13}$$

In a like manner,

$$v/U = \frac{-2yzr^2}{(y^2+z^2)^2} + \frac{1}{2\pi U} \sum_{j=1}^{K} \Gamma_j \left[\frac{-f_j}{g_j^2+f_j^2} + \frac{\bar{f}_j}{\bar{g}_j^2+\bar{f}_j^2} \right] + \frac{rr'}{\tan\alpha} \frac{y}{y^2+z^2} \tag{14}$$

and,

$$w/U = 1 + \frac{r^2(y^2-z^2)}{(y^2+z^2)^2} + \frac{1}{2\pi U} \sum_{j=1}^{K} \Gamma_j \left[\frac{g_j}{g_j^2+f_j^2} - \frac{\bar{g}_j}{\bar{g}_j^2+\bar{f}_j^2} \right] + \frac{rr'}{\tan\alpha} \frac{z}{y^2+z^2} \tag{15}$$

The preceding velocity terms are inviscid; thus the velocities in the above formulation become excessive in magnitude for points near the vortex center. This problem is corrected as shown in Reference 50 by assuming a vortex having a "solid" core. For values of r less than r_{core} the vortex velocity terms in Eqs. 11, 14 and 15 (i.e., the terms within the summation sign) are multiplied, as in Reference 50, by a correction term

$$\left(1-e^{-r_v^2/r_{core}^2}\right)$$

$$\text{where} \quad r_v = \sqrt{(z-z_j)^2 + (y-y_j)^2} \tag{16}$$

Furthermore the correction term can be expanded in a power series to yield

$$\left(1-e^{-r_v^2/r_{core}^2}\right) \cong r_v^2/r_{core}^2$$

$$= \frac{(z-z_j)^2 + (y-y_j)^2}{r_{core}^2} = \frac{f_j^2 + g_j^2}{r_{core}^2} \tag{17}$$

Application of the above correction for r less than r_{core} removes the singularity from Eqs. 11, 14 and 15 when $r = r_j$. For the present application r_{core} was selected to be 0.5a where a is the cylinder radius. The selection of this value for r_{core} is strictly arbitrary and for the present calculations ensured that the pertubation velocity components did not exceed the magnitude of the freestream velocity.

b. Vortex Strengths and Calculated Vortex Paths

The vortex strengths are a function of crossflow Mach number which varies with angle-of-attack (Reference 15, Figure 21). For the present theoretical model this relationship is shown in Figure 88. From the experimental wake data that are representative of maximum local side forces, the vortex paths in the wake and the separation location were determined from data described previously (Section V.2 and Figure 83) for Mach 0.4 and 45-degree angle-of-attack. For the Mach numbers and angles-of-attack for which no experimental wake data were available or was not representative of maximum side force conditions (as discussed in Section III.3.b). the apparent vortex locations were determined by an iterative procedure where reasonable comparisons between the measured and calculated local pressure coefficients on the body were used as a basis for selecting the paths. The results of this study are shown in Figure 89 for angles-of-attack between 25 and 45 degrees and Mach numbers between 0.4 and 0.8. For the Mach 0.4 and 0.6 cases, the first pair of vortices were of equal strength and opposite sign as obtained from Figure 88 for the appropriate crossflow Mach number. In the calculations it became necessary to reduce the trailing vortex strength near the base by approximately 23 percent to give reasonable agreement between the theoretical and experimental pressure coefficients. This obvious breakdown in the mathematical model in the neighborhood of the base may be due to the influence of the base pressure.

At Mach 0.8, the simulation required an entirely different distribution. At this Mach number the local force distributions are

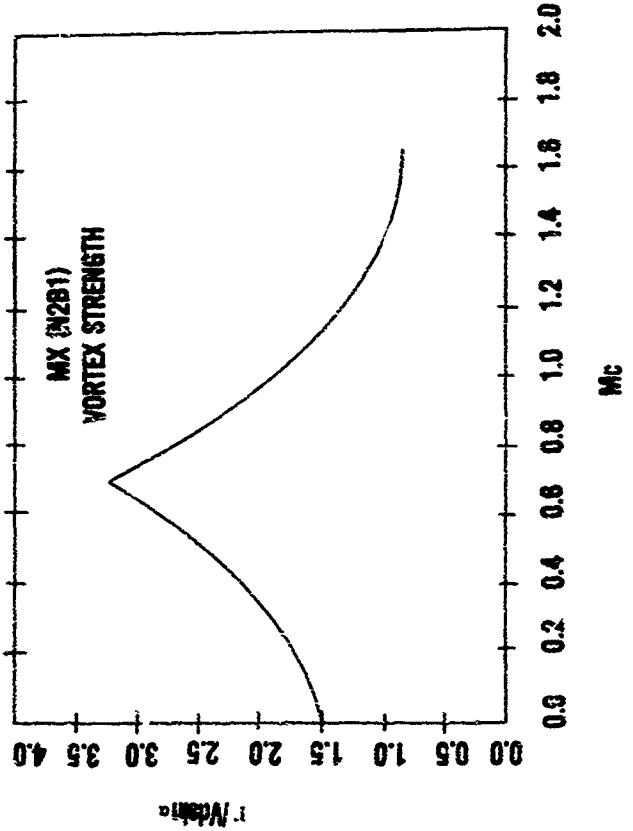

Figure 88. Nondimensional Vortex Strength vs Cross Flow Mach Number

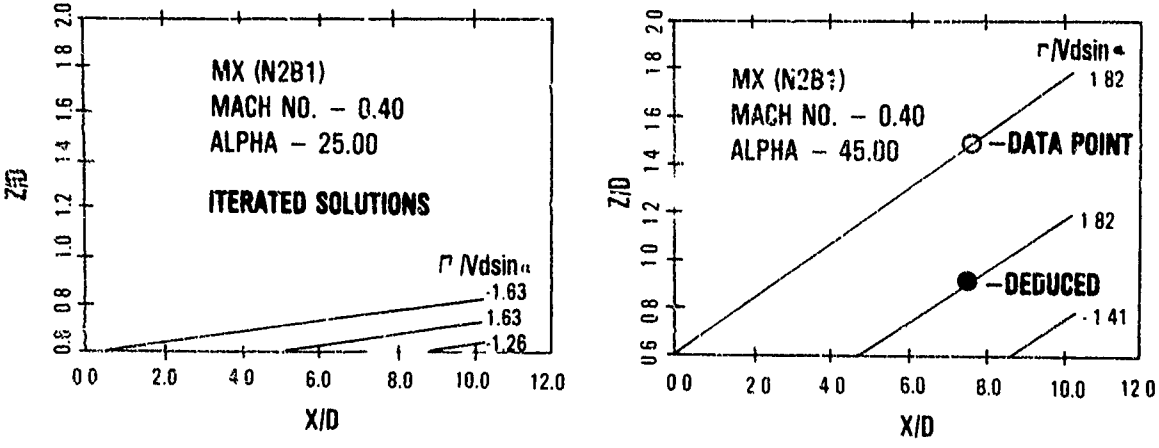

a. Mach 0.4

Figure 89. Estimates of Vortex Paths and Strengths

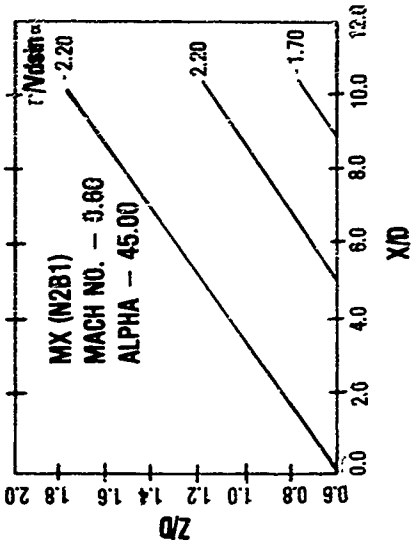

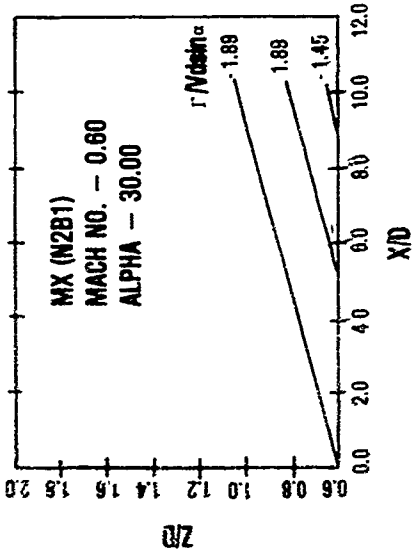

b Mach 0.6

Figure 89 (Continued)

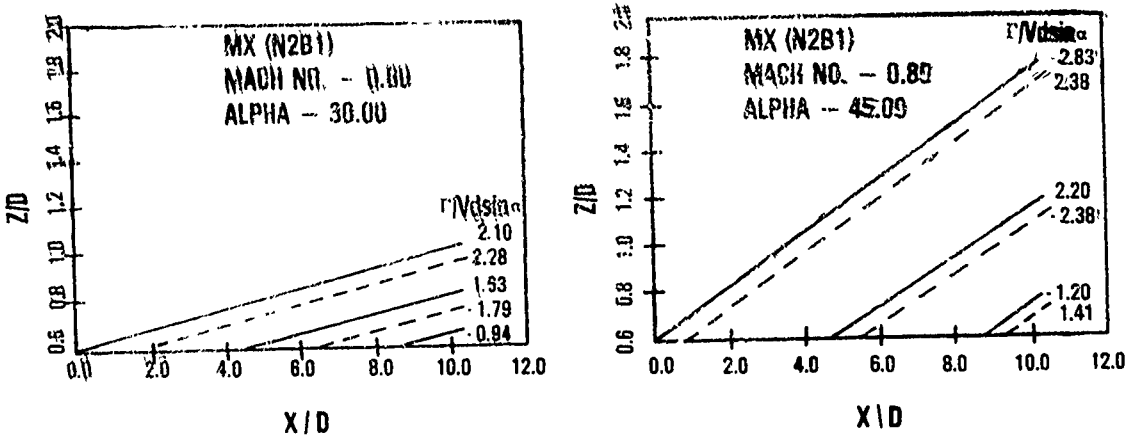

c. Mach 0.8

Figure 89 (Concluded)

characterized by a high normal force coefficient distribution, requiring somewhat strong vortex strengths (as also evidenced by Figure 88). As will be shown later, however, the asymmetrical side force coefficient distribution is small in magnitude. This suggests that the vortices are shed in vortex pairs, only slightly displaced, and each pair nearly equal in vortex strength. The results of the iterative procedure that compared favorably with both the normal force and side force coefficient distributions are shown in Figure 89(c). The first two vortices shed are not of equal strength (compared for example, with the Mach 0.4 and 0.6 simulations). However, the first two vortices form a nearly symmetric pair, one lying only slightly below the other. The second pair of symmetrical vortices that follow are reduced in average strength by approximately 23 percent (as was the case with the Mach 0.4 and 0.6 calculations). They were followed by a third set of symmetrical vortices reduced in strength by 42 percent from the second pair. These reductions in vortex strength gave no experimental verification from the flowfield data of the present study but were necessary in the theoretical model to produce reasonable calculated pressure distributions near the model base. In the crossflow plane, the vortex paths as deduced from the available wake data are shown in Figure 90.

2. THEORY/DATA COMPARISONS

The comparisons in this section are a result of the simulated vortex paths and strengths developed in the previous section as a function of Mach number and angles-of-attack. The results are for the N2B1 configuration.

a. Crossflow Velocity

The crossflow velocity calculations resulting from Equations 14 and 15 with vortex strengths and positions extracted from Figures 88 through 90 are compared to the experimental wake data in Figure 91. One general observation is that while the theory predicts a clearly distinct

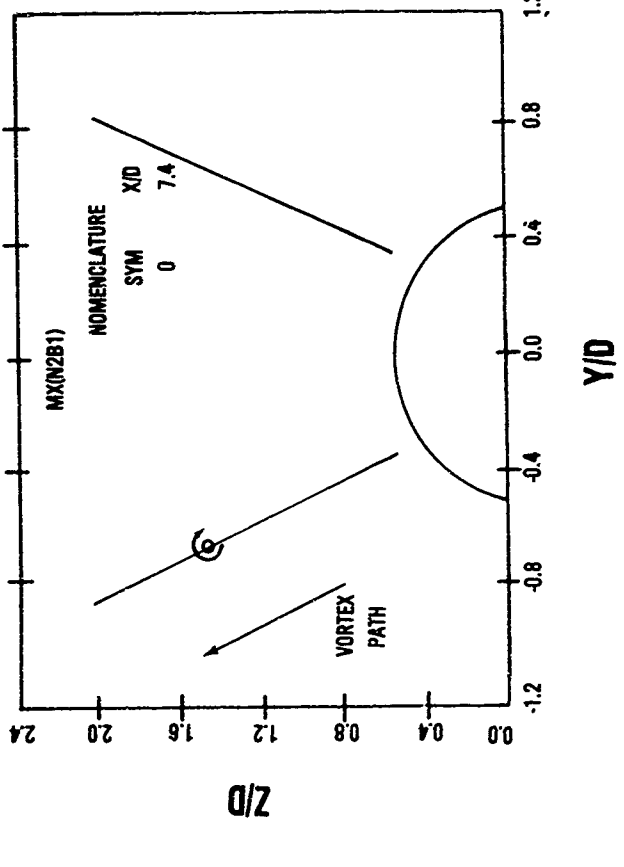

Figure 90. Vortex Path in the Crossflow Plane

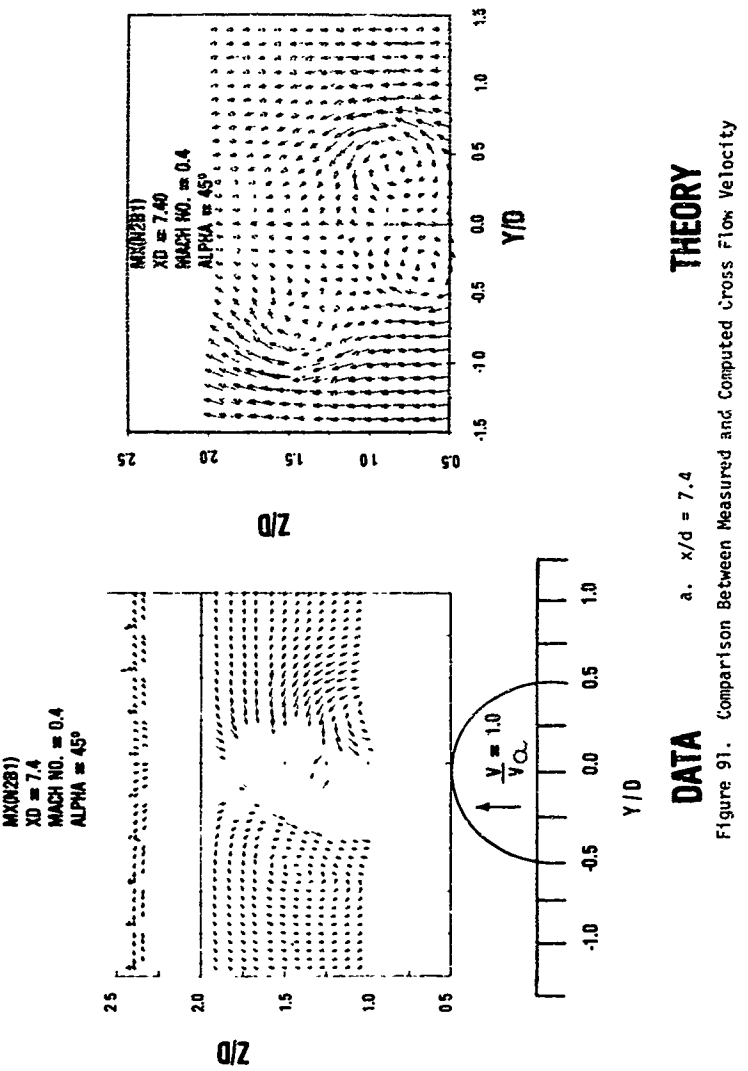

a. x/d = 7.4

Figure 91. Comparison Between Measured and Computed Cross Flow Velocity

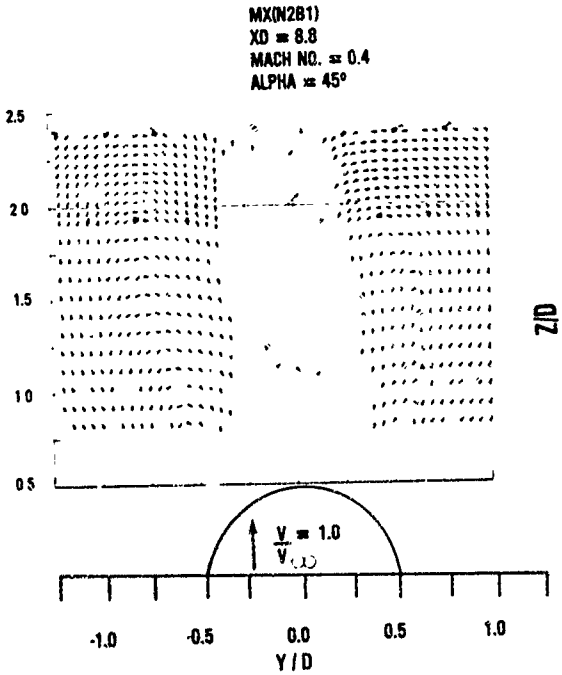

DATA

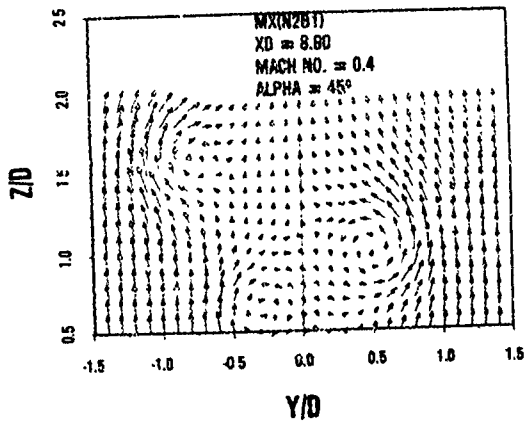

THEORY

b. x/d = 8.8

Figure 91 (Concluded)

vortex centers, the data indicate that the experimental velocity distributions are diffused, with no clearly defined vortex centers evident. One exception was the vortex on the left for the experimental data shown in Figure 80(b). In this case a vortex center is clearly evident at 1.5 diameters above the model surface.

b. Pressure Coefficient Distribution

After the velocities have been calculated from Equations 11, 14 and 15, the pressure coefficient can be obtained by employing the full Bernoulli equation:

$$C_p = \frac{2}{\gamma M_\infty^2} \left\{ \left[1 - \frac{\gamma - 1}{2} M_\infty^2 \left(\frac{2u}{U_\infty} + \frac{u^2 + v^2 + w^2}{U_\infty^2} \right) \right]^{\frac{\gamma}{\gamma - 1}} - 1 \right\} \tag{18}$$

The results of these calculations, along with available data comparisons, are presented in Figure 92. In general, the theory and data compare quite favorably for Mach 0.4 and 0.6, but not at Mach 0.8. The theory consistently experienced overshoots and undershoots around the model periphery in the vicinity of the vortex cores lying near the body surface. This suggests that the theoretical vortex distributions, as shown in Figure 89(c), for Mach 0.8, are lacking in authenticity and require further development.

c. Normal Force and Side Force; Coefficient Distributions

The local normal force and side force coefficient along the longitudinal axis was obtained by integrating the pressure coefficient, Eq. 18, around the model periphery as shown below.

$$\frac{dC_N}{d(x/d)} = \frac{1}{\pi a^2} \oint_0^{2\pi} C_p(\phi) \cos\phi \, r d\phi \tag{19}$$

$$\frac{dC_Y}{d(x/d)} = \frac{1}{\pi a^2} \oint_0^{2\pi} -C_p(\phi) \sin\phi \quad r d\phi \tag{20}$$

where the periphery angle, ϕ, is defined in Figure 87.

The results of the above calculations are presented in Figure 93. While the characteristic behavior of the data is predicted, the theory in general underpredicted the local normal force coefficient on the cylindrical portion of the model at Mach 0.4 and 0.6. The reverse was true for Mach 0.8, where the theoretical results overpredicted the local normal force coefficient on the cylindrical part of the model. Note that at Mach 0.8, the large local normal force coefficient distribution is fairly well estimated for the ogive nose. However, the predictions of C_p, as noted in Figure 92(c) did not follow the data trends sufficiently well. The good agreement between the local loads in Figure 93(c) are thus a result of the averaging that occurs in the integration process and does not reflect a true modeling of the flow phenomena, as indicated by the local pressure distribution in Figure 92(c).

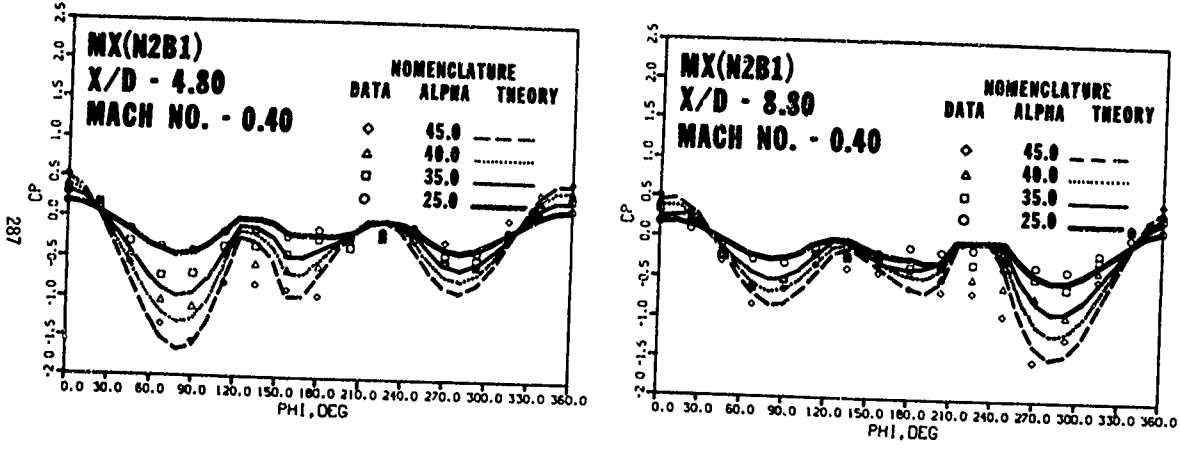

a. Mach 0.4

Figure 92. Theoretical and Experimental Pressure Coefficient Distributions at x/d = 4.8 and 8.8

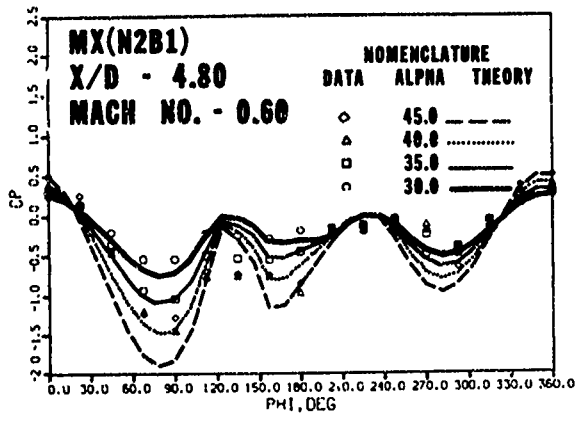

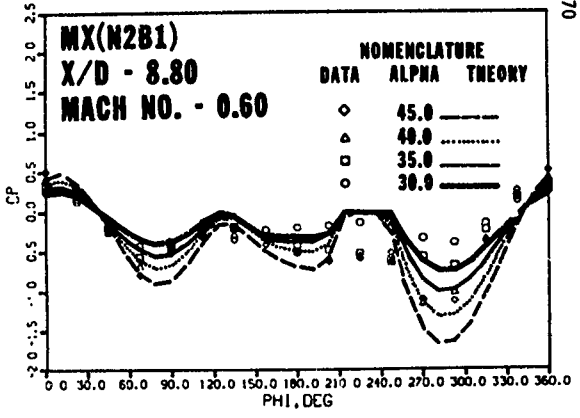

b. Mach 0.6

Figure 92 (Continued)

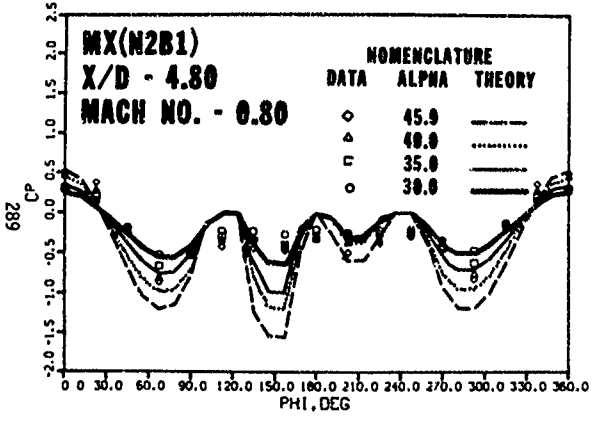

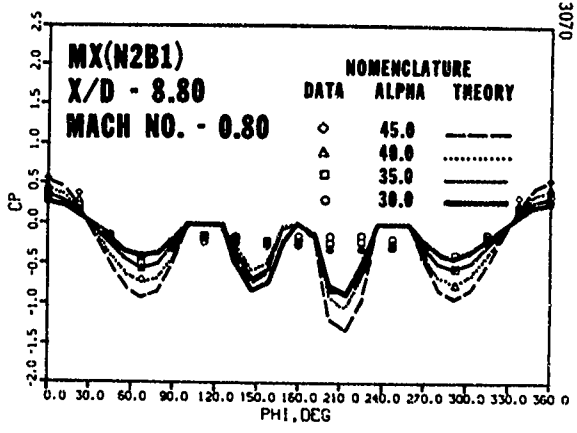

c. Mach 0.8

Figure 92 (Concluded)

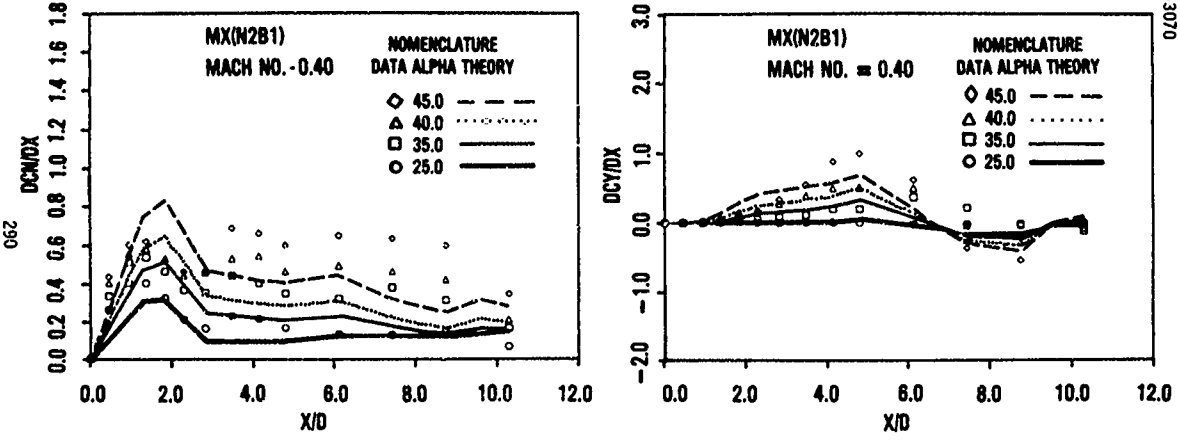

a. Mach 0.4

Figure 93. Comparisons Between Experimental and Computed Normal Force and Side Force Coefficient Distributions

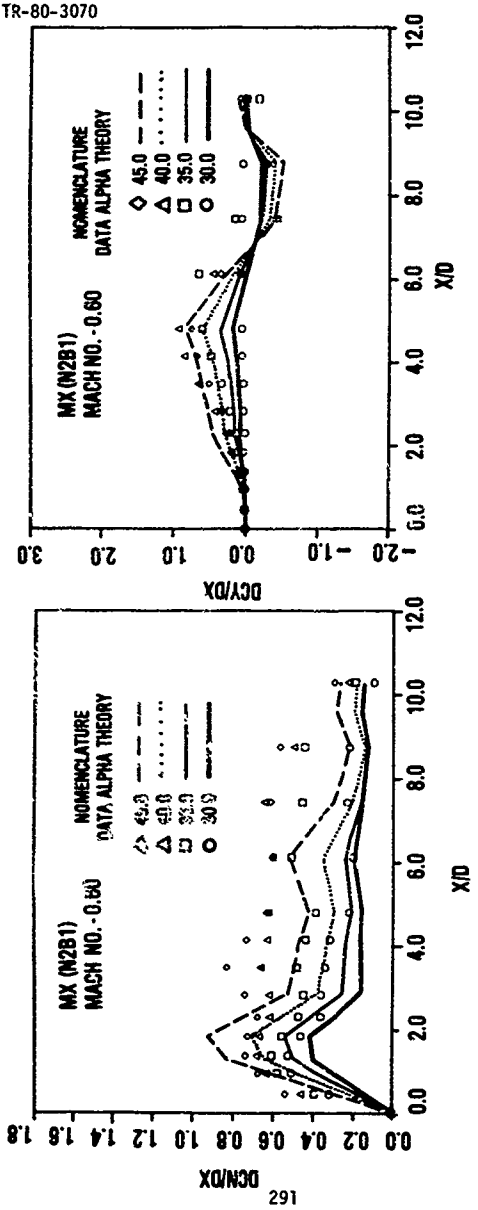

b. Mach 0.6

Figure 93 (Continued)

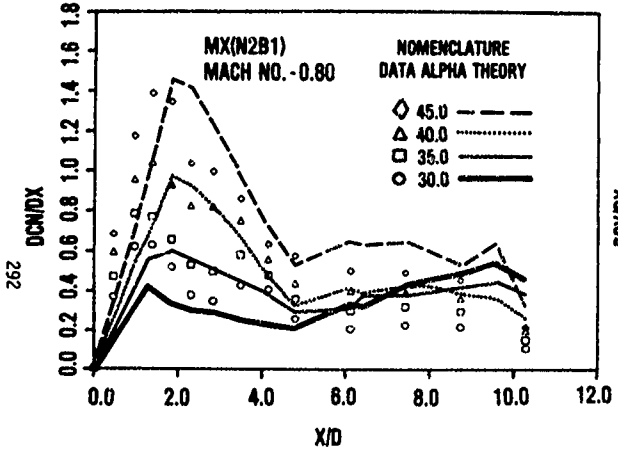

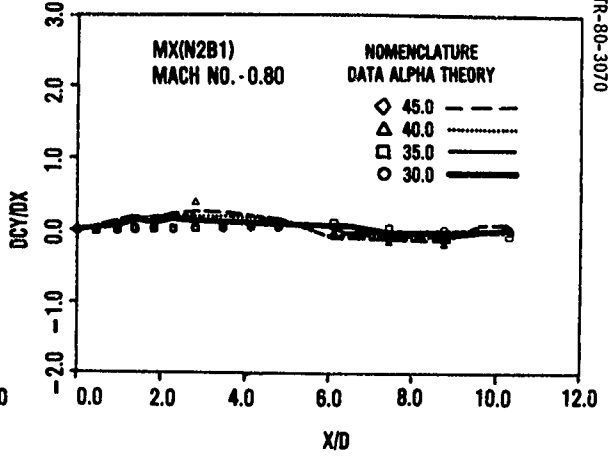

c. Mach 0.8

Figure 93 (Concluded)

SECTION VII

DEVELOPMENT OF AN EMPIRICAL - CORRELATION TECHNIQUE USING PRESSURE DATA

The large amount of pressure data which was generated in the MX program allowed the aerodynamic characteristics to be studied in detail. One unexpected observation was the general lack of repeatability in the out-of-plane forces. This feature of the test data introduced severe difficulties in trying to use existing analytic correlations. A semi-empirical analysis was developed using the test data. The method does not describe a particular value of the side force or yawing moment coefficient that would be developed at a given angle of attack and freestream condition; rather, the analysis describes the upper and lower bounds of regions within which the induced forces are contained.

The characteristic shape of the local side load coefficient per unit length is better illustrated if the values are normalized with respect to the maximum C_y of the particular data set. The maximum is denoted by C_y^*. The period of the function is easily identified and compared with other runs at different angles-of-attack and with different maximum values. Figure 94 is a typical example of the normalized plots.

1. EXPERIMENTAL OBSERVATIONS

The pressure coefficient distribution for a repeat run of the same conditions is shown in Figure 95. Both are the N2B1 configuration at the same Mach number, Reynolds number and angle-of-attack; yet the degree of asymmetry and the magnitude of the side force is markedly different. This was observed frequently, and the implications on the development of a correlation of the data will be considered. The magnitude of the side force loading was calculated at each station by integrating the surface pressure around the cross section.

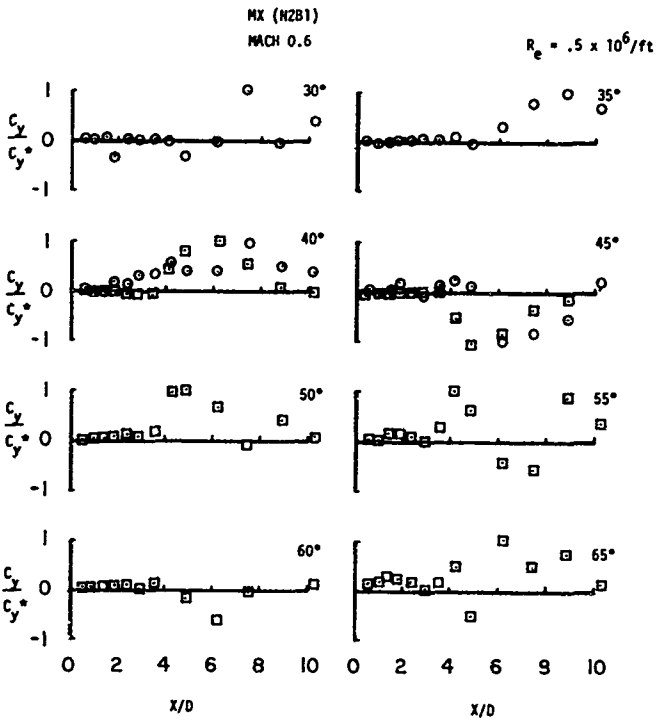

a. R_e = 0.5 x 10^6/ft

Figure 94. Local Side Force Coefficients Normalized by C_y^* at Angles-of-Attack from 30 Degs to 65 Degs/M = 0.6

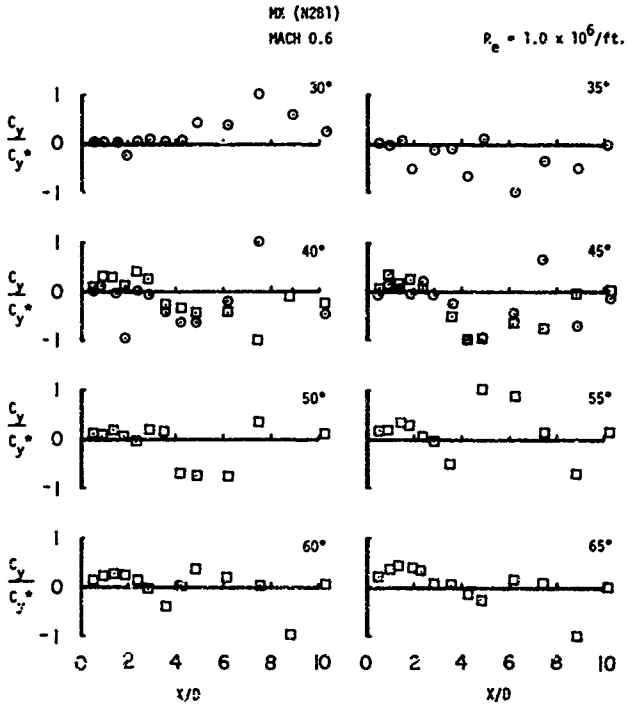

b. R_e = 1.0 x 10^6/ft

Figure 94 (Continued)

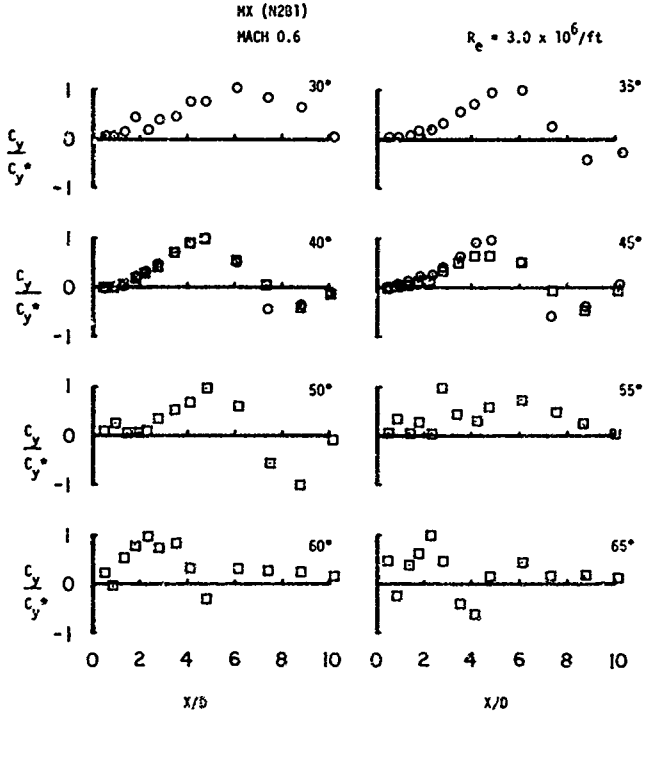

c. R_e = 3.0 x 10^6/ft

Figure 94 (Continued)

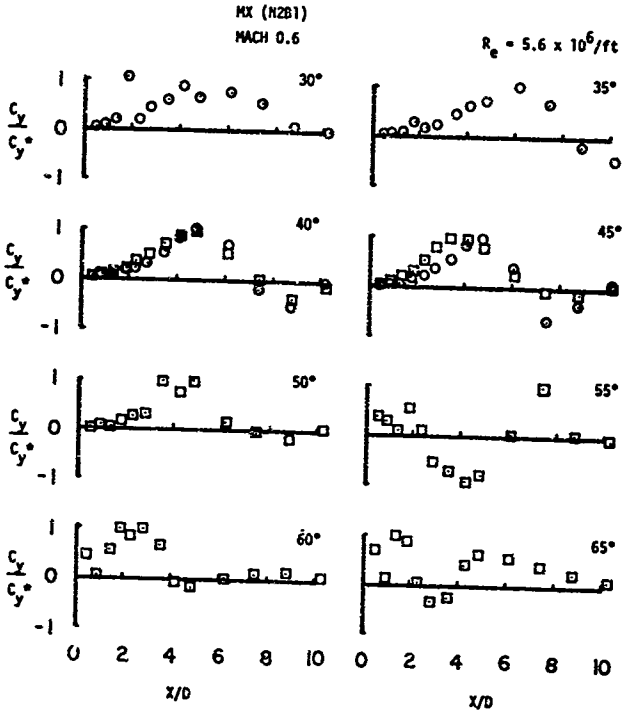

d. R_e = 5.6 x 10^6/ft

Figure 94 (Concluded)

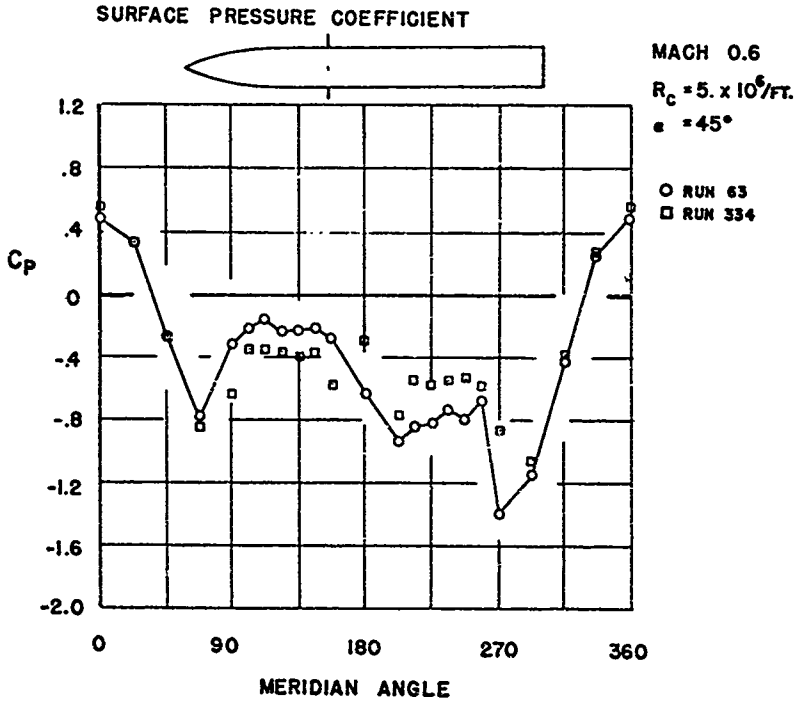

Figure 95. Pressure Coefficient Distribution, N281

This local side force loading usually varied along the length of the missile in a regular pattern. Figure 96 shows the side force loading for a typical test condition. The ordinate of these graphs is evaluated by an integration of the surface pressures using the trapezoidal rule. The nondimensionalizing factors were selected so that

$$C_Y = \int_0^{\ell/D} C_y \, d\,(X/D) \qquad (21)$$

The local side load coefficient per unit length, C_y, is much the same as a section lift coefficient. The area under the curve, when presented as shown in Figure 96, is the value of the total side force coefficient for the missile at that particular condition. A characteristic of the data is the resemblance to a sinusoidal variation along the length of the missile. The measured side loads were therefore described in terms of the period and the amplitude of the side load function.

Throughout the test program the data followed general trends, but enough variance was always present to prevent absolute statements from being made. The origin of these variations is very difficult to identify, although the body of research on the subject strongly suggests the most probable cause is the influence of small disturbances in the freestream flow and nose surface irregularities on the growth and subsequent separation of the boundary layer.

2. CORRELATION DEVELOPMENT

The correlation of the period and amplitude of the load function was related to a flow model for vortex separation from a missile at angle-of-attack. The flow model is depicted in Figure 86. The figure illustrates a concept for relating the experimental data with the assumed vortex functions. The vortices, which are generated by the boundary layer, separate from the missile in alternating positions. The flow model assumes the vortex pattern is fixed in time and space for the wind tunnel case, following the model described in Reference 15.

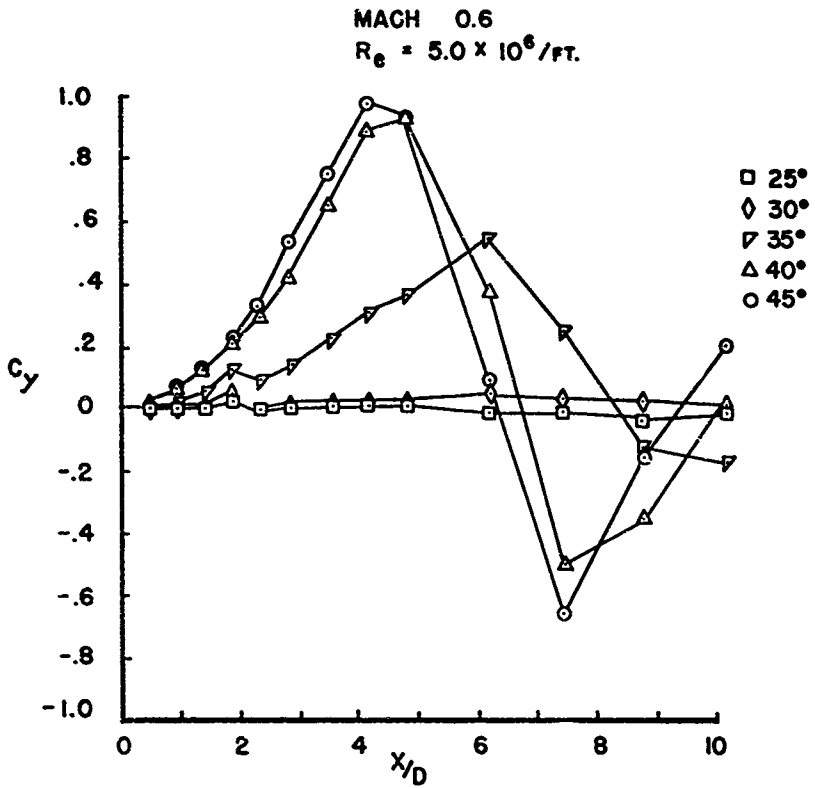

Figure 96. Local Side Force Coefficient Distribution, N2B1

The vortices begin as an attached asymmetric pair of equal strength and opposite sign on the forward part of the missile. Some disturbance in the freestream or on the forward surface of the missile creates an asymmetry in the boundary layer growth and vortex strength. The ultimate result is separation of one vortex before the other. At this point the local side load begins to diverge from zero.

There exists some maximum value of attached vortex strength, beyond which the vortex cannot remain attached to the model. The separation point of the second vortex corresponds to that value; it is the separation point of the vortex which has remained attached the longest. The first maximum of the side load appears at that station. Succeeding separation locations occur at equally spaced intervals. At each of these separations a maximum in the local side load also occurs. It was also observed that the side load tends toward zero at the base of the model.

The data correlation uses the Strouhal number as a nondimensional parameter for describing the period of the side load maxima. The flow model assumes the period of the side load is also the period of vortex separation along the same side of the missile. The Strouhal number was originally developed for application to vortex separation from cylinders normal to the flow.

$$S = \frac{nD}{U} \tag{22}$$

By relating the shedding frequency, n, to the vortex location in space, and by using the velocity component in the crossflow plane, the Strouhal number can be described as

$$S = \frac{D}{g \tan a} \tag{23}$$

where g is the distance between the vortex separation locations along the length of the missile, as shown in Figure 86.

The separated and attached vortices induce a circulation about the missile. The induced circulation about the missile can be thought of as being represented by a single equivalent vortex, Γ_o. The local side force is depicted as the result of the equivalent vortex centered at the center of the missile cross section. Analytical efforts directed at evaluating this circulation about the missile through calculations involving the strength and location of the vortices in the wake were discussed in the previous sections. Accurate results proved particularly difficult using this approach. The experimental data from the MX program were used to develop an alternative semi-empirical prediction method.

A lift force in the Y direction is generated by the circulation about the missile and the Z velocity component, normal to the missile centerline.

$$\text{Side force per unit length} = F_y = \rho\,(V_\infty \sin\alpha)\,\Gamma_o \tag{24}$$

The force may be converted to a force coefficient and the length dimension expressed as X/D, whereupon the expression for local side force coefficient per unit length becomes

$$C_y = \left[\frac{8}{\pi}\,\frac{\Gamma_o}{(V_\infty \sin\alpha)\,D}\right]\sin^2\alpha \tag{25}$$

The side load coefficient varies along the length of the missile, and in this expression is therefore a function of X/D. The maximum side load, C_y^* corresponding to the amplitude of the trigonometric function, is assumed to be an empirical function multiplied by the sine squared of the angle-of-attack. The rigor of this description is of the same order as the use of a crossflow drag coefficient to estimate the normal force coefficient, such as the method of Reference 2. Using the same terminology, the factor in brackets will be called the crossflow lift coefficient, c_{l_c}. The period and amplitude of the side load function are described by the Strouhal number and the maximum crossflow lift coefficient.

The test data from four nose configurations, N1, N2, N3 and N4, were used to evaluate these correlation parameters. The maximum number of test points was obtained for the ogive nose with a radius of 7 body diameters,

N2B1, at a freestream Mach number of 0.6. This nose shape and test condition will be used to illustrate the correlation of experimental results. For each angle-of-attack and Mach number - Reynolds number combination a value of the Strouhal number and maximum crossflow lift coefficient was determined.

The maximum crossflow lift coefficient is shown in Figure 97 as a function of the angle-of-attack. A line was defined which represented the maximum values observed in the tests. The maximum was approximately 2.5 for the N2 nose at Mach 0.6. At all angles-of-attack the average values are approximately equal to 0.5.

The Strouhal number was graphed as a function of the maximum crossflow lift coefficient. At low values of the crossflow lift coefficient the Strouhal number did not have a definite value. At large values of the crossflow lift coefficient the Strouhal number was very close to 0.25. In the crossflow analogy the Strouhal number would be 0.22 if the flow about a cylinder were fully duplicated. The work of Thomson and Morrison, Reference 15, showed a Strouhal number of approximately 0.20 for freestream Mach numbers less than 0.6.

The significance of the correlation shown in these data is that the period of the induced side load is well defined when the crossflow lift coefficient is large. At smaller values of the maximum crossflow lift coefficient the data does not show a clearly defined period, although the range of value is bounded.

The direction of the side force load, to the right or left of the missile, was considered to be completely random. The correlation method does not take it into account.

3. PREDICTION METHOD

The characteristics of the aerodynamic side force coefficients, which are the period and amplitude of the function, have been correlated using the results from a large experimental program. These correlations can be used as the basis for a semi-empirical prediction method which defines the envelopes of the side force and yawing moment coefficients on a missile

a. Mach 0.4

Figure 97. Maximum Crossflow Lift Coefficient for Configuration N2B1

b. Mach 0.6

Figure 97 (Concluded)

at angle-of-attack. The prediction method assumes the crossflow lift coefficient is developed along the length of the missile in a regular fashion. There exists some length from the nose, where the vortices are attached and develop initially as a symmetrical pair. An induced force does not develop along that part of the missile length. The side force begins to be impressed when the vortices develop an asymmetry. The crossflow lift coefficient grows to a maximum in a sine wave pattern, which is repeated along the length of the missile until a station-one diameter from the base of the missile is reached. From that station to the base the crossflow lift coefficient is depicted as a linear decrease to zero at the base.

Having established the loading pattern in the side force direction, it is an elementary procedure to integrate the loading to obtain the side force coefficient and the yawing moment coefficient. In this section the yawing moment is always shown about the nose of the missile. The direction sense of the force and moment coefficient, right or left, is not treated and is shown as absolute magnitude only.

When the average, or most probable, value of the side force and yawing moment coefficient is to be determined, the Strouhal number may have any value in the range of 0.15 and 0.45, while the crossflow lift is taken as 0.5. Since the period of the sine wave loading pattern is not fixed in this case, the locus of maxima produce a simple bound which defines the most probable values of the side force and yawing moment coefficient.

The maximum value of the side force and yawing moment coefficient is determined by a value of the crossflow lift coefficient which is different from that used in the average calculations. A unique value of the Strouhal number is used. For the example case it was fixed at .20.

Figure 98 is a graph of the predicted envelope of the side force coefficient and yawing moment coefficient for a missile 10 diameters long at angle-of-attack from 20 to 45 degrees. Data from the force and moment tests of the N281 configuration at Mach 0.6 are also shown to evaluate the appropriateness of the prediction scheme. The force and moment data were

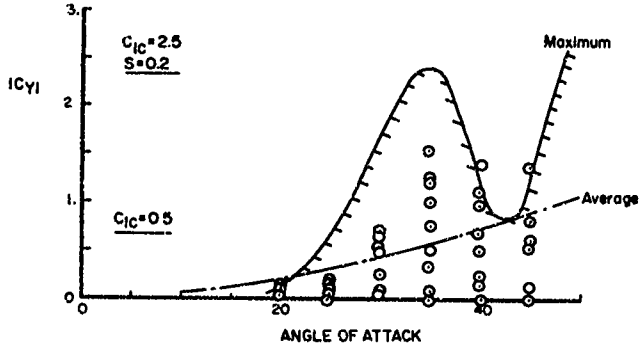

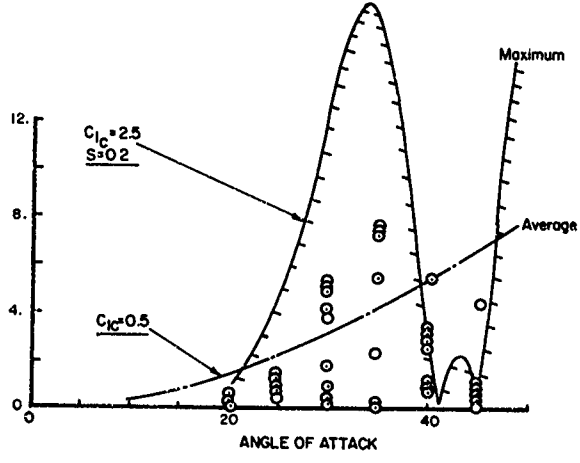

Figure 98. Predicted Envelope of the Side Force and Yawing Moment Coefficient from the Data Correlation Analysis

obtained in a separate test from the pressure experiments and constitute an independent set of data. The force and moment data are within the bounds described by the correlation method.

4. FREESTREAM AND CONFIGURATION EFFECTS

The crossflow drag coefficient is often depicted as a function of the crossflow Reynolds number. The maximum crossflow lift coefficient was plotted versus the crossflow Reynolds number, as shown in Figure 99. The graph illustrates the range of crossflow lift coefficient experienced in these tests. The lack of correlation may be only a reflection of the scarcity of data. A general observation seems to be that the largest values of the crossflow lift coefficient occur at the highest values of the crossflow Reynolds number.

Mach number and nose effects are shown in Figure 100. In the range of 0.4 to 0.6 the Mach number effects are small. The values of the crossflow lift coefficient indicates that the maximum side force at Mach numbers greater than 0.7 is no longer different from the most probable level of the side force.

Among the nose shapes tested, there were three configurations, which comprise a regular variation in nose length. The longest nose shape, with a profile radius equal to 7 nose diameters, was used for the developments of the previous sections. A nose profile radius of 3 and 5 body diameters was also tested. The three nose shapes all had the same bluntness. There were not as many runs in the test sequence for these shapes. Conclusions are therefore limited to the possibility that more data may produce a greater upper bound on the maximum crossflow lift coefficient. In this body of data it appears that a shorter nose produces both a lower maximum value of the crossflow lift coefficient and a lower value of the corresponding Strouhal number.

A nose with a sharp tip was also fabricated for the 7-body-diameter tangent ogive nose. The sharp nose configuration, N1, produced data which are very similar to the more blunt nose with the same profile. A graph of the correlation parameters which resulted from the tests of the sharp nose is also shown in Figure 100.

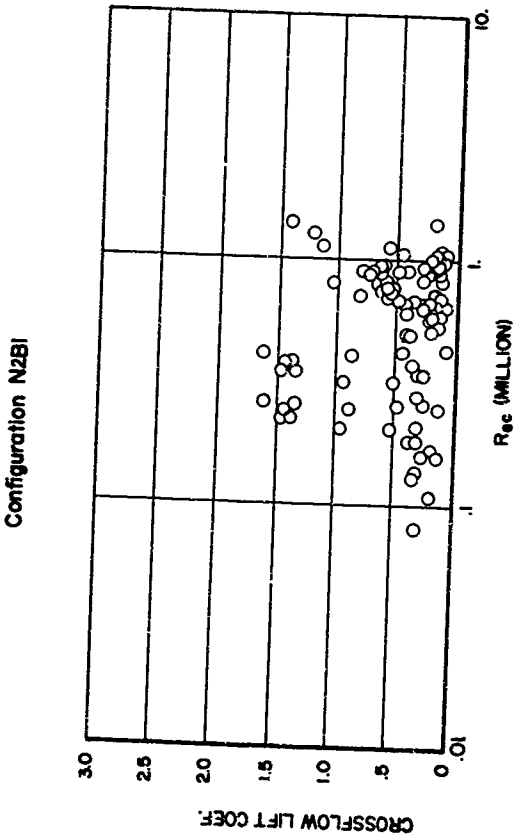

a. Mach 0.4

Figure 99. Crossflow Lift Cuefficient Variation with Crossflow Reynolds Number, Mach 0.4

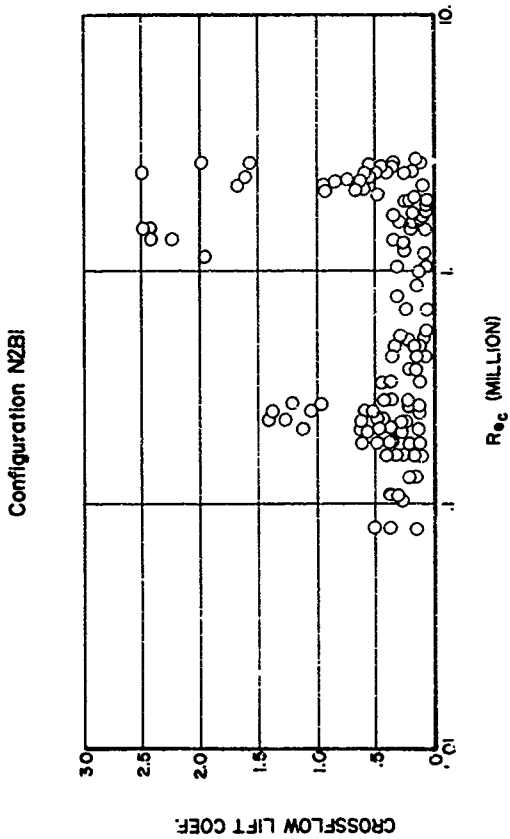

b. Mach 0.6

Figure 99 (Concluded)

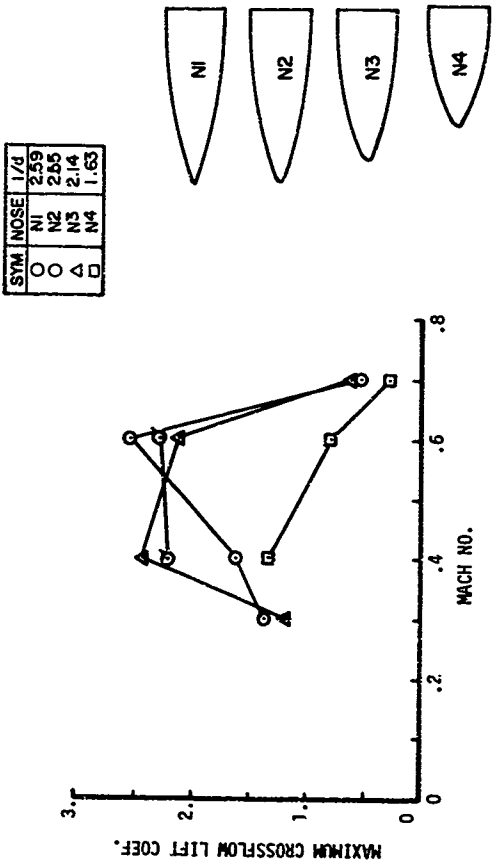

Figure 100. Nose Shape Effects on Crossflow Lift Coefficient

SECTION VIII

CONCLUSIONS AND RECOMMENDATIONS

This study has provided considerable insight into the aerodynamic forces developed on a missile at large angles-of-attack in subsonic flow. The conclusions reached herein fall into two categories: the observations of our experimental investigation and the results of attempts to predict the phenomena associated with asymmetric vortex shedding.

1. PRESSURE AND FORCE TESTS

1) The pressure data provided an excellent insight into the development of asymmetric forces. The pressure patterns can be related to the vortex separation location. The pressures could be integrated to produce force coefficients which match the force balance measurements.

2) The subsonic tests of the MX model at length Reynolds number of over 30 million represent some of the highest Reynolds number tests at high angles-of-attack. Within the range of the tests, there was little effect of Reynolds number at angles-of-attack below 35 degrees. At higher angles-of-attack the trends are not completely consistent. In general though, increasing Reynolds number increased the magnitude of side force and yawing moment coefficients and increased the normal force coefficient.

3) The large side force and yawing moment coefficients are essentially associated with subsonic Mach numbers. As Mach number increases above 0.8 these forces greatly decrease. The general trend of the axial and normal force coefficient show no special change at Mach 1.0; the increase in value is smooth from subsonic to supersonic speeds.

4) Thirteen different nose configurations were tested at various conditions. The 3-caliber ogive nose had the lowest values of induced side force and yawing moment coefficients. The fineness ratio strongly influences the magnitude of the out of plane forces. The triconic nose of comparable fineness ratio to the ogive nose has as large or larger asymmetric forces.

5) Body length effects were not subsequently determined in this test series. The limited data from this study and previously reported data indicate that length alone does not change the aerodynamic flow field.

6) Grit ring effects were small and inconclusive at the high Reynolds numbers. The grit ring/strip combination effects on the asymmetric forces were pronounced but not with the same trends as increasing Reynolds number.

7) The model mounting system affects the aerodynamic data. The sting-mounted data is considered to be the most reliable. A strut mount was required to achieve angles-of-attack above 45 degrees, but there was an offset in the data when strut and sting measurements were compared at the same angles-of-attack. A data offset was also noted when the preset angle of the strut was changed.

8) Rocket exhaust effects were significant at angles-of-attack greater than 60 degrees. The rocket exhaust jet produced a decrease in pressure on the leeside of the missile, which in turn was reflected in an increased normal force coefficient and more negative pitching moment coefficients. Exhaust jet deflections of +15 degrees produced only a small change from the 0° deflection case.

9) The asymmetric forces and moments show a strong dependence on missile roll angle. To assure measurement of the maximum values, the model being tested should be rolled at small intervals to 180 degrees. The continuous-roll technique used in these experiments provides reliable data in a cost effective manner.

2. FLOW FIELD TEST

The key conclusions from the present flow field data are summarized as follows:

1) The only visible vortex centers were at station X/D = 7.4 and were very close to the model (maximum vertical location observed was approximately 1.5 diameters from the model centerline at this station).

2) The shed vortices aft of station X/D = 7.4 were very diffused in nature, but vortex centers could not be clearly identified.

3) By use of the observed vortex centers at station X/D = 7.4, the apparent vortex separation locations from the model surface were deduced with aid of test results by previous investigations (Reference 15).

4) The estimated vortex separation locations thus determined correlated with the sinusoidal peaks in the side force coefficients obtained from integrating the model surface pressure data from the present test.

3. FLOW FIELD ANALYSIS

The following conclusions have been drawn from the present study:

1) In the analysis it was assumed that the vorticity field could be represented by discrete vortices trailing from the body. This assumption is not entirely valid since the experimental data shows diffused vorticity in the wake.

2) For the one condition at Mach 0.4 and 45-degree angle-of-attack where experimental data at observed maximum side force conditions were available to deduce the vortex paths, the calculated pressure distributions, and thus the integrated results for local normal force and side force coefficients, compared reasonably well with the experimental data.

3) For the remaining Mach numbers and angles-of-attack in this study the apparent vortex locations were determined by an iterative procedure where reasonable agreement between the measured and calculated local pressure coefficients on the body were used as a basis for selecting the trailing vortex paths. These results require verification with experimental data.

4) As Mach number increases beyond subsonic values, the local side force values decrease. An attempt to model this result was made at Mach 0.8 by allowing the vortices to trail off the body in nearly symmetrical pairs. Although this did result in reasonable integrated normal force and side force distributions along the body, the comparisons of the

experimental data suggest that the theoretical model is not entirely valid. Perhaps the decrease in the side force is associated with other flow characteristics, such as embedded shocks, at the higher Mach numbers.

5) All of the analytical models used in this study required a significant reduction in vortex strength near the model base to provide reasonable agreement between the calculated and experimental pressure distributions. This is not justified by the present data, and suggests that the concentrated vortex theory is not valid in this region.

4. CORRELATION TECHNIQUE

1) The correlation of the asymmetric aerodynamic data revealed the essential characteristics of the induced loads, based on the concepts contained in the flow model. The correlation was then used to construct a prediction scheme for the effects of vortex separation on which the bounds of a region for the out-of-plane force and moment are described. The method is proposed as an analysis tool for the preliminary design of maneuvering missiles. It is easily applied, and appears appropriate for the range of variables covered in the subject.

2) The use of force and moment data alone to describe the effects of asymmetric vortex separation does not provide the information necessary to develop a correlation that completely defines the variable in the flow model. One may measure a particular value of force coefficient; yet not be able to define the particular axial distribution and magnitude of the impressed side load.

5. RECOMMENDATIONS

1) The prediction method assumes that the maximum crossflow lift coefficient is well defined in the angle-of-attack range of from 0 to 35 degrees. Additional tests specifically designed to obtain the maximum crossflow lift coefficient, such as rolling the model at each angle-of-attack, are needed to determine if the empirical function is overly conservative.

2) In view of the existing questions about flow unsteadiness, it is recommended that the available microphone data from the MX missile tests be very carefully analyzed. Particular attention should be given to the implications of the results on the aerodynamics of the physical model.

3) Finally, this study and others show that considerable detailed wake data must be obtained to properly develop and verify analysis techniques. Probe investigations are not adequate because they are not practical to obtain the tremendous amount of information required to cover the entire three-dimensional wake. New developments in flow field investigations such as laser doppler velocimetry and holography appear to be much more promising.

REFERENCES

1. Maskell, E.C., "Flow Separation in Three Dimensions," RAE Rept. AERO 2565, Nov. 1955.

2. Allen, J.H., "Estimation of the Forces and Moments Acting on Inclined Bodies of Revolution of High Fineness Ratio," NACA TM A9I26.

3. Perkins, E.W. and Jorgensen, L.H., "Comparison of Experimental and Theoretical Normal-Force Distributions (Including Reynolds Number Effects) on an Ogive-Cylinder Body at Mach Number of 1.98," NACA TN 3716, 1956.

4. Jorgensen, L.H. and Perkins, E.W., "Investigation of Some Wake Vortex Characteristics of an Inclined Ogive-Cylinder Body at Mach Number 2," NACA Report 137:, 1958.

5. Tinling, B.E. and Allen, C.Q., "An Investigation of the Normal-Force and Vortex-Wake Characteristics of an Ogive-Cylinder Body at Subsonic Speeds," NASA TN D-1297, 1962.

6. Perkins, E.W. and Kuehn, D.M., "Comparison of the experimental and Theoretical Distributions of Lift on a Slender Inclined Body of Revolution at M = 2," NACA RM A53E01, 1953.

7. Gowen, F.E. and Perkins, E.W., "A Study of the Effects of Body Shape on the Vortex Wakes of Inclined Bodies at a Mach Number of 2," NACA RM 53I17, 1953.

8. Allen, J.H., "Pressure Distribution and Some Effects of Viscosity on Slender Inclined Bodies of Revolution," NACA TN 2044, 1950.

9. Allen, J.H., and Perkins, E.W., "A Study of Effects of Viscosity on Flow Over Slender Inclined Bodies of Revolution," NACA Report 1048, 1951.

10. Allen, J.H. and Perkins, E.W., "Characteristics of Flow Over Inclined Bodies of Revolution," NACA RM A50L07, 1951.

11. Grosche, F.R., "Wind Tunnel Investigation of the Vortex System Near an Inclined Body of Revolution With and Without Wings," AGARD C.P. No. 71, Aerodynamic Interference Conference, September 1970, pp. 2-1 to 2-13.

12. Rodgers, E.J., "Vorticity Generation of a Body of Revolution at an Angle of Attack," J. of Basic Eng., Trans of ASME, Vol. 86, Series D, No. 4, December 1964, pp. 845-850.

13. Atraghji, E.G., "Surface Flow Visualization, Surface Pressure and Surface Preston Tube Pitot Pressure Measurement Over a 6.1 Ellipsoid at Incidence at M = 0.3 and 0.74," Report No. 5 x 5/0032, NEA - High Speed Aerodynamics Section, NCR, Canada, 1968.

REFERENCES (Continued)

14. Letko, W., "A Low-Speed Experimental Study of the Directional Characteristics of a Sharp-Nosed Fuselage Through a Large Angle-Attack Range at Zero Angle of Sideslip," NACA TN 2911, 1953.

15. Thomson, R.D., and Morrison, D.F., "The Spacing, Position, and Strength of Vortices in the Wake of Slender Cylindrical Bodies at Large Incidence," J. Fluid Mech, Vol. 50, Part 4, pp. 751-783, 1971.

16. Pick, G.S., "Investigation of Side Forces On Ogive-Cylinder Bodies at High Angles of Attack in the M = 0.5 to 1.1 Range," AIAA Paper No. 71-570, AIAA 4th Fluid and Plasma Dynamics Conference, Palo Alto, Calif., June 1971 (also J. of Spacecraft and Rockets, Vol. 9, No. 6 June 1972, pp. 389-390.)

17. Coe, P.L., Jr., Chambers, J.R. and Letko, W., "Asymmetric Lateral-Directional Characteristics of Pointed Bodies of Revolution at High Angles of Attack," NASA TN D-7095, November 1972.

18. Clark, W.H., Peoples, J.R. and Briggs, M.M., "Occurence and Inhibition of Large Yawing Moments During High-Incidence Flight of Slender Missile Configurations," AIAA Paper No. 72-968, AIAA 2nd Atmospheric Flight Mechanics Conference, Palo Alto, Calif., Sept. 1972 (also J. of Spacecraft and Rockets, Vol. 10, No. 8, August 1973, pp. 510-519.

19. Lamont, P.J., "The Out-of-Plane Force on an Ogive-Nosed Cylinder at Large Angles of Inclination to a Uniform Stream," Ph.D Thesis, University of Bristol, 1973.

20. Keener, E.R. and Chapman, G.T., "Onset of Aerodynamic Side Force at Zero Sideslip on Symmetric Forebodies at High Angles of Attack," AIAA Paper No. 74-770, AIAA Mechanics and Control of Flight Conference, Anaheim, Calif., August 1974.

21. Fleeman, E.L. and Nelson, R.C., "Aerodynamic Forces and Moments on a Slender Body With a Jet Plume for Angles of Attack up to 180 Degrees," AIAA Paper No. 74-110, AIAA 12th Aerospace Sciences Mtg., Washington, D.C., February 1974.

22. Jorgensen, L.H. and Nelson, E.R., "Experimental Aerodynamic Characteristics for a Cylindrical Body of Revolution With Various Noses at Angles of Attack from 0° to 58° and Mach Numbers from 0.6 to 2.0," NASA TM X-3128, December 1974.

23. Jorgensen, L.H. and Nelson, E.R., "Experimental Aerodynamic Characteristics for Bodies of Elliptic Cross Section at Angles of Attack from 0° to 58° and Mach numbers from 0.6 to 2.0," NASA TM X-3129, February 1975.

REFERENCES (Continued)

24. Jorgensen, L.H. and Nelson, E.R., "Experimental Aerodynamic Characteristics for a Cylindrical Body of Revolution With Side Strakes and Various Noses at Angles of Attack From 0° to 58° and Mach numbers from 0.6 to 2.0," NASA TM X-3130, March 1975.

25. Smith, L.H. and Nunn, R.H., "Aerodynamic Characteristics of an Axisymmetric Body Undergoing a Uniform Pitching Motion," J. of Spacecraft and Rockets, Vol. 13, No. 1, January 1976, pp. 8-14.

26. Clark, W.H. and Nelson, R.C., "Body Vortex Formation on Missiles at High Angles of Attack," AIAA Paper No. 76-65, AIAA 14th Aerospace Sciences Meeting, Washington D.C., January 1976.

27. Keener, E.R., Chapman, G.T. and Kruse, R.L., "Effects of Mach Number and Afterbody Length on Onset of Asymmetric Forces on Bodies at Zero Sideslip and High Angles of Attack," AIAA Paper No. 76-66, AIAA 14th Aerospace Sciences Mtg., Washington, D.C. January 1976.

28. Baker, D.C. and Reichenau, D.E.A., "Aerodynamic Characteristics of an MX Missile at Free-Stream Mach Numbers From 0.3 to 1.3 and Angles of Attack up to 180 Degrees," AEDC-TR-75-34, April 1975.

29. Deffenbaugh, F.D. and Koerner, W.G., "Asymmetric Wake Development and Associated Side Force on Missiles at High Angles of Attack," AIAA Paper No. 76-364, AIAA 9th Fluid and Plasma Dynamics Conference, San Diego, Calif., July 1976.

30. Bursnall, W.J. and Loftin, L.K., Jr., "Experimental Investigation of the Pressure Distribution About a Yawed Cylinder in the Critical Reynolds Number Range," NACA TN 2463, 1951.

31. Lamont, P.J. and Hunt, B.L., "Out-Of-Plane Force on a Circular Cylinder at Large Angles of Inclination to a Uniform Stream," Aero. J. of the Roy. Soc., Vol. 77, No. 1, January 1973, pp. 41-45.

32. Wardlaw, A.B., Jr., "Prediction of Yawing Force at High Angle of Attack," AIAA J., Vol. 12, No. 8, August 1974, pp. 1142-1144.

33. Lamont, P.J. and Hunt, B.L., "The Out-Of-Plane Force on a Circular Cylinder at Large Angles of Inclination to a Uniform Stream," unpublished manuscript.

34. Tunstall, M.J. and Harvey, J.K., "On the Effect of a Sharp Bend in a Fully Developed Turbulent Pipe Flow," J.F.M., Vol. 34, pt. 3, 1968, pp. 595-608.

35. Smith, L.H. and Nunn, R.H., "Aerodynamic Characteristics of an Axisymmetric Body Undergoing a Uniform Pitching Motion," AIAA Paper No. 75-838, AIAA 8th Fluid and Plasma Dynamics Conference, Hartford, Connecticut, June 1975.

REFERENCES (Continued)

36. Drescher, H., "Messung Der Auf Querange-Strömte Zylinder Ausgeubten Zeitlich Veränderten Druck," Z.F. Flugwiss, Vol. 4, No. 1/2, 1956, pp. 17-21.

37. Naumann, Von A. and Pfeiffer, H., "Uber Die Grenzschichtablösung am Zylinder Bei Hohen Geschwindegkeiten," Advances in Aeronautical Sciences, Vol. 3, 1962, pp. 185-206.

38. Naumann, Von A., Morsbach, M. and Kramer, C., "The Conditions of Separation and Vortex Formation Past Cylinders," AGARD C.P. No. 4, Separated Flows, Pt. 2, May 1966, pp. 547-574.

39. Gerrard, J.H., "An Experimental Investigation of the Oscillating Lift and Drag of a Circular Cylinder Shedding Turbulent Vortices," J.F.M., Vol. 11, Pt. 1, 1961, pp. 244-256.

40. Gerrard, J.H., "The Mechanics of the Formation Region of Vortices Behind Bluff Bodies," J.F.M., Vol. 25, Pt. 2, 1966, pp. 401-413.

41. Bloor, M.S. and Gerrard, J.H., "Measurements on Turbulent Vortices in a Cylinder Wake," Proc. of Roy. Soc., A, Vol. 294, 1966, pp. 319-342.

42. Test Facilities Handbook (Tenth Edition) "Propulsion Wind Tunnel Facility, Vol. 4." Arnold Engineering Development Center, May 1974.

43. Burchfield, C.G., "Asymmetric Vortex-Induced Side Force on an MX Missile at Roll Angles From -10 to 190 Degrees at Free-Stream Mach Numbers From 0.4 to 1.5," AEDC-TR-76-169, December 1976.

44. Baker, D.C. and Reichenau, D.E.A., "Aerodynamic Characteristics of an MX Missile at Free-Stream Mach Numbers From 0.3 to 1.3 and Angles of Attack up to 180 Degrees," AEDC-TR-75-34, April 1975.

45. Baker, D.C., MX Missile Pressure Data at Free-Stream Mach Numbers From 0.3 to 1.3 and Angles of Attack From 5 to 55 Degrees," AEDC-DR-75-99, September 1975.

46. Schwind, R.G. and Mullen, J. "Laser Velocimeter Measurements of Slender Body Wake Vortices," Proceedings From AIAA 17th Aerospace Science Meeting, Paper No. 79-0302, January 1979.

47. Owen, F.K. and Johnson, D.A., "Wake Vortex Measurements of Bodies at High Angle of Attack," Proceedings From AIAA 16th Aerospace Sciences Meeting, Paper No. 78-32, January 1978.

REFERENCES (Concluded)

48. Wardlaw, A.B., Jr., "Prediction of Normal Force, Pitching Moment, and Yawing Force on Bodies of Revolution at Angles of Attack up to 50 Degrees Using a Concentrated Vortex Flow-Field Model," NOLTR 73-209, October 1973.

49. Flaherty, J.I., "Experimental and Analytical Investigation of High Angle of Attack Missile Aerodynamics," Proceedings From AIAA Atmospheric Flight Mechanics Conference, August 1978, Paper No. 77-1156, pp. 311-317.

50. Jorgensen, L.H., "Investigation of Some Wake Vortex Characteristics of an Inclined Ogive-Cylindrical Body at Mach," NACA Report 1371, May 1955.

51. Wardlaw, A.B., Jr., "Multivortex Model of Asymmetric Shedding on Slender Bodies at High Angles of Attack," AIAA Paper 75-123, presented at the AIAA 13th Aerospace Sciences Meeting, January 1975.

52. Bolds, Phyllis G., "Analysis of Unsteady Pressures From Missile Model Wind Tunnel Tests," AFFDL-TR-76-109, December 1976.

53. Przirembel, C.E.G., and Shereda, D.E., "Aerodynamics of Slender Bodies at High Angles of Attack," Journal of Spacecraft and Rockets, January - February 1979.

BIBLIOGRAPHY

(Additional Reports Not Reviewed)

1. Saffell, B.F., Jr., Howard, M.L., and Brooks, E.N., Jr., "A Method for Predicting the Static Aerodynamic Characteristics of Typical Missile Configurations for Angles of Attack to 180 Degrees," R & E Report 3645, 1971, Naval Ship Research and Development Center, Washington, D.C.

2. Atraghji, E.G., "The Influence of Mach Number, Reynolds Number, Semi-Nose Angle, and Roll Rate on the Development of Forces and Moments Over a Series of Long Slender Bodies of Revolution at Incidence," NAE Data Report 5 x 5/00200, 1967, NCR of Canada.

3. Atraghji, E.G., "Pressure Distribution Over a Family of Inclined Long Slender Bodies of Revolution at M = 0.5, 2.0 and 3.5," NAE Data 5 x 5/0029 1968, NCR of Canada.

4. Maltby, R.L. and Peckman, D.H., "Low Speed Flow Studies on the Vortex Patterns Above Inclined Slender Bodies Using a New Smoke Technique," Royal Aircraft Establishment, TN No. AERO 2482, 1956.

5. Crabbe, R.S., "Flow Separation About Elliptic Cones at Incidence," National Research Council of Canada, Aero. Report LR-436, August 1965.

6. Rainbird, W.J., Crabbe, R.S. and Jurewiz, L.S., "A Water Tunnel Investigation of the Flow Separation About Circular Cones at Incidence," National Research Council of Canada, Aero. Report LR-385, September 1963.

7. Rainbird, W.J., "Turbulent Boundary Layer Growth and Separation on a Yawed Cone," AIAA J., Vol. 6, No. 12, December 1968, pp. 2410-2416.

8. Rainbird, W.J., "The External Flow Field About Yawed Circular Cones," AGARD CP. No. 30, May 1968.

9. Washington, D.W., "Correlation of Viscous Effects and Comparison Between Experimental and Theoretical Distribution of Potential Normal Force and Pitching Moment for Bodies of Revolution at Supersonic Speeds," U.S.A.M.C. Redstone Arsenal, Rept. RD-TR-12-67, 1967.

10. Jones, G.W., Cincolta, J.J. and Walker, R.W., "Aerodynamic Forces On a Stationary and Oscillating Circular Cylinder at High Reynolds Number," NASA TR R-300, 1969.

11. Fiechter, M., "Uber Wirbelsysteme An Schlanken Rotations Korpern Und Ihren Einfluss Auf Die Aerodynamischen Beiwerte," Deutsch-Franzosisches Forchungs Institute Saint Louis, Report 10/66, 1966.

BIBLIOGRAPHY (Continued)

12. Carlyle, J.E., "Body Alone Characteristics at Angles of Attack," LMSC, Independent Development Tactical Missile Maneuverability Study, Section 3.3 (TM-55-21-92 LMSC/ 806605), 1967.

13. Carlyle, J.E., "Side Forces on Non-Spinning Bodies of Revolution Flying at Incidences," LMSC, Independent Development Tactical Missile Maneuverability Study, Section 3.4 (TM-55-21-92 LMSC/ 806605), May 1967.

14. Krouse, J.R., "Induced Side Forces on Slender Bodies at High Angles of Attack and Mach Numbers of 0.55 and 0.80," NSRDC Test Rept., March 1971.

15. Barth, H., "Datemblatter Zur Ermittlung Aerodynamischer Beiwerte Schlanker Bug Zulinder-Konfigurationen In Transconischen Geschwindigkeitsbereich" (Data Sheets for Determining the Aerodynamic Coefficients of Slender Nose-Cylinder Configurations in the Transonic Speed Range), Messerschmitt-Bolkow-Blohm, GMSH, TN WE 12-88/70, December 1970.

16. Barth, H., "Datenblatter Zur Ermittlung Von Normalkraft, Momenten and Tangentialkraft Characteristiken Schlanker Bug Zylinder-Konfigurationen In Transsonischen Geschwindigkeitsbereich," (Data Sheets for Determining the Normal Force, Moments and Axial Force Characteristics of Slender Nose-Cylinder-Configurations in the Transonic Speed Range), Messerschmitt-Bolkow-Blohm, GMBH, TN WE2-97/69, December 1969.

17. Keener, E.R., and Taleghani, J., "Wind Tunnel Investigation of the Aerodynamic Characteristics of Five Forebody Models at High Angles of Attack at Mach Numbers from 0.25 to 2.0," NASA TM X-73-076, 1975.

18. Dunn, E.L., "A Low-Speed Experimental Study of Yaw Forces on Bodies of Revolution at Large Angles of Pitch and Zero Side-Slip," Ballistics Division, Aerodynamics Branch, U.S. Naval Ordinance Test Station, TM-1588, 1954.

19. Gapeynski, J.P., "An Experimental Investigation of the Flow Phenomena Over Bodies at High Angles of Attack at a Mach Number of 2.01," NACA RM L55H29, 1955.

20. Hartmann, K., "Aerodynamische Unter Suchungen an Flugkorpern In Transsonischen Geschwindigkeitsbereich," Teil II: Systematische Druckverteilungsmessungen, AVA Bericht 69A 06, 1969.

21. Head, M.H., "Observations of Unsteady Flow Phenomena for an Inclined Body Fitted With Stabilizing Fins," NACA TM A51K05, 1952.

BIBLIOGRAPHY (Continued)

22. Smith, L.H. and Nunn, R.H., "Flow Studies of Axisymmetric Bodies at Extreme Angles of Attack," Naval Postgraduate School, NPS 59 NN 72082A, 1972.

23. Kubin, J.S., "An Analysis of Steady Asymmetric Vortex Shedding From a Missile at High Angles of Attack," M.S. Thesis, Air Force Institute of Technology, November 1973.

24. Baker, W.B., Jr., "Static Aerodynamic Characteristics of a Series of Generalized Slender Bodies With and Without Fins at Mach Numbers From 0.6 to 3.0 and Angles of Attack From 0 to 180 Degrees," AEDC-TR-75-124, Vol. I, II, May 1976.

25. Kellock, R.E. and Miller, P.H., "Aerodynamic Characteristics of Basic Nose-Cylinder Bodies for Large Ranges of Angle of Attack," Louisiana State University, 1971.

26. Munk, M.M., "The Aerodynamic Forces on Airship Hulls", NACA Report 184, 1924.

27. Ashley, H. and Landahl, M., Aerodynamics of Wings and Bodies, Addison Wesley Publishing Co., Inc., New York, 1965.

28. Tsien, H.S., "Supersonic Flow Over an Inclined Body of Revolution," J. of Aero. Sci., Vol. 5, No. 12, Oct. 1938, pp. 480-483.

29. Perkins, E.W. and Jorgensen, L.H., "Comparison of Experimental and Theoretical Normal-Force Distributions (Including Reynolds Number Effects) on an Ogive-Cylinder Body at Mach Number 1.98," NACA RM A54H23, 1954.

30. Jorgensen, L.H., "A Method for Estimating Static Aerodynamic Characteristics for Slender Bodies of Circular and Non-Circular Cross Section Alone and With Lifting Surfaces at α = 0 to 90°," NASA TN D-7228, 1973.

31. Jorgensen, L.H., "Estimation of Aerodynamics for Slender Bodies Alone and With Lifting Surfaces at α = 0 to 90°," AIAA J., Vol. 11, No. 3, March 1973, pp. 409-412.

32. Jorgensen, L.H., "Prediction of Static Aerodynamic Characteristics for Space-Shuttle-Like and Other Bodies at Angles of Attack from 0° to 180°," NASA TN D-6996, 1973.

33. Mello, J.F., "Investigation of Normal Force Distributions and Wake Characteristics of Bodies of Revolution at Supersonic Speeds," J. of Aero. Sci., Vol. 26, No. 3, March 1959, pp. 155-168.

BIBLIOGRAPHY (Continued)

34. Goldman, J.S. and Briggs, M.M., "Distribution Airload Analysis Final Report," McDonnell Douglas Astronautics Co., MDAC Rept. MDC G4S41, March 1973.

35. Kelly, H.R., "The Estimation of Normal Force, Drag, and Pitching Moment Coefficients for Blunt-Based Bodies of Revolution at Large Angles of Attack," J. of Aero. Sci., Vol. 21, No. 8, August 1954, pp 549-555.

36. Schwabe, M., "Pressure Distribution in Non-Uniform Two-Dimensional Flow," NACA TM 1039, 1943.

37. Sarokaya, T., "Separated Flow About Lifting Bodies and Impulsive Flow About Cylinders," AIAA J., Vol. 4, No. 3, March 1966, pp. 414-420.

38. Thomson, K.D., "The Estimation of Viscous Normal Force, Pitching Moment, Side Force and Yawing Moment on Bodies of Revolution at Incidence Up to 90°," Australian WRE-Report-782, October 1972.

39. Edwards, R.H., "Leading Edge Separation From Delta Wings", J. of Aero. Sci., Vol. 21, No. 2, February 1954, pp. 134-135.

40. Hill, J.A.F., "A Non-Linear Theory of the Lift on Slender Bodies of Revolution," NAVORD Report 5338. Proceedings U.S. Navy Symposium on Aeroballistics, 1954.

41. Bryson, A.E., "Symmetric Vortex Separation on Circular Cylinders and Cones," J. of Appl. Mech., Vol. 26, No. 4, December 1959, pp. 643-648.

42. Sarpkaya, T. and Garrison, C.J., "Vortex Formation and Resistance in Unsteady Flow," J. Appl. Mech., Trans. of ASME, Series E, No. 1, Vol. 30, 1963, pp. 16-24.

43. Schindel, L.H., "Effects of Vortex Separation on the Lift Distribution on Bodies of Elliptic Cross Section," J. of Aircraft, Vol. 6, No. 6, November 1969, pp. 537-543.

44. Gerrard, J.H., "Numerical Computation of the Magnitude and Frequency of Lift on a Circular Cylinder," Phil. Trans. Roy. Soc., Vol. 261, January 1967, pp. 137-162.

45. Sarpkaya, T., "An Analytical Study of Separated Flow About Circular Cylinders," J. Basic Eng., Trans. of ASME, Series D, Vol. 90, No. 4, December 1968, pp. 511-520.

46. Laird, A.D.K., "Eddy Formation Behind Circular Cylinders," J. of Hydraulics Div., Proc. of the ASCE, Vol. 97, No. HY6, June 1971, pp. 763-775.

BIBLIOGRAPHY (Concluded)

47. Clements, R.R., "An Inviscid Model of Two-Dimensional Vortex Shedding," J.F.M., Vol. 57, Pt. 2, 1973, pp. 321-336.

48. Angelucci, S.B., "A Multi-Vortex Method for Axisymmetric Bodies at Angle of Attack," J. of Aircraft, Vol. 8, No. 12, December 1971, pp. 959-966.

49. Marshall, F.J. and Deffenbaugh, F.D., "Separated Flow Over a Body of Revolution," J. of Aircraft, Vol. 12, No. 2, February 1975, pp. 78-85.

50. Wardlaw, A.B., Jr., "Multivortex Model of Asymmetric Shedding on Slender Bodies at High Angle of Attack," AIAA Paper No. 75-123, AIAA 13th Aerospace Science Mtg. R-9 Pasadena, Calif., January 1975.

51. Stratford, B.S., "The Prediction of Separation of the Turbulent Boundary Layer," J.F.M., Vol. 5, Pt. 1, January 1959, pp. 1-16.

52. Nelson, R.C. and Fleeman, E.L., "High Angle-of-Attack Aerodynamics on a Slender Body With a Jet Plume," J. of Spacecraft and Rockets, Vol. 12 No. 1, January 1975, pp. 12-16.

53. Kao, H.C., "Side Force on Unyawed Slender Inclined Aerodynamic Bodies," J. of Aircraft, Vol. 12, No. 3, March 1975, pp. 142-150.

54. Fidler, J.E. and Bateman, M.C., "Asymmetric Vortex Effects on Missile Configurations," J. of Spacecraft and Rockets, Vol. 12, No. 11, November 1975, pp. 674-681.

55. Schmidt, L.V., "Measurement of Fluctuating Air Loads on a Circular Cylinder," J. of Aircraft, Vol. 2, No. 1, January 1965, pp. 49-55.

56. Peake, D.J., Rainbird, W.J. and Atraghji, E.G., "Three-Dimensional Flow Separations on Aircraft and Missiles," AIAA J., Vol. 10, No. 5, May 1972, pp. 567-580.

57. Chambers, J.R., Anglin, E.L. and Bowman, J.S., Jr., "Effects of a Pointed Nose on Spin Characteristics of a Fighter Airplane Model Including Correlation With Theoretical Calculations," NASA TN D-5921, 1970.

*U.S.Government Printing Office 1981 -- 757-002/569